

SYNTHESIS OF COBALT-IRON
PHOSPHATE/REDUCED GRAPHENE OXIDE
HYBRID ELECTRODES FOR ELECTROCATALYTIC
WATER SPLITTING

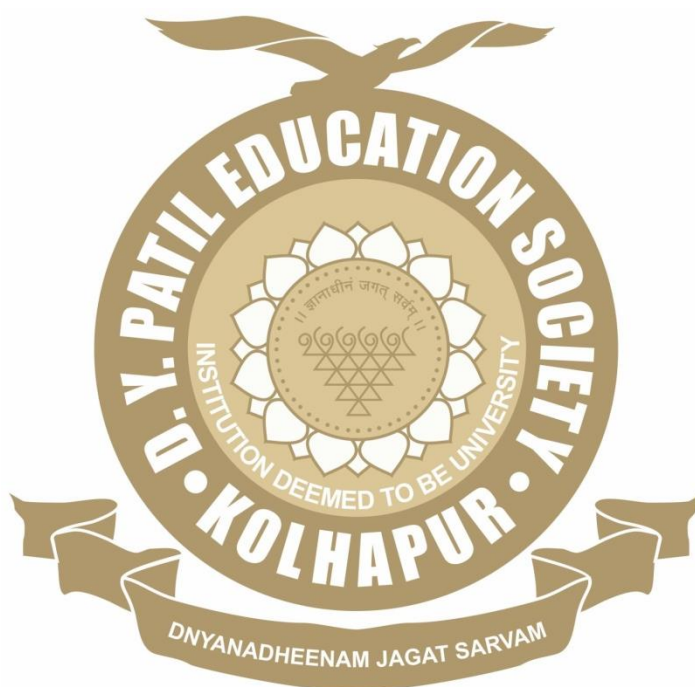
By

Mr. SURAJ ANANDRAO KHALATE

Under the Supervision of

Dr. UMAKANT MAHADEV PATIL

Thesis Submitted to



For the Degree of

Doctor of Philosophy

2021

**SYNTHESIS OF COBALT-IRON PHOSPHATE/REDUCED
GRAPHENE OXIDE HYBRID ELECTRODES FOR
ELECTROCATALYTIC WATER SPLITTING**

A THESIS SUBMITTED

TO

**D. Y. PATIL EDUCATION SOCIETY
(INSTITUTION DEEMED TO BE UNIVERSITY), KOLHAPUR**



FOR THE DEGREE OF

DOCTOR OF PHILOSOPHY

IN

PHYSICS

UNDER THE FACULTY OF

CENTRE FOR INTERDISCIPLINARY STUDIES

BY

Mr. SURAJ ANANDRAO KHALATE

M.Sc.

UNDER THE GUIDANCE OF

Dr. UMAKANT MAHADEV PATIL

M.Sc., Ph.D.

ASSISTANT PROFESSOR, (DST-INSPIRE FACULTY)

CENTRE FOR INTERDISCIPLINARY STUDIES,

D. Y. PATIL EDUCATION SOCIETY

(INSTITUTION DEEMED TO BE UNIVERSITY), KOLHAPUR - 416 006.

YEAR - 2021

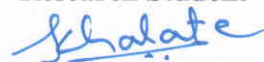
DECLARATION

I hereby declare that the thesis entitled **“SYNTHESIS OF COBALT-IRON PHOSPHATE/REDUCED GRAPHENE OXIDE HYBRID ELECTRODES FOR ELECTROCATALYTIC WATER SPLITTING”** submitted for the award of degree of **Doctor of Philosophy in Physics** under the faculty of **Interdisciplinary studies** of D. Y. Patil Education Society (Institution Deemed to be University), Kolhapur is completed and written by me, has not previously formed the basis for the award of any Degree or Diploma or other similar title of this or any other University in India or any other country or examining body to the best of my knowledge. Further, I declare that I have not violated any of the provisions under Copyright and Piracy/Cyber/IPR Act amended by UGC from time to time.

Place: Kolhapur

Date: 21/10/2021

Research Student



Mr. Suraj Anandrao Khalate

D. Y. Patil Education Society
(Institution Deemed to be University), Kolhapur
Centre for Interdisciplinary Research



Certificate

This is to certify that the thesis entitled ***"Synthesis Of Cobalt-Iron Phosphate/Reduced Graphene Oxide Hybrid Electrodes For Electrocatalytic Water Splitting"*** which is being submitted herewith for the award of the Degree of ***Doctor of Philosophy (Ph.D.) in Physics*** of ***D. Y. Patil Education Society (Institution Deemed to be University), Kolhapur***, is the result of the original research work completed by ***Mr. Suraj Anandrao Khalate*** under my supervision and guidance and to the best of my knowledge and belief the work embodied in this thesis has not formed earlier the basis for the award of any Degree or similar title of this or any other University or examining body.

Place: Kolhapur

Date: 21/10/2024

Research Guide

Dr. Umakant Mahadev Patil

Forwarded through Dean and Research Director

Centre for Interdisciplinary Studies

Prof. C. D. LOKHANDE

Dean

Centre For Interdisciplinary Studies

D. Y. Patil Education Society

(Institution Deemed to be University)

869, 'E', Kasaba Bawada

KOLHAPUR- 416006

ACKNOWLEDGEMENT

I can introduce and thank with deep sense to the unique & genius personality, my beloved research supervisor, respectable Dr. Umakant M. Patil (DST-INSPIRE Faculty, Centre for Interdisciplinary Studies, D. Y. Patil Education Society (Institution Deemed to be University), Kolhapur). It gives me great pleasure to express my sincere gratitude for his supervision, support and encouragement. I salute him to his keenness, high-quality research work and deep quest for scientific knowledge. I express huge gratitude to him not only for the research supervision granted during my Ph.D. course but also for shaping and illuminating the path of my life with deep care, strictness, love, affection, partial anger along with huge humanity by his stunning support. I honestly thank him for his valuable advice, constructive criticism and his extensive discussions about my work. I gratefully acknowledge for his understanding and personal attention, which have provided good and smooth basis for my Ph.D. tenure. His flexibility in scheduling, gentle encouragement and relaxed behavior made for a good working relationship and the impetus for me to finish the work. With his kind support in educational, economic and social stages, I could overcome my personal and scientific troubles. This work could not have been completed without his inspiring supervision and continuous encouragement during the course of research tenure. I am indisputably very much fortunate to have him as my Ph.D. guide.

I sincerely thankful to Prof. C. D. Lokhande, Dean and Research Director, Centre for Interdisciplinary Studies, D. Y. Patil Education Society (Institution Deemed to be University), Kolhapur for generous support, very fruitful discussions, helpful guidance and constructive compliments helped me to achieve the goal.

I would like to express my sincere thanks to Vice-Chancellor Prof. Rakesh Kumar Mudgal, Pro-Vice-Chancellor Dr. Shimpa Sharma and Registrar Dr. V. V. Bhosale for their timely inspiration and support by the motivational speeches on Time Management and research methodology.

I am also thankful to the great scientific personalities Dr. J. L. Gunjekar, Dr. Vishwajeet Khot and Dr. P. N. Pawaskar for their fruitful discussions, valuable suggestions and conducting extracurricular activities during my Ph.D. work. I am very much thankful to all teaching and non-teaching staff of the Centre for Interdisciplinary Studies for their co-operation during my research work.

Exceptional thanks goes to Dr. Sachin B. Kulkarni (Asst. Prof., Tuljaram Chaturchand College, Baramati) for continuous support, brainstorming and fruitful talks, valuable discussions along with characterization facility in his research laboratory.

I would like to express sincere thanks to, my beloved friend Mr. Sujit A. Kadam and his professor, Prof. Yuan-Ron Ma (Dean and Research Director, Department of Physics, National Dong Hwa University, Hualien, Taiwan). Also, Dr. Abhishek C. Lokhande (Applied Quantum Materials Laboratory (AQML), Department of Physics, Khalifa University of Science and Technology, Abu Dhabi, United Arab Emirates) and Dr. Vinayak G. Parale (Department of Materials Science and Engineering, Yonsei University, Seoul, South Korea) for providing me very important sample characterization data, during entire research work.

I would like to extend my thanks to my seniors, colleagues, juniors and Pratik (Tuljaram Chaturchand College, Baramati) who helped me with all possible ways during my work, unforgettable and spectacular patronage.

I acknowledge and express my honest thanks to the Chhatrapati Shahu Maharaj Research Training and Human Development Institute (SARTHI), Pune (Government of Maharashtra) for awarding me as “SARTHI FELLOW” and the financial support under the Chhatrapati Shahu Maharaj National Research Fellowship (CSMNRF-2019).

I hereby express my innermost faithful gratitude and regards to my dearly loving “Mommy-Bhau”. My affable salutation goes to my simple-straightforward father, caring and loving mother, brother and sisters for inexpressible things. Also, I thankful to all my family members, who continuously supported and encouraged me to complete my research.

- Suraj

SUMMARY OF RESEARCH WORK LIST OF PUBLICATIONS

Papers Accepted in International Journals

1. **Suraj A. Khalate**, Sujit A. Kadam, Yuan-Ron Ma, Sachin S. Pujari, Supriya J. Marje, Pranav K. Katkar, Abhishek C. Lokhande, Umakant M. Patil, "Hydrothermally synthesized Iron Phosphate Hydroxide thin film electrocatalyst for electrochemical water splitting" *Electrochimica Acta* 319 (2019) 118-128 (**I.F. - 6.901**).
2. **Suraj A. Khalate**, Sujit A. Kadam, Yuan-Ron Ma, Sachin S. Pujari, Umakant M. Patil, "Cobalt doped iron phosphate thin film: An effective catalyst for electrochemical water splitting" *Journal of Alloys and Compounds* 885 (2021) 160914 (**I.F. - 5.316**).
3. Supriya J. Marje, Pranav K. Katkar, Sachin S. Pujari, **Suraj A. Khalate**, Prashant R. Deshmukh, Umakant M. Patil, "Effect of phosphate (anion) precursor on structural and morphology behavior of nickel phosphate thin films and its supercapacitive performance" *Materials Science & Engineering B* 261 (2020) 114641 (**I.F. - 4.051**).
4. Pranav K. Katkar, Supriya J. Marje, Sachin S. Pujari, **Suraj A. Khalate**, Abhishek C. Lokhande, Umakant M. Patil, "Enhanced Energy Density of All-Solid-State Asymmetric Supercapacitors Based on Morphologically Tuned Hydrous Cobalt Phosphate Electrode as Cathode Material" *ACS Sustainable Chemistry and Engineering* 7 (2019) 11205-11218 (**I.F. - 8.198**).
5. Supriya J. Marje, Pranav K. Katkar, Sachin S. Pujari, **Suraj A. Khalate**, Abhishek C. Lokhande, Umakant M. Patil, "Regulated micro-leaf like nickel pyrophosphate as a cathode electrode for asymmetric supercapacitor" *Synthetic Metals* 259 (2020) 116224 (**I.F. - 3.266**).
6. Sachin S. Pujari, Sujit A. Kadam, Yuan R. Ma, **Suraj A. Khalate**, Pranav K. Katkar, Supriya J. Marje, Umakant M. Patil, "Highly sensitive hydrothermally prepared nickel phosphate electrocatalyst as non-enzymatic glucose sensing electrode" *Journal of Porous Material* (2020) (**I.F. - 2.496**).
7. Pranav K. Katkar, Supriya J. Marje, Sachin S. Pujari, **Suraj A. Khalate**, Prashant R. Deshmukh, Umakant M. Patil, "Single-pot hydrothermal synthesis of manganese phosphate microrods as a cathode material for highly stable flexible solid-state symmetric supercapacitors" *Synthetic Metals* 267 (2020) 116446 (**I.F. - 3.266**).
8. Sachin S. Pujari, Sujit A. Kadam, Yuan-Ron Ma, Pranav K. Katkar, Supriya J. Marje, **Suraj A. Khalate**, Abhishek C. Lokhande, Umakant M. Patil, "Facile Synthesis of Microstrip-Like Copper Phosphate Hydroxide Thin Films for Supercapacitor Applications" *Journal of Electronic Materials* 49 (2020) 3890-3901 (**I.F. - 1.938**).

NATIONAL/INTERNATIONAL CONFERENCES

1. National Conference on Advanced Materials Synthesis, Characterization and Applications (AMSCA-2018) organized by Dept. of Physics, SPPU, Pune during 14-15 Dec. 2018.
2. 4th International Conference on Physics of Materials and Materials Based Device Fabrication (4th ICPM-MDF-2019) held at Dept. of Physics, Shivaji University, Kolhapur during 10-11 Jan. 2019.
3. International E-conference on Cutting Edge Smart Materials & Nanotechnology (ICCESMN-2020) organized by Sadguru Gadage Maharaj College, Karad during 20-21 Aug. 2020.
4. International Virtual conference on Advances in Functional Materials (AFM-2020) held on 26-28 Aug. 2020 at KIIT, Bhubaneswar, Odisha.
5. One Day International Webinar on “Recent Scenario in Energy Generation and Storage Technologies” (IWRSEGST-2020)” held on 5th Sept. 2020 at Dahiwadi College, Dahiwadi, Maharashtra.
6. International Symposium on New Research Horizons in Nano and Radiation Materials, held on 10-11th Sept, 2020 organized by Dada Patil Mahavidyalaya, Karjat.
7. International web conference on Advanced Nanostructured Materials for Energy Generation, Storage and Smart Applications, held on 09-10 Oct, 2020 organized by Shardabai Pawar Mahila Arts, Commerce and Science College, Shardanagar, Baramati.
8. Asian e-Conference on 'Engineered Science' 2020 held online on 5-6 December 2020.

CONTENTS

Chapter No.	Chapter Name	Page No.
I	Introduction to electrochemical water splitting and review of literature	1-36
II	Theoretical background of material synthesis methods and characterization techniques	37-68
III	Hydrothermally synthesized cobalt-iron phosphate and cobalt-iron phosphate/reduced graphene oxide hybrid for electrochemical OER and HER application	69-112
IV	SILAR deposited cobalt-iron phosphate and cobalt-iron phosphate/reduced graphene oxide hybrid for electrochemical OER and HER application	113-154
V	Cobalt-iron phosphate/reduced graphene oxide hybrid electrodes for overall water splitting	155-166
VI	Summary and conclusions	167-174

List of Abbreviations

AC	Alternating current	LSV	Linear sweep voltammetry
ASTM	American standard for testing of materials	NMP	N-methyl 2-pyrrolidone
BET	Brunauer-Emmett-Teller	NRs	Nanorods
BJH	Barrett-Joyner-Halenda	NSs	Nanosheets
CA	Chronoamperometry	NTs	Nanotubes
CC	Carbon cloth	NWs	Nanowires
C_s	General specific capacitance	NCF	Nanocarbon floret
CFP	Carbon fibre paper	NF	Nickel foam
CBD	Chemical bath deposition	OCP	Open circuit potential
C_{dl}	Double layer capacitance	OER	Oxygen evolution reaction
CVD	Chemical vapor deposition	PEC	Photoelectrochemical
CV	Cyclic voltammetry	PVDF	Polyvinylidene fluoride
DC	Direct current	PGF	Porous graphene film
DDW	Double distilled water	rGO	Reduced graphene oxide
E⁰	Standard cell potential	RF	Roughness factor
ECSA	Electrochemically active surface area	R_{ct}	Charge transfer resistance
EIS	Electrochemical impedance spectroscopy	R_s	Solution resistance
EDS	Energy dispersive X-ray spectroscopy	RHE	Reversible hydrogen electrode
E_B	Binding energy	SCE	Saturated calomel electrode
FESEM	Field emission scanning electron microscopy	SDBS	Sodium dodecylbenzenesulphonate
FTO	Fluorine doped tin oxide	SILA	Successive ionic layer adsorption and reaction
FTIR	Fourier transform infrared	R	Stainless steel
GCE	Glassy carbon electrode	SS	Transparent conducting oxide
GF	Graphene foam	TCO	Transparent conducting oxide
GO	Graphene oxide	W	Warburg diffusion impedance
HER	Hydrogen evolution reaction	XRD	X-ray diffraction
j	Current density	XPS	X-ray photoelectron spectroscopy
JCPDS	Joint committee on powder diffraction standards		

CHAPTER – I

INTRODUCTION TO ELECTROCHEMICAL WATER SPLITTING AND REVIEW OF LITERATURE

CHAPTER – I

INTRODUCTION TO ELECTROCHEMICAL WATER SPLITTING AND REVIEW OF LITERATURE

Contents

Sr. No.	Title	Page No.
1.1	Introduction to the topic	3
1.2	Electrochemical water splitting	4
1.3	Mechanism of reactions	6
1.3.1	Mechanism of oxygen evolution reaction (OER)	6
1.3.2	Mechanism of hydrogen evolution reaction (HER)	7
1.4	Performance parameters for HER and OER electrocatalysts	7
1.4.1	Overpotential	7
1.4.2	Tafel slope	8
1.4.3	Stability	8
1.5	Research objectives	9
1.6	Literature review	10
1.6.1	Literature of cobalt phosphate	12
1.6.2	Literature of iron phosphate	18
1.6.3	Literature of cobalt-iron phosphate	20
1.7	Orientation and purpose of the dissertation	23
1.8	Thesis outline	25
1.9	References	27

1.1 Introduction to the topic: Increase in energy demand exceeds to a serious value due to gradually rising population. There is need to generate energy at local level to cut down the cost and associated risks with storage of energy and transportation [1]. Due to depletion of fossil fuels and increase in the worldwide energy demand, fuel cell technologies gained the attention of researchers. More than 78% of energy demand of this power-hungry world is fulfilled by non-renewable energy sources [2]. The non-renewable sources such as natural gas, coal and oil contributes significant portion of energy production, followed by nuclear, hydro dynamical and sustainable energy sources. The pie chart shown in **Figure 1.1** illustrates the energy conversion from numerous sources.

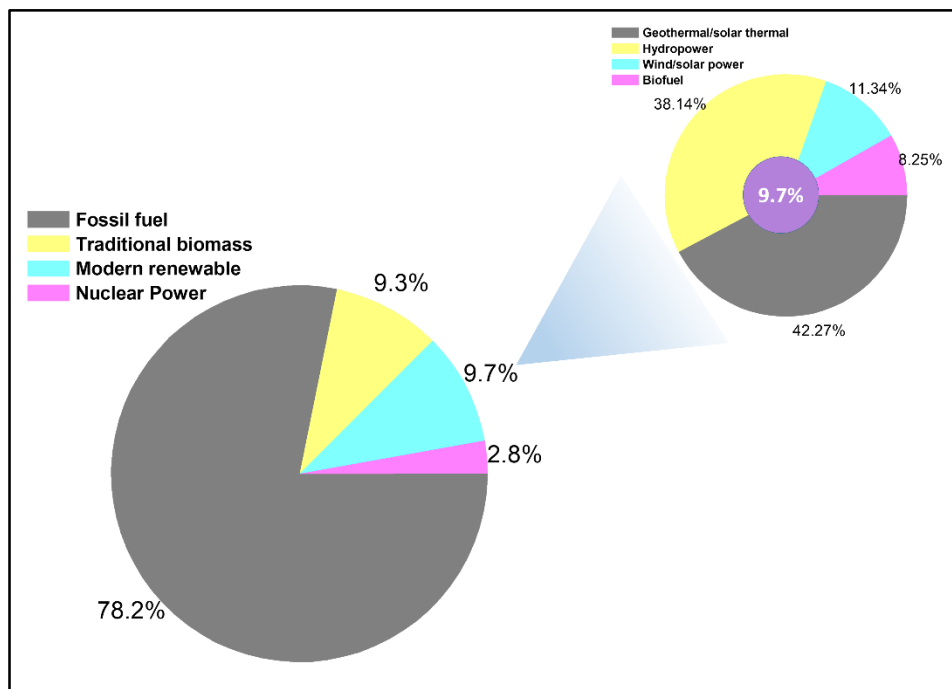


Figure 1.1: Shares of current energy production of year 2019.

Because of considerable utilization of fossil fuels in the last 50 years, the possibility of end of these sources is increased. Among all the various non-renewable energy sources, fossil fuels are serious candidate for other sources. The major difficulty raised due to non-renewable energy sources is their remarkable impact on environment. Composition of planetary atmosphere affect the temperature of planetary surface [3]. This impression is in terms of emitted carbon dioxide which is a strong greenhouse gas responsible for habitable temperature range on the earth's surface. Broadly, the atmospheric concentration of greenhouse gases can be categorized into different gases and have progressively increasing over the last century [4]. Yearly, more than 30 giga metric tons of carbon dioxide is

produced due to consumption of fossil fuels. The ordinary carbon cycle is the carbon-flow between the atmosphere and oceans, and the fixation of CO₂ by plants and microorganisms, which is well-adjusted by emission of CO₂ from plants, animals and volcanoes [5]. Rapid expansion of sea levels, increase in precipitation and melting of ice at earth's poles are some dreadful impacts caused by greenhouse gases worldwide [6]. According to available literature, there is excess of approximately 3.9 % CO₂ with respect to ordinary carbon cycle and 1.9 °C rise in universal mean temperature [7,8].

Hazardous effects of CO₂ emission and global warming awakened human being to utilize clean and eco-friendly renewable energy sources in place of harmful non-renewable energy sources. The available key pathways are (i) solar energy as radiation and heat, (ii) geothermal energy, (iii) nuclear energy, (iv) ocean tidal energy [9,10]. Therefore, there is huge focus towards the renewable energy production via various sources like wind [11], solar [12], hydro-dynamical [13], tidal [14] and geothermal [15]. Produced renewable energy can be utilized in the electrical energy form to stopover the global energy crisis and minimize environmental problems. Among various cleanest renewable energy sources, hydrogen is the prospective energy source which can be produced by electrolysis of water in the byproduct of oxygen and hydrogen energy is profitable to catch renewable energy [16-19]. Therefore, hydrogen has been proposed as possibly the main carrier for the new wave of renewable form of energy and has been termed as the hydrogen economy [20,21] or more recently transitioning to a hydrogen society [22-24]. Various methods are used to produce hydrogen from different sources such as, steam reforming of natural gas, oxidation of methane, coal gasification, carbon/hydrocarbon assisted water electrolysis, radiolysis, thermolysis, photobiological water splitting, photocatalytic water splitting, fermentative hydrogen production, enzymatic hydrogen generation, biocatalysed electrolysis, etc. [16, 25-33]. Among all the production processes, electrochemical water splitting to produce oxygen and hydrogen is the economical and effective pathway [17-19].

1.2 Electrochemical water splitting: The process of splitting liquid water into hydrogen and oxygen with the help of electricity, commonly known as electrolysis, is widely studied catalytic approach for oxidation of water, predating even the development of the concept of chemical catalysis. Electrochemical water splitting mainly involves two half-reactions: hydrogen evolution reaction (HER) on the cathode and oxygen evolution reaction (OER) on the anode as shown schematically in **Figure 1.2**. The theoretical potential of 1.23 V ($\Delta G = 237.2$ kJ/mol) is required to initiate water splitting [34,35].

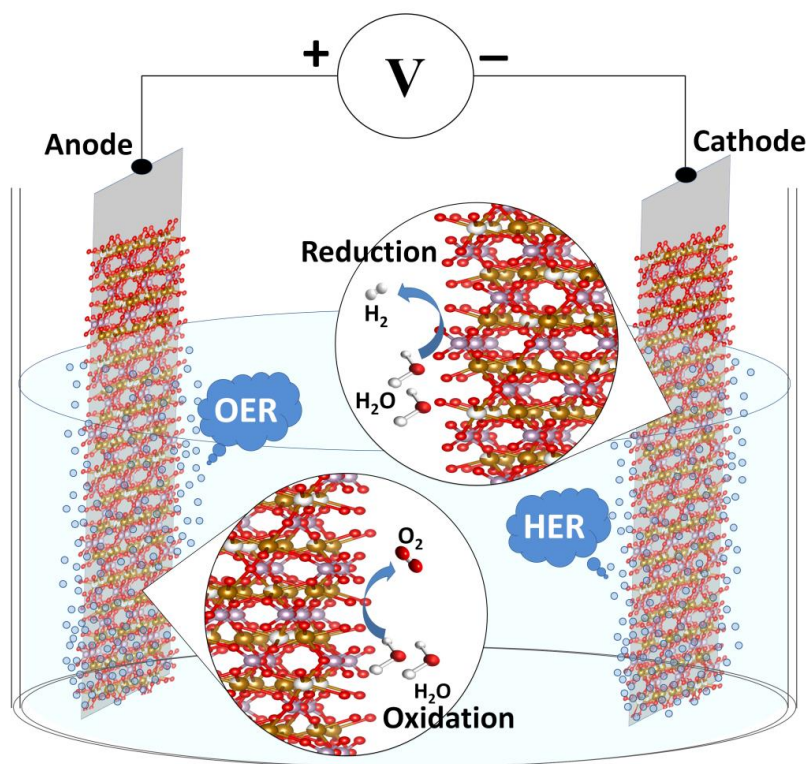


Figure 1.2: Schematic representation of overall water splitting by electrolysis process using a cathode and an anode electrode.

To begin the reaction, there is requirement of additional voltage between the cathode and anode owing to kinetics effects. On that account, researchers have taken lot of efforts to develop outstanding catalyst to reduce the overpotential for overall water splitting. To split water an activation energy barrier needs to be overcome which requires excess energy or in electrochemical terms an overpotential. However, the thermodynamics does not favor the direct decomposition of water into hydrogen and oxygen under normal temperature and pressure. Even though the HER process is much promising in acidic electrolytic environment, the overall splitting of water depending on non-noble metal catalysts is generally worked out using alkaline solution medium. Therefore, the whole reaction for water splitting is given as follows [36]:



The reduction process at the cathode (HER) proceeds according to:



while the oxidation process (OER) at the anode of the electrolyzer is:



In the total process, two electrons are transferred per formula or a total charge of 192928 C ($=2 F$) crosses the electrocatalytic interface per mole of water converted.

1.3 Mechanism of reactions: As described above, the electrochemical splitting of water involves two simultaneous catalytic half-cell reactions according to the equation (1.2) (HER) and equation (1.3) (OER). Clearly, oxygen evolution being a 4 electron process is more complex as compared to the evolution of hydrogen and involves several surface adsorbed intermediates [37,38]. As either process may contribute to voltage and efficiency losses, a discussion of the electrocatalysis of water splitting should in principle touch upon both the HER and OER. In electrochemical environments, HER on selected noble metals shows extremely high exchange current densities (J_0), which is a measure of the intrinsic turnover frequency of an electrochemical half-cell process. On Pt electrodes, HER shows values of J_0 up to several hundred mA/cm^2 [39], resulting in a very reversible half-cell electrode with high forward and backward reaction rates. However, OER on Pt, the catalytically most active element for this reaction, exhibits values of J_0 in the order of $10^{-9} \text{ A}/\text{cm}^2$, and that is why much recent work has shifted toward OER kinetics.

1.3.1 Mechanism of oxygen evolution reaction (OER): The electrochemical OER processes differently in different media. Oxidization of water into oxygen and hydrogen ions occurs in acidic solution whereas oxidation of hydroxyl ions into water and oxygen take place in neutral and alkaline solutions. The thermodynamic potential value of OER is 1.23 V at 25 °C vs RHE independent of the medium in which OER takes place. However, we generally must apply a higher potential to expedite the electrochemical OER, in comparison to the thermodynamic potential value, thus resulting in the consumption of excess energy and decreasing the conversion efficiency [38]. The extra potential (also called overpotential) (η), is mainly caused by the intrinsic reaction activation barriers and some other resistances like solution resistance (R_s) and contact resistance. Thus, it is highly desirable to develop highly efficient and cost-effective electrocatalysts for the OER. In comparison to HER, the reaction kinetics of OER is much sluggish and complicated due to involvement of three adsorption intermediate states viz. OOH^* , O^* and OH^* . The OER mechanism begin with dissociation of H_2O in acidic electrolytes or coordination of $-\text{OH}$ species in alkaline solution. The second step involves oxidization of OH^* into O^* , O^* into OOH^* and lastly OOH^* into O_2 . In alkaline media, the projected path of 4-electron reaction is as follows:



Where, * signifies the active site of the surface of catalyst, OOH*, O* and OH* are the adsorption intermediates of each step.

1.3.2 Mechanism of hydrogen evolution reaction (HER): HER consist of two steps. In acidic medium, HER begins by the Volmer step in which hydrogen intermediates (H*) developed from discharge of hydronium ions, get adsorbed on the catalysts; subsequently evolution of hydrogen take place by either the chemical Tafel recombination step or the electrochemical Heyrovsky step [40]. Thus, the Volmer-Tafel mechanism and the Volmer-Heyrovsky mechanism are the two mechanisms for HER in both acidic and alkaline media, which can be determined by Tafel slope drawn from experimental plot of overpotential vs $\log[\text{current density (mA/cm}^2)]$ [41]. The HER process in alkaline electrolyte is analogous excepting that H* is generated by discharge of water molecule [40]. By taking acidic electrolytes as an example, the two-step process of HER is as follows:



Where, step 1 reaction is Volmer reaction and step 2 reaction is Tafel reaction. * signifies the surface of catalysts, H* is absorbed hydrogen intermediates [42,43].

1.4 Performance parameters for HER and OER electrocatalysts:

1.4.1 Overpotential: In comparison with the equilibrium potential of HER (0 V vs RHE) and OER (1.23 V vs RHE), both the reactions require some additional potential known as overpotential, to initiate the reaction because of kinetic barrier. There are three types of overpotentials such as activation overpotential, concentration overpotential and resistance overpotential which contribute to the total values [44,45]. One need to minimize the overpotentials and can be minimized by several methods. Selection of appropriate material can significantly lower the activation potential of catalyst. Concentration potential can be

decreased by stirring the electrolyte solution while performing electrochemical test. The minimization of resistance overpotential can be achieved by iR compensation from electrochemical workstation or manual retraction from original data by multiplication of current density and resistance calculated from Nyquist equation as:

$$E = E^0 - \frac{RT}{nF} \ln Q \quad (1.10)$$

Where, E (V) is the cell potential at a temperature T (K), E^0 is the standard cell potential, R is the universal gas constant ($R = 8.31446$ J/K.mol), n is the number of electrons transferred in the cell reaction or half-reaction, F is the Faraday constant, the number of coulombs per mole of electrons: $F = 96485.332$ C/mol, and Q is the reaction quotient of the cell reaction which measures the relative amounts of products and reactants present during a reaction at a particular point in time.

1.4.2 Tafel slope: Tafel slope demonstrates the ability of charge transfer. Higher charge transfer ability gives lower Tafel slope. There are two different methods to obtain Tafel slope, either by replotting the polarization plot by the logarithmic of absolute values of current density versus overpotential or by electrochemical impedance spectroscopy (EIS) method, logarithmic of reciprocal of charge transfer resistance (R_{ct}) versus overpotential [46]. Equation (1.11) represents the linear equation for Tafel slope as follows:

$$\eta = a + b \log(j) \quad (1.11)$$

Where, η , j , b and a are the overpotential, current density, Tafel slope and Tafel constant, respectively [44]. While plotting logarithm of steady state current density recorded at various potentials vs. overpotential one must consider the linear portion of the plot that follows above equation. Tafel slope is the slope of the linear portion of $\log(1/R_{ct})$ vs. η plot or can be calculated from equation (1.11), indicates the charge transfer capability. As R_{ct} only reveals the charge transfer ability, Tafel slope obtained from $\log(1/R_{ct})$ vs. η is closer to its real value [41].

1.4.3 Stability: Stability, a significant parameter for catalysts, can be calculated either by cyclic voltammetry (CV) or electrolysis technique (amperometric or potentiometric electrolysis). CV is generally performed over large number of cycles (thousands of cycles for HER and hundreds of cycles for OER) and is also known as accelerated degradation test [45]. The stability of catalyst is determined from shift of overpotential. When

amperometric or potentiometric electrolysis is applied for stability test, it normally continues for at least 10 h. The decrease in the current density at a constant potential or the rise in the overpotential at a constant current density (typically at 10 mA/cm²) displays the stability of the catalysts. Small shift in current density or overpotential results in better stability. Till now, some researchers have studied electrocatalysis for several catalysts over four days (96 h) or more [47].

As demonstrated above in equations (1.4-1.7), the OER requires a large potential to drive the four electron oxidation of water to oxygen at the anode interface. Electrocatalysts play an important role in facilitating this reaction by increasing the kinetics of electron transfer. Usually the overpotential for oxygen evolution is defined as the potential required to facilitate the reaction above the value of 1.23 V within the range of 0.3 ~ 0.5 V vs. RHE. In contrast the overpotential required to drive the HER is essentially 0 V vs. RHE at the Pt electrode interface. However, Pt being an expensive material gives rise to the question of cost effectiveness. Noble metal-based expensive catalyst materials as the state-of-the-art like platinum (Pt), ruthenium (Ru) and iridium oxide (IrO₂) stamped as top OER catalysts because of their low overpotential, good current density, low Tafel slope, etc. [48-51]. However, these widely used noble metal based catalysts suffers instability in both acidic and alkaline electrolyte media at higher potentials with degradation, oxidization, corrosion, sintering and dissolution of catalysts [52-55]. Nevertheless, noble metals have very rare resources available in the earth's crust and hence are very expensive; also, these catalysts have poor OER performance at higher current densities in alkaline medium than transition metal based catalysts [56-59]. Besides other factors such as ion mobility and concentration, contact resistance, surface hindrance, bubble formation, entropy, etc. generate additional barriers which need to be overcome during the water splitting reaction and contribute to the overpotential required to facilitate the reaction. Other precious materials for example ruthenium (Ru) and iridium (Ir) and their oxides in acidic medium and first row transition metal oxides in alkaline medium have been identified as efficient OER electrocatalysts [60]. Hence, the researchers focused their efforts towards finding alternatives to the expensive noble metal based catalysts, with best electrocatalytic performance and high stability.

1.5 Research objectives: The main objective of this research work was to develop cobalt-iron phosphate and their hybridization with reduced graphene oxide (rGO) i.e. cobalt-iron phosphate/reduced graphene oxide hybrid electrodes which can work as efficient

electrocatalysts for OER, HER and overall water splitting. Also, a major objective of this work was to focus on an effective method for synthesizing electrocatalysts while maintaining high activity towards the OER and HER with a low overpotentials and long term stability. A hydrothermal and Successive Ionic Layer Adsorption and Reaction (SILAR) methods were proposed to synthesize the cobalt-iron phosphate/reduced graphene oxide hybrid catalysts on conducting substrates like stainless steel (SS) for the present research work. It is also expressively important to get the detailed understanding of the electrochemical behavior of deposited cobalt-iron phosphate/reduced graphene oxide hybrid electrodes for their application as catalyst for overall water splitting. The synergistic effect between two metals and between metal phosphate and rGO on the OER and HER in alkaline and acidic media, respectively was thoroughly investigated. Also, the full cell overall water splitting in alkaline medium was demonstrated by using synthesized electrocatalysts for commercial application. Furthermore, the variation in compositional ratio of cobalt and iron and their synergistic effect on overpotential for water splitting were examined. Additionally, hybrid electrodes were prepared by adding rGO at different concentrations in the cobalt-iron phosphate samples at optimized conditions and studied thoroughly to split water electrochemically in the form of OER and HER.

In order to understand the activity of transition metal based HER and OER electrocatalysts, properties such as size, shape, porosity, crystallographic orientation, phase, composition, etc. were also explored. All these above mentioned investigations were mainly focused in the search of the synergistic effects between metal-metal phosphate, metal phosphate and rGO for efficient hydrogen and oxygen evolution to support a robust electrochemical water splitting reaction.

1.6 Literature review: Up to now various transition metals such as nickel, cobalt, iron, manganese, vanadium, copper, zinc, molybdenum, chromium, titanium, tungsten, etc. and their compounds such as oxides, hydroxides, sulphides, selenides, nitrides, phosphides, borides, carbides, etc. show diverse performances for electrochemical water splitting [61-78]. But, they suffer from low electrochemical performance, due to poor electrical conductivity and self-high electrical resistance and hence slow ion transfer rate [79-81]. There is an urgent need to develop alternative versatile materials for electrochemical water splitting which have low cost, high abundance, and high electrochemical performance.

Transition metal phosphates have wide variety of applications such as solar cells, supercapacitors, batteries, catalysts, gas, humidity and glucose sensors, glasses, fuel cells, metal-air batteries, etc. due to their attractive dominance regarding higher reaction kinetics and superior structure/performance stability. Apart from all these applications, transition metal phosphate materials have attracted substantial attention in the applications of electrochemical energy conversion and storage, and have great potential to overcome the problems regarding achievement of lower overpotentials for OER and HER. Incorporation of carbon based materials with transition metal based materials gives the effective electrochemical performance. Many metal phosphate materials are mainly found outstanding electrical conductivity and metalloid characteristics, some of them are highly abundant and eco-friendly [82,83]. In addition, electronic and electrochemical properties of the electrodes are highly affecting by the surface morphological, crystallographical open structures and surface activation and reconstruction properties [84-88]. Therefore, metal phosphates have expectation about their candidature for electrode material for several applications. Comparing with metal oxides/hydroxides, metal phosphates are dynamic for ease electron transport [89,90]. Many metal phosphates and phosphides demonstrate electrical conductivity to a large extent or flexibility in terms of fine-tuning the micro and nanostructures [91,92].

From last few years, transition metal phosphates as i) single-metal phosphate, ii) di-metal phosphate, iii) tri- and multi-metal phosphate, and iv) metal phosphates coupled with carbon based materials (i.e. composite/hybrid) as shown in **Figure 1.3** are studied for water splitting and also for energy storage devices. Verity of compounds of different transition metals such as, nickel, cobalt, iron, manganese, etc. have been reported with OER and HER mechanisms for electrochemical water splitting. Due to structural properties of metal phosphate materials, it can be able to enhance the catalytic performance with reducing the overpotential and Tafel slope with enhanced catalytic stability. Most of the researchers have reported single metal phosphate materials for catalytic water splitting since they are ease to synthesize. Cobalt phosphate and iron phosphate are effective catalysts for OER in alkaline solution, their electrochemical properties are reviewed and tabulated further in **Table 1.1** and **Table 1.2**. Similarly, few research groups have worked and reported very good results for di-metal phosphate (cobalt-iron phosphate) materials in application of water splitting because both transition metals show synergistic effect for water splitting (**Table 1.3**). Here,

some reports on cobalt phosphate, iron phosphate and cobalt-iron phosphate materials are discussed briefly.

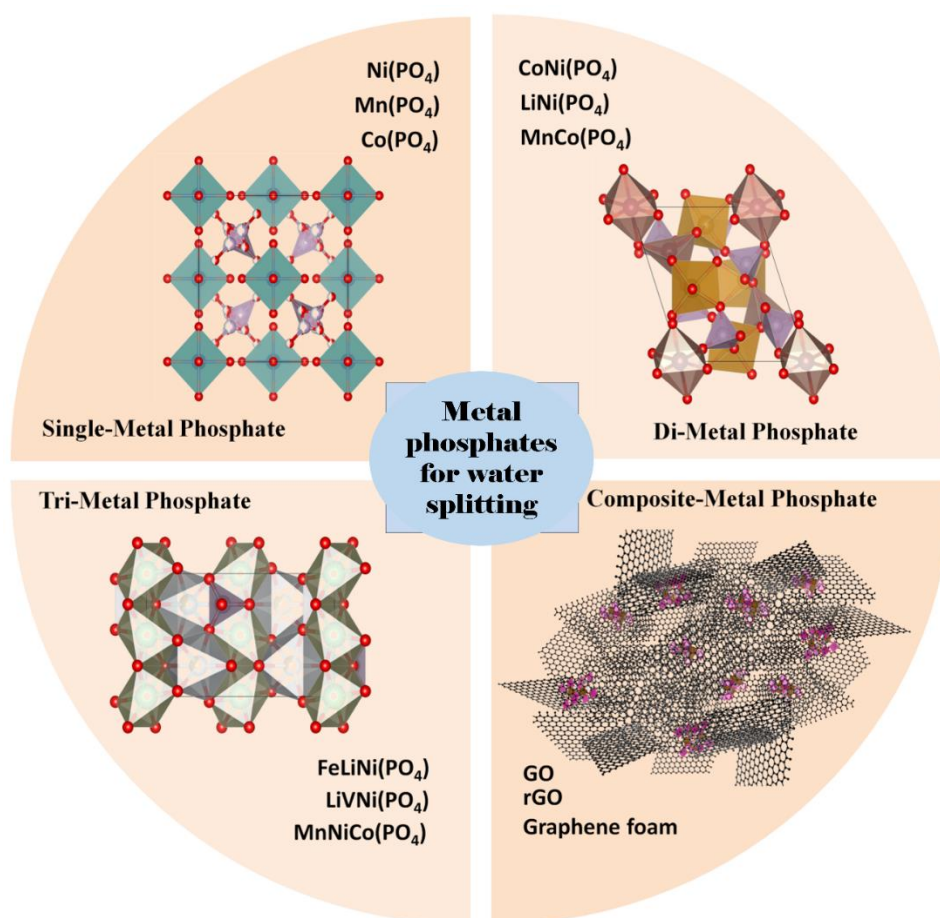


Figure 1.3: Schematic of various transition metal phosphate materials in application of water splitting.

1.6.1 Literature of cobalt phosphate: As per the literature, cobalt phosphate is a good electrocatalyst for water splitting. Chen et. al. [93] prepared hollow spherical hybrids composed of cobalt phosphate and sufficient heteroatoms-doped carbon by the direct pyrolysis of organic-inorganic cobalt phosphonate. The as-prepared hollow spherical hybrids composed of cobalt phosphate exhibited extraordinary electrocatalytic activity for OER with overpotential of 320 mV to attain 10 mA/cm^2 and robust stability in alkaline conditions. Katkar et. al. [94] reported hydrous cobalt phosphate thin films synthesized by varying concentration of urea as oxydizing agent using one pot hydrothermal method on SS substrates at 393 K. Upon urea variation, morphological modification was observed as the changes in thickness and width, resulted in transformation of microplates into microflakes. The remarkable electrocatalytic performance of hydrous cobalt phosphate thin

films were observed towards the OER and exhibited overpotential of 292 mV (vs. RHE) to attain 10 mA/cm² current density with a Tafel slope of 98 mV/dec in 1 M potassium hydroxide (KOH) electrolyte and showed electrochemical stability for 10 h with 10 mA/cm² constant current density. The in-situ formed heterostructural Co₁₁(HPO₃)₈(OH)₆/Co₁₁(PO₃)₈O₆ core-shell structured nanowires (NWs) with microporous 1D channels were synthesized with remarkable catalytic performance of overpotential of ~340 mV and Tafel slope of 60 mV/dec to achieve 10 mA/cm² at pH-14 [95]. A facile and scalable technique, to anodically fabricate Co oxide porous thin film followed by reaction with phosphorus vapor to convert the oxides into Co phosphide/phosphate without the collapse of the ordered porous structure, was developed by Yang et. al. [96]. In this synthesis process, Co was electrodeposited on plasma treated glass substrate coated with gold and chromium by sputter deposition. Anodic treatment of the Co layer was performed potentiostatically to form the Co oxide porous thin film with ~80 nm pore size. Finally, phosphoralization was done in phosphorous vapors at 300 °C for 2 h to convert the Co oxide to the porous Co phosphide/phosphate thin film without damaging its ordered porous structure. Mixed-phase porous thin film of Co phosphide/Co phosphate showed lower overpotentials for HER and OER. For HER in 0.5 M H₂SO₄ electrolyte, it showed 35 mV overpotential at 10 mA/cm² current density with 53 mV/dec Tafel slope. Catalytic durability test was performed galvanostatically at 10 mA/cm² current density in 0.5 M H₂SO₄ electrolyte for 50000 s. Similarly, HER was performed in 1 M KOH aqueous electrolyte solution to study the effect of electrolyte change and observed 430 mV overpotential to reach 30 mA/cm² current density. OER tests were performed in 1 M KOH electrolyte, it showed 220 mV overpotential to achieve 10 mA/cm² current density with 65 mV/dec Tafel slope. Long term OER catalytic durability performed for 50000 s in 1 M KOH electrolyte revealed very stable Co phosphide/phosphate. The overall water electrolysis in a single electrolyzer (1 M KOH) was performed for Co phosphide/phosphate, Pt and RuO₂. Co phosphide/phosphate deliver both HER and OER activity, but Pt and RuO₂ cannot performed bifunctional activity due to the detrimental catalyst deactivation caused by either oxidation of Pt or reduction of RuO₂. Furthermore, porous graphene film (PGF) and cobalt phosphate (Co-Pi) was prepared by a convenient charge-controlled electrodeposition method. The Co-Pi@PGF showed high catalytic activity and stability towards water oxidation, superseding those of the Co-Pi planar film directly deposited on the electrode [97]. Co(H₂PO₄)₂/Co(PO₃)₂ on unique nanoporous lamellar nanocarbon florets (NCF) resulting in favorable surface oxygen vacancies showed onset overpotential

of 301 mV at current density of 30 mA cm² @ 577 mV [98]. A Mott-Schottky heterojunction electrocatalyst of the Co₂P₂O₇@N, P co-doped carbon nanocages, in which the metallic N, P co-doping carbon layer as a co-catalyst can effectively modulate the overfilled Co center e_g orbital occupation of the Co₂P₂O₇ nanoparticles and stabilize the microstructure which perform with an overpotential of 310 mV at a current density of 50 mA/cm² and negligible current loss for 100 h in 1 M KOH [99].

The electrochemical water splitting in the form of OER and HER performance for cobalt phosphate reported earlier are reviewed in **Table 1.1**. From the literature survey, it is observed that, cobalt phosphate has quite large overpotential. Still more work is needed to enhance its electrochemical performance for water splitting.

Table 1.1: Literature survey of cobalt phosphate catalyst for electrochemical water splitting.

Sr. No.	Deposited material	Method of preparation	Substrate	Electrolyte	Overpotential [mV]	Tafel slope [mV/dec]	Ref. No.
1.	$\text{Co}_3(\text{PO}_4)_2$	Hydrothermal & calcination	Glassy carbon electrode (GCE)	1 M KOH	320 (OER) [10 mA/cm ²]	85 (OER)	[93]
2.	$\text{Co}_3(\text{PO}_4)_2 \cdot 8\text{H}_2\text{O}$	Hydrothermal	SS	1 M KOH	292 (OER) [10 mA/cm ²]	65 (OER)	[94]
3.	$\text{Co}_{11}(\text{HPO}_3)_8(\text{OH})_6 / \text{Co}_{11}(\text{PO}_3)_8\text{O}_6$	Hydrothermal	GCE	1 M KOH	340 (OER) [10 mA/cm ²]	60 (OER)	[95]
4.	$\text{Co}_3(\text{PO}_4)_2$	Co-Electrodeposition and CVD	Au/Cr/Glass	0.5 M H_2SO_4 1 M KOH	35 (HER) 220 (OER) [10 mA/cm ²]	53 (HER) 65 (OER)	[96]
5.	Graphene/Cobalt phosphate	Electrodeposition	PGF	0.1 M NaOH	--	55.8 (OER)	[97]
6.	$\text{Co}(\text{H}_2\text{PO}_4)_2 / \text{Co}(\text{PO}_3)_2$	Stirring in organic solvent and calcination	NCF	0.1 M phosphate buffer	577 (OER) [30 mA/cm ²]	129 (OER)	[98]
7.	$\text{Co}_2\text{P}_2\text{O}_7 @ \text{N,P-C}$	Precipitation	Carbon fiber paper (CFP)	1 M KOH	310 (OER) [50 mA/cm ²]	49.1 (OER)	[99]
8.	Co/Zn phosphate	Hydrothermal	Nickel foam (NF)	1 M KOH 0.5 M H_2SO_4	307 (OER) 136 (HER) [10 mA/cm ²]	56.6 (OER) 60.79 (HER)	[100]

9.	Cobalt borophosphate	Hydrothermal	Fluorine doped tin oxide (FTO)	1 M KOH	441 (OER) [10 mA/cm ²]	57 (OER)	[101]
10.	Cobalt phosphate	Electrodeposition	NF	1 M Potassium phosphate	442 (OER) [100 mA/cm ²]	35 (OER)	[102]
11.	Cobalt phosphate	Hydrothermal	GCE	1 M KOH	281 (OER) [10 mA/cm ²]	98 (OER)	[103]
12.	Co ₃ (OH) ₂ (HPO ₄) ₂	Electrophoresis	NF	1 M KOH	240 (OER) 130 (HER) [10 mA/cm ²]	69 (OER) 91 (HER)	[104]
13.	Co ₃ (PO ₄) ₂ @N-C	Hydrothermal	GCE	1 M KOH	317 (OER) [10 mA/cm ²]	62 (OER)	[105]
14.	Cobalt phosphate	Precipitation	GCE	1 M KOH	380 (OER) [10 mA/cm ²]	58.7 (OER)	[106]
15.	Cobalt phosphate	Precipitation	GCE	0.1 M KOH	350 (OER) [10 mA/cm ²]	62 (OER)	[107]
16.	Co ₃ (PO ₄) ₂	Sol-gel	GCE	0.1 M Phosphate buffer	340 (OER) [5 mA/cm ²]	70 (OER)	[108]
17.	Cobalt phosphate	Hydrothermal	NF	1 M KOH	116 (OER) [10 mA/cm ²]	65.6 (OER)	[109]
18.	Cobalt phenylphosphonate	Hydrothermal	GCE	0.1 M Phosphate buffer	393 (OER) [1 mA/cm ²]	81 (OER)	[110]

19.	$\text{Co}_3(\text{PO}_4)_2$	Hydrothermal	Graphite felt	0.1 M Phosphate-buffered saline	370 (OER) [Onset]	133 (OER)	[111]
20.	$\text{Na}_2\text{CoP}_2\text{O}_7$	Wet-Ball Milling	FTO	0.5 M Sodium phosphate	420 (OER) [10 mA/cm ²]	82 (OER)	[112]
21.	Cobalt phosphate	Electrodeposition	Graphene foam (GF)	0.1 mol/L KPi	390 (OER) [1 mA/cm ²]	68 (OER)	[113]
22.	Cobalt phosphonate	Precipitation	--	1 M KOH	278 (OER) [10 mA/cm ²]	80 (OER)	[114]

1.6.2 Literature of iron phosphate: Xu et. al. [115] reported template-free approach to the fabrication of hollow nanotubes (NTs) of iron phosphide-phosphate ($\text{FeP-FeP}_x\text{O}_y$) composite by hydrothermal growth of iron oxy-hydroxide nanorods (NRs) and a subsequent post-phosphorization treatment. Hollow iron phosphide-phosphate ($\text{FeP-FeP}_x\text{O}_y$) composite NTs performed OER in basic medium, delivered the benchmark current density of 10 mA/cm^2 at a overpotential of 280 mV and showed Tafel slope of 48 mV/dec and a high turnover frequency of 0.10 /s at the overpotential of 350 mV and exhibits excellent catalytic activity up to 40 h without increasing overpotential. Zhong et. al. [116] synthesized iron phosphate on NF by SILAR method and exhibited outstanding activity and excellent durability for the OER, outperforming most Earth-abundant catalysts reported to date. It required overpotentials of 215 and 257 mV to drive current densities of 10 and 100 mA/cm^2 , respectively, in 1 M KOH solution. The Tafel slope was 28 mV/dec at current densities between 30 and 125 mA/cm^2 and long term durability up to 90 h. Also, Babar et. al. [117] synthesized iron phosphate by SILAR method on NF and the as synthesized material showed overpotential of 230 mV and 157 mV towards the OER and HER, respectively, with superior long-term stability. A full cell exploited FePi as both the anode and the cathode, and required a cell potential of 1.67 V to achieve 10 mA/cm^2 current density in 1 M KOH solution. The in situ derived iron phosphate–borate nanosheet array on carbon cloth (Fe–Pi–Bi/CC) show overpotential of 434 mV to achieve 10 mA/cm^2 current density in 0.1 M potassium borate (KBi) solution [118]. The electrochemical performances are tabulated in **Table 1.2**.

Table 1.2: Literature survey of iron phosphate catalyst for electrochemical water splitting.

Sr. No.	Deposited material	Method of preparation	Substrate	Electrolyte	Overpotential [mV]	Tafel slope [mV/dec]	Ref. No.
1.	FeP–FeP _x O _y	Hydrothermal and Postphosphorization	GCE	1 M KOH	280 (OER) [10 mA/cm ²]	48 (OER)	[115]
2.	Fe-Pi	SILAR	NF	1 M KOH	215 (OER) [10 mA/cm ²]	28 (OER)	[116]
3.	FePi	SILAR	NF	1 M KOH	230 (OER) 157 (HER) [10 mA/cm ²]	70 (OER) 47 (HER)	[117]
4.	Fe–Pi–Bi	Oxidative polarization	CC	0.1 M Potassium borate (KBi)	434 (OER) [10 mA/cm ²]	94 (OER)	[118]

1.6.3 Literature of cobalt-iron phosphate: Few research groups have worked and reported very good results for di-metal phosphate materials in application of water splitting because both transition metals show synergistic effect for water splitting. Here, some reports on cobalt-iron phosphate material are briefly discussed for water splitting. Amorphous iron and cobalt based phosphate catalysts supported on the NF ($\text{Fe}_{0.72}\text{Co}_{0.42}\text{PO}_4/\text{NF}$) were developed using the colloidal chemical hydrothermal method [119]. $\text{Fe}_{0.72}\text{Co}_{0.42}\text{PO}_4/\text{NF}$ electrode showed overpotential of 77 mV for HER at current density of 10 mA/cm^2 and attributed to the activation effect of Fe, which accelerated the charge transfer efficiency of Co to the benefit of catalyzing the reduction reaction of the hydrogen ions. Zhou et. al. [120] developed a facile bitemplate coprecipitation method to generate amorphous hierarchically porous 3D networks of Co-based phosphate including CoPi, binary CoM_1Pi , and ternary $\text{CoM}_1\text{M}_2\text{Pi}$ ($\text{M}_i = \text{Ni}^{\text{II}}$, Fe^{III} , or Ce^{III}) at room temperature. Primary micelles of sodium dodecylbenzenesulphonate (SDBS) were formed by taking into the consideration of critical micelle concentration (CMC), with a size around 2.2 nm. When Co^{II} cations were introduced into the clear and colorless SDBS aqueous solution, Tyndall effect was observed and the solution becomes opalescent gradually with the formation of well-dispersed colloidal droplets whose charge-neutral chemical composition was $\text{Co}(\text{DBS})_2$ complex between Co^{II} cations and DBS^- anions intuitively, further interconnection of these vesicles was usual to serve as soft-templates for the growth of 3D CoPi network with mesopores. Thus-prepared CoFePi networks generally resemble that of the CoPi network, and pores with different sizes could be easily spotted. The Co-based phosphate integrated with Fe^{III} ions was found to be excellent OER catalysts which exhibited activity of 277 mV overpotential to attain 10 mA/cm^2 current density with Tafel slope of 31 mV/dec and stability around 10 h of constant electrolysis. 1D amorphous ultrathin NWs of iron-doped cobalt phosphate delivered overpotential of 245 mV at 10 mA/cm^2 in 1.0 M KOH, a small Tafel slope of 42 mV/dec [121].

Furthermore, the bimetallic cobalt-iron phosphate nanosheets (NSs) having high activity toward OER were prepared by a rapid microwave-assisted method containing sodium hypophosphite and ethylene glycol as the phosphorus source and reaction solvent, correspondingly. To get an exceptional morphology and higher performance of metal phosphate, Yin et. al. [122] applied a suitable microwave-heated method for the fabrication of bimetallic phosphates structure on carbon fibre paper (CFP). The mixture was boiled to achieve

a relative high temperature during microwave-assisted heating. A phosphorylation reaction occurred in this process, thus leading to the formation of bi-metallic phosphate catalysts. The time-dependent microscopy was carried out to study the evolution of material. With increase in time, cauliflower-shaped microstructures (210 s), product was partly surrounded by the ripple-like NSs (300 s) and tremella-like catalyst composed of thin NSs (360 s) formed. The catalyst delivered good OER performance with overpotential to attain 10 mA/cm^2 (267 mV), a small Tafel slope (30 mV/dec) and good stability (catalytic activity was retained up to 94 % after 10 h water oxidation). Chemically converted layer double hydroxide in to cobalt-iron phosphate NSs exhibited overpotential of 278 mV to deliver 10 mA/cm^2 current density with Tafel slope of 34 mV/dec [123]. Literature survey of cobalt-iron phosphate catalyst electrodes is tabulated in **Table 1.3**. From the literature, it is observed that, there is only a paper published on cobalt-iron phosphate/reduced graphene oxide hybrid material for OER till date (**Table 1.4**). Hydrothermally synthesized composite of cobalt-iron phosphate with rGO showed the overpotential of 338 mV to achieve 10 mA/cm^2 current density for OER, which was attributed to the synergistic effects between Fe and Co species, as well as conductive channels provided by rGO substrate [124].

Table 1.3: Literature survey of cobalt-iron phosphate catalyst for electrochemical water splitting.

Sr. No.	Deposited material	Method of preparation	Substrate	Electrolyte	Overpotential [mV]	Tafel slope [mV/dec]	Ref. No.
1.	$\text{Fe}_{0.72}\text{Co}_{0.42}\text{PO}_4$	Hydrothermal	NF	1 M KOH	77 (HER) [10 mA/cm ²]	80.7	[119]
2.	CoFePi	Coprecipitation	Carbon black GCE	1 M KOH	277 [10 mA/cm ²]	31	[120]
3.	Fe-doped $\text{Co}_3(\text{PO}_4)_2$	Solvothermal	NF	1 M KOH	245 [10 mA/cm ²]	42	[121]
4.	Co-Fe-P-O	Microwave Heating	CFP	1 M KOH	267 [10 mA/cm ²]	30	[122]
5.	CoFePi	Solution plasma method	GCE	1 M KOH	278 [10 mA/cm ²]	34	[123]
6.	FeCo-phosphate	Co-precipitation	Carbon paper	1 M KOH	273 [10 mA/cm ²]	35.9	[125]

Table 1.4: Literature survey of cobalt-iron phosphate/reduced graphene oxide catalyst for electrochemical water splitting.

Sr. No.	Deposited material	Method of preparation	Substrate	Electrolyte	Overpotential [mV]	Tafel slope [mV/dec]	Ref. No.
1.	$\text{Co}_{0.75}\text{Fe}_{0.25}$ phosphate/rGO	Hydrothermal	GCE	1 M KOH	338 [10 mA/cm ²]	51.9	[124]

In summary, there are very few reports available on the cobalt phosphate, iron phosphate and cobalt-iron phosphate materials for the electrochemical water splitting application. There is only one report on cobalt-iron phosphate/reduced graphene oxide hybrid electrode material till date for OER application. There is no a report which present OER, HER and overall water splitting by using cobalt-iron phosphate/reduced graphene oxide hybrid material. The presence of the phosphate groups acts as proton acceptors that facilitate the oxidation of metal atoms as well as develops distorted local geometry that preferred water adsorption and further water oxidation. According to previous reports, it is clear that, amorphous materials synthesized at low temperature are electrochemically more active than well crystalline materials synthesized at higher temperature, by the reason of huge number of coordinatively unsaturated sites and surface defects. Metal phosphate materials having low dimensionality, such as one-dimensional (1D) NWs/NTs/NRs and two-dimensional (2D) NSs/nanoplates, three-dimensional (3D) hollow core-shells, nanocages, nanospheres or nanocubes, etc. showed remarkable catalytic performance along with large surface area and atomic utilization efficiency in comparison with their bulk counterparts. Due to exceptional structural and distinctive electronic and physicochemical properties of transition metal phosphate materials such as high specific surface area, high density of surface unsaturated atoms and high electron mobility, transition metal phosphates are most applicable as catalyst electrode material in electrochemical water splitting.

1.7 Orientation and purpose of the dissertation: The expansion of energy conversion and storage technologies has augmented in recent years as global requirement for energy supplies continuously increasing. The global requirement for energy and ecological concerns and social reliance on fossil fuels are grown, efforts to electrify the transportation area are rapidly advancing, opening up a new and huge market for fuel cell technologies. Exploring more efficient and environment-friendly power devices has attracted tremendous attention for last 50 years [126]. Among many approaches, one has been identified since the 1970s, which is using non-polluting hydrogen as the main energy carrier, where the overall system was termed as the hydrogen economy by Bockris [127]. In energy conversion technology, water splitting by electrochemical process is one of the cleanest and sustainable way for the hydrogen production. Today, various institutes and companies are working on the hydrogen production from water electrolysis, storage of the hydrogen, and its different possible applications where,

hybrid and fuel cell cars are contemporary attractions of society. Hence, a crucial determinant to the solution of efficient energy conversion problem through water electrolysis is to develop an inexpensive, robust and stable catalyst that would be able to withstand with low overpotential over a long period of time.

Though the hydrogen economy concept is nothing new, hydrogen as a fuel covers only 4 % of current energy demands. There are some major economic factors such as unavailability of cost effective systems, high cost for the installation and expensive energy input are inhibiting the wide range use of hydrogen as a fuel [128]. Electrolysis of water and electrocatalytic energy conversion reactions mainly include the transfer of electrons and are dominated by the electrode material. Hence, the selection of electrode materials or electrocatalysts is not only crucial for increase in overall performances of water electrolyzers and fuel cells, but also can reduce the cost of these electrochemical processes by determining the rate of reactions and overpotentials. Reactions associated with water splitting such as HER and OER are mainly occur at the surface of the electrode materials or catalysts [129-131]. When it comes to industrial applications, the required overpotentials during these electrochemical conversions and processes is the key parameter for system efficiency. Since all the electrochemical processes occur at the surface of an electrocatalyst, it is the most important area to be focused on. Especially the surface morphology along with the active sites, porosity and effects of crystallinity need to be taken into account greatly while designing catalysts for industrial applications. Mainly there are two different ways to increase the activity of an electrocatalyst, either altering the intrinsic activity or changing the morphology of the catalysts which results in the increased number of active sites [132].

The literature survey illustrates that a new class of material as cobalt-iron phosphate/reduced graphene oxide electrode materials can be prepared on low cost SS substrates. Cobalt phosphate, iron phosphate and cobalt-iron phosphate having different morphologies could be synthesized via chemical methods and can be used as catalyst for electrochemical water splitting. Our prior aim is to synthesize cobalt-iron phosphate and cobalt-iron phosphate/reduced graphene oxide electrode materials and their characterization using different physico-chemical techniques. During synthesis, various preparative parameters were optimized such as, pH, reaction temperature, reaction time, concentration, etc.

The prepared electrodes of cobalt-iron phosphate and cobalt-iron phosphate/reduced graphene oxide materials further evaluated for crystallographic information such as crystal structure, phase, etc., surface morphology, compositional analysis, molecular bond vibration analysis, electronic states, etc. The electrochemical characteristics were carried by conducting CV, linear sweep voltammetry (LSV), chronoamperometry (CA), and EIS using electrochemical workstation for half-cell and full-cell; and analyzed by different electrochemical parameters such as overpotential, onset potential, Tafel slope, R_{ct} , etc.

1.8 Thesis outline: There are six chapters outlined in this thesis as follows:

Chapter 1: Introduction to electrochemical water splitting and review of literature

This chapter contains the background of the research topic, overall significance of research, and objectives. Also, it contains a summary of electrocatalysts which have been already reported for water splitting reactions. The methodical reviewing process of electrocatalysts for particularly the OER and HER aims to identify the research gap and questions in this field.

Chapter 2: Theoretical background of material synthesis methods and characterization techniques

This chapter leads to the brief discussion of experimental methods adopted during this work. There are two major parts of this research design, one is the synthesis of materials and another part is the characterizations of those materials for their identification and physico-chemical properties, as well as the application oriented tests. For the present study, there are two chemical synthesis methods are chosen; one is hydrothermal and another is SILAR. The theoretical background of both the techniques, also some major characterization techniques such as X-ray diffraction (XRD), Fourier transform infrared (FTIR) spectroscopy, X-ray photoelectron spectroscopy (XPS), field emission scanning electron microscopy (FESEM), Energy dispersive X-ray spectroscopy (EDS), Brunauer-Emmett-Teller (BET) technique and electrochemical analysis techniques such as CV, LSV, CA, and electrochemical impedance spectroscopy (EIS) have discussed.

Chapter 3: Hydrothermally synthesized cobalt-iron phosphate and cobalt-iron phosphate/reduced graphene oxide hybrid for electrochemical OER and HER application

Chapter-3 have two sections: section A contains the synthesis of pristine cobalt-iron phosphate catalyst materials by using hydrothermal method. During the synthesis, molar ratio of cobalt and iron was varied by keeping all other reaction parameters such as, reaction temperature, complexing agent concentration, deposition time, etc. fixed at their optimized conditions. The effect of molar ratio variation on structural, morphological electronic and electrochemical properties were studied. Electrochemical OER and HER characteristics were studied for electrochemical water splitting. In section B, the best performing material was further carried to make the hybrid with rGO. Cobalt-iron phosphate/reduced graphene oxide was synthesized by hydrothermal method and characterized further for their physico-chemical properties. Electrochemical characteristics were studied in terms of OER and HER.

Chapter 4: SILAR deposited cobalt-iron phosphate and cobalt-iron phosphate/reduced graphene oxide hybrid for electrochemical OER and HER application

Chapter-4 have two sections, in section A, pristine cobalt-iron phosphate catalysts were deposited using SILAR method. The molar concentration ratio in cobalt and iron is varied to study their effect on the physico-chemical, and electrochemical properties. During the molar concentration variation, all other reaction parameters such as, dipping time, cycle number and reaction temperature were kept constant at their optimized values. The effect of molar ratio variation on structural, morphological electronic and electrochemical properties were studied. Electrochemical OER and HER characteristics were studied for electrochemical water splitting. In section B, the best performing pristine cobalt-iron phosphate catalyst was selected to prepare hybrid with rGO. By keeping all other reaction parameters constant, the concentration of rGO was varied and their effect on physico-chemical and electrochemical properties was studied for electrochemical water splitting.

Chapter 5: Cobalt-iron phosphate/reduced graphene oxide hybrid electrodes for overall water splitting

In chapter-5, the full cell (device) testing for overall water splitting was performed. In particular, among the all electrodes (pristine cobalt-iron phosphate, cobalt-iron phosphate/reduced graphene oxide) synthesized by hydrothermal and SILAR methods, the best performing electrode was selected for electrochemical characterization to study the required potential for overall water splitting in alkaline media. Long duration catalytic stability test was performed by CA tests for the best performing catalyst electrode. Also, the post-mortem physico-chemical characterizations were performed to understand the chemical changes during the catalysis.

Chapter 6: Summary and conclusions

In this last chapter, the summary and the results drawn from the earlier five chapters are given. Finally, the chapter concluded the outcomes of this research work.

1.9 References:

- [1] T. G. Gutowski, S. B. Gershwin, T. Bounassisi, Proc. IEEE IntSymp Sustainable Systems and Technol, Washington D.C., (2010).
- [2] Independent Statistics and Analysis. U.S. Energy Information Administration www.eia.gov, (accessed Feb. 2021).
- [3] R. T. Pierrehumbert, Concept warming the world, Nature 432 (2004) 677.
- [4] H. Balat, C. Öz, Technical and economic aspects of carbon capture and storage -A review, Energy Exploration and Exploitation 25 (2007) 357.
- [5] D. Archer, Checking the thermostat, Nature Geoscience 1 (2008) 289.
- [6] H. Khatib, IEA world energy outlook 2011-a comment, Energy Policy 48 (2012) 737.
- [7] M. Aresta, A. Dibenedetto, Utilisation of CO₂ as a chemical feedstock: Opportunities and challenges, Dalton Transactions 28 (2007) 2975.
- [8] K. Li, X. An, K. H. Park, M. Khraisheh, J. Tang, A critical review of CO₂ photoconversion: Catalysts and reactors, Catalysis Today 224 (2014) 3.
- [9] N. Armaroli, V. Balzani, Towards an electricity-powered world, Energy & Environmental Science 4 (2011) 3193.
- [10] N. Armaroli, V. Balzani, Energy for a Sustainable World. From the Oil Age to a Sun Powered Future, Wiley-VCH, Weinheim, Germany, (2011).
- [11] J. Bosch, I. Staffell, A. D. Hawkes, Temporally explicit and spatially resolved global offshore wind energy potentials, Energy 163 (2018) 766.
- [12] S. A. Khalate, R. S. Kate, R. J. Deokate, A review on energy economics and the recent research and development in energy and the Cu₂ZnSnS₄ (CZTS) solar cells: A focus towards efficiency, Solar Energy 169 (2018) 616.
- [13] Z. Şen, 1.14 Hydro Energy, Comprehensive Energy Systems 1 (2018) 606.

- [14] V. Khare, C. Khare, S. Nema, P. Baredar, Tidal energy systems design, optimization and control, Elsevier, The Netherlands, (2019).
- [15] S. N. Pandey, V. Vishal, A. Chaudhuri, Geothermal reservoir modeling in a coupled thermo-hydro-mechanical-chemical approach: A review, *Earth-Science Reviews* 185 (2018) 1157.
- [16] M. Grätzel, Photoelectrochemical cells, *Nature* 414 (2001) 338.
- [17] X. Zou, Y. Zhang, Noble metal-free hydrogen evolution catalysts for water splitting, *Chemical Society Reviews* 44 (2015) 5148.
- [18] B. Liu, Y. Zhao, H. Peng, Z. Zhang, C. Sit, M. Yuen, T. Zhang, C. Lee, W. Zhang, Nickel–cobalt diselenide 3D mesoporous nanosheet networks supported on Ni foam: An all-pH highly efficient integrated electrocatalyst for hydrogen evolution, *Advanced Materials* 29 (2017) 1606521.
- [19] C. C. L. McCrory, S. Jung, J. C. Peters, T. F. Jaramillo, Benchmarking heterogeneous electrocatalysts for the oxygen evolution reaction, *Journal of American Chemical Society* 135 (2013) 16977.
- [20] D. A. J. Rand, R. Dell, Hydrogen energy: Challenges and prospects, Vol. 1, Royal Society of Chemistry, United Kingdom, (2008).
- [21] V. W. H. Lau, A. F. Masters, A. M. Bond, T. Maschmeyer, Ionic-liquid-mediated active-site control of MoS₂ for the electrocatalytic hydrogen evolution reaction, *Chemistry—A European Journal* 18 (2012) 8230.
- [22] M. Sakamoto, D. Izuhara, H. Sotouchi, F. Aoyagi, P2G system technology development aiming at building a CO₂-Free hydrogen society, Meeting Abstracts, The Electrochemical Society, IOP Publishing 46 (2018) 1589.
- [23] T. Yoshida, K. Kojima, Toyota MIRAI fuel cell vehicle and progress toward a future hydrogen society, *The Electrochemical Society Interface* 24 (2015) 45.
- [24] A. Landman, H. Dotan, G. E. Shter, M. Wullenkord, A. Houaijia, A. Maljusch, G. S. Grader, A. Rothschild, Photoelectrochemical water splitting in separate oxygen and hydrogen cells, *Nature materials* 16 (2017) 646.
- [25] G. Iaquaniello, F. Giacobbe, B. Morico, S. Cosenza, A. Farace, Membrane reforming in converting natural gas to hydrogen: Production costs, Part II, *International Journal of Hydrogen Energy* 33 (2008) 6595.
- [26] S. Liu, L. Li, L. Guo, H. Jin, J. Kou, G. Li, Sulfur transformation characteristics and mechanisms during hydrogen production by coal gasification in supercritical water, *Energy Fuels* 31 (2017) 12046.
- [27] W. Lubitz, B. Tumas, Hydrogen: An overview, *Chemical Reviews* 107 (2007) 3900.
- [28] L. V. Mattos, G. Jacobs, B. H. Davis, F. B. Noronha, Production of hydrogen from ethanol: Review of reaction mechanism and catalyst deactivation, *Chemical Reviews* 112 (2012) 4094.
- [29] R. M. Navarro, M. A. Pena, J. L. G. Fierro, Hydrogen production reactions from carbon feedstocks: Fossil fuels and biomass, *Chemical Reviews* 107 (2007) 3952.
- [30] M. Shahbaz, S. Yusup, A. Inayat, D. O. Patrick, M. Ammar, A. Pratama, Cleaner production of hydrogen and syngas from catalytic steam palm kernel shell gasification using CaO sorbent and coal bottom ash as a catalyst, *Energy & Fuels* 31 (2017) 13824.

- [31] X. Xu, Y. Xiao, C. Qiao, System design and analysis of a direct hydrogen from coal system with CO₂ capture, *Energy & Fuels* 21 (2007) 1688.
- [32] A. F. S. Muhammad, A. Awad, R. Saidur, N. Masiran, A. Salam, B. Abdullah, Recent advances in cleaner hydrogen productions via thermo-catalytic decomposition of methane: Admixture with hydrocarbon, *International Journal of Hydrogen Energy* 43 (2018) 18713.
- [33] J. Zhang, X. Li, H. Chen, M. Qi, G. Zhang, H. Hu, X. Ma, Hydrogen production by catalytic methane decomposition: Carbon materials as catalysts or catalyst supports, *International Journal of Hydrogen Energy* 42 (2017) 19755.
- [34] M. Bajdich, M. García-Mota, A. Vojvodic, J. K. Nørskov, A. T. Bell, Theoretical investigation of the activity of cobalt oxides for the electrochemical oxidation of water, *Journal of American Chemical Society* 135 (2013) 13521.
- [35] W. M. Haynes, *CRC handbook of chemistry and physics*, CRC press, Boca Raton, (2014).
- [36] J. P. Hoare, *The Electrochemistry of Oxygen*, Wiley, New York, (1968).
- [37] J. K. Hurst, In pursuit of water oxidation catalysts for solar fuel production, *Science* 328 (2010) 315.
- [38] N. T. Suen, S. F. Hung, Q. Quan, N. Zhang, Y. J. Xu, H. M. Chen, Electrocatalysis for the oxygen evolution reaction: Recent development and future perspectives, *Chemical Society Reviews* 46 (2017) 337.
- [39] K. C. Neyerlin, W. B. Gu, J. Jorne, H. A. Gasteiger, Study of the exchange current density for the hydrogen oxidation and evolution reactions, *Journal of Electrochemical Society* 154 (2007) B631.
- [40] D. Strmcnik, P. P. Lopes, B. Genorio, V. R. Stamenkovic, N. M. Markovic, Design principles for hydrogen evolution reaction catalyst materials, *Nano Energy* 29 (2016) 29.
- [41] Z. Huang, Z. Chen, Z. Chen, C. Lv, M. G. Humphrey, C. Zhang, Cobalt phosphide nanorods as an efficient electrocatalyst for the hydrogen evolution reaction, *Nano Energy* 9 (2014) 373.
- [42] B. Conway, G. Jerkiewicz, Relation of energies and coverages of underpotential and overpotential deposited H at Pt and other metals to the ‘volcano curve’ for cathodic H₂ evolution kinetics, *Electrochimica Acta* 45 (2000) 4075.
- [43] B. You, Y. Sun, Chalcogenide and phosphide solid-state electrocatalysts for hydrogen generation, *ChemPlusChem* 81 (2016) 1045.
- [44] Y. Shi, B. Zhang, Recent advances in transition metal phosphide nanomaterials: Synthesis and applications in hydrogen evolution reaction, *Chemical Society Reviews* 45 (2016) 1529.
- [45] S. Anantharaj, S. R. Ede, K. Sakthikumar, K. Karthick, S. Mishra, S. Kundu, Recent trends and perspectives in electrochemical water splitting with an emphasis on sulfide, selenide, and phosphide catalysts of Fe, Co, and Ni: A review, *ACS Catalysis* 6 (2016) 8069.
- [46] H. Vrubel, T. Moehl, M. Gratzel, X. Hu, Revealing and accelerating slow electron transport in amorphous molybdenum sulphide particles for hydrogen evolution reaction, *Chemical Communications* 49 (2013) 8985.
- [47] P. W. Menezes, C. Panda, S. Loos, F. Bunschei-Bruns, C. Walter, M. Schwarze, X. Deng, H. Dau, M. Driess, A structurally versatile nickel phosphite acting as

- a robust bifunctional electrocatalyst for overall water splitting, *Energy & Environmental Science* 11 (2018) 1287.
- [48] L. Cao, Q. Luo, J. Chen, L. Wang, Y. Lin, H. Wang, X. Liu, X. Shen, W. Zhang, W. Liu, Z. Qi, Z. Jiang, J. Yang, T. Yao, Dynamic oxygen adsorption on single-atomic Ruthenium catalyst with high performance for acidic oxygen evolution reaction, *Nature Communications* 10 (2019) 4849.
- [49] Y. Lee, J. Suntivich, K. J. May, E. E. Perry, Y. S.-Horn, Synthesis and activities of rutile IrO₂ and RuO₂ nanoparticles for oxygen evolution in acid and alkaline solutions, *Journal of Physical Chemistry Letters* 3 (2012) 399.
- [50] R. Jiang, S. Tung, Z. Tang, L. Li, L. Ding, X. Xi, Y. Liu, L. Zhang, J. Zhang, A review of core-shell nanostructured electrocatalysts for oxygen reduction reaction, *Energy Storage Materials* 12 (2018) 260.
- [51] S. Siracusano, N. V. Dijk, E. P.-Johnson, V. Baglio, A. S. Aricò, Nanosized IrO_x and IrRuO_x electrocatalysts for the O₂ evolution reaction in PEM water electrolyzers, *Applied Catalysis B: Environmental* 164 (2015) 488.
- [52] S. Cherevko, S. Geiger, O. Kasian, N. Kulyk, J. P. Grote, A. Savan, B. R. Shrestha, S. Merzlikin, B. Breitbach, A. Ludwig, K. J. J. Mayrhofer, Oxygen and hydrogen evolution reactions on Ru, RuO₂, Ir, and IrO₂ thin film electrodes in acidic and alkaline electrolytes: A comparative study on activity and stability, *Catalysis Today* 262 (2016) 170.
- [53] C.-Z. Yuan, Y.-F. Jiang, Z.-W. Zhao, S.-J. Zhao, X. Zhou, T.-Y. Cheang, A.-W. Xu, Molecule-assisted synthesis of highly dispersed ultrasmall RuO₂ nanoparticles on nitrogen-doped carbon matrix as ultraefficient bifunctional electrocatalysts for overall water splitting, *ACS Sustainable Chemistry and Engineering* 6 (2018) 11529.
- [54] Y.-J. Wang, D. P. Wilkinson, J. Zhang, Noncarbon support materials for polymer electrolyte membrane fuel cell electrocatalysts, *Chemical Reviews* 111 (2011) 7625.
- [55] S. H. Ahn, H. Tan, M. Haensch, Y. Liu, L. A. Bendersky, T. P. Moffat, Self-terminated electrodeposition of iridium electrocatalysts, *Energy & Environmental Science* 8 (2015) 3557.
- [56] M. W. Kanan, D. G. Nocera, In situ formation of an oxygen-evolving catalyst in neutral water containing phosphate and Co²⁺, *Science* 321 (2008) 1072.
- [57] A. Bergmann, I. Zaharieva, H. Dau, P. Strasser, Electrochemical water splitting by layered and 3D cross-linked manganese oxides: Correlating structural motifs and catalytic activity, *Energy & Environmental Science* 6 (2013) 2745.
- [58] G. Fan, F. Li, D. G. Evans, X. Duan, Catalytic applications of layered double hydroxides: Recent advances and perspectives, *Chemical Society Reviews* 43 (2014) 7040.
- [59] M. Risch, F. Ringleb, M. Kohlhoff, P. Bogdanoff, P. Chernev, I. Zaharieva, H. Dau, Water oxidation by amorphous cobalt-based oxides: In situ tracking of redox transitions and mode of catalysis, *Energy & Environmental Science* 8 (2015) 661.
- [60] S. Trasatti, Electrocatalysis by oxides-attempt at a unifying approach, *Journal of Electroanalytical Chemistry and Interfacial Electrochemistry* 111 (1980) 125.

- [61] J. R. McKone, B. F. Sadler, C. A. Werlang, N. S. Lewis, H. B. Gray, Ni–Mo nanopowders for efficient electrochemical hydrogen evolution, *ACS Catalysis* 3 (2013) 166.
- [62] Q. Lu, G. S. Hutchings, W. Yu, Y. Zhou, R. V. Forest, R. Tao, J. Rosen, B. T. Yonemoto, Z. Cao, H. Zheng, J. Q. Xiao, Highly porous non-precious bimetallic electrocatalysts for efficient hydrogen evolution, *Nature Communications* 6 (2015) 6567.
- [63] X. Wang, R. Su, H. Aslan, J. Kibsgaard, S. Wendt, L. Meng, M. Dong, Y. Huang, F. Besenbacher, Tweaking the composition of NiMoZn alloy electrocatalyst for enhanced hydrogen evolution reaction performance, *Nano Energy* 12 (2015) 9.
- [64] S. Chandrasekaran, L. Yao, L. Deng, C. Bowen, Y. Zhang, S. Chen, Z. Lin, F. Peng, P. Zhang, Recent advances in metal sulfides: From controlled fabrication to electrocatalytic, photocatalytic and photoelectrochemical water splitting and beyond, *Chemical Society Reviews* 48 (2019) 4178.
- [65] L. Chen, Z. Liu, Z. Guo, X. J. Huang, Regulation of intrinsic physicochemical properties of metal oxide nanomaterials for energy conversion and environmental detection applications, *Journal of Materials Chemistry A* 8 (2020) 17326.
- [66] M. Gong, W. Zhou, M. C. Tsai, J. Zhou, M. Guan, M. C. Lin, B. Zhang, Y. Hu, D. Y. Wang, J. Yang, S. J. Pennycook, Nanoscale nickel oxide/nickel heterostructures for active hydrogen evolution electrocatalysis, *Nature Communications* 5 (2014) 4695.
- [67] L. Li, P. Wang, Q. Shao, X. Huang, Metallic nanostructures with low dimensionality for electrochemical water splitting, *Chemical Society Reviews* 49 (2020) 3072.
- [68] Y. Yan, B. Y. Xia, B. Zhao, X. Wang, A review on noble-metal-free bifunctional heterogeneous catalysts for overall electrochemical water splitting, *Journal of Materials Chemistry A* 4 (2016) 17587.
- [69] M. Wang, L. Zhang, Y. He, H. Zhu, Recent advances in transition-metal-sulfide-based bifunctional electrocatalysts for overall water splitting, *Journal of Materials Chemistry A* 9 (2021) 5320.
- [70] J. B. Tan, G. R. Li, Recent progress on metal–organic frameworks and their derived materials for electrocatalytic water splitting, *Journal of Materials Chemistry A* 8 (2020) 14326.
- [71] L. Trotochaud, S. L. Young, J. K. Ranney, S. W. Boettcher, Nickel–iron oxyhydroxide oxygen-evolution electrocatalysts: the role of intentional and incidental iron incorporation, *Journal of American Chemical Society* 136 (2014) 6744.
- [72] Y. Sun, T. Zhang, C. Li, K. Xu, Y. Li, Compositional engineering of sulfides, phosphides, carbides, nitrides, oxides, and hydroxides for water splitting, *Journal of Materials Chemistry A* 8 (2020) 13415.
- [73] S. Nayak, K. Parida, Superactive NiFe-LDH/graphene nanocomposites as competent catalysts for water splitting reactions, *Inorganic Chemistry Frontiers* 7 (2020) 3805.

- [74] P. M. Bodhankar, P. B. Sarawade, G. Singh, A. Vinu, D. S. Dhawale, Recent advances in highly active nanostructured NiFe LDH catalyst for electrochemical water splitting, *Journal of Materials Chemistry A* 9 (2021) 3180.
- [75] Y. Jiang, Y. Lu, Designing transition-metal-boride-based electrocatalysts for applications in electrochemical water splitting, *Nanoscale* 12 (2020) 9327.
- [76] V. D. Palma, G. Zafeiropoulos, T. Goldsweer, W. M. M. Kessels, M. C. M. van de Sandena, M. Creatore, M. N. Tsampas, Atomic layer deposition of cobalt phosphate thin films for the oxygen evolution reaction, *Electrochemistry Communications* 98 (2019) 73.
- [77] N. Han, P. Liu, J. Jiang, L. Ai, Z. Shao, S. Liu, Recent advances in nanostructured metal nitrides for water splitting, *Journal of Materials Chemistry A* 6 (2018) 19912.
- [78] Y. Wang, B. Kong, D. Zhao, H. Wang, C. Selomulya, Strategies for developing transition metal phosphides as heterogeneous electrocatalysts for water splitting, *Nano Today* 15 (2017) 26.
- [79] H. Pang, Z. Yan, W. Wang, J. Chen, J. Zhang, H. Zheng, Facile fabrication of $\text{NH}_4\text{CoPO}_4 \cdot \text{H}_2\text{O}$ nano/microstructures and their primarily application as electrochemical supercapacitor, *Nanoscale* 4 (2012) 5946.
- [80] Y. H. Dai, L. B. Kong, K. Yan, M. Shi, Y. C. Luo, L. Kang, Facile fabrication of manganese phosphate nanosheets for supercapacitor applications, *Ionics* 22 (2016) 1461.
- [81] J. Ling, H. Zou, W. Yang and S. Chen, Urchin-like NiCoP coated with carbon layer as high performance electrodes for all-solid-state asymmetric supercapacitors, *Materials Advances* 1 (2020) 481.
- [82] X. Wang, H. Kim, Y. Xiao, Y. Sun, Nanostructured metal phosphide-based materials for electrochemical energy storage, *Journal of Materials Chemistry A* 4 (2016) 14915.
- [83] Y. Lu, J. Liu, X. Liu, S. Huang, T. Wang, X. Wang, C. Gu, J. Tu, S. Mao, Facile synthesis of Ni-coated Ni_2P for supercapacitor applications, *CrystEngComm* 15 (2013) 7071.
- [84] M. S. Burke, L. J. Enman, A. S. Batchellor, S. Zou, S. W. Boettcher, Oxygen evolution reaction electrocatalysis on transition metal oxides and (oxy)hydroxides: Activity trends and design principles, *Chemistry of Materials* 27 (2015) 7549.
- [85] S. Natarajan, S. Mandal, Open-framework structures of transition-metal compounds, *Angewandte Chemie* 47 (2008) 4798.
- [86] R. Murugavel, Amitava Choudhury, M. G. Walawalkar, R. Pothiraja, C. N. R. Rao, Metal complexes of organophosphate esters and open-framework metal phosphates: Synthesis, structure, transformations, and applications, *Chemical Reviews* 108 (2008) 3549.
- [87] A. Morozan, F. Jaouen, Metal organic frameworks for electrochemical applications, *Energy & Environmental Science* 5 (2012) 9269.
- [88] T. Li, S. Kaercher, P. W. Roesky, Synthesis, structure and reactivity of rare-earth metal complexes containing anionic phosphorus ligands, *Chemical Society Reviews* 43 (2014) 42.

-
- [89] S. Faraji, F. N. Ani, Microwave-assisted synthesis of metal oxide/hydroxide composite electrodes for high power supercapacitors-A review, *Journal of Power Sources* 263 (2014) 338.
 - [90] H. Ma, J. He, D. B. Xiong, J. Wu, Q. Li, V. Dravid, Y. Zhao, Nickel cobalt hydroxide @reduced graphene oxide hybrid nanolayers for high performance asymmetric supercapacitors with remarkable cycling stability, *ACS Applied Materials & Interfaces* 8 (2016) 1992.
 - [91] M. Hidouri, A. Wattiaux, M. L. López, C. Pico, M. B. Amara, Structural study and properties of a new iron phosphate $\text{Rb}_9\text{Fe}_7(\text{PO}_4)_{10}$, *Journal of Alloys and Compounds* 506 (2010) 569.
 - [92] Y. Shao, Y. Zhao, H. Li, C. Xu, Three-dimensional hierarchical $\text{Ni}_x\text{Co}_{1-x}\text{O}/\text{Ni}_y\text{Co}_{2-y}\text{P}@C$ hybrids on nickel foam for excellent supercapacitors, *ACS Applied Materials & Interfaces* 8 (2016) 35368.
 - [93] L. Chen, J. -T. Ren, Y. -S. Wang, W. -W. Tian, L. -J. Gao, Z. -Y. Yuan, Organic-inorganic cobalt-phosphonate-derived hollow cobalt phosphate spherical hybrids for highly efficient oxygen evolution, *ACS Sustainable Chemistry & Engineering* 7 (2019) 13559.
 - [94] P. K. Katkar, S. J. Marje, S. B. Kale, A. C. Lokhande, C. D. Lokhande, U. M. Patil, Synthesis of hydrous cobalt phosphate electrocatalysts by a facile hydrothermal method for enhanced oxygen evolution reaction: Effect of urea variation, *CrystEngComm* 21 (2019) 884.
 - [95] Y. Ni, B. He, S. Luo, X. Wu, X. Feng, Y. Luo, J. Lin, J. Sunf, K. Fan, Y. Ji, G. Zhang, H. Chen, Microporous core-shell $\text{Co}_{11}(\text{HPO}_3)_8(\text{OH})_6/\text{Co}_{11}(\text{PO}_3)_8\text{O}_6$ nanowires for highly efficient electrocatalytic oxygen evolution reaction, *Applied Catalysis B: Environmental* 259 (2019) 118091.
 - [96] Y. Yang, H. Fei, G. Ruan, J. M. Tour, Porous cobalt-based thin film as a bifunctional catalyst for hydrogen generation and oxygen generation, *Advanced Materials* 27 (2015) 3175.
 - [97] Y. Li, Y. Zhao, Z. Zhang, A porous graphene/cobalt phosphate composite as an efficient oxygen evolving catalyst, *Electrochemistry Communications* 48 (2014) 35.
 - [98] J. Saha, S. Verma, R. Ball, C. Subramaniam, R. Murugavel, Compositional control as the key for achieving highly efficient oer electrocatalysis with cobalt phosphates decorated nanocarbon florets, *Small* 16 (2019) 1903334.
 - [99] D. Liang, C. Lian, Q. Xu, M. Liu, H. Liu, H. Jiang, C. Li, Interfacial charge polarization in $\text{Co}_2\text{P}_2\text{O}_7@\text{N}$, P co-doped carbon nanocages as mott-schottky electrocatalysts for accelerating oxygen evolution reaction, *Applied Catalysis B: Environmental* 268 (2019) 118417.
 - [100] L. Qian, Y. Miao, Nanosheet organized flower-like Co/Zn phosphate on nickel foam for efficient water splitting in both acid and basic solutions, *Polyhedron* 160 (2019) 213.
 - [101] E. Ülker, Hydrothermally synthesized cobalt borophosphate as an electrocatalyst for water oxidation in the pH range from 7 to 14, *ChemElectroChem* 6 (2019) 3132.
-

- [102] A. J. Esswein, Y. Surendranath, S. Y. Reece, D. G. Nocer, Highly active cobalt phosphate and borate based oxygen evolving catalysts operating in neutral and natural waters, *Energy & Environmental Science* 4 (2011) 499.
- [103] J. Qi, J. Xie, Z. Wei, S. Lou, P. Hao, F. Lei, B. Tang, Modulation of crystal water in cobalt phosphate for promoted water oxidation, *Chemical Communications* 56 (2020) 4575.
- [104] P. W. Menezes, C. Panda, C. Walter, M. Schwarze, M. Driess, A cobalt-based amorphous bifunctional electrocatalysts for water-splitting evolved from a single-source lazulite cobalt phosphate, *Advanced Functional Materials* 29 (2019) 1808632.
- [105] C. -Z. Yuan, Y. -F. Jiang, Z. Wang, X. Xie, Z. -K. Yang, A. B. Yousaf, A. -W. Xu, Cobalt phosphate nanoparticles decorated with nitrogen-doped carbon layers as highly active and stable electrocatalysts for the oxygen evolution reaction, *Journal of Materials Chemistry A* 4 (2016) 8155.
- [106] M. Pramanik, C. Li, M. Imura, V. Malgras, Y. -M. Kang, Y. Yamauchi, Ordered mesoporous cobalt phosphate with crystallized walls toward highly active water oxidation electrocatalysts, ordered mesoporous cobalt phosphate with crystallized walls toward highly active water oxidation electrocatalysts, *Small* 12 (2016) 1709.
- [107] S. Zhao, C. Li, H. Huang, Y. Liu, Z. Kang, Carbon nanodots modified cobalt phosphate as efficient electrocatalyst for water oxidation, *Journal of Materiomics* 1 (2015) 236.
- [108] Y. Shao, X. Xiao, Y. -P. Zhu, T. -Y. Ma, Single-crystal cobalt phosphate nanosheets for biomimetic oxygen evolution in neutral electrolytes, *Angewandte Chemie* 131 (2019) 14741.
- [109] Y. Liu, D. Yang, Z. Liu, J. H. Yang, Nickel foam supported cobalt phosphate electrocatalyst for alkaline oxygen evolution reaction, *Journal of Power Sources* 461 (2020) 228165.
- [110] L. Meirong, L. Yangpeng, W. Kai, C. Shumei, W. Fei, Z. Tianhua, High-efficiency electrocatalytic water oxidation of multi-level cobalt hornflower phenylphosphonate at neutral pH, *Chinese Journal of Catalysis* 10 (2020) 1654.
- [111] L. Liu, D. Zhang, D. Duan, Y. Li, Q. Yuan, L. Chen, S. Liu, In situ fabrication of 3D self-supporting cobalt phosphate-modified graphite felt electrocatalysts for oxygen evolution reaction in neutral solution, *Journal of Electroanalytical Chemistry* 862 (2020) 114031.
- [112] J. Kim, S. V. Chankeshwara, F. Thielbeer, J. Jeong, K. Donaldson, M. Bradley, W. S. Cho, Surface charge determines the lung inflammogenicity: A study with polystyrene nanoparticles, *Nanotoxicology* 10 (2016) 94.
- [113] M. Zeng, H. Wang, C. Zhao, J. Wei, W. Wang, X. Bai, 3D graphene foam-supported cobalt phosphate and borate electrocatalysts for high-efficiency water oxidation, *Science Bulletin* 60 (2015) 1426.
- [114] X. Guo, Y. Xu, Y. Cheng, Y. Zhang, H. Pang, Amorphous cobalt phosphate porous nanosheets derived from two-dimensional cobalt phosphonate organic frameworks for high performance of oxygen evolution reaction, *Applied Materials Today* 18 (2020) 100517.

- [115] J. Xu, D. Xiong, I. Amorim, L. Liu, Template-free synthesis of hollow iron phosphide-phosphate composite nanotubes for use as active and stable oxygen evolution electrocatalysts, *ACS Applied Nano Materials* 1 (2018) 617.
- [116] D. Zhong, L. Liu, D. Li, C. Wei, Q. Wang, G. Hao, Q. Zhao, J. Li, Facile and fast fabrication of iron-phosphate supported on nickel foam as a highly efficient and stable oxygen evolution catalyst, *Journal of Materials Chemistry A* 5 (2017) 18627.
- [117] P. T. Babar, A. C. Lokhande, H. J. shim, M. G. Gang, B. S. Pawar, S. M. Pawar, J. H. Kim, SILAR deposited iron phosphate as a bifunctional electrocatalyst for efficient water splitting, *Journal of Colloid and Interface Science* 534 (2019) 350.
- [118] W. Wang, D. Liu, S. Hao, F. Qu, Y. Ma, G. Du, A. M. Asiri, Y. Yao, X. Sun, High-efficiency and durable water oxidation under mild pH conditions: An iron phosphate-borate nanosheet array as a non-noble-metal catalyst electrode, *Inorganic Chemistry* 56 (2017) 3131.
- [119] C. Li, X. Mei, F. L. -Y. Lam, X. Hu, Amorphous iron and cobalt based phosphate nanosheets supported on Ni foam as superior catalysts for hydrogen evolution reaction, *ACS Applied Energy & Materials* 1 (2018) 6764.
- [120] Y. Zhou, H. C. Zeng, 3D networks of CoFePi with hierarchical porosity for effective OER electrocatalysis, *Small* 14 (2018) 1704403.
- [121] J. Zhang, X. Tan, W. Wang, L. Cao, B. Dong, Iron-doped cobalt phosphate 1D amorphous ultrathin nanowires as highly efficient electrocatalyst for water oxidation, *Sustainable Energy & Fuels* 4 (2020) 4704.
- [122] D. Yin, Z. Jin, M. Liu, T. Gao, H. Yuan, D. Xiao, Microwave-assisted synthesis of the cobalt-iron phosphates nanosheets as an efficient electrocatalyst for water oxidation, *Electrochimica Acta* 260 (2018) 420.
- [123] Y. Zou, Z. Liu, R. Liu, D. Liu, C. Dong, Y. Wang, S. Wang, Disordered CoFePi nanosheets with rich vacancies as oxygen evolving electrocatalysts: Insight into the local atomic environment, *Journal of Power Sources* 427 (2019) 215.
- [124] G. Zhu, X. Xie, L. Xiao, X. Li, X. Shen, Co-Fe bimetal phosphate composite loaded on reduced graphene oxide for oxygen evolution, *NANO* 14 (2019) 1950003.
- [125] Z. Wang, M. Liu, J. Du, Y. Lin, S. Wei, X. Lu, and J. Zhang, A facile co-precipitation synthesis of robust FeCo phosphate electrocatalysts for efficient oxygen evolution, *Electrochimica Acta* 264 (2018) 244.
- [126] M. S. Aziz, U. Saleem, E. Ali, K. Siddiq, A review on bi-source, off-grid hybrid power generation systems based on alternative energy sources, *Journal of Renewable & Sustainable Energy* 7 (2015) 043142.
- [127] J. Bockris, Hydrogen Economy, *Science* 176 (1972) 1323.
- [128] G. Cipriani, V. Di Dio, F. Genduso, D. La Cascia, R. Liga, R. Miceli, G. R. Galluzzo, Perspective on hydrogen energy carrier and its automotive applications, *International Journal of Hydrogen Energy* 39 (2014) 8482.
- [129] R. R. Adžić, A. Tripković, V. Vesšović, Structural effects in electrocatalysis: Oxidation of formic acid and hydrogen adsorption on platinum single-crystal stepped surfaces, *Journal of electroanalytical chemistry and interfacial electrochemistry* 204 (1986) 329.

- [130] C. Lamy, J. M. Leger, J. Clavilier, R. Parsons, Structural effects in electrocatalysis: A comparative study of the oxidation of CO, HCOOH and CH₃OH on single crystal Pt electrodes, *Journal of Electroanalytical Chemistry and Interfacial Electrochemistry* 150 (1983) 71.
- [131] N. M. Marković, R. R. Adžić, B. D. Cahan, E. B. Yeager, Structural effects in electrocatalysis: Oxygen reduction on platinum low index single-crystal surfaces in perchloric acid solutions, *Journal of Electroanalytical Chemistry* 377 (1994) 249.
- [132] Z. W. Seh, J. Kibsgaard, C. F. Dickens, I. B. Chorkendorff, J. K. Nørskov, T. F. Jaramillo, Combining theory and experiment in electrocatalysis: Insights into materials design, *Science* 355 (2017) eaad4998.

CHAPTER – II

THEORETICAL BACKGROUND OF MATERIAL SYNTHESIS METHODS AND CHARACTERIZATION TECHNIQUES

CHAPTER – II

THEORETICAL BACKGROUND OF MATERIAL SYNTHESIS METHODS AND CHARACTERIZATION TECHNIQUES

Contents

Sr. No.	Title	Page No.
	Section A: Methods for material synthesis	39
2.A.1	Introduction	39
2.A.2	Introduction to material synthesis methods	40
2.A.3	Hydrothermal method for material synthesis	42
2.A.3.1	Theoretical background	42
2.A.3.2	Mechanism of hydrothermal method	43
2.A.3.3	Effect of preparative parameters	43
2.A.3.4	Advantages of hydrothermal method	45
2.A.4	Successive Ionic Layer Adsorption and Reaction (SILAR) method for material synthesis	45
2.A.4.1	Theoretical background	45
2.A.4.2	Mechanism of SILAR method	46
2.A.4.3	Effect of preparative parameters	48
2.A.4.4	Advantages of SILAR method	48
	Section B: Material characterization techniques	48
2.B.1	Introduction	48
2.B.2	Physico-chemical characterization techniques	49
2.B.2.1	X-Ray diffraction (XRD)	49
2.B.2.2	Fourier transform infrared (FTIR) spectroscopy	50
2.B.2.3	X-Ray photoelectron spectroscopy (XPS)	52
2.B.2.4	Field emission electron microscopy (FESEM) and energy dispersive X-Ray spectroscopy (EDS)	54
2.B.2.5	Brunauer-Emmett-Teller (BET) technique	57
2.B.3	Electrochemical characterization techniques	58
2.B.3.1	Potentiometry	59

2.B.3.2	Voltammetry	59
2.B.3.3	Electrochemical impedance spectroscopy (EIS)	63
2.C.1	References	65

Section A: Methods for material synthesis

2.A.1 Introduction: Latest energy conversion technologies, such as electrocatalytic water splitting and fuel cells are a symbol of the next conversion energy production processes. For the handy applications of these technologies, best performance electrocatalysts having properties as ease and fast reaction rate, low overpotential, robustness, long term stability and especially within low cost so that, common people can afford it. Active sites are very important during the catalytic activity. Large open porous structure, high specific surface area, and tailored reaction interface for facilitating an accessibility of the active sites, mass transport, and gas release are the conditions of ideal water splitting catalyst. The electrochemical activation process subsequently establishes more oxygen vacancies into the material and enlarges the lattice, leading to the facilitated charge transfer kinetics and enhanced electrocatalytic performance [1,2].

For the electrochemical water splitting, variety of materials such as, iron phosphate, cobalt phosphate, nickel phosphate, cobalt-nickel phosphate, cobalt-iron phosphate, etc. have studied till date. Transition metal phosphate materials with its novel structural and morphological properties have been applicable for the new energy conversion (electrocatalysis) technology. There are variety of chemical structures of metal-phosphorus group having different oxidation states such as phosphate, phosphite, hypophosphite, pyrophosphate, etc. Transition metal phosphates can serve as ideal electrocatalyst material for electrochemical water splitting due to its unique crystallographic arrangement, structural charge balancing by phosphate ligands and hierarchical morphologies [3].

The presence of the phosphate groups acts as proton acceptors that facilitate the oxidation of metal atoms as well as develops distorted local geometry that preferred water adsorption and further water oxidation. Basically, these materials have structured in tetrahedral, pentahedral, octahedral, trigonal-bipyramidal or mixed-octahedral/trigonal-bipyramidal crystal phases depending on the Lewis bases and their oxidation states, and can produce much empty space by large number of tunnels and channels throughout the structure forming metal phosphate framework (**Figure 2.1**). Phosphate ligands $[(\text{PO}_4)^{-3}]$ forms tetrahedral structure by arranging phosphorous atom at the center of tetrahedron and four oxygen atoms at the corners with three electron donating states sharing their corner oxygen atoms with transition metals i.e. with Lewis bases.

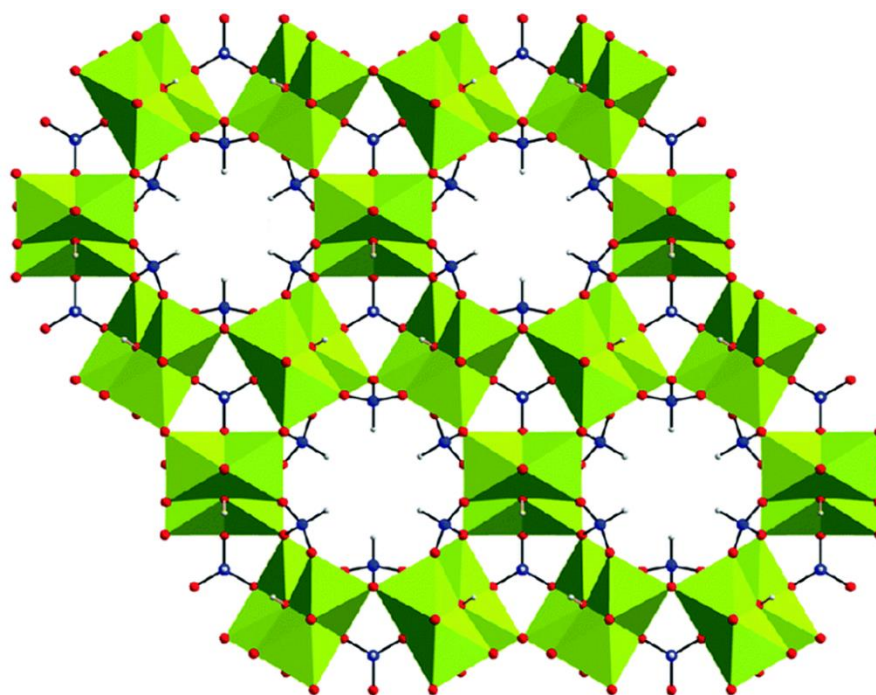


Figure 2.1: Crystal structure of metal phosphate material (for example, hexagonal $\text{Ni}_{11}(\text{HPO}_3)_8(\text{OH})_6$ consists of zigzag $(\text{Ni}_4\text{O}_{12})_n$ double chains (represented by chartreuse octahedra) with $(\text{HPO}_3)^{2-}$ pseudotetrahedra (P: blue; O: red; H: grey) via corner-sharing [3]).

In metal phosphates, transition metal forms a polygon such as tetrahedral, or octahedral, or polyhedral structures having central metal atom covered with oxygen atom making corners of the polygon. The phosphate ligand gives the supportive situations for ion adsorption and oxidation by disturbing native atomic configuration and enabling the oxidation of metal atoms at the time of proton coupled electron transfer process.

2.A.2 Introduction to materials synthesis methods: The development in electronics and energy sector is growing rapidly. To bare the load of required energy, production of energy in large scale is necessary. Energy conversion and storage is possible only due to the development in the materials and their process technologies. Materials in nano or micro size, can enhance their basic physico-chemical characteristics [4]. Materials processing technology is very applicable today in various fields such as industries, medical, food processing, automobiles, energy harvesting and storage, electronics, memory storage, home appliances, etc. The importance of coatings and the synthesis of new materials for industry have resulted in a tremendous increase of pioneering materials processing technologies. The major exploitation of materials science is still in the field of nanotechnology,

microelectronics, optical and magnetic devices, electrochemistry, catalysis, gas sensor, supercapacitors, etc. With the control on the nanocrystalline size of materials, the active surface area, diffusivity, electrical conductivity, hardness with reduction in density, optical transmittance, absorbance, thermal conductivity, etc. can be tuned in contrast with their bulk counterparts.

Nanomaterial is defined as a material created by the random nucleation and growth processes of individually condensing/reacting atomic/ionic/molecular species. The advantages of nanomaterials devices over the bulk materials are low material consumption, easy processing and possible use in various applications [5,6]. As far as the synthesis of nanomaterials is concern, there are two main ways: one is top-down approach and another one is bottom-up approach. Nanomaterials synthesized via breaking of bulk material into nanoscale pieces with the chemical or mechanical processes is called the top-down approach. On the other hand, bottom-up approach where material allows to grow from atomic or molecular species [7]. Nanomaterials can be synthesized by both the ways as shown in the chart given in **Figure 2.2**.

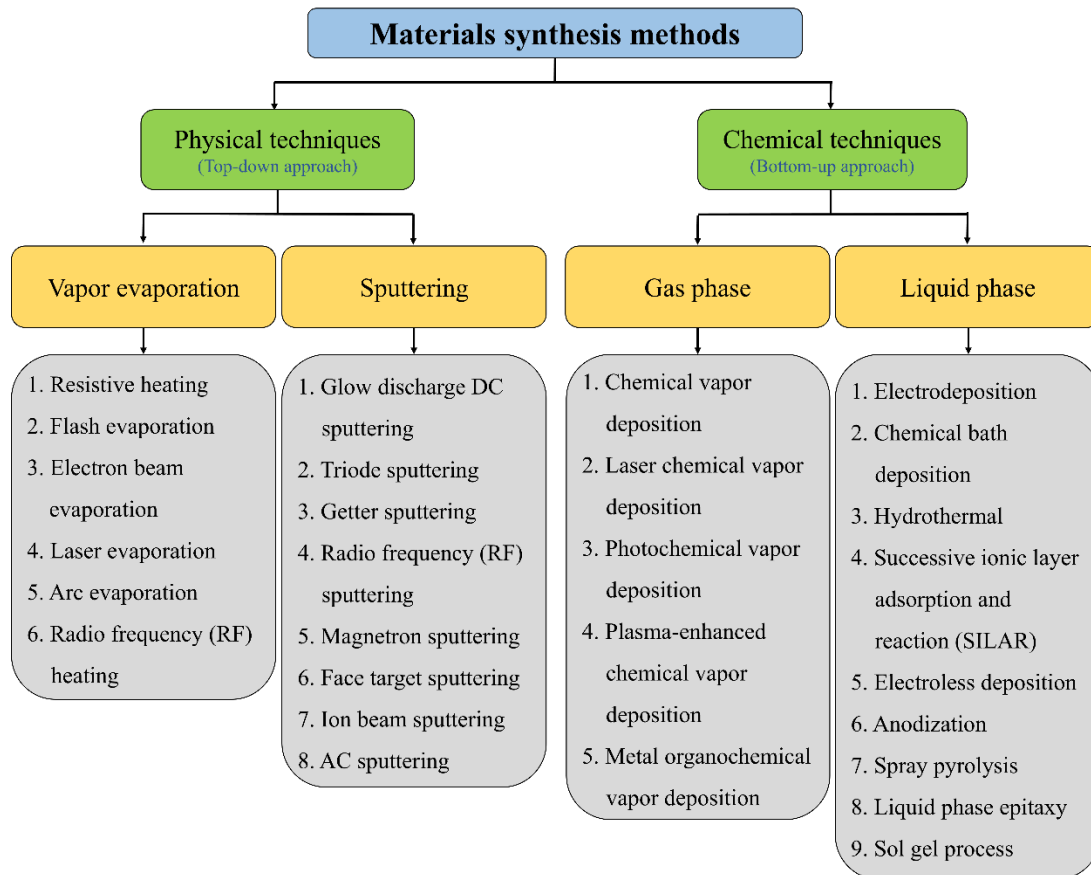


Figure 2.2: Taxonomy of materials synthesis methods.

There are two broad classes of nanomaterials synthesis methods as physical and chemical methods. Vacuum evaporation and sputtering are included in physical methods, where the material to be deposited can be converted in a gaseous state by evaporation or an impact process and deposited on solid substrate [8]. The chemical methods have two different processes depending on the phase of material as gas phase processes and liquid phase chemical processes. In gas phase chemical process, various types of chemical vapor deposition (CVD) methods are included such as, conventional CVD, laser CVD, photo CVD, metal-organo CVD (MOCVD). The liquid phase chemical synthesis process includes electrodeposition, co-precipitation, chemical bath deposition (CBD), modified CBD (M-CBD), hydrothermal, SILAR, spray pyrolysis, sol-gel, etc. [7]. The chemical methods have the specialty that the material growth is from chemical solution. The physical synthesis methods have some major disadvantages such as requirement of high working pressure, sophisticated and highly expensive instruments, etc. On the other hand, chemical synthesis methods are facile, economic and appropriate for the synthesis of diverse materials such as metal oxides, hydroxides, chalcogenides, phosphates, and materials with complex chemical compositions [9-11].

Due to the simplicity and inexpensiveness of chemical methods than that of the physical methods, chemical methods have been applied for the synthesis of nanomaterials. The theoretical background of the chemical synthesis methods i.e. hydrothermal, SILAR, which are used to synthesize the material catalysts in the present research are discussed below in brief.

2.A.3 Hydrothermal method for material synthesis:

2.A.3.1 Theoretical background: Hydrothermal synthesis includes the immense field of crystallizing substances from high-temperature aqueous solutions at high vapor pressures. Nanomaterials can be synthesized in an extensive temperature range from room temperature to very high temperature using hydrothermal method. Morphology of the materials can be controlled by using appropriate pressure (either low or high) depending on the vapor pressure of chief compound in the reaction. Till now, various types of nanomaterials have been successfully prepared using this method. Using liquid phase or multiphase chemical reactions, the composition of nanomaterials can be controlled. By cautiously selecting the parameters like ratio of precursors, pH of the solution, deposition time and temperature, the qualitative characteristics like crystal size, morphology and

agglomeration level of various ceramic oxides can be controlled. Various sized (nano, submicron, micron) particles of many oxides, also the solid solutions of them, inorganic semiconducting nanostructures, perovskites and pyrochlores, paramagnetic-TM-substituted polyoxometalates (TM = Mn, Fe, Co, Ni, Cu), zeolites, carbon based materials, etc. have been prepared by this way. This has made the method a more valuable one in the low temperature production of fine ceramics, clays, and zeolites [12-17].

The perfect hydrothermal autoclave should have the following features [18]:

- I. Non-reactive in acidic, basic or oxidizing agents.
- II. Simple to handle, assemble and disassemble.
- III. An appropriate dimension to get a required temperature gradient.
- IV. Leakage free and unrestricted capabilities for getting necessary temperature and pressure.
- V. Sturdy sufficient to tolerate the large pressure and temperature experiments for long time, so that there should no requirement of treatment after each experimental run.

2.A.3.2 Mechanism of hydrothermal method: Photograph of hydrothermal bomb is shown in **Figure 2.3** below. It consists of a reaction vessel called as liner made up of non-reactive and thermally stable material such as Teflon. To synthesize materials, the chemical solutions or precursor solutions prepared in the solvents like water, or alcohol, etc. can be poured into the Teflon liner and sealed by Teflon lead. The Teflon lead sealed Teflon liner can then be kept in the outer jacket made up of thick walls of SS and closed by the thick SS lead with the help of nut and bolt. The closely tight assembly called hydrothermal bomb then can be kept in laboratory oven or muffle furnace at particular required temperature for required duration of time. Due to high temperature, solvent start to evaporate and hence increase the pressure inside the liner. At high temperature and pressure material get recrystallized and synthesis of required material.

2.A.3.3 Effect of preparative parameters: The material growth rate and particle size varies with the number of nucleation centers, supersaturation of the solution, temperature and pressure. The ion concentration, and their velocities affects the growth kinetics of reaction. The influence of various preparative conditions on these parameters are deliberated underneath.



Figure 2.3: Teflon lined hydrothermal bomb for the synthesis of materials.

a) pH of the bath: The rate of chemical reaction and also the growth rate of nanomaterials depends on the supersaturation condition of the reaction solution. As the pH of the reaction solution is increased, the metal complex usually becomes more stable by reducing the availability of free metal ions. This will decrease the reaction rate resulting in nanoscale of particle size.

b) Complexing agent: As the complexing agent's concentration increases, the concentration of free metal ions decreases. Hence, the reaction rate as well as precipitation lowers which gives rise to controlled morphologies with higher terminal size of the material.

c) Temperature: The decomposition of complex and the anion of the compound (X compound) depend on the temperature. The decomposition is higher at higher temperature and provides greater concentrations of M and X ions leading to higher particle growth rates. Supersaturation is high even at low temperature and increases further with increasing temperature resulting in precipitate formation. At higher temperature, thermal dissociation of complex and anion compound increases in order to obtain more M and X available for MX formation.

d) Precursor concentration: In chemical synthesis methods, the particle growth is affected by changing the concentration of precursor solution. If concentration of metal ion is above the certain ion concentration, the rate of reaction becomes high and lower the crystallinity of the material. In other ways, rate of precipitation increases due to higher reaction rates leads to decrease in crystallinity. However, if concentration of ionic precursors is less than its optimum value, then the material growth cannot take place.

2.A.3.4 Advantages of hydrothermal method:

1. The hydrothermal is facile, simple and convenient method for the synthesis of homogeneous material in nanoscale sizes as well as heterogeneous deposition.
2. The synthesis process is not line-of-sight, like variety of physical synthesis methods. There are no organo-metallic solvents and no emission of toxic or pyrolyzed gases.
3. Facile synthesis processing at large temperature range which facilitates superior alignment of crystalline solids with enhanced grain structure.
4. Stoichiometric material can be achieved since the basic building blocks are ions instead of atoms.

2.A.4 Successive Ionic Layer Adsorption and Reaction (SILAR) method for material synthesis:

2.A.4.1 Theoretical background: The SILAR originally termed as multiple dipping chemical method is a chemical based thin film synthesis process [19]. Considering that the process involves adsorption of a layer of ion on the substrate followed by reaction of the adsorbed ion layer, Nicolau et al. [20] termed the process as SILAR. In comparison with sophisticated physical methods where deposition is performed in vacuum, the SILAR deposition method is very cheap since the deposition is performed in ambient air and no requirement of any sophisticated instrumentation.

In typical CBD method, when ionic product exceeds solubility product, formation of thin film takes place. However, this leads to formation of bulk precipitate into the solution and therefore cannot be eliminated. To overcome the drawbacks like formation of unnecessary bulk precipitate and loss of material, the method is modified and called as SILAR [21]. The SILAR method involves adsorption and reaction of ions from the precursor solutions and rinsing with distilled water between every immersion to avoid

homogeneous precipitation in the solution. The term adsorption refers to the physical attachment of substance on the surface of other substance, which is the fundamental building block of this method. Attractive force between ions in the solution and substrate surface is responsible for adsorption which is surface phenomenon between ions and substrate surface. These forces may be cohesive or Van der Waals or chemical attractive. Adsorption process can be affected by various parameters like solution temperature, nature of substrate, concentration of solution and area of substrate, etc. When freshly adsorbed ions (anions) react with pre-adsorbed ions (cations), the film formation takes place of the preferred material.

2.A.4.2 Mechanism of SILAR method: The SILAR is based on sequential adsorption and reaction steps at the substrate surface. Heterogeneous reaction between solid phase and the solvated ions in the solution was enabled by rinsing between every steps. **Figure 2.4** shows the schematic of reaction steps of SILAR deposition method. SILAR method is proposed to develop thin films of water soluble ionic or ion covalent compounds of the MaXd type by heterogeneous chemical reaction at the solid solution boundary among adsorbed cations aM^{p+} and anion dX^{s-} , the reaction is with equal ionic product:

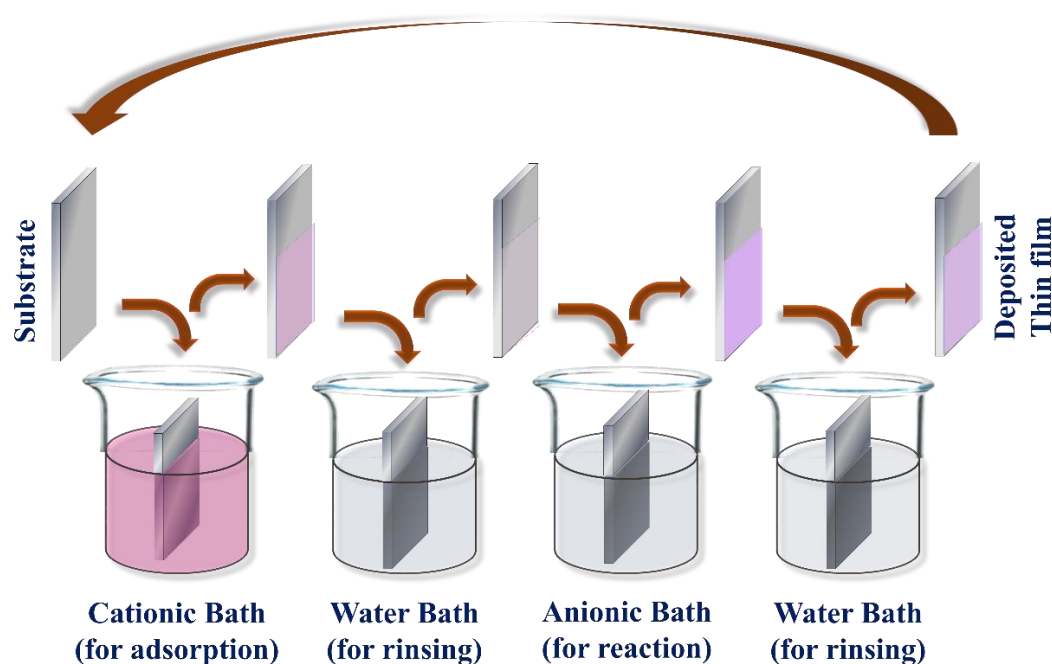
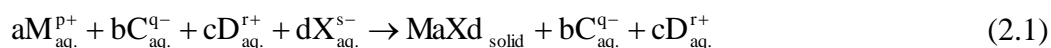


Figure 2.4: Schematic of SILAR thin film deposition method.

Where, $aM_{aq.}^{p+}$ are the cations (i.e. metal ions) in the aqueous cationic solution, a stands for the number of cations and $p+$ stands for the charge on the cation. $bC_{aq.}^{q-}$ are the anions present along with the cations in the aqueous cationic solution, b stands for the number of anions and $q+$ stands for charge on the anion. $cD_{aq.}^{r+}$ are the cations present along with the anions in the aqueous anionic solution, c stands for the number of cations and $r+$ stands for charge on the cation. $dX_{aq.}^{s-}$ are the anions in the aqueous anionic solution, d stands for the number of anions and $s-$ stands for the charge on the anion.

SILAR deposition method consists of four beaker system as shown in **Figure 2.4**. This system generally implemented for the deposition of single or binary metal oxides, hydroxides, sulfides, selenides, phosphates, etc. at room temperature or higher. Material growth can be depending on the different reaction steps as discussed below:

- 1. Adsorption:** This process happens in the first beaker of the reaction, where the cationic precursor solution is kept. In this step, the Helmholtz electric double layer is formed due to the adsorption of cations present in the precursor solution. The adsorbed layer is nothing but the two layers of the inner (positively charged) and outer (negatively charged) layers. The positive layer contains of the cations (M^{p+}) and the negative forms the counter ions (C^{q-}) of the cations as given in the general chemical reaction equation (2.1).
- 2. Rinsing:** This step generally used to remove unadsorbed or loosely adsorbed ions from the diffusion layer. This results in to the saturation of Helmholtz electric double layer.
- 3. Reaction:** This step completes the remaining half part of the reaction by dipping the substrate in third beaker containing the precursor solution of anions. Due to dipping, the aM^{p+} surface species and the anionic precursor X^{s-} starts to react and get neutralize. Due to the instability of the ions, material $MaXd$ in the form of solid substance is formed on the surface of substrate.
- 4. Rinsing:** In this step, the unreacted and excess species of the chemicals and the byproducts after the reaction can be removed from the surface. This is the last step of complete reaction cycle.

Depending on the concentration of precursors and the time of immersion and rinsing, the number of reaction cycles can be optimized for the required thickness and growth of

the film. There are two measures for the film formation process in SILAR as at least one ion must be assigned specifically to substrate interface and the maximum growth rate per immersion cannot exceed the lattice constant of the material. Homogeneous solution precipitation can occur when the measured growth rate surpasses the lattice constant of the material.

2.A.4.3 Effect of preparative parameters: As we know, in the chemical reaction synthesis process, there are large number of factors affecting the reaction, growth and the quality of the thin film. In SILAR deposition, one can control the film thickness and quality of the film by controlling the basic parameters during film deposition such as concentration of cationic and anionic precursors, pH of the precursors, temperature of the solutions, immersion and rinsing time, number of cycles, etc. Also, the particle size, morphology and the thickness can be controlled by using complexing agents and surfactants.

2.A.4.4 Advantages of SILAR method:

1. This method is simple, inexpensive and convenient for large area deposition.
2. Due to low temperature process, different types of substrates such as metal, semiconductor, and insulator possible to use. This method offers extremely easy way to dope film with virtually any element in any proportion by merely adding it in some form of cationic solution.
3. It neither requires high quality targets and/or substrates nor require vacuum at any stage.
4. The deposition rate and the thickness of the film can be easily controlled over a wide range by changing the deposition cycles.
5. The preparative parameters can be easily controlled.

Section B: Material characterization techniques

2.B.1 Introduction: For the effective development in the field of materials science, the testing and identification of the materials and there physico-chemical characteristics are very essential. In the aspect of quality of the synthesized material, the characterization of that material is very important to investigate their applicability. The complete characterization of any material consists of structural, phase as well compositional and micro-structural analysis, surface studies, etc. which have great significance towards

properties of materials. Also characterization techniques help to explain the reasons behind various phenomena occur and assist to establish scientific support to the proposed theories.

In the present section, some characterization techniques are discussed in brief which have used during this research work. For the physico-chemical characterizations, techniques such as XRD, FTIR spectroscopy, XPS, FESEM, EDS analysis, BET surface area analysis, etc. are used. To study the application based properties of the synthesized materials, electrochemical analysis was carried out. Herein, the electrochemical techniques are discussed shortly for the better understanding of the topic.

2.B.2 Physico-chemical characterization techniques:

2.B.2.1 X-Ray diffraction (XRD): In 1859, the German physicist Roentgen discovered the radiation and were so named because their nature was unknown at the time known by X-rays. Radiography was thus initiated without any precise understanding of the radiation used, because until 1912 it was not the exact nature of X-rays established [22]. In that year the phenomenon of XRD by crystals was discovered, and this discovery simultaneously proved the wave nature of X-rays and provided a new method for investigating the fine structure of matter.

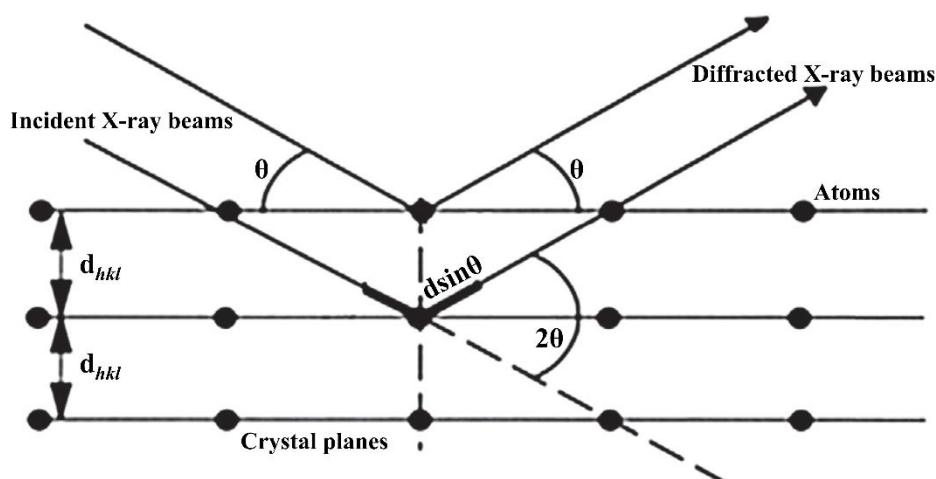


Figure 2.5: Schematic representation of Bragg's diffraction.

At first, XRD was used only for the determination of crystal structure. Later on, it is applied to distinctively recognize the crystalline phases existing in materials and to analyze the structural characteristics (strain, stacking faults, grain size, texture coefficient, epitaxy, defect structure, preferred orientation, etc.) of these phases. Materials composed of any element can be effectively analyzed with XRD [23]. As a significance, the sensitivity of

XRD is dependent on the concerned material. Superior X-ray detection techniques, the accessibility of commercial monochromators and intense microfocus X-ray sources have made XRD method applicable to films as thin as 100 Å.

Figure 2.5 displays the basic features of an XRD instrument, where the diffraction angle 2θ is the angle among the incident and diffracted X-rays. Typically, the intensity of diffracted rays is measured versus the diffracted angle 2θ and the orientation of the specimen, which produces the diffraction pattern. The XRD technique based on monochromatic radiation is more important because the spacing of the planes (d-spacing) can be deduced from the observed diffraction angles using Bragg's equation [24]. Also, the size of a nanocrystal can be predicted using XRD data by combining the Scherrer and Warren formula [25]. This method permits the size of crystals to be determined, but not the size of the particle itself. Since, crystalline size is usually smaller than particle size. For single crystalline nanoparticles, the crystalline size approximates the particle size. The widening of the peaks replicates either crystallinity or the size of nanocrystal. If one can consider the identical crystallinity of nanoparticles, then from the widening of the peaks, size of nanocrystals can be found out; smaller the nanocrystals, broader the XRD peak.

Thin films are commonly in a class of materials intermediate amongst single crystals and powders. That is, all the crystallites in the film have the same atomic planes parallel to the substrate surface, but are otherwise arbitrarily scattered. The XRD offers phase identification and categorization of the materials. This categorization is done by matching the observed 'd' spacing in the diffraction pattern and to a smaller amount, their integrated intensities with known standards in the powder diffraction file stored in Joint Committee on Powder Diffraction Standards (JCPDS) or American Standard for Testing of Materials (ASTM). Preferred orientations of thin films cause the mismatch between measured intensities and JCPDS file, since the provided intensities are for random orientations. For the films having mixed phases, the integrated intensities in the diffraction pattern can provide the measure of each phase present in the film. The sample used may be in the powder, single crystal or thin film form.

2.B.2.2 Fourier transform infrared (FTIR) spectroscopy: For more than a century, the physical principles of infrared spectroscopy have been appreciated essentially. Among the limited techniques, FTIR can afford data regarding the chemical bonds present in substance mostly beneficial for the non-destructive examination of solids and thin films [26]. FTIR

spectroscopy is a technique used to determine qualitative (identification) and quantitative (amount) features of IR active materials. Instead of application as a common tool, the FTIR has a potential of investigation as a function of chemical bond of interest. Basic principle of the FTIR is to identify the variation in intensity of the IR radiation beam interacted with the specimen with respect to the incident radiation as a function of wave number (200-4000 /cm). These absorptions occur at resonant frequencies, i.e. the frequency of the absorbed radiation matches the vibrational frequency [27]. The energies are affected by the shape of the molecular potential energy surfaces, the masses of the atoms, and the associated vibronic coupling.

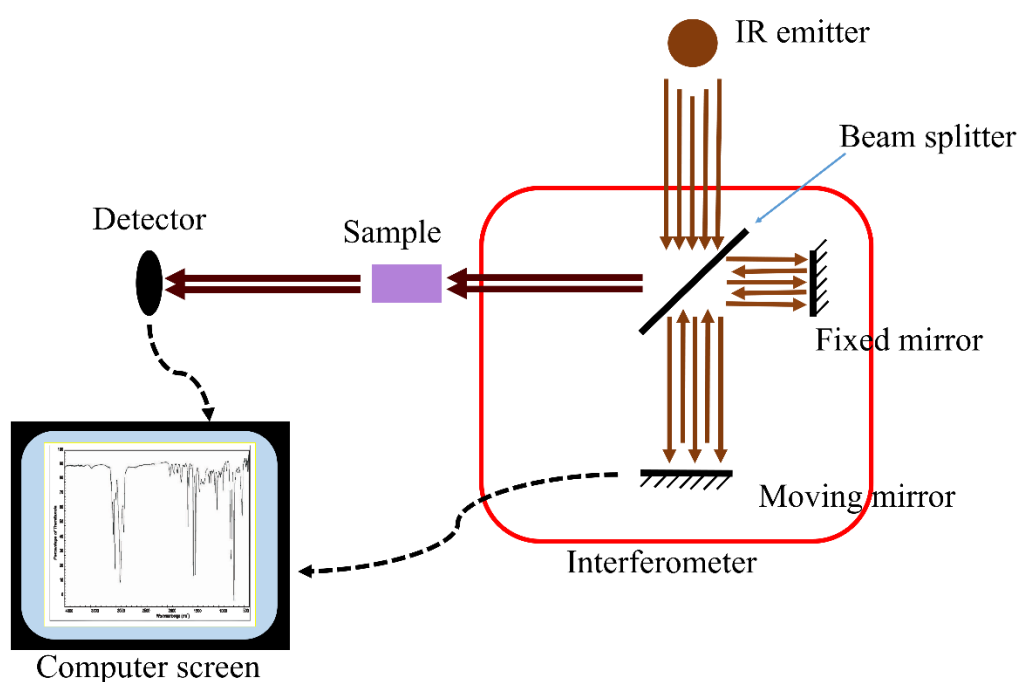


Figure 2.6: Schematic ray diagram of FTIR spectroscopy.

The infrared spectrophotometer is the centerpiece of most equipment configurations. Its major work is to measure the intensity of dispersed light at each frequency from the broadband of infrared source. Infrared light is guided through an interferometer and then through the sample (or vice versa). A moving mirror inside the apparatus alters the distribution of infrared light that passes through the interferometer. The signal directly recorded, called an "interferogram", represents light output as a function of mirror position. A data-processing technique called Fourier transform turns this raw data into the desired result (the sample's spectrum): Light output as a function of infrared wavelength (or equivalently, wavenumber). The proportion between the intensities before and after the

light interacts with the sample is calculated and plotted this proportion against the frequency is nothing but the output infrared spectrum. The ray schematic diagram of FTIR is shown in **Figure 2.6**.

Infrared spectroscopy works on the principle that the chemical bonds have characteristic frequencies at which they vibrate. These resonant frequencies are dependent on the length of the bond and the masses of the atoms at either ends of it. An absorption peak in the IR spectrum results when the incident IR frequency matches with the resonant frequency. There are nine possible ways of the molecular vibrations as they are symmetric stretching (ν_s), asymmetric stretching (ν_{as}), scissoring bending (δ), rocking bending (ρ), wagging bending (ω), twisting bending (T), and out of plane bending (γ). FTIR is useful for the analysis of chemical composition of many organic or inorganic chemicals, solid, liquid or gas samples, polymers, paints, coatings, adhesives, lubricants, semiconductor materials, coolants, gases, biological samples, and minerals [28].

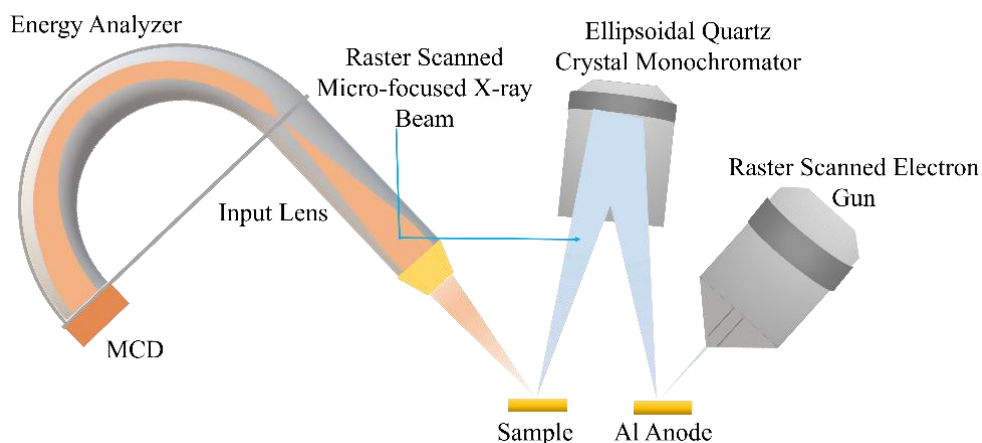
2.B.2.3 X-Ray photoelectron spectroscopy (XPS): Surface modification can be used to alter or improve characteristics such as corrosion rates, catalytic activity, adhesive properties, wettability, contact potential and failure mechanisms, and so surface analysis is used to understand surface chemistry of a material, and investigate the efficacy of surface engineering. XPS is one of the standard tools for surface characterization. XPS, also known as electron spectroscopy for chemical analysis (ESCA), is a technique for analyzing the surface chemistry of a material. XPS can measure the elemental composition, empirical formula, chemical state and electronic state of the elements within a material. It can be obtained by irradiating a solid surface with a beam of X-rays while simultaneously measuring the kinetic energy of electrons that are emitted from the top 1-10 nm of the material being analyzed. The schematic of XPS machine is represented in **Figure 2.7(A)**.

A photoelectron spectrum is recorded by counting ejected electrons over a range of electron kinetic energies. Peaks appear in the spectrum from atoms emitting electrons of a particular characteristic energy. The energies and intensities of the photoelectron peaks enable identification and quantification of all surface elements (except hydrogen). XPS is a surface sensitive technique based on photoelectric effect where the sample is illuminated with X-rays which have enough energy to eject an electron from the atom as shown in **Figure 2.7(B)**. The kinetic energy of these emitted electrons is characteristic of the element

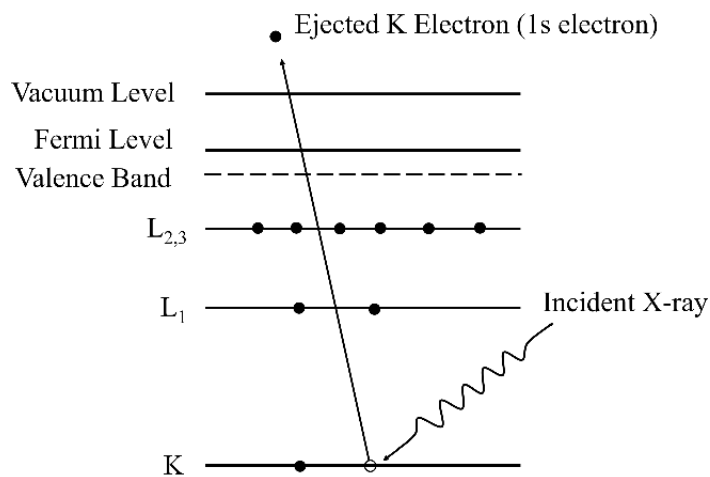
from which the photoelectron originated. Binding energy (E_B) can be calculated from the following equation [29]:

$$E_K = h\nu - E_B - E_W \quad (2.2)$$

Where, E_K is the kinetic energy of emitted electron, $h\nu$ is the incident x-ray photon energy, and E_W is the work function.



(A)



(B)

Figure 2.7: (A) Schematic of XPS instrument, (B) photoelectron emission process involved in XPS analysis.

The position and intensity of the peaks in an energy spectrum provide the desired chemical state and quantitative information. The surface sensitivity of XPS is determined

by the distance that photoelectron can travel through the material without losing any kinetic energy. These elastically scattered photoelectrons contribute to the photoelectron peak, whilst photoelectrons that have been inelastically scattered, losing some kinetic energy before leaving the material, will contribute to the spectral background.

There are several features that make XPS particularly attractive for analytical applications; (1) detection of all elements in the periodic table except hydrogen, (2) E_B data gives insight into the chemical nature of a species, and (3) application to surface analysis [30]. XPS is applicable in the detection of very small amount about 10 ppb of adsorbed elements in the samples like water, etc. [31]. The detection of heavy metals or toxic elements dissolved into water or food can be analyzed for water treatment, pollution control and health [32]. To determine the electronic state of the elements present in the material, XPS analysis technique is effective. The material conversion from one to another phase and phase percentage can be easily identified from the binding energies of corresponding oxidation states and their photoelectron count of the metal elements present in the material.

2.B.2.4 Field emission scanning electron microscopy (FESEM) and energy dispersive X-Ray spectroscopy (EDS): FESEM is widely used microscopy technique to study the surface topography, that works with beam of electrons instead of light. These electrons are liberated by a field emission source. The object is scanned by electrons according to a zig-zag (raster) pattern. The schematic of FESEM is shown in below **Figure 2.8**. A field-emission cathode in the electron gun of a scanning electron microscope provides narrower probing beams at low as well as high electron energy, resulting in both improved spatial resolution and minimized sample charging and damage [33]. Highly energetic electron beam generated from field emission electron gun interacted with matter in elastic and inelastic manner provides variety of information in terms of signals. The electrons emitted from the specimen can be collected with the help of suitable detectors and can be modulated as an output image on the computer screen. The specimen can be scanned in raster manner i.e. in x-y coordinates by varying voltage in scanning coils. By this way, an image is generated on the screen; each point that the beam strikes on the specimen is plotted directly at the consisting point on the screen [34].

FESEM provides topographical and elemental information at magnifications of 10 X to 300 kX, with virtually unlimited depth of field. During this process the characteristic X-ray of an element is produced and detected by the energy dispersive spectroscopy (EDS)

detector in SEM instrument [35]. The ability to examine smaller-area contamination spots at electron accelerating voltages compatible with EDS. High-quality, low-voltage images with negligible electrical charging of samples (accelerating voltages ranging from 0.5 to 30 kilovolts).

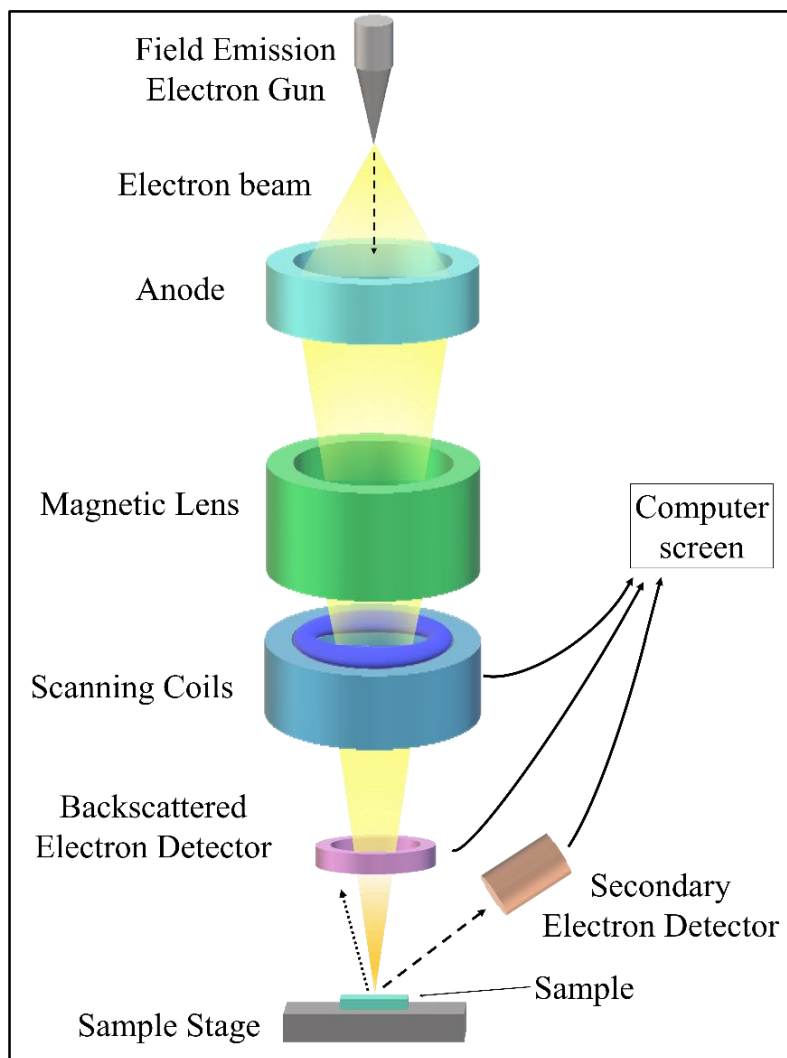


Figure 2.8: Schematic of FESEM instrument.

EDS (or EDX) is an analytical technique used for the elemental analysis or chemical characterization of a sample [36]. Such analytical technique involves fine electron probes specially constructed for an analytical mode. It is one of the variants of X-ray fluorescence spectroscopy which relies on the investigation of a sample through interactions between electromagnetic radiation and matter, analyzing X-rays emitted by the matter in response to being hit with charged particles [37]. Its characterization capabilities are due in large part to the fundamental principle that each element has a unique atomic structure allowing X-rays that are characteristic of an element's atomic structure to be identified uniquely from

one another. As illustrated in **Figure 2.9**, the knockout of innermost electron with the bombardment of collimated beam of electrons to the atom causing a creation of hole at that place. To fulfil the vacancy of shell, the electronic transition from nearest higher level can takes place. During the transition, energy may emit in the form of radiation having the energy equals to the energy difference between two levels. From the energy level L to the level K, the radiations are emitted having energy equals to the X-ray energy. The wavelength of the emitted X-ray will be characteristic to the specific element [38]. Those X-rays are called characteristic X-rays which carry the information of the atom of that element.

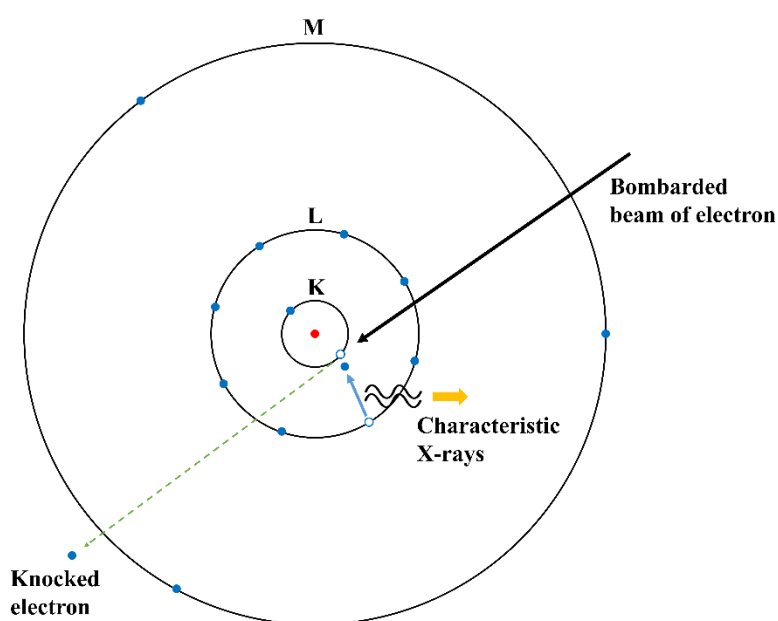


Figure 2.9: Illustration of the principle of EDS analysis.

With modern detectors and electronics most EDS instruments can identify X-rays from almost all the elements in the periodic table beyond beryllium, $Z=4$, if present in sufficient quantity. A spectrum of the energy versus relative counts of the detected X-rays is obtained and evaluated for qualitative and quantitative determinations of the elements present in the sampled volume. The lower limit of detection for elements with atomic numbers more than $Z=11$ is as small as 0.02 wt%, if the peaks are separated and the spectrum has a total count of minimum 2.5×10^5 .

There are various applications of EDS analysis in the research and industrial level. EDS technique has been employed to test analysis of metals, semiconductors, polymers, cement and paper. Also, in medical field, EDS is used for an atomization of organs, blood,

bones and tissues. The other applications of EDS include identification of forgery detection in fine arts, forensic investigation in law enforcement, in pollution control, identification of asbestos in archeology and oceanography.

There are several applications of FESEM and also FESEM along with EDS technique. Few of them are given below:

1. FESEM uses the focused beam of electrons to generate an image of to analyze the surface morphology of the specimen.
2. Semiconductor device cross section analyses for gate widths, gate oxides, film thicknesses, and construction details.
3. Advanced coating thickness and structure uniformity determination.
4. Small contamination feature geometry and elemental composition measurement.
5. FESEM with EDS is applicable to analyze the composition of the specimen.

2.B.2.5 Brunauer-Emmett-Teller (BET) technique: The specific surface area and porosity of the synthesized materials can be determined using BET analysis. In 1938, Stephen Brunauer, Paul Hugh Emmett, and Edward Teller discovered the theory for the surface characterization known as BET theory [39]. In this technique, actual surface area of the material can be determined by the adsorption of a gas on the solid surface of the material. Gas adsorbed on the surface and pores of the material sample at a same time and the amount of gas condensed or adsorbed at a constant temperature on the solid surface is depends on the applied pressure of the gas.

The adsorbed and condensed gas provides the pore structure information of solids. For this technique of the surface area and pore size measurement, generally non-corrosive gases are used. The most commonly usable gas for the surface area measurement is the nitrogen (N₂) [40]. The amount of N₂ adsorbed over the adsorbent at the temperatures of liquid nitrogen (77 K) is measured as a function of pressure [41]. The surface area obtained by applying the BET method on adsorption isotherms obtained on microporous solids does not reflect the true surface area and can be used purely as an empirical value to compare porosity of materials of the same kind [42,43]. For this measurement, the dynamic flow method apparatus is used as shown schematically in **Figure 2.10**.

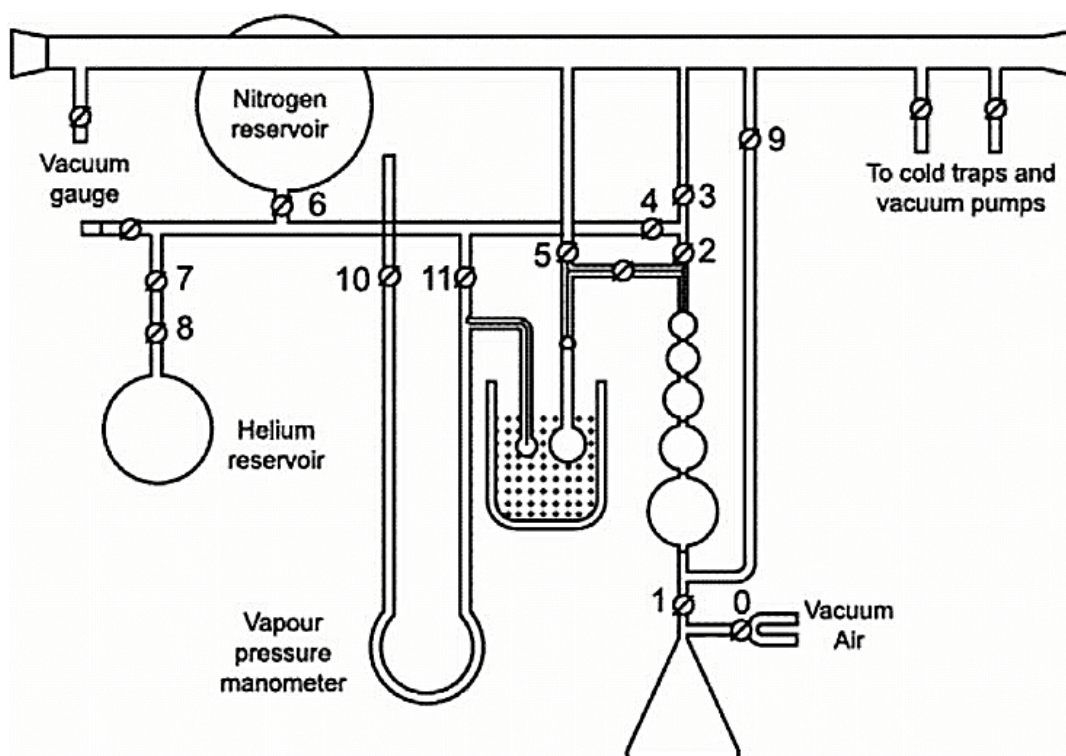


Figure 2.10: Schematic diagram of BET surface area measurement instrument [44].

The BET theory is the extension of Langmuir theory for the monolayer molecular to multilayer adsorption with the hypotheses as: i) physical adsorption of gas molecules on solids, ii) no interaction between each adsorption layer and iii) this theory applied to each layer. The distribution of pore volume with respect to pore size is called a pore size distribution and known as Barrett-Joyner-Halenda (BJH) analysis. It is well accepted that the desorption isotherm is appropriate than the adsorption isotherm values for evolution of pore size distribution of an adsorbent.

2.B.3 Electrochemical characterizations: Electrochemical analysis is a collection of techniques that use electrical stimulation to analyze the chemical reactivity of a sample or a solution [45]. Oxidation and reduction reaction rates are controlled and measured by a potentiostat, connected to electrodes submerged in an electrolyte. The electrochemical analysis methods have different categories depending on the parameters to be applied in controlled manner and the parameters to be measured. The types of electrochemical analysis techniques could be used for electrocatalysis of water, as given in tree diagram (Figure 2.11).

The prime categories are static techniques and dynamic techniques, which are further categorized as potentiometry, coulometry, and voltammetry. The frequency response of the

material to the alternating current (AC) can be analyzed by the impedance measurements with the help of EIS. This technique measures the impedance of a system over a range of frequencies, and it reveals the charge transfer processes.

2.B.3.1 Potentiometry: This technique measures the potential of a solution between two electrodes, affecting the solution very little in the process. One electrode is called the reference electrode which is at constant potential itself, while the other one is a working electrode whose potential changes with the composition of the sample. Therefore, the difference of potential between the two electrodes gives an assessment of the sample.

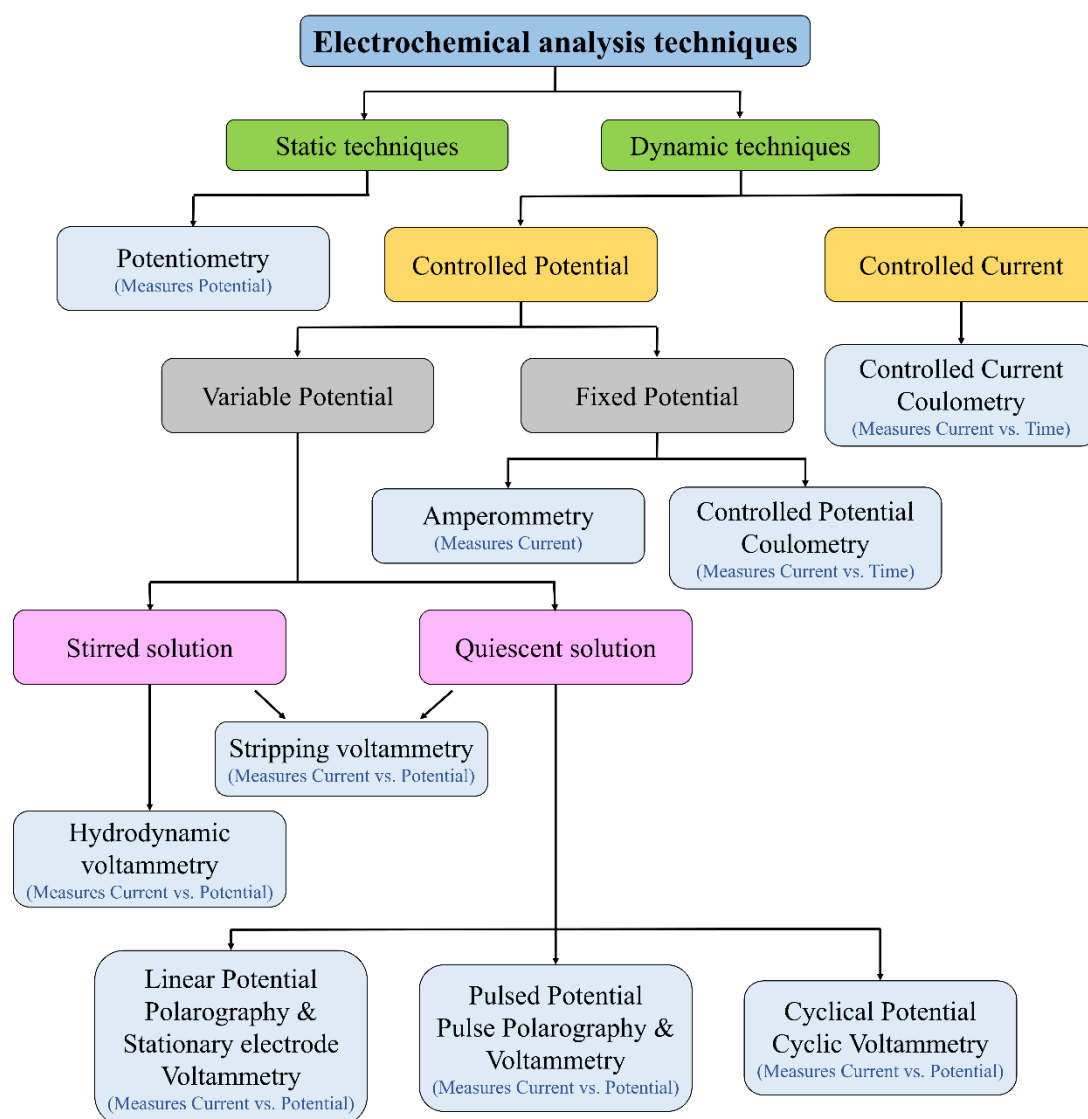


Figure 2.11: Electrochemical analysis techniques.

2.B.3.2 Voltammetry: In this technique, constant or varying potential is applied to an electrode and the resulting current is measured using three electrode system. The

investigative information for a voltammetric experimentation arises in the form of a voltammogram which schemes the current produced versus the potential of the working electrode. The potential is varied arbitrarily either step by step or continuously, and the actual current value is measured as the dependent variable [46]. The shape of the curves depends on the speed of potential variation and on whether the solution is stirred or quiescent. There are various types in voltammetry, some of them are further discussed briefly.

A) Cyclic voltammetry (CV): CV is a potentiodynamic test in which potential of working electrodes is varied (ramped) linearly within the given potential range against time [47,48]. The rate of ramping the potential is controlled by setting the time for each potential step, it is called as scan rate and has the general usable unit is mV/s. After the given potential is reached to the final stage, the potential is ramped in reverse trend up to the given starting potential. This journey completes one cycle. The potential-time (V-t) plot is shown in **Figure 2.12(A)**. As we know, no one can control voltage and current simultaneously, the variation in current with respect to the change in potential can be recorded to understand the current response of the particular electrode material. The voltage is applied amongst working and reference electrodes, whereas the current is measured amongst working and counter electrodes.

As plotted in **Figure 2.12(B)**, there is an example taken for the understanding of change in current response with respect to the time. At the time of starting accelerative scan (from t_0 to t_1) a progressively reducing potential is supplied; so that the cathodic current will primarily increase over this time period considering that there are reducible analytes in the system. At some point after the reduction potential of the analyte is reached, the cathodic current will decline as the concentration of reducible analyte is depleted. If the redox couple is reversible, then at the time of opposite scan (from t_1 to t_2), the reduced analyte will start to be re-oxidized, giving increase to a current of opposite polarity (anodic current) to earlier. The more reversible the redox couple is, the more similar the oxidation peak will be in shape to the reduction peak. Hence, CV data can afford the information regarding the redox potentials and electrochemical reaction rates as shown in **Figure 2.12(C)**. In electrochemical water splitting, the CV is measured for the calculation of electrochemical double layer capacitance (C_{dl}) and electrochemically active surface area (ECSA).

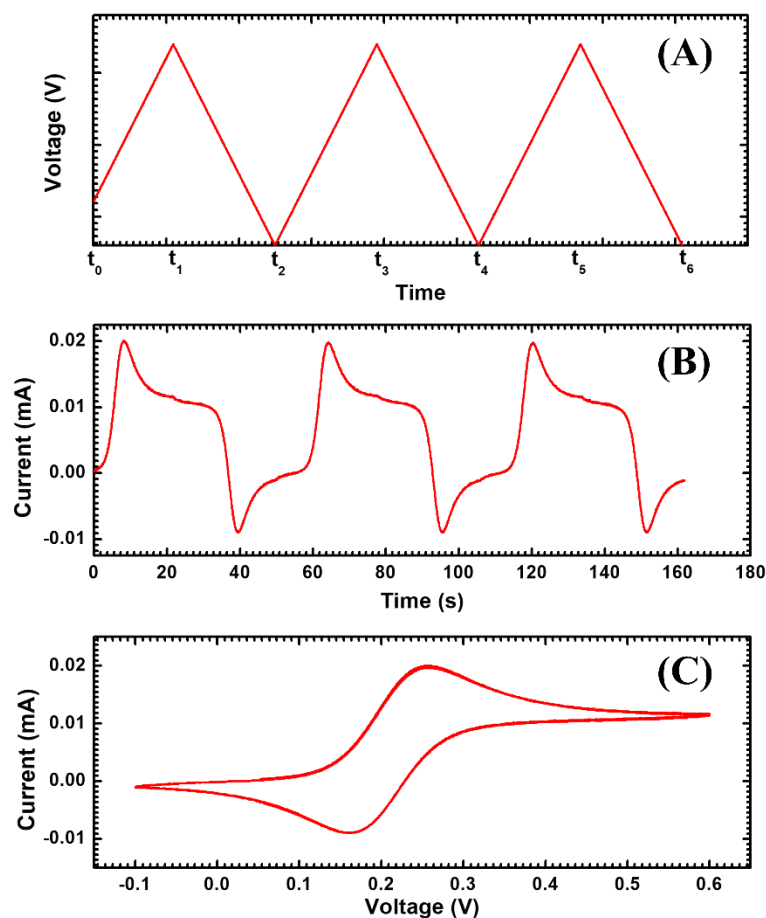


Figure 2.12: (A) Voltage versus time plot, (B) current versus time plot and (C) voltammogram (current versus potential plot), reversible redox couple diffusing freely in solution.

ECSA is directly related to the C_{dl} of the material. For that purpose, one should record CV curves in the region of potential, where the faradaic process cannot be happening. Generally, that region is around the open circuit potential (OCP), hence the CV can be measured in the potential range with the OCP is at the middle of that window, where Faradic reactions not occurred. C_{dl} is calculated by plotting the anodic charging currents (i_c) at OCP of each CV curve against the scan rate by the equation:

$$i_c = vC_{dl} \quad (2.3)$$

Where, v is the scan rate. It yields a straight line with slope equals to C_{dl} .

The ECSA were further calculated by the following equation:

$$ECSA = C_{dl} / C_s \quad (2.4)$$

Where, C_s is the general specific capacitance of an atomically smooth planar surface of the material per unit area under identical electrolyte conditions. Typically, C_s in alkaline solution is 0.04 mF [49]. The roughness factor (RF) is an index which gives the electrocatalytic interface texture, which can be calculated by dividing the ECSA with the geometric area of the electrode in contact with electrolyte.

$$RF = ECSA / A_{geo.} \quad (2.5)$$

Where, $A_{geo.}$ is the geometric area of the electrode.

B) Linear sweep voltammetry (LSV): LSV is nothing but the half part of cycle of CV, where the current is counted at a working electrode during the voltage amongst working and reference electrodes is scanned linearly in period with scan (sweep) rate. Application of scan rate to conduct LSV is dependent on the size of geometric area of the working electrode. Generally, scan rate ranges are: from 1 mV/s to 1 V/s for conventional electrodes whose surface area in between 0.1 to 2 cm², from 1 to 1000 V/s for micro electrodes, and from 1000 V/s to 10⁶ V/s for ultramicro electrodes. The scan is started at a potential where no electrochemical reaction occurs. At the potential where the charge transfer begins, a current can be observed which increases with the potential [45,50].

To study water splitting activity, LSV curve can be recorded and the overpotential is measured at particular current density. The overpotential necessary to attain current density of 10 mA/cm² per geometrical area of the catalyst at ambient temperature and 1 atmospheric O₂ is the required characteristic quantitative measure [51,52]. The measured overpotential should be in the form of the RHE to identify the difference from theoretical values of OER (1.23 V) and HER (0 V). RHE is the reference electrode whose measured potential does not change with the pH. Hence, it can attain a constant potential with a changing pH value. The relation between potential of the RHE (V_{RHE}) and the pH value is:

$$V_{RHE} = 0.000 - 0.059 \times pH \quad (2.5)$$

The regular practically use of RHE is not so easy because there are various limitations and it need safety and cleanroom [53]. The alternative to RHE are other regularly usable reference electrodes such as, saturated calomel electrode (SCE) (saturated KCl),

silver/silver chloride (Ag/AgCl) electrode, mercury/mercury oxide (Hg/HgO) electrode, etc. Potentials are must to convert from the recorded potentials by used reference electrode to RHE. In present study, electrochemical tests were carried by using SCE reference electrode. From SCE potentials to reversible hydrogen electrode (RHE) potentials were transformed by the equation:

$$V_{\text{RHE}} = V_{\text{SCE}} + 0.059 \times \text{pH} + 0.241 \quad (2.6)$$

Where, V_{SCE} is the observed (recorded) potential during experiment, the value 0.241 is the standard potential of the SCE in volts. The overpotential (η) can be calculated by the equation:

$$\eta = V_{\text{RHE}} - 1.23 \quad (2.7)$$

The Tafel slope can be calculated by plotting linear graph of potential against the logarithmic current density which follows the equation:

$$\eta = \pm A \times \log_{10} \left(\frac{i}{i_0} \right) \quad (2.8)$$

Where, A is the Tafel slope, i is the current density and i_0 is the exchange current density [54,55]. The simplified form of Tafel equation to obtain Tafel slope is given as follows:

$$\eta = a + b \times \log|j| \quad (2.9)$$

Where, a is intercept, b is the slope and j is current density.

C) Chronoamperometry (CA): CA is dynamic test where potential is controlled and current response is measured. In CA, potential of the working electrode is stepped and the resulting current from faradaic processes occurring at the electrode (caused by the potential step) is monitored as a function of time [56]. By providing one or paired voltage steps between working and reference, the functional correlation within current response and time is studied. For the electrochemical catalytic stability study, this technique is useful. For the long duration of time, the overpotential value observed at 10 mA/cm² can be applied to working electrode and the response current recorded throughout the time. For the stability study, material should deliver almost 10 mA/cm² current density by applying the overpotential as input for the given time duration.

2.B.3.3 Electrochemical impedance spectroscopy (EIS): EIS is another large branch of electrochemical analysis. It is very useful technique to study the electrochemical process

of electrode materials applicable in the fields such as batteries, supercapacitors, solar cells, and electro/photocatalysis [57-59]. It is an AC technique utilizes a small amplitude having frequency ranging ~ 1 mHz to 1 MHz to probe the impedance characteristics of a cell. The AC signal is scanned over a wide range of frequencies to generate an impedance spectrum for the electrochemical cell under test. EIS differs from direct current (DC) techniques in that it allows the study of capacitive, inductive, and resistive (impedance) processes taking place in the electrochemical cell, where an applied potential (V_t) is modulated over a time with an amplitude ranges 5 to 10 mV and at a controlled frequency (ω) where the small perturbed potential (V_0) is required to ensure linear behavior of the current following the Butler-Volmer model [45].

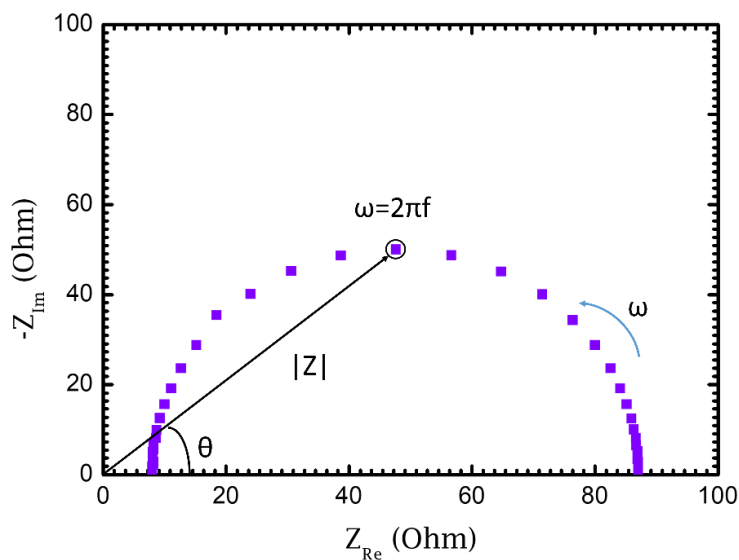


Figure 2.13: A typical Nyquist plot of the circuit having parallel combination of resistor (R) and a capacitance (C).

Collected data is then interpreted using a variety of plots. **Figure 2.13** shows the typical Nyquist plot of the R-C parallel combination. The most important is the Nyquist plot, in which impedance is plotted as a complex number ($J = \sqrt{-1}$) according to equation (2.10) with Z_{Im} (Z'') along the y-axis and Z_{Re} (Z') along the x-axis as shown in **Figure 2.13**.

$$Z(\omega) = |Z|(\cos\theta - j\sin\theta) = Z_{Re} - jZ_{Im} \quad (2.10)$$

Where $|Z|$ is magnitude of impedance as $|Z| = (Z_{Re}^2 + Z_{Im}^2)^{1/2}$ and Z_{Re} , Z_{Im} are real and imaginary parts of impedance. Each data point in a Nyquist plot represents a different frequency with ω decreasing from left to right. At infinitely low frequencies, the applied potential is essentially constant, and this condition is considered the DC limit where $Z_{Re} =$

$R_s + R_{ct}$. The R_s depending on the types of ions and their concentrations, the temperature, and the geometry of the area in which current is carried through solutions due to movement of ionic species. R_{ct} is raised during the electron transfer from the electrode surface into an electrolyte solution or vice versa. The unit of R_{ct} is Ω/cm^2 . R_{ct} is also called activation resistance. Also, the impedance due to the diffusion of mobile ions into the material electrode is called Warburg diffusion impedance (W) which is a transport-related interfacial impedance element. In general, the electrode processes involve mass transport of the species from and to the electrode surface; when calculating the impedance due to mass transport, the effects of diffusion, migration, and convection are to be considered. W is raised at lower frequency region.

2.C.1 References:

1. W. Zhang, K. Zhou, Ultrathin two-dimensional nanostructured materials for highly efficient water oxidation, *Small* 13 (2017) 1700806.
2. H. Dau, C. Limberg, T. Reier, M. Risch, S. Roggan, P. Strasser, The mechanism of water oxidation: From electrolysis via homogeneous to biological catalysis, *ChemCatChem* 2 (2010) 724.
3. P. W. Menezes, C. Panda, S. Loos, F. Bunschei-Bruns, C. Walter, M. Schwarze, X. Deng, H. Dau, M. Driess, A structurally versatile nickel phosphite acting as a robust bifunctional electrocatalyst for overall water splitting, *Energy & Environmental Science* 11 (2018) 1287.
4. L. J. Fu, H. Liu, C. Li, Y. P. Wu, E. Rahm, R. Holze, H. Q. Wu, Surface modifications of electrode materials for lithium ion batteries, *Solid State Science* 8 (2006) 113.
5. C. Königstein, M. N. Spallart, Mechanistic studies on the electrodeposition of ZnTe, *Journal of Electrochemical Society* 145 (1998) 337.
6. I. Gurrapp, L. Binder, Electrodeposition of nanostructured coatings and their characterization-a review, *Science and Technology of Advanced Materials* 9 (2008) 043001.
7. J. George, Preparation of thin films, Marcel Dekker, Inc., New York, (1992) pp. 13-19.
8. D. M. Mattox, Handbook of Physical Vapor Deposition (PVD) Processing, William Andrew, Burlington, (2010) pp. 2-6.
9. T. P. Niesen, M. R. De Guire, Deposition of ceramic thin films at low temperatures from aqueous solutions, *Solid State Ionics* 151 (2002) 61.
10. R. S. Mane, C. D. Lokhande, Chemical deposition method for metal chalcogenide thin films, *Materials Chemistry and Physics* 65 (2000) 1.
11. R. K. Pandey, S. N. Sahu, S. Chandra, Handbook of Semiconductor Electrodeposition, Marcel Dekker Inc., New York, (1996) pp. 205-245.
12. W. Shi, S. Song, H. Zhang, Hydrothermal synthetic strategies of inorganic semiconducting nanostructures, *Chemical Society Reviews* 42 (2013) 5714.
13. D. R. Modeshia, R. I. Walton, Solvothermal synthesis of perovskites and pyrochlores: Crystallisation of functional oxides under mild conditions, *Chemical Society Reviews* 39 (2010) 4303.

14. M. Titirici, M. Antonietti, Chemistry and materials options of sustainable carbon materials made by hydrothermal carbonization, *Chemical Society Reviews* 39 (2010) 103.
15. S. Zheng, G. Yang, Recent advances in paramagnetic-TM-substituted polyoxometalates (TM = Mn, Fe, Co, Ni, Cu), *Chemical Society Reviews* 41 (2012) 7623.
16. H. E. van der Bij, B. M. Weckhuysen, Phosphorus promotion and poisoning in zeolite-based materials: Synthesis, characterisation and catalysis, *Chemical Society Reviews* 44 (2015) 7406.
17. M. Shamzhy, M. Opanasenko, P. Concepción, A. Martínez, New trends in tailoring active sites in zeolite-based catalysts, *Chemical Society Reviews* 48 (2019) 1095.
18. K. Byrappa, M. Yoshimura, *Handbook of hydrothermal technology*, William Andrew., Norwich, (2012) pp. 83.
19. M. Ristov, G. J. Sinadinovski, I. Grozdanov M. Mitreski, Chemical deposition of ZnO films, *Thin Solid Films* 149 (1987) 65.
20. Y. F. Nicolau, J. C. Menard, Solution growth of ZnS, CdS and $Zn_{1-x}Cd_xS$ thin films by the successive ionic-layer adsorption and reaction process; growth mechanism, *Journal of Crystal Growth* 92 (1988) 128.
21. H. M. Pathan, C. D. Lokhande, Deposition of metal chalcogenide thin films by successive ionic layer adsorption and reaction (SILAR) method, *Bulletin of Materials Science* 27 (2004) 85.
22. B. Berman, *Zapped: From Infrared to X-rays, the Curious History of Invisible Light*, Little, Simon and Schuster, (2017) pp. 1.
23. B. D. Cullity, *Elements of x-rays diffraction*, Second Edition, Addison-Wesley, London, (1978) pp. 324-345.
24. D. Sirdeshmukh, L. Sirdeshmukh, K. Subhadra, Diffraction of radiation by crystals (principles and experimental methods), in *atomistic properties of solids*, Springer, Heidelberg, (2011) pp. 115-164.
25. S. A. Khalate, R. S. Kate, J. H. Kim, S. M. Pawar, R. J. Deokate, Effect of deposition temperature on the properties of Cu_2ZnSnS_4 (CZTS) thin films, *Superlattices and Microstructures* 103 (2017) 335.
26. M. L. Hair, *Infrared spectroscopy in surface chemistry*, Marcel Dekker Inc., New York, (1967).
27. J. Preudhomme, P. Tarte, Infrared spectrum of spinels-III: The normal II-III spinel, *Spectrochimica Acta Part A: Molecular Spectroscopy* 27 (1971) 1817.
28. R. A. Nyquist, R. O. Kagel, *Handbook of infrared and raman spectra of inorganic compounds and organic salts*, infrared spectra of inorganic compounds, Academic Press Inc., New York, (1971) pp. 1.
29. S. J. Kerber, T. L. Barr, G. P. Mann, W. A. Brantley, E. Papazoglou, J. C. Mitchell, The complementary nature of x-ray photoelectron spectroscopy and angle-resolved x-ray diffraction part II: Analysis of oxides on dental alloys, *Journal of Materials Engineering and Performance* 7 (1998) 334.
30. M. H. Koppelman, J. G. Dillard, The application of x-ray photoelectron spectroscopy (XPS or ESCA) to the study of mineral surface chemistry, *Developments in Sedimentology* 27 (1979) 153.
31. D. M. Hercules, L. E. Cox, S. Onisick, G. D. Nichols, J. C. Carver, Electron spectroscopy (ESCA): use for trace analysis, *Analytical Chemistry* 45 (1973) 1973.

32. M. Czuha, W. M. Riggs, X-ray photoelectron spectroscopy for trace metal determination by ion-exchange absorption from solution, *Analytical Chemistry* 47 (1975) 1836.
33. J. I. Goldstein, D. E. Newbury, J. R. Michael, N. W. Ritchie, J. H. J. Scott, D. C. Joy, *Scanning electron microscopy and X-ray microanalysis*, Springer, New York, (2017).
34. C. R. Brundle, C. A. Evans, J. S. Wilson, *Encyclopedia of materials characterization: surfaces, interfaces, thin films*, Butterworth-Heinemann, a division of Reed Publishing Inc., USA, (1992).
35. E. Jensen, Types of imaging, Part 1: Electron microscopy, *The Anatomical Record: Advances in Integrative Anatomy and Evolutionary Biology* 295 (2012) 716.
36. K. P. Severin, *Energy Dispersive Spectrometry of Common Rock Forming Minerals*, Kluwer Academic Publishers, The Netherlands, (2004) pp. 23.
37. R. F. Egerton, *Physical principles of electron microscopy: An introduction to TEM, SEM, and AEM*, Springer, New York, (2005) pp. 161-165.
38. A. Beiser, *Perspectives of modern physics*, McGraw-Hill Inc., US (1978) pp. 59-64.
39. S. Brunauer, P. H. Emmett, E. Teller, Adsorption of gases in multimolecular layers, *Journal of American Chemical Society* 60 (1938) 309.
40. J. B. Condon, *Surface Area and Porosity Determinations by Physisorption Measurements and Theory*, Elsevier, The Netherlands, (2006) pp. 15.
41. E. P. Barrett, L. G. Joyner, P. P. Halenda, The determination of pore volume and area distributions in porous substances. I. Computations from nitrogen isotherms, *Journal of American Chemical Society* 73 (1951) 373.
42. G. Ertl, H. Knozinger, F. Schuth, J. Weitkamp, *Handbook of heterogeneous catalysis, Second Enlarged Edition, Volume 1*, WileyVCH Verlag GmbH & Co. KGaA, Weinheim, Germany, (2008).
43. M. Thommes, *Textural characterization of zeolites and ordered mesoporous materials by physical adsorption, Introduction to Zeolite Science and Practice*, 3rd ed., Elsevier B.V., (2007).
44. <https://particle.dk/methods-analytical-laboratory/surface-area-bet-2/> (Web accessed on 16th July 2021).
45. Allen, J. Bard, R. Faulkner Larry, *Electrochemical methods fundamentals and applications*, John Wiley & Sons, New York, (2001) pp. 226.
46. P. Kissinger, W. R. Heineman, *Laboratory techniques in electroanalytical chemistry, revised and expanded*, CRC press, (2018).
47. R. S. Nicholson, I. Shain, Theory of stationary electrode polarography, single scan and cyclic methods applied to reversible, irreversible, and kinetic systems, *Analytical Chemistry* 36 (1964) 706.
48. N. Elgrishi, K. J. Rountree, B. D. McCarthy, E. S. Rountree, T. T. Eisenhart, J. L. Dempsey, A practical beginner's guide to cyclic voltammetry, *Journal of Chemical Education* 95 (2018) 197.
49. C. C. McCrory, S. Jung, J. C. Peters, T. F. Jaramillo, Benchmarking heterogeneous electrocatalysts for the oxygen evolution reaction, *Journal of American Chemical Society* 135 (2013) 16977.
50. A. J. Bard, G. Inzelt, F. Scholz, *Electrochemical dictionary*, Springer-Verlag, Berlin Heidelberg, (2008) pp. 402.

51. M. G. Walter, E. L. Warren, J. R. McKone, S. W. Boettcher, Q. Mi, E. A. Santori, N. S. Lewis, Solar water splitting cells, *Chemical Reviews* 110 (2010) 6446.
52. Y. Gorlin, T. F. Jaramillo, A bifunctional nonprecious metal catalyst for oxygen reduction and water oxidation, *Journal of American Chemical Society* 132 (2010) 13612.
53. G. Jerkiewicz, Standard and reversible hydrogen electrodes: Theory, design, operation, and applications, *ACS Catalysis* 10 (2020) 8409.
54. K. J. Vetter, *Electrochemical kinetics: Theoretical and experimental aspects*, Academic press Inc., London, (2013) pp.143.
55. J. A. V. Butler, Hydrogen overvoltage and the reversible hydrogen electrode, *Proceedings of the Royal Society of London Series-A Mathematical and Physical Sciences* 157 (1936) 423.
56. C. G. Zoski, *Handbook of electrochemistry*, Elsevier, The Netherlands, (2006) pp. 836.
57. B. Klahr, S. Gimenez, F. Fabregat-Santiago, T. Hamann, J. Bisquert, Water oxidation at hematite photoelectrodes: The role of surface states, *Journal of American Chemical Society* 134 (2012) 4294.
58. B. Klahr, S. Gimenez, F. Fabregat-Santiago, J. Bisquert, T. W. Hamann, Photoelectrochemical and impedance spectroscopic investigation of water oxidation with “Co–Pi”-coated hematite electrodes, *Journal of American Chemical Society* 134 (2012) 16693.
59. E. von Hauff, Impedance spectroscopy for emerging photovoltaics, *Journal of Physical Chemistry C* 123 (2019) 11329.

CHAPTER – III

**HYDROTHERMALLY SYNTHESIZED
COBALT-IRON PHOSPHATE AND
COBALT-IRON
PHOSPHATE/REDUCED
GRAPHENE OXIDE HYBRID FOR
ELECTROCHEMICAL OER AND HER
APPLICATION**

CHAPTER – III

HYDROTHERMALLY SYNTHESIZED COBALT-IRON PHOSPHATE AND COBALT-IRON PHOSPHATE/REDUCED GRAPHENE OXIDE HYBRID FOR ELECTROCHEMICAL OER AND HER APPLICATION

Contents

Sr. No.	Title	Page No.
3.1	Introduction	71
3.2	Section-A: Hydrothermal synthesis of cobalt-iron phosphate and their characterization for electrochemical OER and HER	72
3.2.A.1	Introduction	72
3.2.A.2	Experimental details	73
3.2.A.2.1	Materials used and substrate cleaning	73
3.2.A.2.2	Synthesis of cobalt-iron phosphate	73
3.2.A.2.3	Physico-chemical characterizations	74
3.2.A.2.4	Electrochemical characterizations	74
3.2.A.3	Results and discussion	75
3.2.A.3.1	Reaction mechanism	75
3.2.A.3.2	XRD analysis	76
3.2.A.3.3	FTIR analysis	77
3.2.A.3.4	XPS analysis	78
3.2.A.3.5	Surface morphological and elemental analysis	79
3.2.A.3.6	N ₂ adsorption-desorption isotherm analysis	82
3.2.A.3.7	Electrochemical catalytic performance analysis	83
3.3	Conclusions	90
3.4	Section B: Hydrothermal synthesis of cobalt-iron phosphate/reduced graphene oxide hybrid and their characterization for electrochemical OER and HER	91
3.4.B.1	Introduction	91
3.4.B.2	Experimental details	92
3.4.B.2.1	Materials used and substrate cleaning	92
3.4.B.2.2	Synthesis of graphene oxide (GO)	92

3.4.B.2.3	Synthesis of cobalt-iron phosphate/reduced graphene oxide	93
3.4.B.2.4	Cobalt-iron phosphate/reduced graphene oxide electrode preparation	94
3.4.B.3	Results and discussion	95
3.4.B.3.1	XRD analysis	95
3.4.B.3.2	FTIR analysis	95
3.4.B.3.3	XPS analysis	96
3.4.B.3.4	Surface morphological and elemental analysis	98
3.4.B.3.5	N ₂ adsorption-desorption isotherm analysis	99
3.4.B.3.6	Electrochemical catalytic performance analysis	101
3.5	Conclusions	108
3.6	References	109

3.1 Introduction: Today, there is need to harvest energy through the green and sustainable energy sources to avoid future energy catastrophe, ecological contamination and global warming. It is interesting thing that, there is rapid transition from non-renewable to the renewable energy sources. Solar, wind, hydrodynamic, etc. are popular renewable energy sources. Hydrogen is one of the energy source which has high potential to change the situation of energy demand and generation in a future sustainable energy sector [1]. There are enormous techniques to produce hydrogen, from which splitting of water by the application of electricity (electrochemical) or solar radiation (Photochemical) or electricity and solar radiation (PEC) are effective ways [2,3]. For the electrical energy conversion in chemical one in the form of gaseous hydrogen, electrochemical splitting of water is the best technique in presence of apposite catalyst electrodes. There are two half parts of electrochemical water splitting, one half part of reaction is nothing but the HER on the cathode and another half part of reaction is OER on the anode. But these reactions are not thermodynamically favorable. Electrocatalysts play an important role in minimizing the overpotential by providing active sites, easy charge transfer, and high ion adsorption energy. To diminish the overpotential and energy wastage for OER, the requirements of a worthy electrocatalyst are high catalytic activity, greater electrical conductivity, easy mass transport and gas release and satisfactory electrocatalytic stability [4].

The state-of-the-art catalysts like platinum, ruthenium/iridium and their oxides are extensively applied at present as the top electrocatalysts with high efficiency. But, because of their inadequacy, expensiveness, high overpotentials for large current densities and deprived stability, the marketable usage of these precious materials is not possible [5]. Many alternatives to the noble metal catalysts have been discovered to minimize the cost of catalyst material. Among the all non-noble electrocatalysts, materials of the metals from first row 3d-orbital transition states such as oxides, hydroxides, nitrides, phosphides, phosphates, chalcogenides, borides, etc. are highly attractive because of the superficial conversion of their oxidation states, low cost and relatively high activity [6-8]. Transition metal phosphate catalysts are promising for electrochemical water splitting who provides adsorption and alleviating active cites, moreover simultaneously phosphate ligands contribute the advantageous situations for electrolyte ion adsorption and oxidation by disturbing native atomic configuration and enabling the oxidation of metal atoms at the time of proton coupled electron transfer.

In the present research, cobalt-iron phosphate and cobalt-iron phosphate/reduced graphene oxide catalysts were prepared by using the hydrothermal synthesis method. The effect of chemical compositional variation on the structure, morphology, etc. was analyzed. Furthermore, the influence of the composition and the morphology variation on electrochemical water splitting was thoroughly studied. This chapter is divided into two sections as section-A and section-B. Section-A contains the synthesis of cobalt-iron phosphate catalyst electrodes via superficial hydrothermal process and their characterization for physico-chemical and electrochemical water splitting study. In section-B, the cobalt-iron phosphate/reduced graphene oxide hybrid electrodes were prepared and the effect of rGO concentration variation in the optimized cobalt-iron phosphate sample (in section A) was studied for electrochemical water splitting.

3.2 Section-A: Hydrothermal synthesis of cobalt-iron phosphate and their characterization for electrochemical OER and HER

3.2.A.1 Introduction: In binary metal compounds, the electrochemical performance can be depending on unique synthesis process, metal atoms synergistic effect, increase in the amount of active sites, channels for electrolyte ion migration, high surface area, pore volume, and high mesoporosity. Deposition process and composition of precursors greatly affect the architecture of prepared material. The composition can affect on the morphology of material and change in corresponding results can affect on the physico-chemical properties and electrochemical performance. A small number of published articles are accessible on cobalt-iron phosphate catalyst material electrode for OER and HER. Liu et. al. [9] synthesized cross linked porous cobalt-iron pyrophosphate by co-precipitation method which showed the overpotential of 276 mV to deliver current density of 10 mA/cm² and around 30000 s (8.33 h) OER stability. Tremella-like cobalt-iron phosphate NSs were synthesized via microwave-assisted precipitation which delivered 94 % current density retention at constant water oxidation with overpotential of 267 mV at 10 mA/cm² current density for OER [10]. These reports reveals that, there were powder coating techniques used for the preparation of catalyst electrodes. It is worth noting that, there is only a report of direct growth (binder free) cobalt-iron phosphate on NF for HER study [11]. NF offers excellent conductivity as a substrate but itself shows catalytic behavior in alkaline electrolyte. Still there is no any report for OER, HER and overall water splitting by using cobalt-iron phosphate catalyst electrodes.

Here, as pioneering, cobalt-iron phosphate was synthesized via single step hydrothermal approach. In the present work, the morphological evolution due to change in compositional ratio of cobalt and iron, and their effect on the electrochemical splitting of water in the form of OER and HER is studied. Meanwhile, cobalt-iron phosphate at different compositional ratio, cobalt phosphate, and iron phosphate are synthesized and compared their electrochemical study to investigate the best performing catalyst.

3.2.A.2 Experimental details:

3.2.A.2.1 Materials used and substrate cleaning: For the preparation of cobalt-iron phosphate, the analytical grade chemicals were used as $\text{CoCl}_2 \cdot 6\text{H}_2\text{O}$, FeCl_2 , KH_2PO_4 , and urea ($\text{CO}(\text{NH}_2)_2$) purchased from Sigma-Aldrich and Thomas Baker. The as-purchased chemicals were used for catalyst synthesis without further purification. As compared to other substrates like NF or CC, SS substrates have low cost, easy availability, high electrical conductivity and most importantly the non-reactivity in acidic or alkaline media. Before the preparation for reaction, SS substrates were systematically washed. The $1\text{ cm} \times 6\text{ cm}$ pieces of SS were polished by very fine zero grade polish paper and rinsed with laboratory soap solution and double distilled water (DDW) severally. After wash, substrates were transferred to the solution of ethanol and water and ultrasonicated for 20 min.

3.2.A.2.2 Synthesis of cobalt-iron phosphate: A facile hydrothermal method was used to synthesize cobalt-iron phosphate electrodes on SS substrates. The solutions were prepared separately in 50 ml DDW by dissolving 0.1 M KH_2PO_4 , 0.1 M urea and the molar ratio was varied for $\text{CoCl}_2 \cdot 6\text{H}_2\text{O}$ and FeCl_2 as described in **Table 3.1**. The prepared individual solutions were mixed together and stirred at room temperature for 30 min to become it homogenous. After stirring, the solutions were transferred to Teflon lined SS hydrothermal bombs. The systematically washed SS substrates were set aside straight properly in the solutions and bombs were sealed tightly. Hydrothermal bombs were then placed in laboratory oven for 14 h and temperature was maintained at $130\text{ }^\circ\text{C}$. After completing the reaction time, the reactions allow to cool naturally and the electrodes were removed, washed by means of DDW twice to remove unbonded material particles and dried in atmospheric temperature. The prepared cobalt-iron phosphate (CFP-H series) electrodes were named as CFP-H2, CFP-H3 and CFP-H4. For comparison, the cobalt phosphate was prepared by keeping ratio of Co:Fe as 100:0 named as CFP-H1 and the iron phosphate with the ratio of Co:Fe as 0:100 named as CFP-H5.

Table 3.1: Concentration variation of cobalt and iron in the cobalt-iron phosphate electrodes.

Sr. No.	CoCl ₂ .6H ₂ O (M)	FeCl ₂ (M)	% Ratio	KH ₂ PO ₄ (M)	Notation
1.	0.1	0	100:0	0.1	CFP-H1
2.	0.075	0.025	75:25	0.1	CFP-H2
3.	0.05	0.05	50:50	0.1	CFP-H3
4.	0.025	0.075	25:75	0.1	CFP-H4
5.	0	0.1	0:100	0.1	CFP-H5

3.2.A.2.3 Physico-chemical characterizations: From Rigaku Miniflex 600 X-ray diffractometer using Cu-K α target radiation ($\lambda=1.5406$ Å), the XRD patterns of the materials were collected in 2θ range from 5 to 80°. Molecular vibrational analysis was performed by FTIR spectroscopy using alpha (II) Bruker spectroscope in the wavenumber range 400 to 4000 /cm. XPS conducted for electronic state information using X-ray photoelectron spectrometer (XPS, Thermo Scientific Inc. K-alpha) having microfocus monochromatic radiations of Al K α X-ray. Compositional and surface morphological characteristics were carried by EDS and Field Emission Scanning Electron Microscopy by FESEM, JEOL JSM-6500F. The surface analysis was carried by Belsorp II mini via N₂ adsorption-desorption isotherms.

3.2.A.2.4 Electrochemical characterizations: Entire electrochemical characteristics carried on ZIVE MP1 electrochemical workstation using typical three electrodes electrochemical cell configuration. The as-deposited samples and platinum strip act as a working and counter electrodes. As a reference, SCE electrode was used. The OER was studied in 1 M KOH having pH equals to 13.7 and HER in 1 M H₃PO₄ having pH equals to 1.5, electrolyte solutions. Voltages were transformed from SCE to RHE by using the equation (2.6) given in **chapter 2, section B, subsection 2.B.3.2**. CV curves were recorded to measure ECSA in the potential window 1 to 1.15 V vs RHE at different scan rates. The polarization curves were recorded by LSV at 1 mV/s scan rate in the potential window 1.05 to 1.75 V vs RHE (for OER) and 0.33 to -0.85 V vs RHE (for HER). The Tafel plots were obtained by the equation (2.9) given in **chapter 2, section B, subsection 2.B.3.2**. The EIS studied with 10 mV AC amplitude in 0.1 MHz to 100 mHz frequency range. Long term catalytic stability studies were accomplished by CA test at overpotentials. Further,

overpotentials η (V) were calculated for OER by subtracting the thermodynamic potential value for OER (1.23 V) from the observed potential in terms of RHE.

3.2.A.3 Results and discussion:

3.2.A.3.1 Reaction mechanism: Growth mechanism for film preparation is mainly divided into two types. In ion-by-ion mechanism growth of materials takes place by deposition of ions on the substrate surface at the nucleation sites. On the other hand, in cluster-by-cluster mechanism adsorption of colloidal particles leads to formation of nuclei and aggregation and coalescence facilitates the growth of material [12]. Synthesis of cobalt-iron phosphate was accomplished using superficial hydrothermal method on conducting SS-substrates. Fundamentally, the stages of solution reaction are the nucleation, coalescence and growth of particle from liquid to solid phase formation which is nothing but the bottom-up approach. There are two classes of particle development such as heterogeneous and homogeneous nucleation followed by successive crystal growth. In homogeneous growth, the particle seeds formed within the solution and produced the precipitation of material, on the other hand, in heterogeneous growth, the nucleation of particle seeds formed at the substrate surface and consequently development of uniform material is possible. The photograph of deposited material is shown in **Figure 3.1(A)** and the mass loading for each sample calculated by weight difference method is shown in **Figure 3.1(B)**.

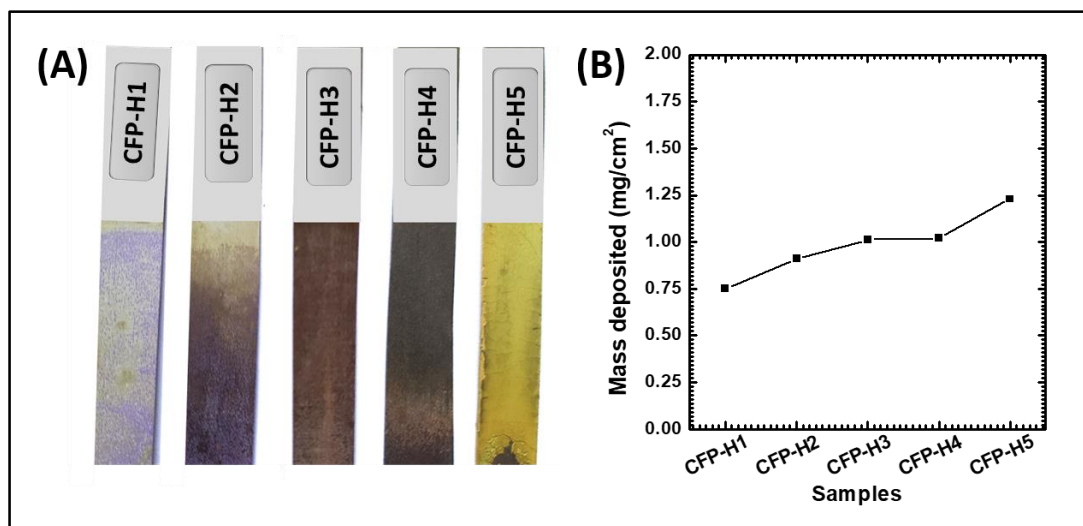


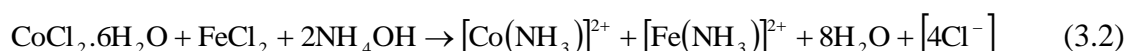
Figure 3.1: (A) Photograph of cobalt-iron phosphate deposited using hydrothermal method, (B) mass loading per unit area of CFP-H series.

Cobalt-iron phosphate synthesized by varying the concentration ratio of cobalt and iron. The hydrolyzing agent used for the reaction is urea ($\text{CO}(\text{NH}_2)_2$) along with the precursors cobalt (II) chloride ($\text{CoCl}_2 \cdot 6\text{H}_2\text{O}$), iron (II) chloride (FeCl_2), and potassium dihydrogen orthophosphate (KH_2PO_4). At optimized reaction temperature (130°C), water dissolved urea gets decomposed into ammonium hydroxide (NH_4OH) with the release of carbon dioxide (CO_2).

Following reaction gives decomposition of water dissolved urea:



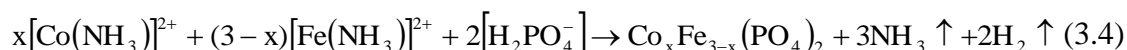
The formation of ammonium hydroxide in the reaction bath increases the pH of the solution to alkaline which further complexes the metal ions as:



Simultaneously, KH_2PO_4 gets decomposed into the dihydrogen phosphate ion as:



The amine cations of cobalt $[\text{Co}(\text{NH}_3)]^{2+}$ and iron $[\text{Fe}(\text{NH}_3)]^{2+}$ get reacted with the phosphate anions $[\text{H}_2\text{PO}_4^-]$ and starts the nucleation of cobalt-iron phosphate.



The growth of cobalt-iron phosphate at the molecular stage take place with heterogeneous nucleation on the surface of SS-substrate. The superior and even thin layer of cobalt-iron phosphate formed by the growth of nuclides through coalescence. At 130°C reaction time, the SS substrates get covered with uniform coating of material within the optimized reaction time.

3.2.A.3.2 XRD analysis: The structural properties of cobalt-iron phosphate at different compositional ratio, cobalt phosphate, and iron phosphate synthesized on SS-substrate which were examined by XRD analysis and presented in **Figure 3.2**. It is observed that, the cobalt phosphate (CFP-H1) show crystalline nature. The diffraction peaks at $2\theta = 10.8^\circ$, 13.26° , 26.7° , 35.6° , and 69.8° can be indexed to (0 0 1), (0 2 0), (1 2 1), (2 3 1), and (2 9 1) planes, respectively corresponding to $\text{Co}_3(\text{PO}_4)_2 \cdot 4\text{H}_2\text{O}$ (JCPDS card no. 34-0844). The similar crystalline nature was reported earlier for cobalt phosphate by Katkar et al. [13].

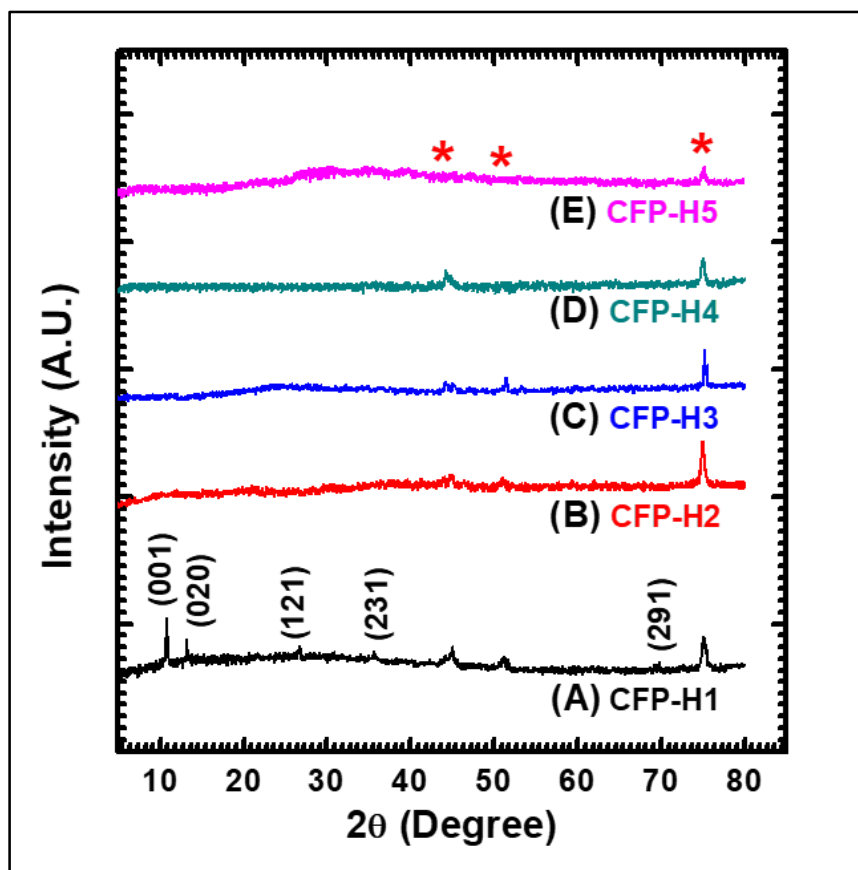


Figure 3.2: XRD patterns of (A) CFP-H1, (B) CFP-H2, (C) CFP-H3, (D) CFP-H4, and (E) CFP-H5 on SS substrates.

The peaks marked with ‘*’ are the diffraction peaks of SS substrate. As the small amount of iron was introduced (CFP-H2), the diffraction peaks of $\text{Co}_3(\text{PO}_4)_2 \cdot 4\text{H}_2\text{O}$ disappeared and the material becomes amorphous. The all other cobalt-iron phosphate at different compositional ratio, and iron phosphate materials are showing amorphous nature. The amorphous materials may give the large surface area and high electrocatalytic active sites which are favorable for water molecule adsorption and decomposition into O_2 and H_2 .

3.2.A.3.3 FTIR analysis: FTIR spectra of the prepared materials which reveals the intermolecular bonding and their vibrational modes. As given in **Figure 3.3**, the absorption peak at 599 /cm reveals the asymmetric bending vibrations of PO_4 bonding. It is observed that, as iron content increases in the material, absorption of the peak goes on increasing. It reveals that, with iron concentration, PO_4 bond becomes stronger. The asymmetric stretching vibrations of PO_4 are observed by the sharp absorption at 1048 /cm [14]. Very small absorption band at 1361 /cm is assigned to the vibration of the CO_2 molecules raised from urea [15].

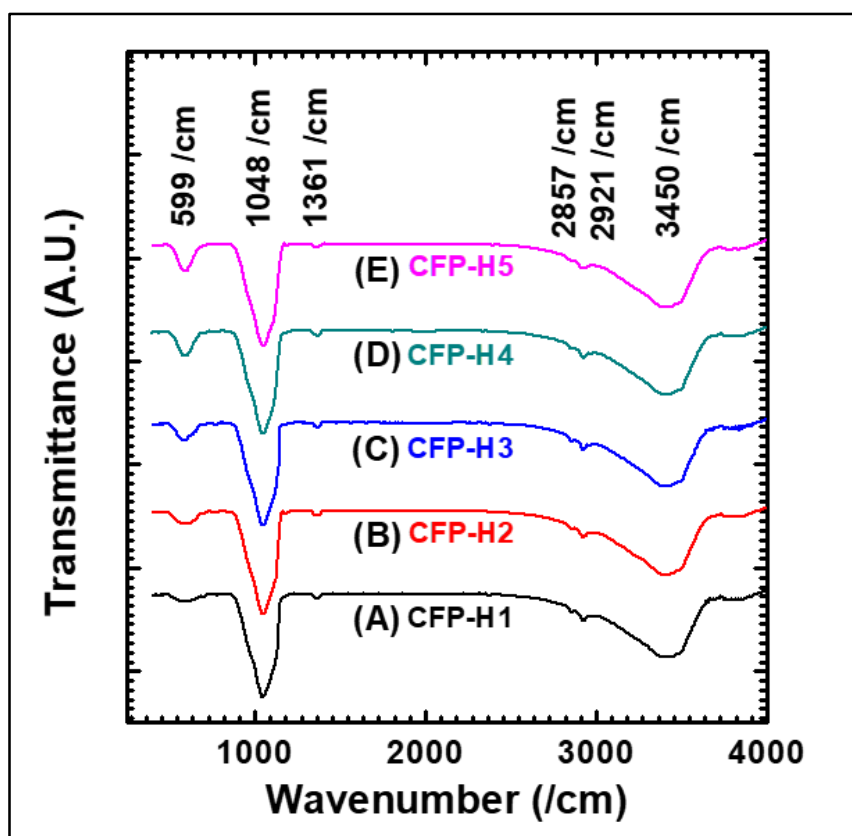


Figure 3.3: FTIR patterns of hydrothermally synthesized (A) CFP-H1, (B) CFP-H2, (C) CFP-H3, (D) CFP-H4, and (E) CFP-H5.

The hydrogen bonding in the interlayer is observed by the pair of small absorption peaks at 2857 /cm and 2921 /cm. Broad range at higher wavenumber around 3450 /cm is accredited to the stretching vibrations of the O-H molecules from the structural water.

3.2.A.3.4 XPS analysis: For the analysis of valance electronic states existing in the elements of the synthesized material, XPS measurement was conducted. XPS spectra of CFP-H3 are presented in **Figure 3.4**. In the survey scan spectrum, the occurrence of phosphorus, oxygen, iron and cobalt elements are observed as presented in the **Figure 3.4(A)**. The spectrum of Co2p given in **Figure 3.4(B)** depicts the existence of prominent peaks as Co2p_{3/2} at 781.66 eV and Co2p_{1/2} at 797.29 eV and the alongside satellite peaks at 785.57 eV and 802.80 eV, correspondingly. It is confirmed from peaks position that the detected Co element has Co²⁺ electronic state [16]. Also for the Fe element, the main peak Fe2p_{3/2} positioned at 710.93 eV and Fe2p_{1/2} positioned at 724.45 eV (**Figure 3.4(C)**) and have composed by two distinct peaks at 710.48 and 712.58 eV. Also, the peaks at 724.13 and 725.67 eV conforming Fe³⁺ and Fe²⁺ states in prepared sample.

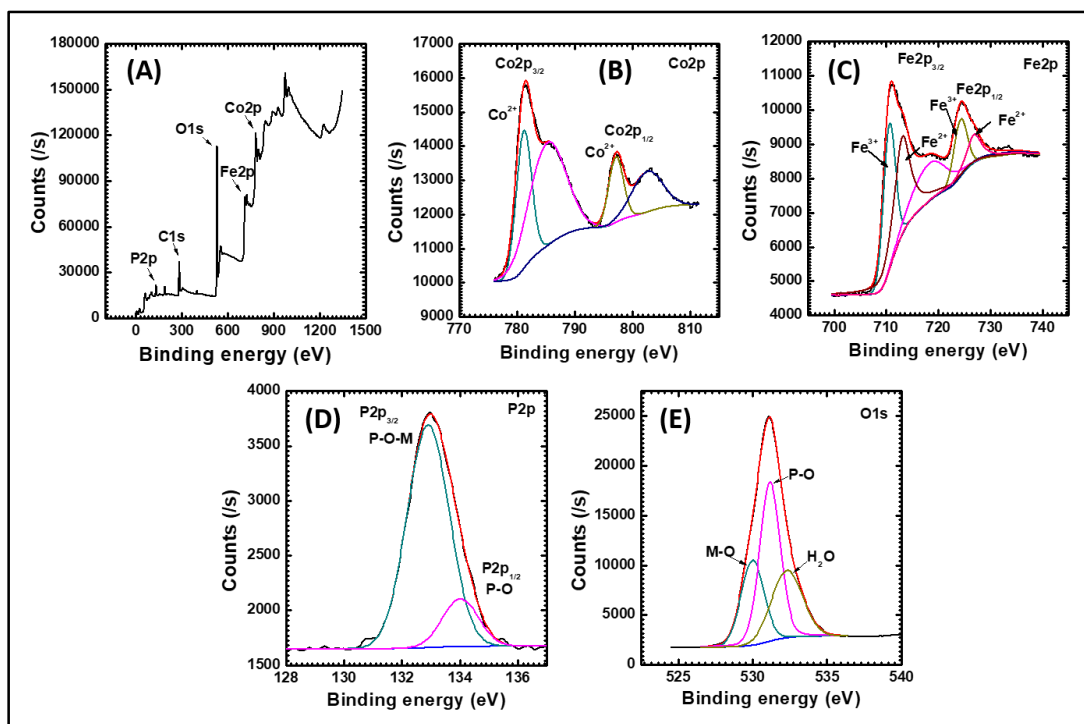


Figure 3.4: XPS spectra of CFP-H3 sample (A) survey spectrum, high resolution spectra of (B) Co2p, (C) Fe2p, (D) P2p, and (E) O1s.

As shown in **Figure 3.4(D)**, the high resolution part of P element, P2p is composed of two diverse peaks, P2p_{3/2} at 132.93 eV and P2p_{1/2} at 134.08 eV which are accredited to the metal phosphate (P-O-M) bond and phosphate group (P-O) related to P⁵⁺ oxidation state in phosphate series [17,18]. The O1s main peak is composed of three distinct peaks located at 529.58, 530.98 and 531.78 eV as shown in **Figure 3.4(E)**. The deconvoluted peaks (529.58 and 530.98 eV) denote the M-O and P-O bonding in metal, oxygen and phosphorus and the peak at 531.78 eV corresponds to surface adsorbed water molecules [19].

3.2.A.3.5 Surface morphological and elemental analysis: Topographical change with the variation in composition of cobalt and iron is observed by FESEM and shown in **Figure 3.5**. Images at different magnifications (1kX, 10 kX, 20 kX) showed that, as the composition varies from CFP-H1 to CFP-H5, the topography varies from microchips (CFP-H1) (**Figure 3.5(A-C)**) to submicrometric strips having nanometric thickness (CFP-H3) (**Figure 3.5(G-I)**) to micrometric cubes and pyramids (CFP-H5) (**Figure 3.5(M-O)**). As iron content introduced (CFP-H2), microchips get turned into microplates having thickness around 300 nm and length around 1.5 μm (**Figure 3.5(D-F)**).

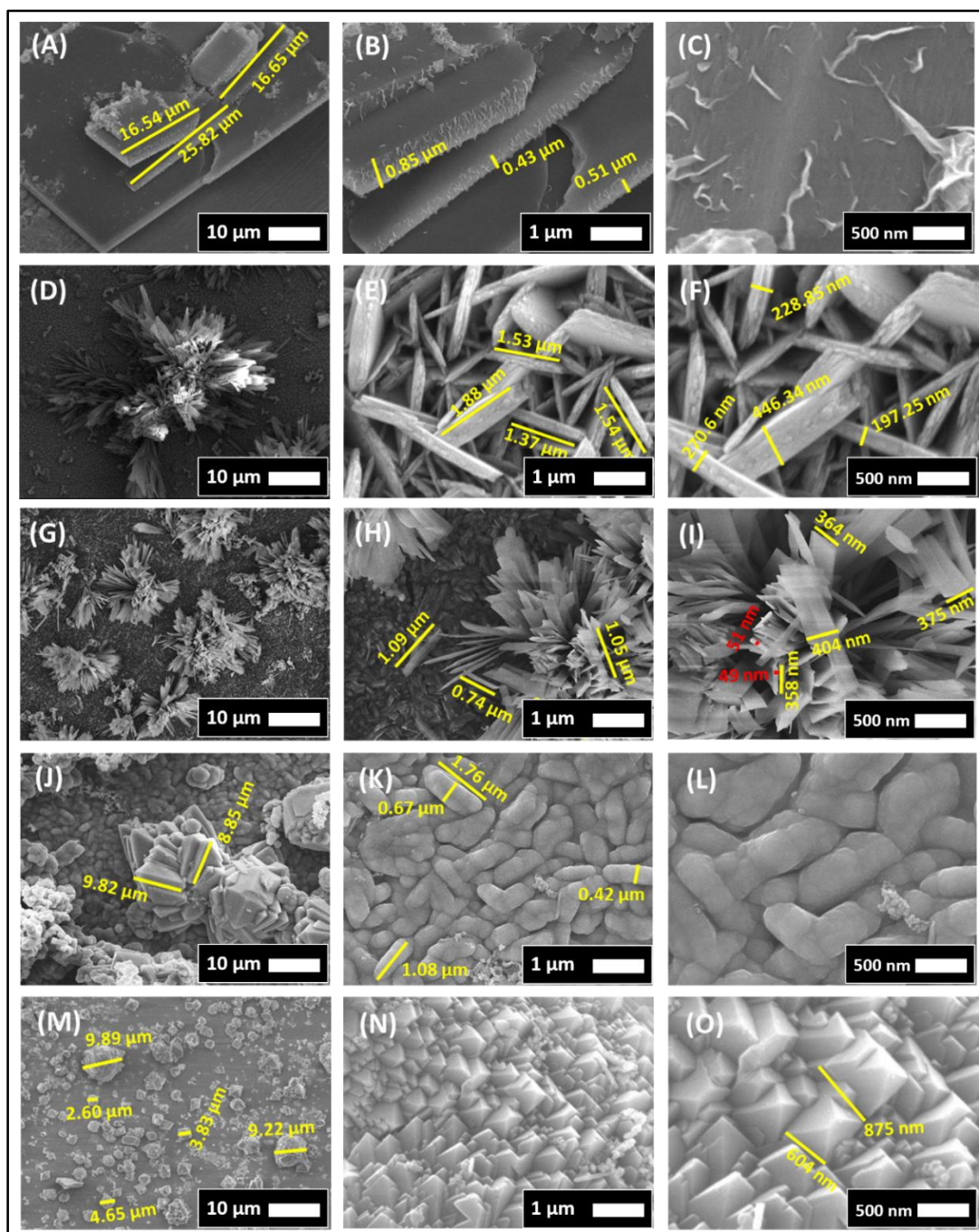


Figure 3.5: FESEM images at different magnifications (1 kX, 10 kX, and 20 kX) of (A-C) CFP-H1, (D-F) CFP-H2, (G-I) CFP-H3, (J-L) CFP-H4, and (M-O) CFP-H5.

As further increase in iron to equal contribution of cobalt (CFP-H3), thickness of the microplates reduced to around 45 nm, width becomes 380 nm and length becomes around 0.8 μm . Such a microstrip like structure shown in **Figure 3.5(G-I)** may offer enormous surface area and hence huge number of electrochemical active locates for water molecule adsorption and oxidation. For the sample CFP-H4, iron concentration exceeds and surface

starts to convert into large and agglomerated grains (**Figure 3.5(J-L)**). Whole area covered with grains having size around 3 to 4 μm and some agglomerated large particle with size 9 μm . It is observed that, large particles around 10 to 20 μm made from the agglomeration of submicrometric pyramids distributed over the substrate in the CFP-H5 sample.

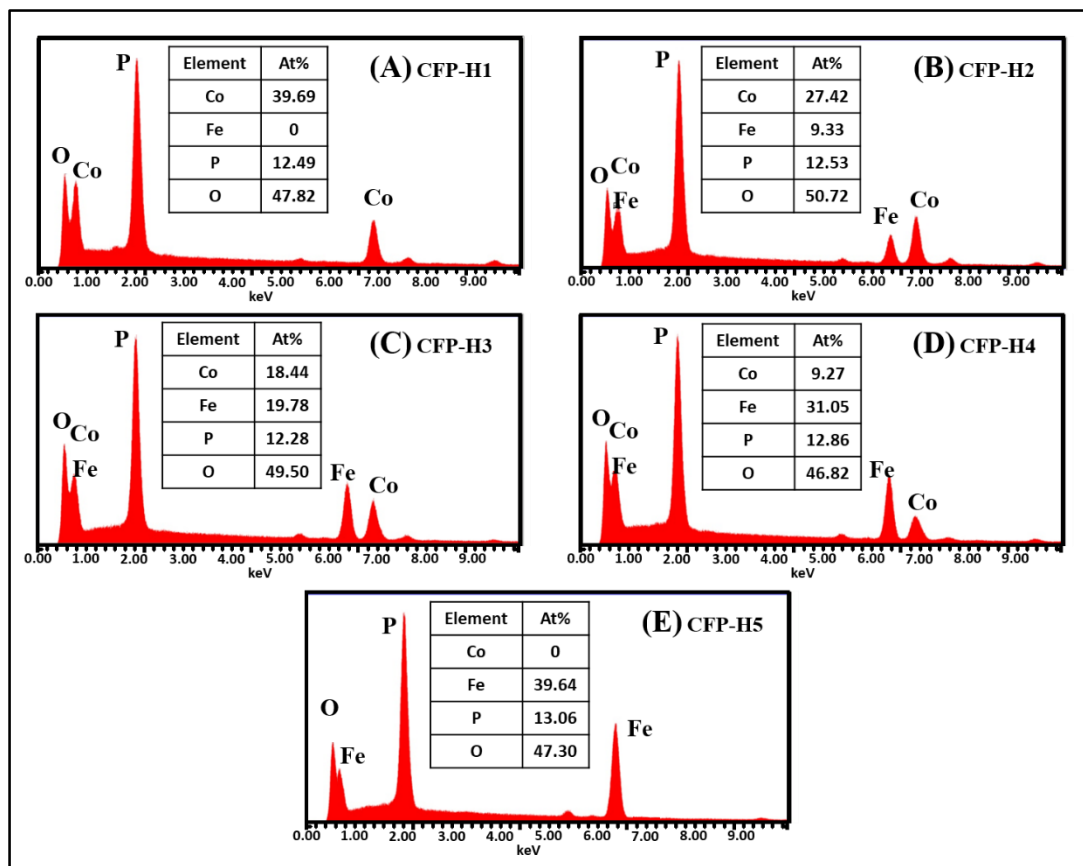


Figure 3.6: EDS spectra of cobalt-iron phosphate catalysts (A) CFP-H1, (B) CFP-H2, (C) CFP-H3, (D) CFP-H4, and (E) CFP-H5.

This reveals that, cobalt phosphate and iron phosphate materials have large particle size and may have smaller surface area. On the other hand, cobalt-iron phosphate (CFP-H3) material have smaller particle size microplates with nanometer thickness may have enormous surface area and is advantageous to water splitting application. The corresponding microstructures are formed by the aggregation of amorphous nanoparticles, and similar amorphous microstructures have reported previously [20,21]. Chemical compositional analysis made with the help of EDS analysis associated with FESEM. The as prepared materials were EDS characterized and there mapping plotted in **Figure 3.6(A-E)**. The EDS spectra evidenced that, the hydrous cobalt-iron phosphate consisted of cobalt, iron, phosphorus, and oxygen elements without any other impurity.

Table 3.2: Experimental and observed cobalt and iron atomic ratio with obtained phases of cobalt-iron phosphate samples.

Sample name	Experimental ratio (Co : Fe)	Observed ratio (Co : Fe)	Obtained phase
CFP-H1	100 : 0	100 : 0	$\text{Co}_3(\text{PO}_4)_2 \cdot \text{H}_2\text{O}$
CFP-H2	75 : 25	74.61 : 24.39	$\text{Co}_{2.25}\text{Fe}_{0.75}(\text{PO}_4)_2 \cdot \text{H}_2\text{O}$
CFP-H3	50 : 50	48.24 : 51.76	$\text{Co}_{1.5}\text{Fe}_{1.5}(\text{PO}_4)_2 \cdot \text{H}_2\text{O}$
CFP-H4	25 : 75	22.99 : 77.01	$\text{Co}_{0.75}\text{Fe}_{2.25}(\text{PO}_4)_2 \cdot \text{H}_2\text{O}$
CFP-H5	0 : 100	0 : 100	$\text{Fe}_3(\text{PO}_4)_2 \cdot \text{H}_2\text{O}$

The atomic percentage ratios of cobalt to iron are 100:0, 74.61:24.39, 48.24:51.76, 22.99:77.01, and 0:100 for CFP-H1, CFP-H2, CFP-H3, CFP-H4, and CFP-H5, respectively. Also, it is observed that, approximately constant phosphorous and oxygen atomic percentage is found in all samples, only difference is observed in the cobalt and iron atomic ratio and it is quite similar to experimental ratio. As shown in **Table 3.2**, as per the synthesis ratio, the atomic percentage of cobalt in the prepared material decreases and atomic percentage of iron increases. The observed atomic ratios are very close to the experimental molar ratios of the materials. The EDS result confirms change in molar ratio of cobalt and iron, and it is responsible for morphological evolution.

3.2.A.3.6 N₂ adsorption-desorption isotherm analysis: The material surface properties such as surface area, pore structure and pore size distribution of the CFP-H1, CFP-H3 and CFP-H5 samples were studied by the N₂ adsorption-desorption isotherm and BJH method as shown in **Figure 3.7**. The adsorption-desorption isotherms of the samples regarded to BET and isotherm of type-IV shape representing the mesoporosity and large adsorption energy (**Figure 3.7(A)**) [22]. With the 8.93 m²/g, 11.86 m²/g, and 4.45 m²/g specific surface area of CFP-H1, CFP-H3 and CFP-H5, respectively, sample CFP-H3 shows highest specific surface area. This result underscores the usefulness of addition of iron into the cobalt in the escalating the surface area of the material. The decrease in the surface area for CFP-H1 and CFP-H5 samples can be attributed to the observed dependence of surface area on the uneven overgrowth into a particle size distribution which is further observed in the FESEM images, and final Ostwald ripening which tends to the blocking of pores.

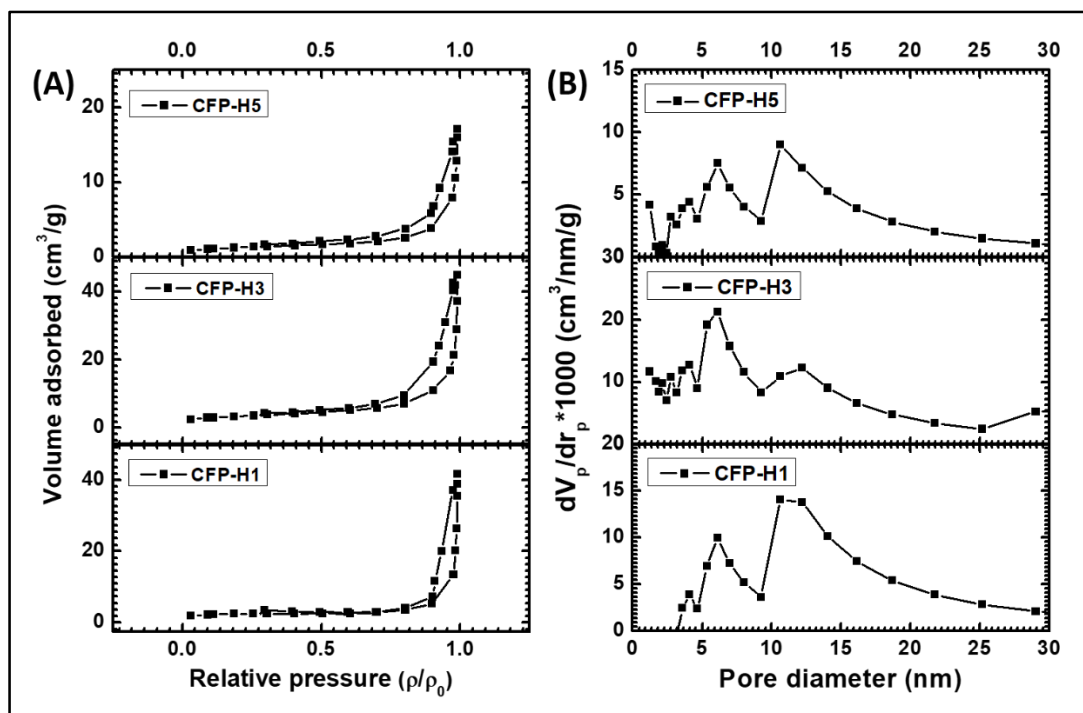


Figure 3.7: (A) N₂ adsorption-desorption isotherms (BET) and (B) pore size distribution (BJH) of hydrothermally prepared CFP-H1, CFP-H3 and CFP-H5.

The pore size distribution curves of the materials are studied by BJH method shown in **Figure 3.7(B)**. Figure illustrates the pore sizes of the samples range from 5 to 15 nm, confirming the mesoporous structure of the active materials and the average pore sizes are 10.64 nm, 6.12 nm, and 10.65 nm corresponding to CFP-H1, CFP-H3, and CFP-H5. The large specific surface area and small pore size can improve the electrolyte-electrode interface area, and huge number of electroactive positions for the –OH species adsorption and mass transfer, which may leads to enhanced electrochemical properties of the material.

3.2.A.3.7 Electrochemical catalytic performance analysis: The electrochemical catalytic performance of the materials may influence by the composition of the metals (cobalt and iron), for this purpose the atomic percentage of cobalt and iron was optimized to choose the best catalyst. In order to confirm the hypothesis, the electrocatalytic oxygen and hydrogen evaluation activities were investigated. The cobalt phosphate, cobalt-iron phosphate and iron phosphate materials were electrochemically examined to split water in the forms of OER and HER in basic and acidic electrolytes, correspondingly.

i) ECSA analysis: Before going to study electrocatalysis in terms of OER and HER, it is important to measure ECSA of the prepared materials. ECSA is directly related to the

C_{dl} of the material. To measure C_{dl} , CVs were recorded for each electrode in the small potential range where Faradic reactions are absent. **Figure 3.8(A-E)** shows the CV curves of the electrodes recorded at different scan rates. C_{dl} is calculated by plotting the anodic charging currents (i_c) of each CV curve against the scan rate by the equation (2.3) given in **chapter 2, section-B, subsection-2.B.3.2**. It yields a straight line with slope equals to C_{dl} as shown in **Figure 3.8(F)**. The plot reveals the values of C_{dl} are 0.42, 1.93, 3.31, 2.52, and 0.28 mF/cm^2 for CFP-H1, CFP-H2, CFP-H3, CFP-H4, and CFP-H5 electrodes, respectively. The ECSA were further calculated by using the C_s in alkaline solution as 0.04 mF [23]. The highest calculated ECSA is 82.75 cm^2 for CFP-H3 electrode. In contrast, other electrodes show quite fare values such as 10.55, 48.25, 63, and 7.05 cm^2 for CFP-H1, CFP-H2, CFP-H4, and CFP-H5 electrodes, respectively.

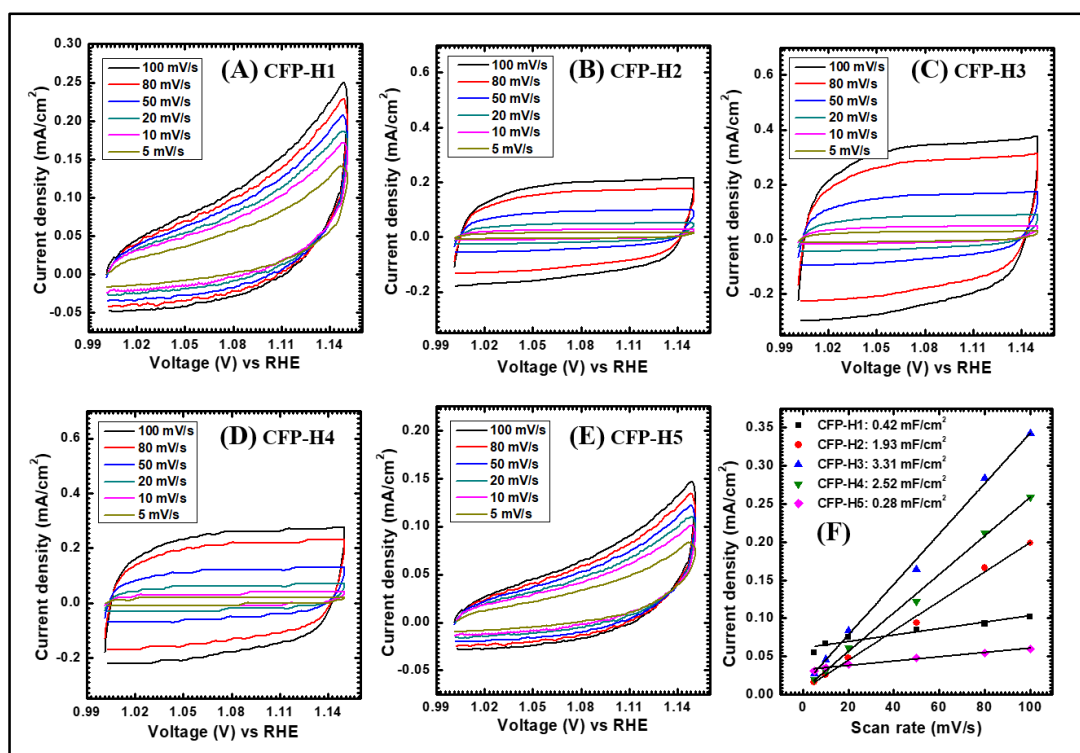


Figure 3.8: The CV curves of (A) CFP-H1, (B) CFP-H2, (C) CFP-H3, (D) CFP-H4, and (E) CFP-H5 at various scan rates in a small potential range (1.00 - 1.15 V vs. RHE), and (F) their anodic current linear fit for C_{dl} values.

The roughness factor (RF) is an index which gives the electrocatalytic interface texture and can be calculated by dividing the ECSA with the geometric area of the electrode in contact with electrolyte. In present study, electrode having 1 cm^2 area was used to measure electrochemical activity. Hence the RF are 10.55, 48.25, 82.75, 63, and 7.05 for

CFP-H1, CFP-H2, CFP-H3, CFP-H4, and CFP-H5 electrodes, respectively. The relatively large RF indicates the high electrocatalytic sites for exposing with electrolyte and favorable diffusion kinetics for the reactants. The sample CFP-H3 demonstrate very high ECSA and RF than the others are consistent with the BET surface analysis.

ii) OER analysis: To study OER of the prepared materials, the LSV were recorded at 1 mV/s scan rate in the potential range 1.05 to 1.75 V vs. RHE as shown in **Figure 3.9(A)**.

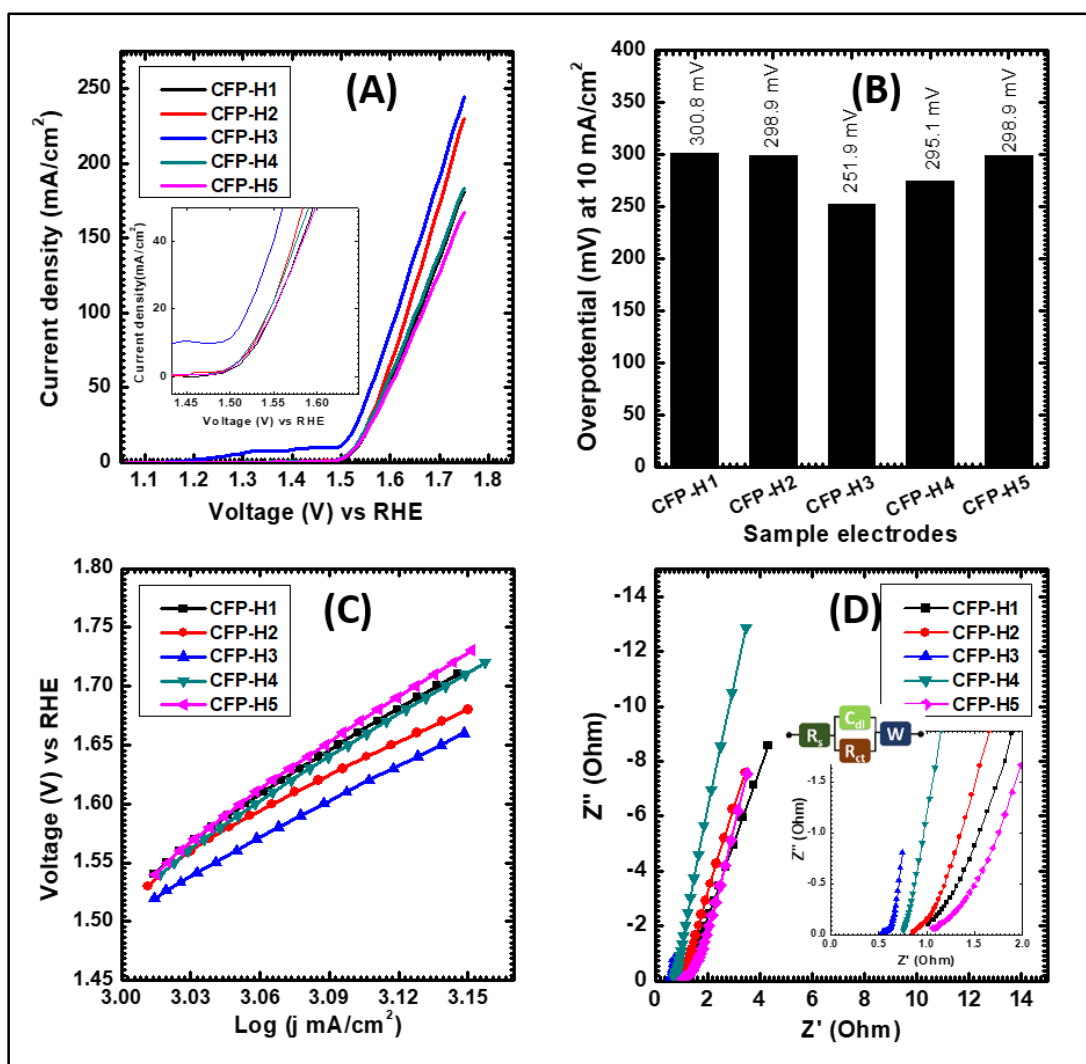


Figure 3.9: Electrochemical OER analysis (A) LSV polarization curves, (B) comparative bar diagram of overpotentials, (C) Tafel plots, (D) EIS of the CFP-H1, CFP-H2, CFP-H3, CFP-H4, and CFP-H5 catalysts.

The nature of the all LSV polarization curves is similar and continuous rise in current density by the change of cobalt to iron ratio from 100:0 to 50:50. It is observed and

confirmed that most electrochemically active material composition is 50:50 (sample CFP-H3). Sample CFP-H3 shows exponentially lowest overpotential of 251.9 mV to attain the current density of 10 mA/cm² suggesting outstanding catalyst for oxygen evolution. In contrast, other materials CFP-H1 (300.8 mV), CFP-H2 (298.9 mV), CFP-H4 (295.1 mV) and CFP-H5 (298.9 mV) exhibited considerably high overpotentials to reach the current density of 10 mA/cm² as comparatively shown by bar diagram in **Figure 3.9(B)**. When the catalyst has greater OH⁻ ion attraction for the adsorption at the catalyst surface to procedure intermediate states, O₂ molecule formation at the catalyst surface is proficient. If those intermediate states formation is faster, then these reaction steps are rate determining. The reaction rate kinetics for OER were determined by the Tafel slope, which can be obtained by plotting applied overpotential against the logarithmic current density at the shoot-point of current density. The Tafel plot is shown in **Figure 3.9(C)**. It reveals the Tafel slope of 39.3 mV/dec for the electrode CFP-H3 is lower than 45.7 mV/dec (CFP-H1), 43.9 mV/dec (CFP-H2), 41.5 mV/dec (CFP-H4), and 44.7 mV/dec (CFP-H5). It indicates that, highly efficient reaction kinetics at CFP-H3 electrode surface and the OER reaction process is faster. The EIS plot has shown that there is much smaller R_{ct} to CFP-H3 electrode (**Figure 3.9(D)**). The fitted R_{ct} values are 0.58, 0.342, 0.088, 0.671, and 0.663 Ω for CFP-H1, CFP-H2, CFP-H3, CFP-H4, and CFP-H5 electrodes, respectively. It reveals that, easy charge transfer process is one of the reason for low overpotential.

Catalytic stability is crucial criteria to evaluate the electrode material for long term usage as OER or HER catalyst. The CA test at fixed overpotential to deliver 10 mA/cm² current density was further studied for 24 h. The stability test is shown in **Figure 3.10(A)** which reveals that, material was activated continuously for initial 8 h and hence, current density becomes almost double and it remains stable up to 24 h. It is observed that, during the catalysis, material become catalytically more active and shows enhanced performance. It may be due to the involvement of Co²⁺, Co³⁺ and likely Co⁴⁺, and similarly Fe²⁺, and Fe³⁺ oxidation states in the redox cycles of active centers [24]. From the stability test, it is concluded that, the CFP-H3 is favorable for long duration catalysis with enhanced performance. The comparative LSV plot before and after 24 h catalysis is shown in **Figure 3.10(B)**, which discloses that overpotential decreases from 251.9 to 250.0 mV and current density increases rapidly at higher potential. Inset figure shows the change in Tafel slope from 39.3 to 35.2 mV/dec after catalytic stability. The EIS was performed after stability

test and it is observed that, the R_{ct} decreases from 0.088Ω to 0.037Ω (**Figure 3.10(C)**). The fitted EIS parameters are tabulated in **Table 3.3**.

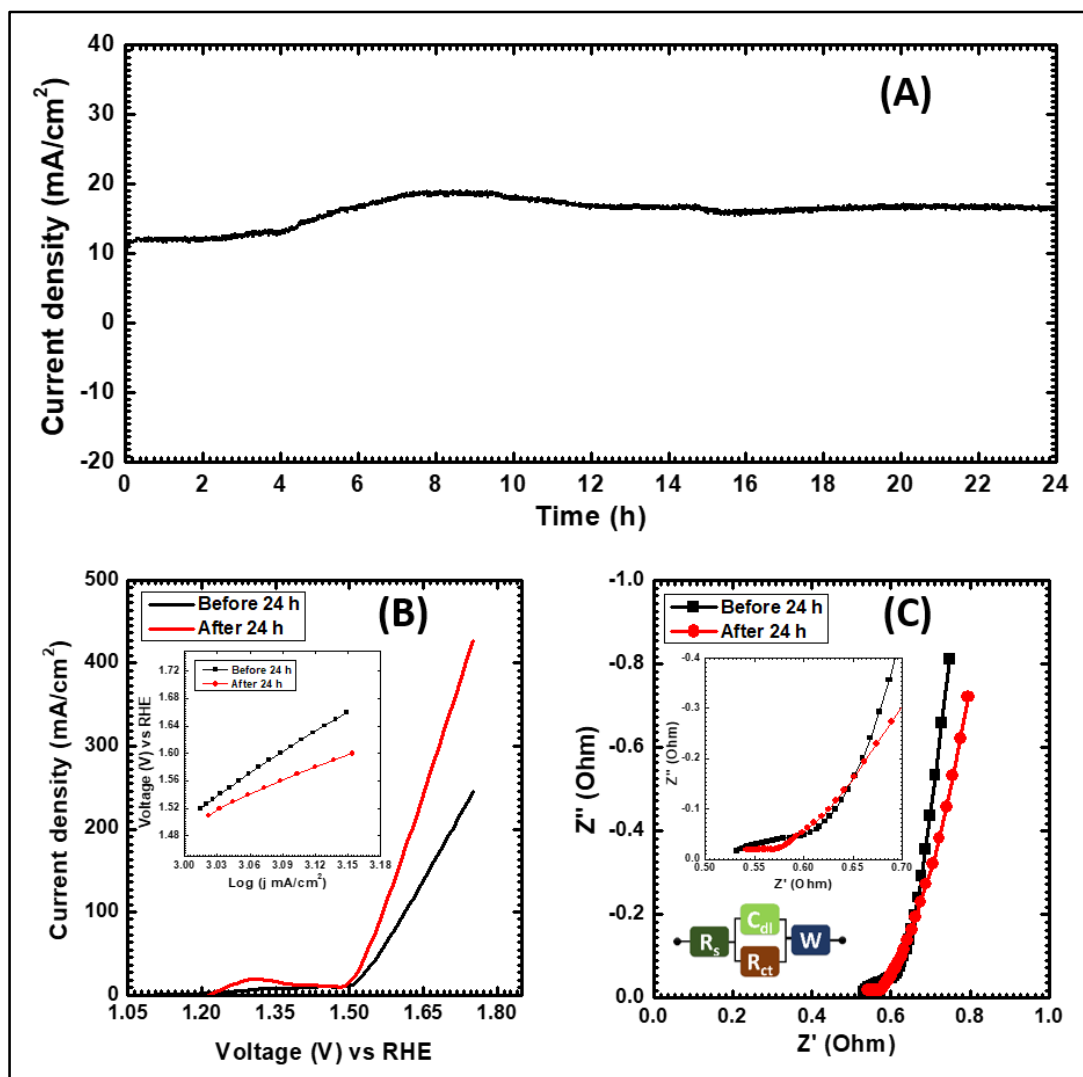


Figure 3.10: (A) CA (I-t) curve for OER stability, (B) LSV before and after 24 h OER catalysis, and (C) EIS after 24 h catalysis of CFP-H3 electrode.

iii) HER analysis: Theoretically HER require 0 V potential vs RHE, although it is more favorable in acidic media. To study HER, here 1 M H₃PO₄ solution was used as electrolyte. The polarization curves were recorded in the potential window of 0.33 to -0.85 V vs RHE as presented in **Figure 3.11(A)**. It indicates analogous nature with rapid and steeper current increase by the increase in potential. The overpotentials measured at 10 mA/cm² current density as 282.57, 202.93, 55.50, 152.25, and 368.01 mV for CFP-H1, CFP-H2, CFP-H3, CFP-H4, and CFP-H5 electrodes, respectively.

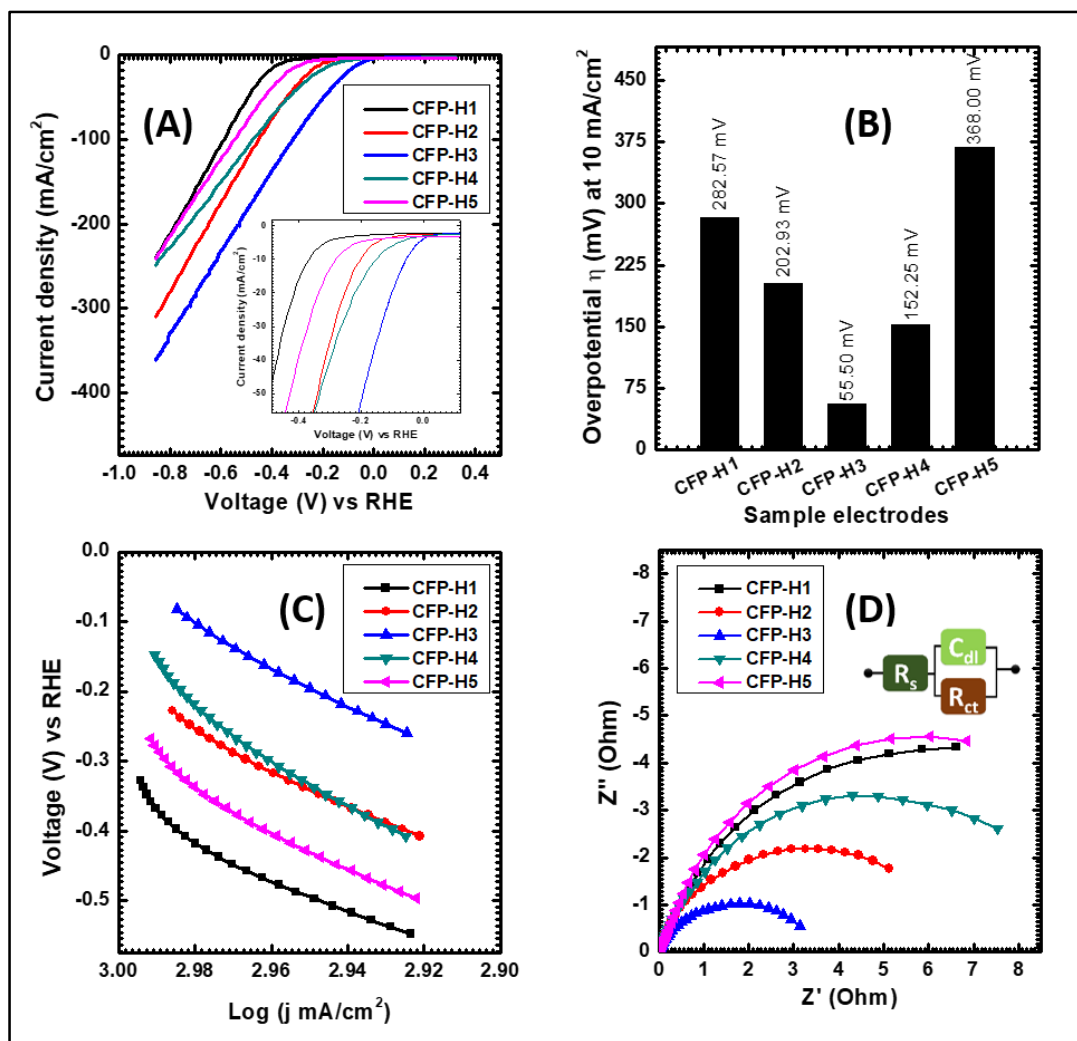


Figure 3.11: Electrochemical HER analysis: (A) LSV polarization curves, (B) comparative bar diagram of overpotentials, (C) Tafel plots, (D) EIS of CFP-H1, CFP-H2, CFP-H3, CFP-H4, and CFP-H5.

Values revealed that, CFP-H3 electrode show lowest overpotential to attain the current density of 10 mA/cm². The trend of overpotential is shown in **Figure 3.11(B)** by bar diagram. The rate determining kinetics was studied by plotting Tafel slope to evaluate faster HER. **Figure 3.11(C)** gives the Tafel plot determined from LSV curves for all sample electrodes, which depicts lower Tafel slope for the same material which have low overpotential. The Tafel slope for CFP-H1, CFP-H2, CFP-H3, CFP-H4, and CFP-H5 electrodes are 94.78, 90.15, 73.64, 85.25, and 91.72 mV/dec, respectively. The EIS was measured for each electrode and plotted in **Figure 3.11(D)**, where charge transfer becomes easier (3.63 Ω) for CFP-H3 electrode. The fitted R_{ct} values are 13.14, 6.52, 3.63, 9.54, and 11.09 Ω for CFP-H1, CFP-H2, CFP-H3, CFP-H4, and CFP-H5 electrodes, respectively.

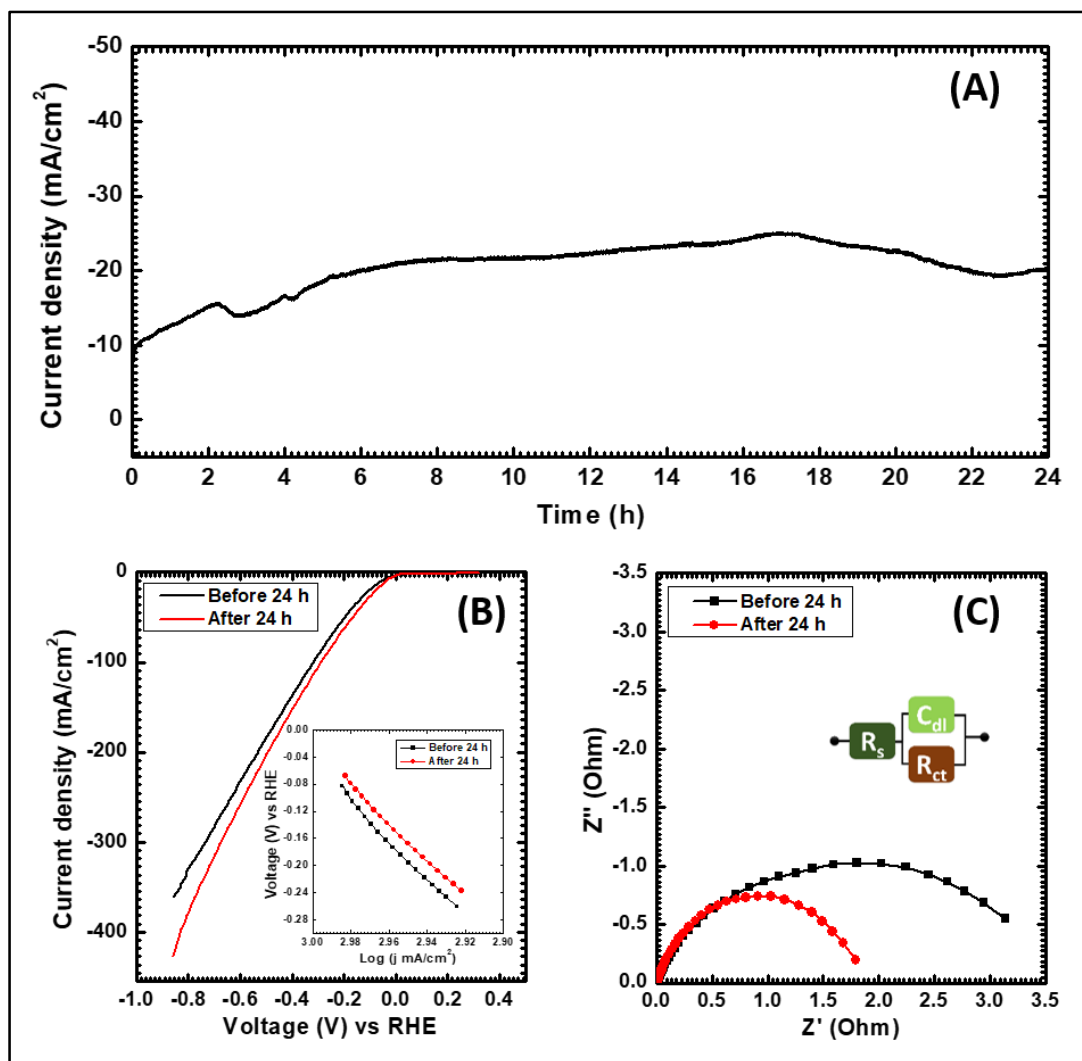


Figure 3.12: (A) CA (I-t) curve for HER stability, (B) LSV before and after 24 h OER catalysis, and (C) EIS after 24 h catalysis of CFP-H3 electrode.

HER catalytic stability test was performed by CA at overpotential for 24 h. By the test, it is observed that, material become very much active continuously and showed enhanced current density throughout the time (**Figure 3.12(A)**). The performance is compared by comparing overpotential before and after the HER catalysis. It is observed that, overpotential decreased after 24 h catalysis from 55.5 to 37.3 mV due to the continuous activation of the catalytic sites (**Figure 3.12(B)**). Inset of **Figure 3.12(B)** give the comparative plot of Tafel slope, and it appears to be 68.97 mV/dec after 24 h catalysis. Fitted EIS curves before and after stability test shows that the R_{ct} decreased from 3.63 to 1.87 Ω after 24 h catalysis which is predictable for the enhancement in performance (**Figure 3.12(C)**). The fitted EIS parameters are tabulated in **Table 3.3**. From the 24 h HER catalytic stability, it is concluded that, the material does not show stable current density, with time

the current goes on increasing and hence the performance is also increasing. From the HER continuous 24 h catalysis and analysis after the catalysis, it is concluded that, the continuous increase in electrochemical performance with decrease in overpotential for the CFP-H3 catalyst.

Table 3.3: Electrochemical OER and HER analysis before and after 24 h catalytic stability study.

	Test	Overpotential η (mV vs RHE) at 10 mA/cm ²	Tafel slope (mV/dec)	R _s (Ω)	R _{ct} (Ω)	W (Ω)
Before stability	OER	251.9	39.3	0.53	0.7	0.336
After stability		250	35.2	0.54	0.56	0.358
Before stability	HER	55.5	73.64	0.015	3.63	--
After stability		37.3	68.97	0.009	1.88	--

3.3 Conclusions: In sum of section-A, facile hydrothermal deposition method was employed for the preparation of cobalt-iron phosphate electrodes. Amorphous nature of cobalt-iron phosphate was confirmed by XRD analysis. Estimation of metal phosphate content and their corresponding bonds in the prepared samples by FT-IR, EDS and XPS techniques confirms the formation of hydrous cobalt-iron phosphate ($\text{Co}_x\text{Fe}_{3-x}(\text{PO}_4)_2 \cdot \text{H}_2\text{O}$) material. Reaction kinetics and hence the morphology of the material was influenced due to composition variation i.e., molar ratio of cobalt and iron species. The as synthesized cobalt-iron phosphate at different compositional ratio, cobalt phosphate, and iron phosphate catalyst materials presented exceptional water splitting in the forms of OER and HER. Excellent performing CFP-H3 catalyst electrode demonstrated lowest overpotential of 251.9 mV for the evolution of oxygen and to achieve 10 mA/cm² current density with Tafel slope 39.3 mV/dec and more than 100 % catalytic OER stability for 24 h in alkaline medium. Also, it can perform HER with 55.5 mV overpotential at 10 mA/cm² current density with 73.64 mV/dec Tafel slope. After catalytic stability test of hydrogen evolution

for 24 h in acidic bath, it is observed that the overpotential reduced to 37.3 mV. As a benchmark, the overpotentials for OER and HER to achieve the current density of 10 mA/cm², corresponding Tafel slopes and stability study were comparative to the formerly published cobalt-iron phosphate catalyst materials (**Table 3.4**), which confirms the outstanding performance of present investigation. This can be attributed to the amorphous nature of the material, synergistic effect of both the metals (Co and Fe), improved electronic conduction and metal-to-metal partial charge transfer process. Moreover, cobalt-iron phosphate increases the adsorption of OH⁻ ions at the surface of electrode with the decrease of adsorption energy of the surface by altering the surface electronic states.

Table 3.4: Comparative study of present work with the earlier published cobalt-iron phosphate materials.

Materials	Substrate	Electrolyte	η (mV)	Tafel slope (mV/dec)	Stability (h)	Ref.
Cobalt-iron phosphate	GCE	1 M KOH	267 (OER)	30	10	[10]
Fe _{0.72} Co _{0.4} PO ₄	NF	1 M KOH	77 (HER)	80.7	25	[11]
Cobalt-iron pyrophosphate	GCE	1 M KOH	276 (OER)	32	8.33	[9]
FeCo phosphate	Carbon paper	1 M KOH	273 (OER)	35.9	16	[25]
CoFePi	GCE	1 M KOH	277 (OER)	31	10	[26]
S-doped Co-Fe-Pi	GCE	1 M KOH	273 (OER)	35	10	[27]
Cobalt-iron phosphate	SS	1 M KOH	251.9 (OER)	35.2	24	Present work
		1 M H ₃ PO ₄	37.3 (HER)	68.9	24	

3.4 Section-B: Hydrothermal synthesis of cobalt-iron phosphate/reduced graphene oxide hybrid and their characterization for electrochemical OER and HER

3.4.B.1 Introduction: The hydrothermal is a facile and low cost technique used to synthesize variety of nanostructures by governing parameters like temperature, deposition

time, and precursor concentration. In this investigation, cobalt-iron phosphate/reduced graphene oxide hybrid materials were synthesized. By using hydrothermal approach, the synthesized hybrid materials are in powder form and they are deposited by slurry coating on SS substrates which create dead volume caused by tedious process of mixing active material with binders [28].

In the present work, effect of change in concentration of rGO on physico-chemical properties, and their effect on the electrochemical water splitting in terms of OER and HER is studied. Meanwhile, pristine cobalt-iron phosphate at 50% : 50% compositional ratio and cobalt-iron phosphate/reduced graphene oxide hybrid at different concentrations (0.02 mg/ml, 0.04 mg/ml, 0.06 mg/ml, 0.08 mg/ml, and 0.1 mg/ml) are synthesized and compared their electrochemical study to investigate the best performing catalyst. As per the literature survey mentioned previously in chapter-1, only a report available on cobalt-iron phosphate/reduced graphene oxide loaded on rGO for the OER study [29]. Present investigation gives the detailed study of cobalt-iron phosphate/reduced graphene oxide hybrid materials by characterizing physico-chemically. Thorough analysis of slurry coated electrodes were done for the electrochemical splitting of water in the forms of OER and HER.

3.4.B.2 Experimental details:

3.4.B.2.1 Materials used and substrate cleaning: To prepare the GO, the analytical grade sulfuric acid (H_2SO_4), sodium nitrate (NaNO_3), graphite flakes, potassium permanganate (KMnO_4), hydrogen chloride (HCl) and hydrogen peroxide (H_2O_2), etc. chemicals were required. For the synthesis of cobalt-iron phosphate/reduced graphene oxide, $\text{CoCl}_2 \cdot 6\text{H}_2\text{O}$, FeCl_2 , KH_2PO_4 , and urea ($\text{CO}(\text{NH}_2)_2$) purchased from Sigma-Aldrich and Thomas Baker and used as received. The SS substrates were cleaned by the procedure given earlier in section A, subsection 3.2.A.2.1.

3.4.B.2.2 Synthesis of graphene oxide (GO): The Hummer's method was used to synthesize GO [30]. First of all, NaNO_3 (2.5 g) and graphite flakes (5 g) mixed in 1 L Beaker in H_2SO_4 (120 ml) and stirred for 30 min at room temperature. After 30 min, the reaction bath was kept in ice to maintain the reaction temperature below 5°C . After that, KMnO_4 (15 gm) was slowly added to the reaction bath [rate: $\sim 1\text{g}/6\text{min}$] (**Figure 3.13(A)**). After completion of addition, the prepared mixture was stirred for 6 h at room temperature (**Figure 3.13(B)**). After 12 h, the reaction color transferred black to dark reddish as shown

in photographs below in **Figure 3.13(C)**. Later, DDW (50 ml) was added and reaction temperature increase to 95 °C for 30 min (color changes to brown). The mixture of 50 ml 30 % H₂O₂ and 150 ml DDW was slowly added maintaining temperature of solution to room temperature. During the addition of H₂O₂, the color of solution turns dark brown to yellow as shown in **Figure 3.13(D)**. Furthermore, 100 ml solution containing 25 ml HCl and 75 ml DDW was added in the mixture for washing purpose (color changes to blackish brown) as shown in **Figure 3.13(E)**.

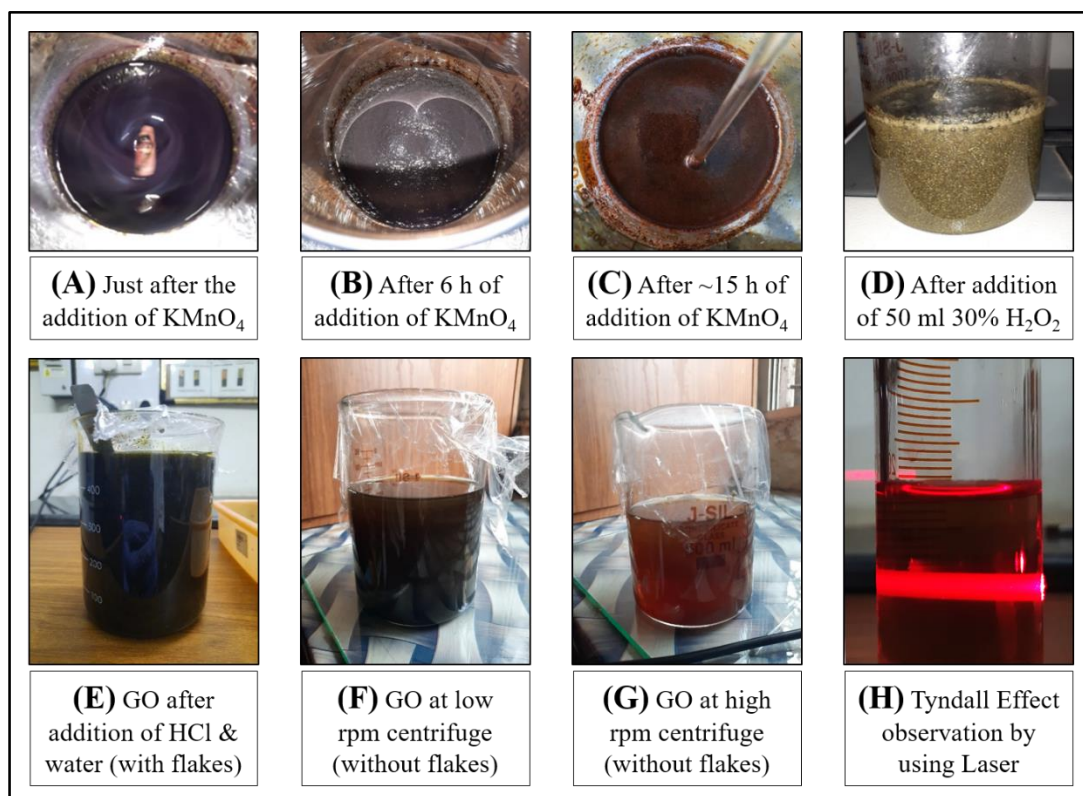


Figure 3.13: (A-H) Photographs during the synthesis of GO.

Then, resultant mixture was centrifuged at low rpm (2000) to remove unreacted graphite flakes (**Figure 3.13(F)**) and further centrifuged at high rpm (10000) several times to wash GO NSs and the pH becomes ~7, brown colored GO solution is as shown in **Figure 3.13(G)**. After completion of washing, Tyndall effect was observed for brown colored GO solution by Laser pointer (**Figure 3.13(H)**). A first indication of the nanometric dimensions of the dispersed GO particles was provided by the occurrence of the Tyndall effect [31].

3.4.B.2.3 Synthesis of cobalt-iron phosphate/reduced graphene oxide: The cobalt-iron phosphate/reduced graphene oxide hybrids were synthesized by facile hydrothermal method. The concentrations of precursors were kept constant as the previously given in **section A, subsection 3.2.A.2.2** for the sample CFP-H3. The GO solution was added with

different concentrations (0.02 mg/ml, 0.04 mg/ml, 0.06 mg/ml, 0.08 mg/ml, and 0.1 mg/ml) in the precursor solution and stirred for 30 min to become homogeneous mixture. After stirring, the solutions were transferred to Teflon lined SS hydrothermal bombs. Hydrothermal bombs were then placed in laboratory oven and temperature at 130 °C was maintained for 14 h. Once completing the reaction time, the reactions were allowed to cool naturally. The precipitates were collected and washed by means of DDW severally and dried at ambient temperature. The synthesized cobalt-iron phosphate/reduced graphene oxide hybrid materials were named as CFP/rGO series (CFP/rGO-H0, CFP/rGO-H1, CFP/rGO-H2, CFP/rGO-H3, CFP/rGO-H4, and CFP/rGO-H5). The as prepared materials were further used for their physico-chemical characterizations.

3.4.B.2.4 Cobalt-iron phosphate/reduced graphene oxide electrode preparation: The electrodes of cobalt-iron phosphate/reduced graphene oxide hybrid were prepared by slurry coating technique on SS substrates. The slurry was prepared by combining 75 % cobalt-iron phosphate material, 20 % carbon black, 5 % polyvinylidene fluoride (PVDF) with N-methyl 2-pyrrolidone (NMP).

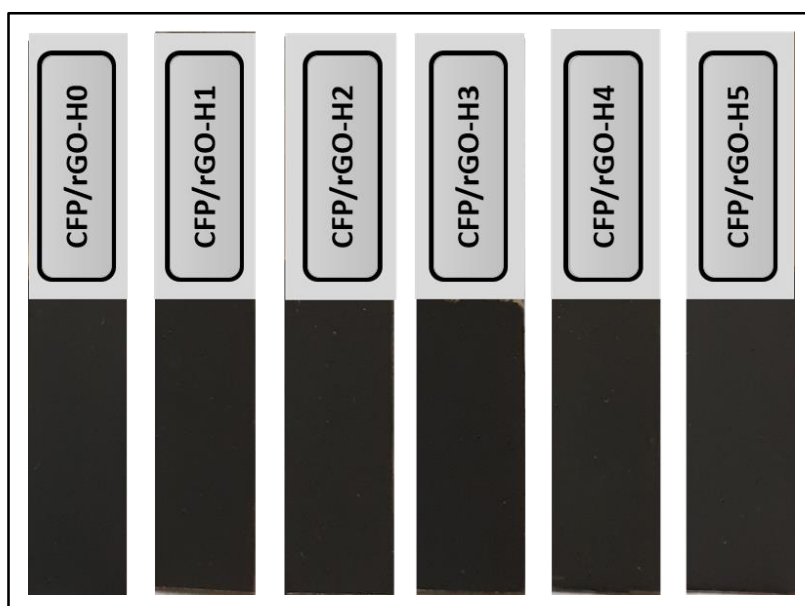


Figure 3.14: Photograph of cobalt-iron phosphate/reduced graphene oxide hybrid electrodes.

The prepared slurry coated on SS substrate by keeping mass loading constant at 1 mg/cm² and dried overnight at 60 °C. The prepared electrodes shown in **Figure 3.14**, were further used for electrochemical study.

3.4.B.3 Results and discussion:

3.4.B.3.1 XRD analysis: The XRD patterns of cobalt-iron phosphate/reduced graphene oxide hybrid materials at different concentrations of rGO were studied and shown in **Figure 3.15**. As previously observed in **section A, subsection 3.2.A.3.2**, the sample CFP-H3 showing amorphous nature, all the hybrid materials (CFP/rGO-H0, CFP/rGO-H1, CFP/rGO-H2, CFP/rGO-H3, CFP/rGO-H4, and CFP/rGO-H5) also show amorphous nature. The broad hump observed around $2\theta = 25.4^\circ$ indicates stacking of GO sheets due to removal of oxygen containing groups and also it indicates formation of multilayered rGO NSs of (0 0 2) planes [30,32]. Also, it is observed that, the peak intensity of (0 0 2) plane goes on increasing with increase in GO concentration.

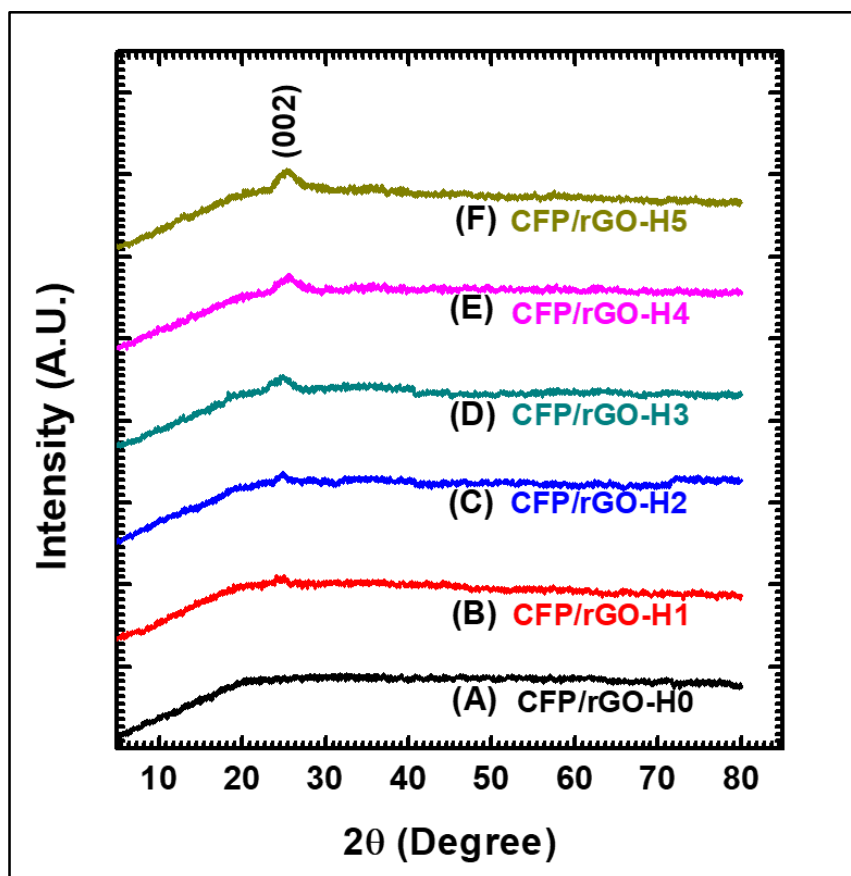


Figure 3.15: XRD patterns of (A) CFP/rGO-H0, (B) CFP/rGO-H1, (C) CFP/rGO-H2, (D) CFP/rGO-H3, (E) CFP/rGO-H4, and (F) CFP/rGO-H5.

3.4.B.3.2 FTIR analysis: FTIR spectroscopy is an effective technique to analyze the molecular bond development in the prepared cobalt-iron phosphate/reduced graphene oxide hybrids. The FTIR spectra of all the prepared CFP/rGO series materials from

wavenumber 400 to 4000 /cm as shown in **Figure 3.16**. The region in between the wavenumbers 500 to 650 /cm displays the absorptions of symmetric and asymmetric bending vibrational modes of PO₄ ligands at 576 /cm and 619 /cm, correspondingly. The bands of absorption at 771 /cm and 1049 /cm are corresponds to =C-H and alkoxy C-O vibrations [33,34]. The absorption bands of –OH, –COOH symmetric stretching and C=C skeletal vibrations are observed at 1111 /cm, 1359 /cm, and 1598 /cm, respectively [35]. The high absorption band at 1629 /cm is due to the sp² hybridization (C=C) in rGO is confirmed. The large band of small absorption in the region of wavenumber 3000-4000 /cm shows the broad vibrational band of structural water molecules.

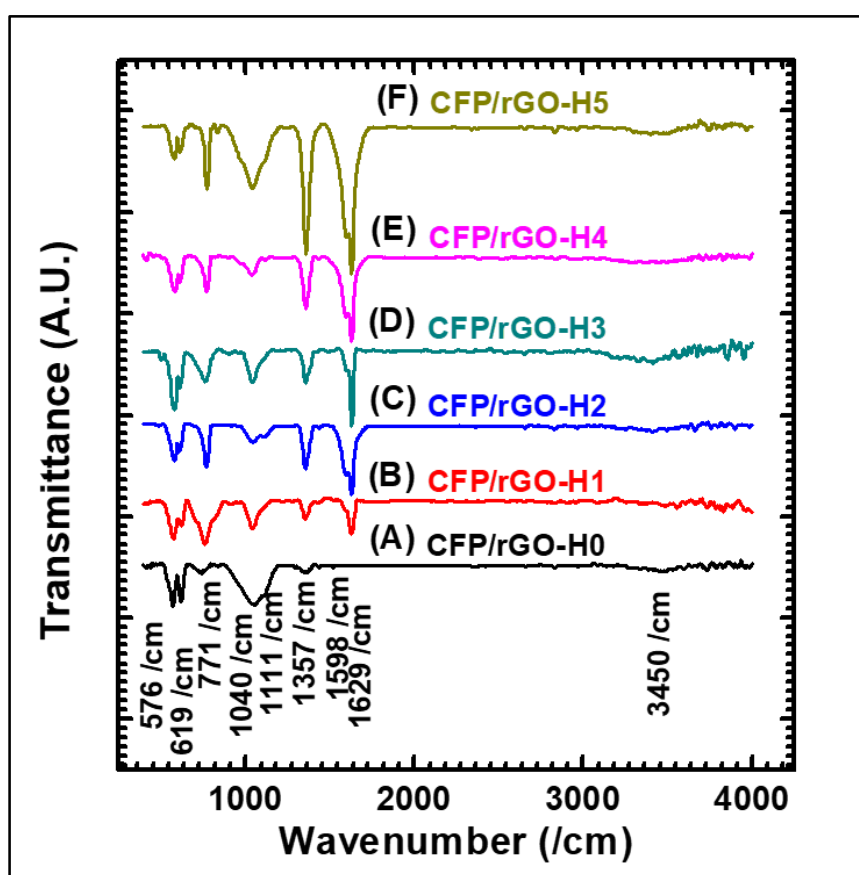


Figure 3.16: FTIR patterns of (A) CFP/rGO-H0, (B) CFP/rGO-H1, (C) CFP/rGO-H2, (D) CFP/rGO-H3, (E) CFP/rGO-H4, and (F) CFP/rGO-H5.

3.4.B.3.3 XPS analysis: The surface composition and the chemical states are investigated by XPS. The XPS survey spectrum of cobalt-iron phosphate/reduced graphene oxide is shown in **Figure 3.17(A)**, the survey spectrum confirms Co, Fe, P, O and C elements are present in the sample. In the high resolution of cobalt (**Figure 3.17(B)**), there are two major peaks at 781.2 eV and 797.5 eV along with two satellite peaks at 786.1 eV and 803 eV

corresponding to $\text{Co}2p_{3/2}$ and $\text{Co}2p_{1/2}$, correspondingly. The peak positions revealed and confirmed that, the detected Co metal atoms have Co^{2+} electronic state [17]. In the high resolution spectrum of iron (**Figure 3.17(C)**), the prominent peaks located at 711.8 and 725 eV are alongside to $\text{Fe}2p_{3/2}$ and $\text{Fe}2p_{1/2}$, and are composed by the two peaks at 711.2 and 713.4 eV, also peaks at 724.7 and 726.4 eV related to Fe^{3+} and Fe^{2+} states in prepared sample. Deconvoluted phosphorous peak is made with the two peaks with high intense $\text{P}2p_{3/2}$ at 132.9 eV are accredited to the metal phosphate (P-O-M) bond, and $\text{P}2p_{1/2}$ at 134 eV having low intensity known as phosphate group (P-O) in phosphate series presenting P^{5+} oxidation state (**Figure 3.17(D)**) [18]. The observed broad peak of oxygen is at 531.3 eV, which is deconvoluted into three as 530.1 eV, 531.3 eV, and 532.3 eV, where the peaks at 530.1 and 531.3 corresponding to the M-O and P-O bonding and peak at 532.3 eV is due to surface adsorbed water (**Figure 3.17(E)**).

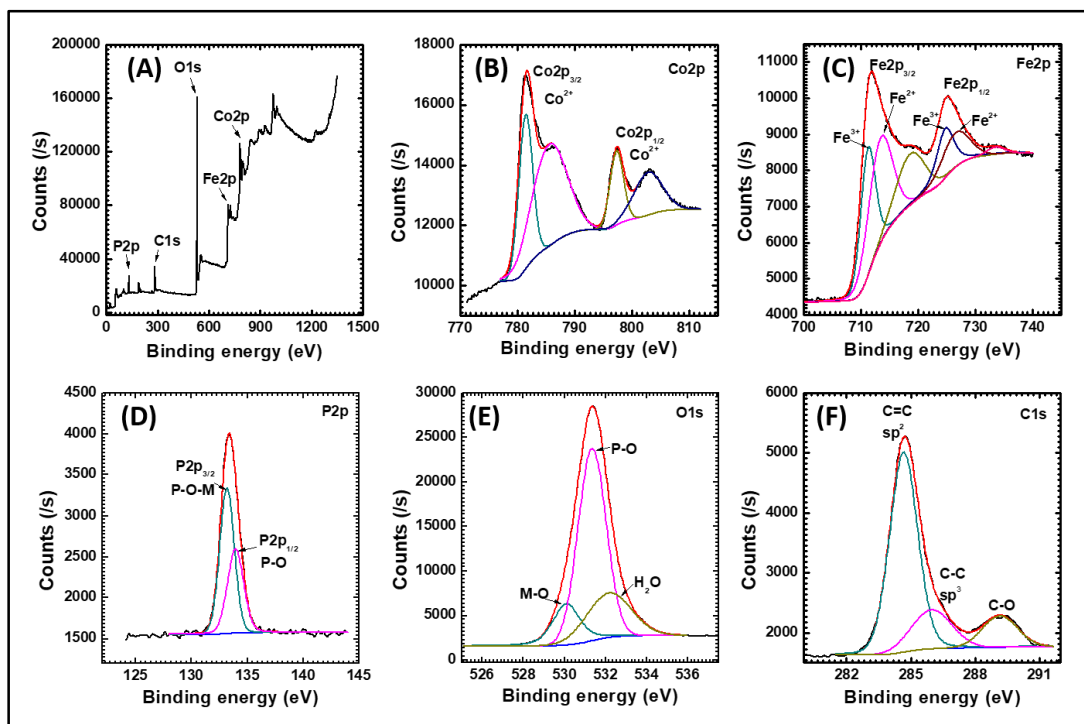


Figure 3.17: XPS spectra of CFP/rGO-H0 sample (A) survey spectrum, high resolution spectra of (B) $\text{Co}2p$, (C) $\text{Fe}2p$, (D) $\text{P}2p$, (E) $\text{O}1s$ and (F) $\text{C}1s$.

High resolution $\text{C}1s$ peaks in the XPS prove that oxygen-containing groups have been less due to reduction of GO at high temperature in hydrothermal process. The intense peak as shown in **Figure 3.17(F)** at 284.7 eV is due to $\text{C}=\text{C}$ in-plane bonding of sp^2 hybridization. On the other hand, out of plane bonding of sp^3 hybridized C-C is very short.

The present result provides the explicit indication regarding reduction of GO. The carboxylate carbon (O-C=O) is observed at 289.1 eV [36].

3.4.B.3.4 Surface morphological and elemental analysis: Topographical picture of the hydrothermally synthesized cobalt-iron phosphate/reduced graphene oxide hybrid materials are shown in **Figure 3.18(A-F)**. The CFP/rGO-H0 material have micro needles like morphology with around 0.25 μm thickness. The needles having length more than 5 μm which are randomly oriented. Upon addition of rGO, the NSs of rGO get appeared. It is observed that, the rGO NSs (highlighted in figure) have lateral size around 1 μm which are distributed along with the micro needles of cobalt-iron phosphate. As the concentration of rGO goes on increasing, the segregated stacking of rGO NSs observed as shown in **Figure 3.18(E,F)**.

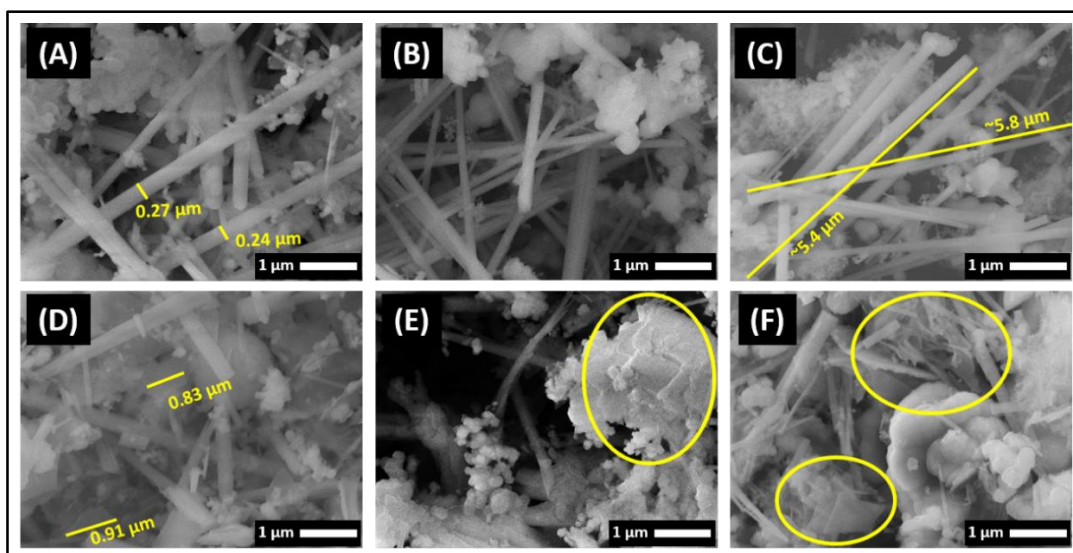


Figure 3.18: FESEM images at 20 kX magnification of (A) CFP/rGO-H0, (B) CFP/rGO-H1, (C) CFP/rGO-H2, (D) CFP/rGO-H3, (E) CFP/rGO-H4, and (F) CFP/rGO-H5.

The EDS analysis of CFP/rGO series was studied further for the confirmation of presence of carbon element from the rGO. **Figure 3.19(A-F)** shows the EDS spectra of all the hydrothermally prepared cobalt-iron phosphate/reduced graphene oxide samples. It is evidenced that the prepared materials consisted of cobalt, iron, phosphorus, oxygen, and carbon elements. The observed At% of carbon in the as prepared samples are 0 %, 9.03 %, 15.24 %, 16.92 %, 18.06 % and 20.14 % for CFP/rGO-H0, CFP/rGO-H1, CFP/rGO-H2, CFP/rGO-H3, CFP/rGO-H4, and CFP/rGO-H5 hybrid materials. The ratio of the cobalt to

iron was remained around 50:50 and for the phosphorous to oxygen, it was 20:80. The EDS analysis evidenced that the successful hybridization of cobalt-iron phosphate with the rGO.

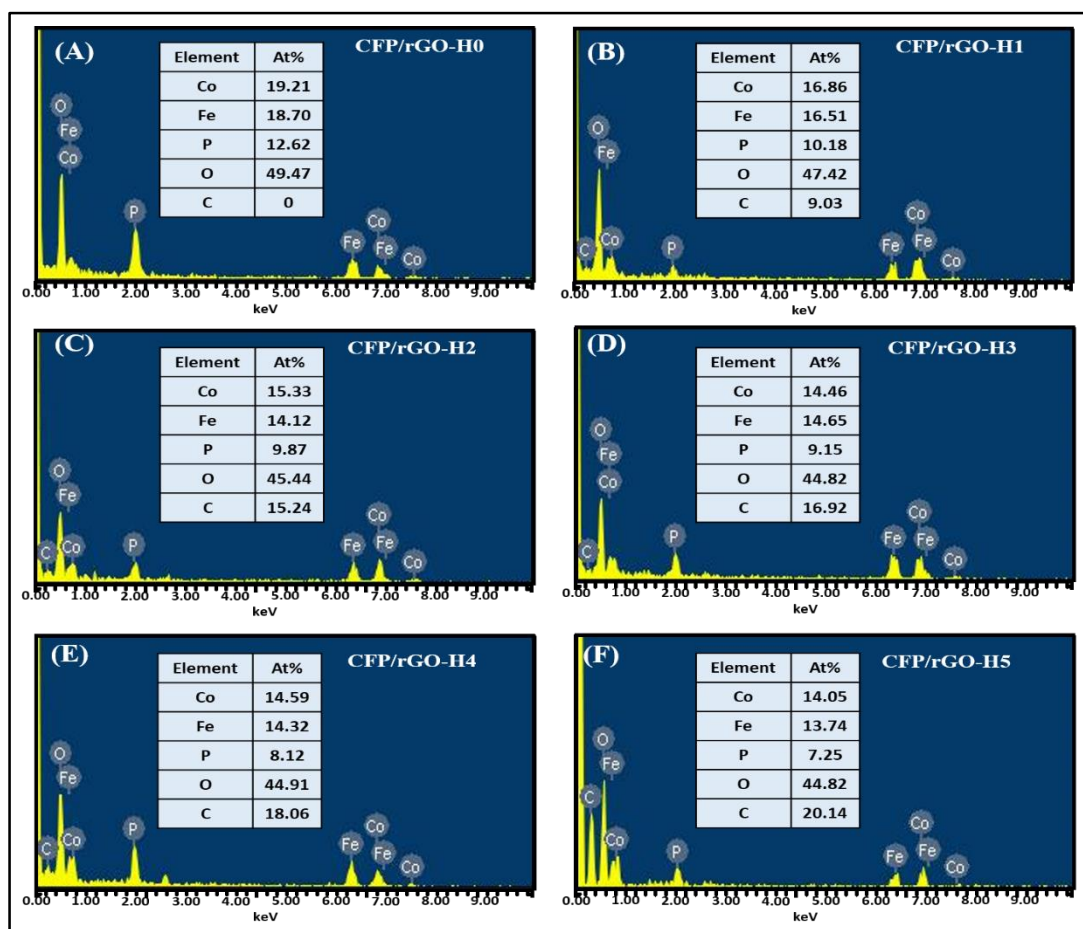


Figure 3.19: EDS spectra of (A) CFP/rGO-H0, (B) CFP/rGO-H1, (C) CFP/rGO-H2, (D) CFP/rGO-H3, (E) CFP/rGO-H4, and (F) CFP/rGO-H5.

3.4.B.3.5 N₂ adsorption-desorption isotherm analysis: To further analyze the porous structure, the surface areas of CFP/rGO series measured by a BET method. BET revealing type-IV isotherm profile observed by adsorption-desorption isotherms of all the samples shown in **Figure 3.20(A-F)**, which confirms all prepared materials have mesoporosity and large adsorption energy [22]. The specific surface area of CFP/rGO-H0, CFP/rGO-H1, CFP/rGO-H2, CFP/rGO-H3, CFP/rGO-H4, and CFP/rGO-H5 samples are 13.04 m²/g, 12.36 m²/g, 10.86 m²/g, 10.19 m²/g, 7.92 m²/g, and 9.62 m²/g, respectively. It is observed that, there is no such large change in surface area with the increase in concentration of rGO in the material. On the other hand, the pore-size distribution curves of the catalysts are obtained from BJH technique and becomes narrow, indicating the homogenization of the particles (**Figure 3.21(A-F)**).

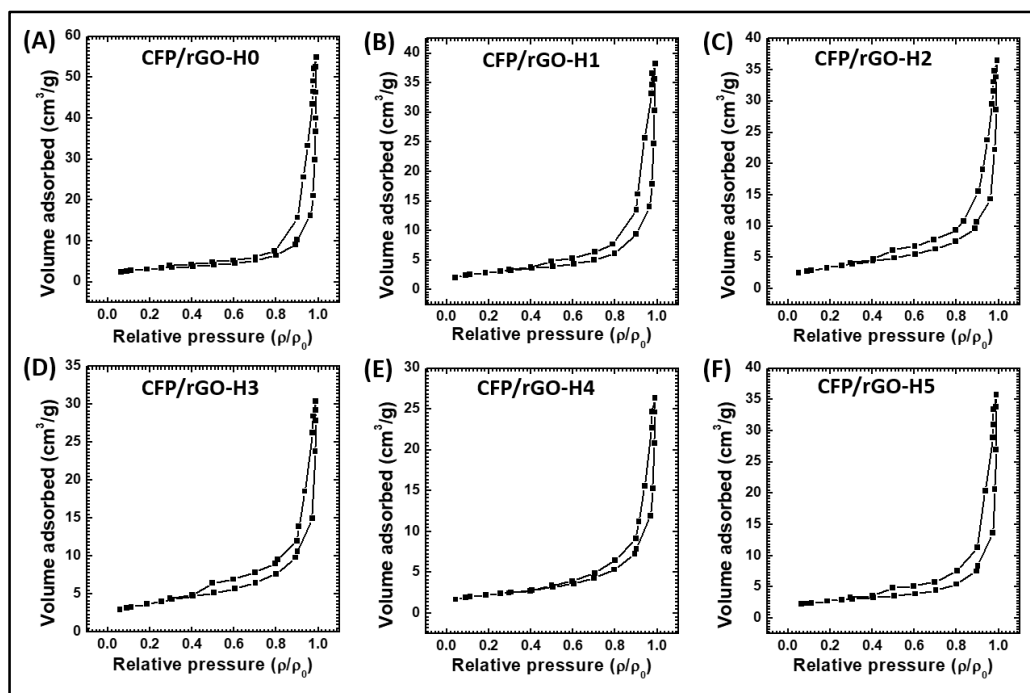


Figure 3.20: N₂ adsorption/desorption isotherms (BET) curves of (A) CFP/rGO-H0, (B) CFP/rGO-H1, (C) CFP/rGO-H2, (D) CFP/rGO-H3, (E) CFP/rGO-H4, and (F) CFP/rGO-H5.

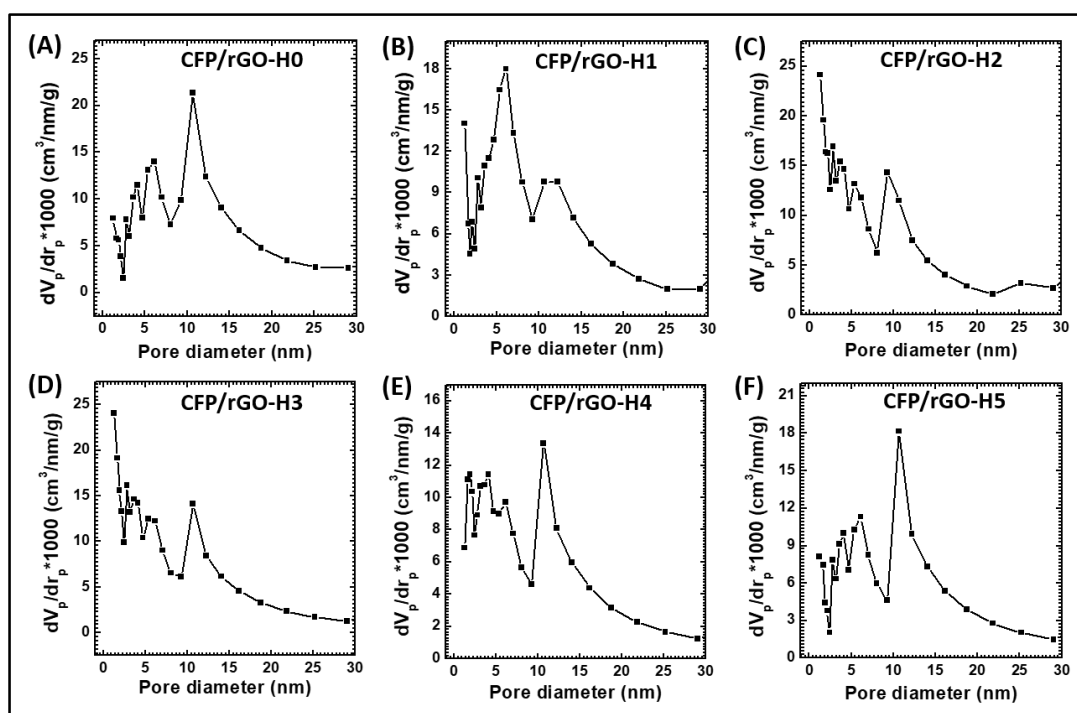


Figure 3.21: pore size distribution (BJH) curves of (A) CFP/rGO-H0, (B) CFP/rGO-H1, (C) CFP/rGO-H2, (D) CFP/rGO-H3, (E) CFP/rGO-H4, and (F) CFP/rGO-H5.

The observed pore sizes are 10.65, 6.12, 1.22, 1.22, 10.65 and 10.65 nm for the CFP/rGO-H0, CFP/rGO-H1, CFP/rGO-H2, CFP/rGO-H3, CFP/rGO-H4, and CFP/rGO-H5 samples, respectively.

3.4.B.3.6 Electrochemical catalytic performance analysis: The influence on electrochemical water splitting due to the incorporation of rGO into the active catalyst material was further studied. The concentration of rGO in the reaction solution was varied and the electrochemical performances were analyzed in terms of OER and HER in basic and acidic aqueous electrolytes, individually. For that purpose, the electrodes were made by depositing material on SS substrates by means of slurry coating technique.

i) ECSA analysis: It is necessary to calculate ECSA related to the C_{dl} of the prepared materials prior to study electrocatalytic OER and HER. The cyclic voltamograms were recorded at different scan rates in non-Faradic region with small potential range as shown in **Figure 3.22(A-F)** for all electrodes. C_{dl} is calculated by plotting the anodic charging currents (i_c) of each CV curve against the scan rate by the equation (2.3) given in **chapter 2, section-B, subsection-2.B.3.2**.

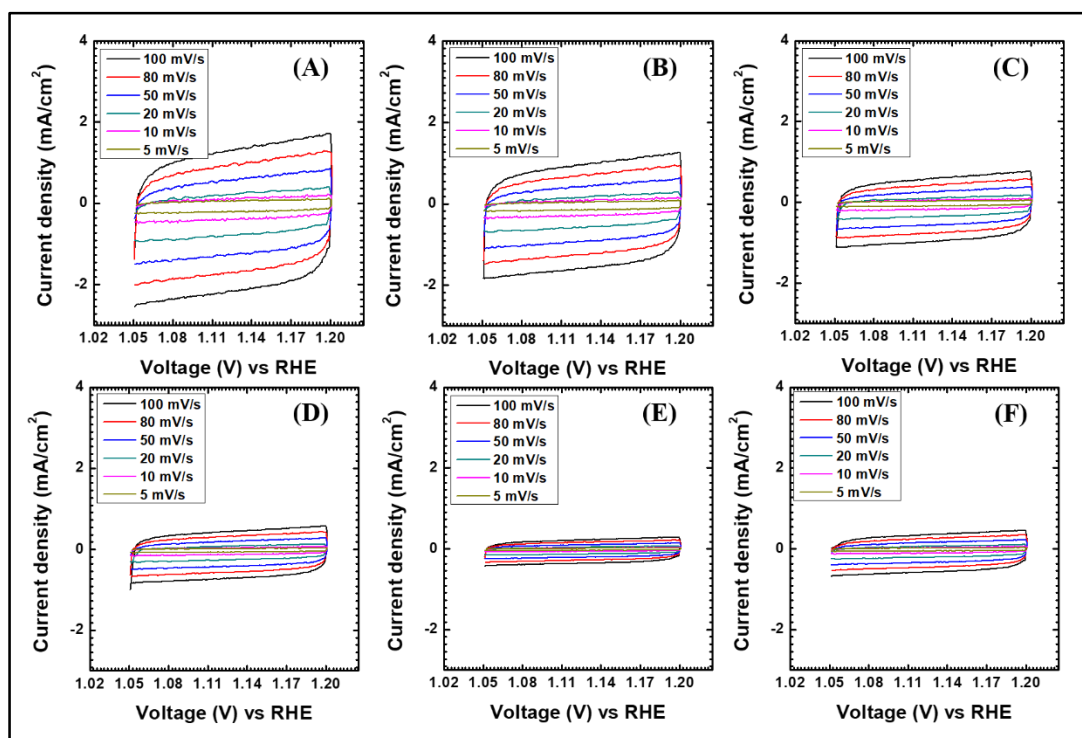


Figure 3.22: The CV curves of (A) CFP/rGO-H0, (B) CFP/rGO-H1, (C) CFP/rGO-H2, (D) CFP/rGO-H3, (E) CFP/rGO-H4, and (F) CFP/rGO-H5 at various scan rates in a small potential window (1.05 - 1.2 V vs RHE).

By plotting the anodic current versus scan rate (**Figure 3.23**), the values of C_{dl} have been calculated which are 1.29, 0.94, 0.57, 0.43, 0.21, and 0.34 mF/cm^2 for CFP/rGO-H0, CFP/rGO-H1, CFP/rGO-H2, CFP/rGO-H3, CFP/rGO-H4, and CFP/rGO-H5 electrodes, respectively. The ECSA can be calculated by equation (2.4) using C_{dl} values and corresponding values of ECSA are 32.25, 23.5, 14.25, 10.75, 5.24, and 8.5 cm^2 . The electrocatalytic interface texture can be derived from RF by dividing the ECSA with the geometric area of the electrode in contact with electrolyte. The values of RF are the same as ECSA values due to the 1 cm^2 geometric area in contact with electrolyte. The sample CFP/rGO-H0 showed high ECSA and RF than the others and these results are reliable with the BET surface analysis.

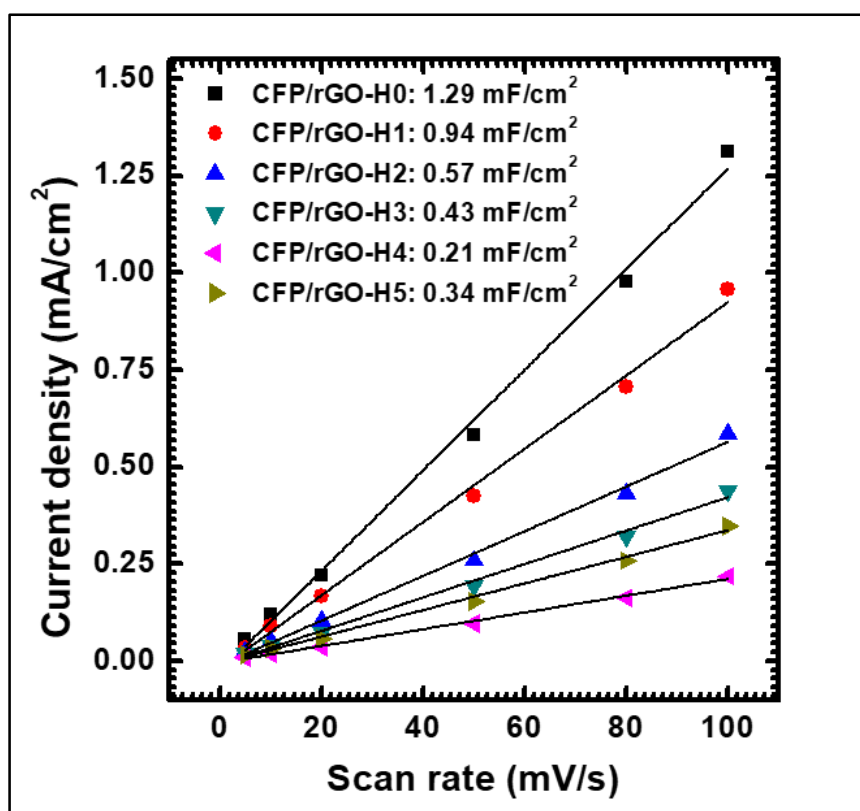


Figure 3.23: Anodic current linear fit for C_{dl} values to calculate ECSA of the CFP/rGO-H series hybrid electrodes.

ii) OER analysis: The oxygen evolution characteristics of the synthesized electrodes were studied for the electrochemical water splitting in the form of OER. For this catalytic activity investigation, the LSV curves were performed in 1 M KOH electrolyte and scan rate of 1 mV/s as shown in **Figure 3.24(A)**. The nature of the all LSV polarization curves is similar and persistent change in current density along with change in concentration of rGO from 0.00

to 0.1 mg/ml. It is observed and confirmed that most electrochemically active material is CFP/rGO-H0.

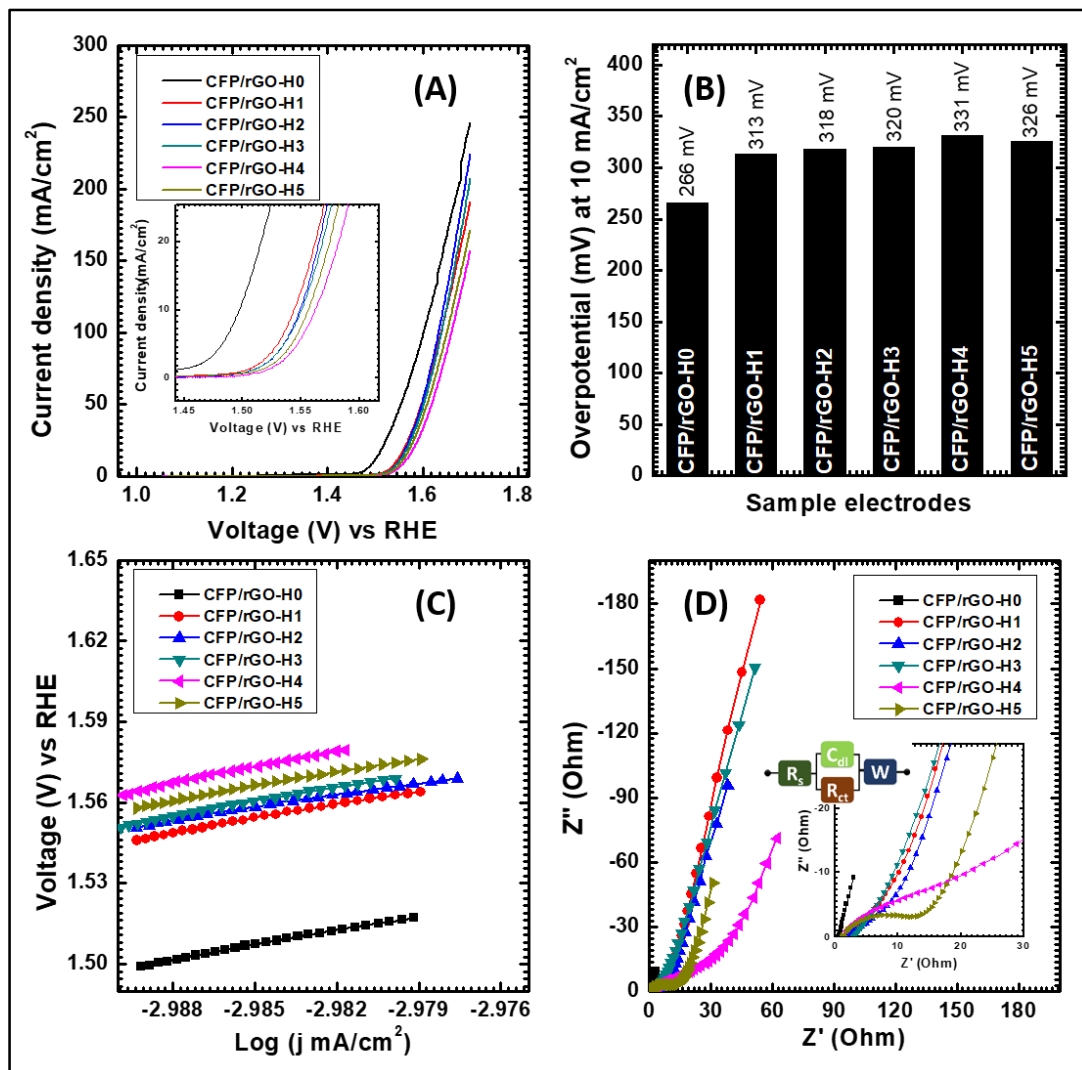


Figure 3.24: Electrochemical OER analysis (A) LSV polarization curves, (B) comparative bar diagram of overpotentials, (C) Tafel plots, (D) EIS of CFP/rGO-H0, CFP/rGO-H1, CFP/rGO-H2, CFP/rGO-H3, CFP/rGO-H4, and CFP/rGO-H5 hybrid electrodes.

Sample CFP/rGO-H0 shows the smallest overpotential of 266 mV to deliver current density of 10 mA/cm² suggesting outstanding oxygen evolution catalyst than the previously reported cobalt-iron phosphate catalysts (**Table 3.4 in section-A**). The overpotential values of all other electrode materials are given in bar diagram **Figure 3.24(B)**. The Tafel slope gives the catalytic activity in the form of reaction rate kinetics which indicate diverse rate determining steps surrounded in the reaction process. Tafel plot can be obtained by plotting applied potential against the logarithmic current density at the shoot-point of current

density as shown in **Figure 3.24(C)**. Figure reveals that the sample CFP/rGO-H0 shows smallest Tafel slope of 61.5 mV/dec. Tafel slopes for other samples are 67.9, 69.4, 69.5, 76.3, and 68.0 mV/dec for CFP/rGO-H1, CFP/rGO-H2, CFP/rGO-H3, CFP/rGO-H4, and CFP/rGO-H5 sample electrodes, respectively.

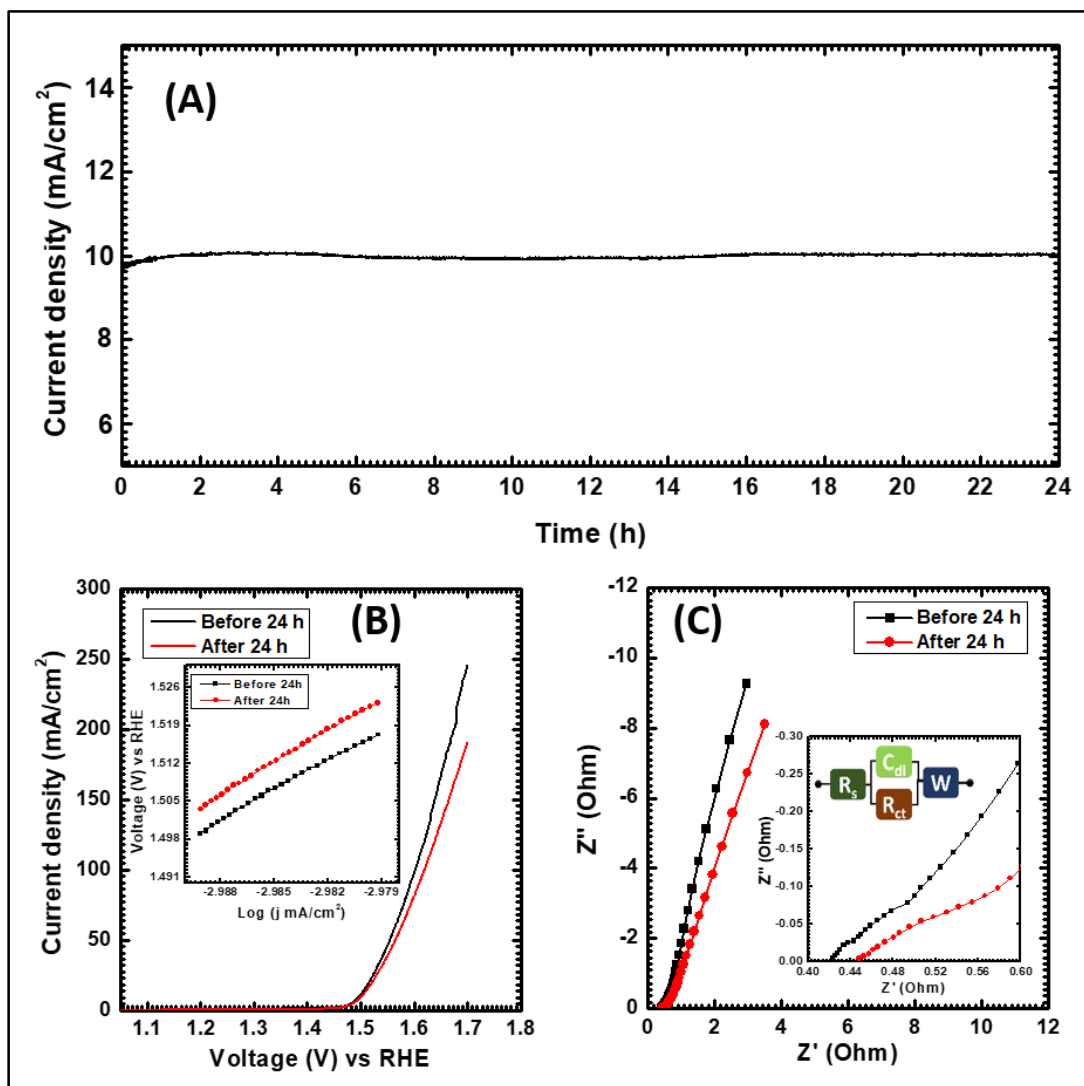


Figure 3.25: (A) CA (I-t) curve for OER stability, (B) LSV before and after 24 h OER catalysis, and (C) EIS after 24 h catalysis of (CFP/rGO-H0) electrode.

It suggests that, highly efficient reaction kinetics at CFP/rGO-H0 electrode surface and the OER process is faster. For the exploration of kinetics of electrochemical processes, EIS was conducted. **Figure 3.24(D)** shows typical Nyquist plots for the CFP/rGO series catalysts with fitted equivalent circuit. The fitted R_{ct} values are 0.714, 9.852, 12.125, 13.294, 28.842, and 16.329 Ω for CFP/rGO-H0, CFP/rGO-H1, CFP/rGO-H2, CFP/rGO-H3, CFP/rGO-H4, and CFP/rGO-H5 electrodes, respectively. It reveals that, easy charge

transfer process is one of the reason for low overpotential. It is also observed that, the charge transfer process becomes sluggish after the addition of rGO, it can be predicted to the addition of resistances to the total resistance from rGO, carbon black and the binder.

The catalytic stability for OER at overpotential was studied by three electrode cell in 1 M KOH bath to achieve 10 mA/cm² current density for the best performing catalyst. **Figure 3.25(A)** gives the OER catalytic stability test by CA for 24 h. At the initial stage, material has been starts to activate electrochemically and current density rises to 10 mA/cm² and becomes stable. After 24 h, the catalysis remained 98 % stable and overpotential becomes 271 mV with loss of small amount of current density as shown by comparative LSV plot (**Figure 3.25(B)**). Because of the material consumption in the electrolyte during the catalytic activity, the decrement in catalytic performance observed by LSV curve [37]. Inset figure gives the comparative Tafel slope before and after 24 h catalysis and increase in Tafel slope predicted the quite slowed down the reaction rate. The reaction rate further investigated by the measurement of EIS. The typical Nyquist plots are shown in **Figure 3.25(C)**, which revealed the small increment in the R_{ct} from 0.291 to 0.304 Ω . The fitted EIS parameters are tabulated in **Table 3.5**.

iii) HER analysis: The HER was analyzed for the CFP/rGO series electrodes by scanning in potential window of 0.33 to -0.65 V vs RHE in 1 M H₃PO₄ solution. The LSV curves of prepared electrodes were studied and exposed in **Figure 3.26(A)**, represents quick cathodic current increase and sharper curves of all catalyst electrodes. The overpotentials of CFP/rGO-H0, CFP/rGO-H1, CFP/rGO-H2, CFP/rGO-H3, CFP/rGO-H4, and CFP/rGO-H5 electrodes are recorded as 110.7, 144.9, 159.5, 174.7, 225.4, and 205.2 mV to attain the current density of 10 mA/cm² which is shown as bar diagram in **Figure 3.26(B)**. The CFP/rGO-H0 material electrode demonstrates good catalysis in comparison with other catalysts. The process of converting proton into hydrogen was examined by Tafel slope, and study revealed that lesser the slope carries quicker hydrogen evolution. The **Figure 3.26(C)** depicts that fast reaction rate and lesser Tafel slope (74.63 mV/dec) for CFP/rGO-H0 catalyst electrode. EIS was studied by the analysis of Nyquist plots of all the prepared electrodes as shown in **Figure 3.26(D)**. The R_{ct} of the CFP/rGO-H0 catalyst electrode is smaller (0.26 Ω) as compared to other electrodes CFP/rGO-H1 (1.28 Ω), CFP/rGO-H2 (3.06 Ω), CFP/rGO-H3 (2.93 Ω), CFP/rGO-H4 (14.66 Ω), and CFP/rGO-H5 (7.62 Ω) as examined by equivalent circuit fitting. This can be predicted that, low R_{ct} leads to the fast reaction kinetics, easy catalysis process and low overpotential.

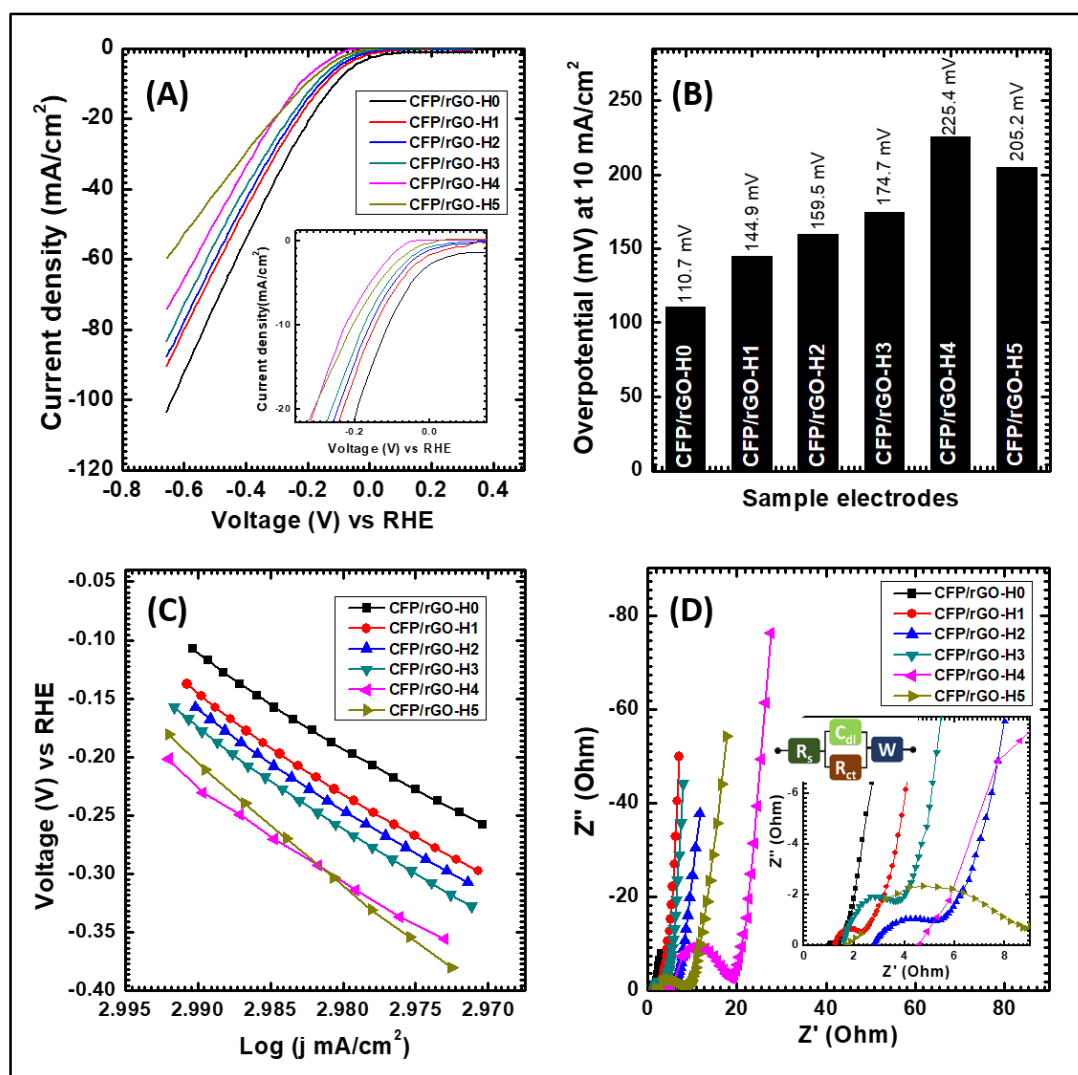


Figure 3.26: Electrochemical HER analysis: (A) LSV polarization curves, (B) comparative bar diagram of overpotentials, (C) Tafel plots, (D) EIS of CFP/rGO-H0, CFP/rGO-H1, CFP/rGO-H2, CFP/rGO-H3, CFP/rGO-H4, and CFP/rGO-H5 catalysts.

The large duration HER catalytic stability was measured with 24 h catalysis in CA mode for the best performing electrode. A constant overpotential was given to CFP/rGO-H0 catalyst electrode to attain the current density of $10 \text{ mA}/\text{cm}^2$ through CA stability and shown in **Figure 3.27(A)**. Initially, material has been start to activate electrochemically and it delivers quite higher current density throughout the period as shown in figure. Further the stability, HER catalytic process was examined and compared with previous one as shown in **Figure 3.27(B)**. After stability of 24 h, the overpotential get reduced to 95.5 mV at current density of $10 \text{ mA}/\text{cm}^2$. The inset figure gives the comparative plot of Tafel slopes, which becomes 72.3 mV/dec after 24 h catalysis.

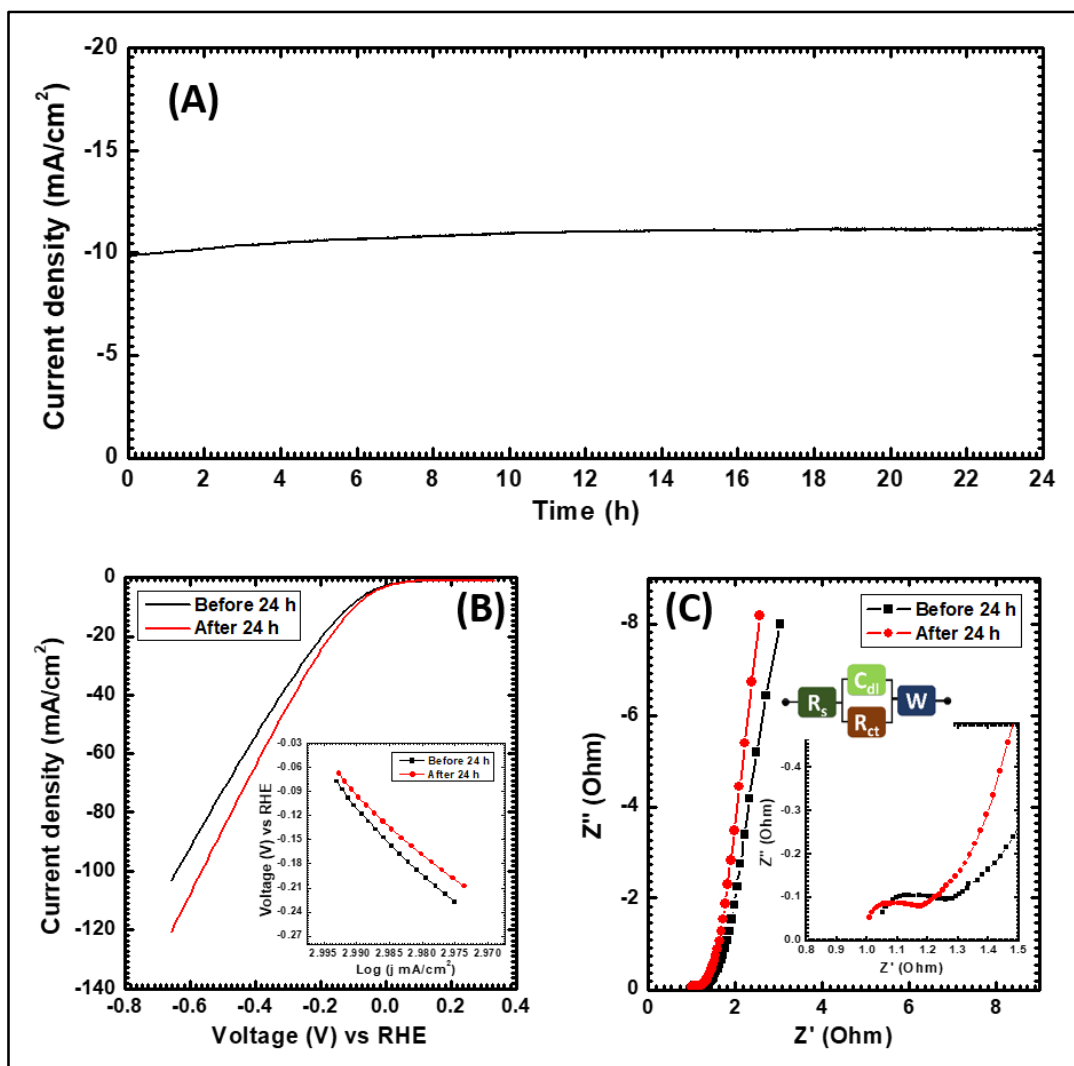


Figure 3.27: (A) CA (I-t) curve for HER stability, (B) LSV before and after 24 h OER catalysis, and (C) EIS after 24 h catalysis of (CFP/rGO-H0) electrode.

By fitting electronic equivalent circuit to the Nyquist plots, it is confirmed that, the R_{ct} decreased from 0.263Ω to 0.186Ω after catalysis as shown in **Figure 3.27(C)**. The decrease in Tafel slope and R_{ct} suggests that the reaction kinetics become easier after continuous catalysis. The fitted EIS parameters are tabulated in **Table 3.5**. From the 24 h CA stability and the EIS after stability, it is concluded that, there is better stability of the catalyst material.

Table 3.5: Electrochemical OER and HER analysis before and after 24 h catalytic stability study.

	Test	Overpotential η (mV) at 10 mA/cm ²	Tafel slope (mV/dec)	R _s (Ω)	R _{ct} (Ω)	W (Ω)
Before stability	OER	266	61.5	0.423	0.291	0.52
After stability		271	62.7	0.448	0.304	0.58
Before stability	HER	110.7	74.6	1.052	0.263	0.23
After stability		95.5	72.3	1.009	0.186	0.19

3.5 Conclusions: In conclusion of section-B, cobalt-iron phosphate/reduced graphene oxide materials at various rGO concentrations were synthesized via hydrothermal method. The prepared hybrid materials were characterized physico-chemically for their determination. The amorphous nature of cobalt-iron phosphate/reduced graphene oxide materials was confirmed by XRD analysis. The formation of cobalt-iron phosphate/reduced graphene oxide hybrid material was confirmed by observing elemental content and their corresponding bonds in the prepared samples via FTIR, EDS and XPS. The prepared hybrid materials were coated on SS substrates by slurry coating technique and tested electrochemically for water splitting in the forms of OER and HER. It is concluded that, CFP/rGO-H0 sample demonstrated minimum overpotential of 266 mV for OER to deliver the current density of 10 mA/cm² with Tafel slope of 61.5 mV/dec and almost 98 % catalytic OER retention after 24 h in alkaline medium. Also, the same material was performed HER with 110.7 mV overpotential with current density of 10 mA/cm² and 74.6 mV/dec Tafel slope. After HER stability for 24 h in acidic medium, it is observed that the overpotential reduced to 95.5 mV. It is also observed that, the CFP/rGO-H0 electrode deposited by slurry coating shows best performance than the hybrid materials. The electrochemical performance of hybrid materials decreases because of the restacking of rGO NSs due to chemical reduction and the aggregation of material with rGO [38,39]. Also, rGO may cover the active material due to which the electrochemical active centers may get

reduced [29,40,41]. It can also predict that, as the concentration of rGO increases, intermolecular contacts of active material diminished and hence the internal resistance and R_{ct} goes on increasing which result in the decreasing performance.

It is also concluded that, the binder free synthesis of pristine cobalt-iron phosphate electrodes (CFP-H series) by hydrothermal method, as discussed earlier in section A, show best electrochemical OER and HER performances than the slurry coated pristine cobalt-iron phosphate (CFP/rGO-H0) and cobalt-iron phosphate/reduced graphene oxide (CFP/rGO-H series) hybrid electrodes discussed earlier in section B. It is due to the direct deposition of material facilitates the easy charge transfer path without any additional resistances which result in the good electrical conductivity and hence good electrochemical performance. On the other hand, to coat powder material on to the conducting substrate, there is requirement of the binder. The binder increases the resistance for charge transfer between material to substrate. Thus it is concluded that, the binder free synthesis of electrodes demonstrates best performance and good applicability in electrochemistry.

3.6 References:

1. Y. Shi, B. Zhang, Recent advances in transition metal phosphide nanomaterials: Synthesis and applications in hydrogen evolution reaction, *Chemical Society Reviews* 45 (2016) 1529.
2. D. Kang, T. W. Kim, S. R. Kubota, A. C. Cardiel, H. G. Cha, K.-S. Choi, Electrochemical synthesis of photoelectrodes and catalysts for use in solar water splitting, *Chemical Reviews* 115 (2015) 12839.
3. M. Grätzel, Photoelectrochemical cells, *Nature* 414 (2001) 338.
4. S. A. Khalate, S. A. Kadam, Y. -R. Ma, S. S. Pujari, S. J. Marje, P. K. Katkar, A. C. Lokhande, U. M. Patil, Hydrothermally synthesized iron phosphate hydroxide thin film electrocatalyst for electrochemical water splitting, *Electrochimica Acta* 319 (2019) 118.
5. S. Cherevko, S. Geiger, O. Kasian, N. Kulyk, J. P. Grote, A. Savan, B. R. Shrestha, S. Merzlikin, B. Breitbach, A. Ludwig, K. J. J. Mayrhofer, Oxygen and hydrogen evolution reactions on Ru, RuO₂, Ir, and IrO₂ thin film electrodes in acidic and alkaline electrolytes: A comparative study on activity and stability, *Catalysis Today* 262 (2016) 170.
6. J. Zhu L. Hu, P. Zhao, L. Y. S. Lee, K.-Y. Wong, Recent advances in electrocatalytic hydrogen evolution using nanoparticles, *Chemical Reviews* 120 (2020) 851.
7. B. S. Yeo, A. T. Bell, Enhanced activity of gold-supported cobalt oxide for the electrochemical evolution of oxygen, *Journal of American Chemical Society* 133 (2011) 5587.
8. X. Long, J. Li, S. Xiao, K. Yan, Z. Wang, H. Chen, S. Yang, A strongly coupled graphene and FeNi double hydroxide hybrid as an excellent electrocatalyst for the oxygen evolution reaction, *Angewandte Chemie* 126 (2014) 7714.

9. M. Liu, Z. Qu, D. Yin, X. Chen, Y. Zhang, Y. Guo, D. Xiao, Cobalt–iron pyrophosphate porous nanosheets as highly active electrocatalysts for the oxygen evolution reaction, *ChemElectroChem* 5 (2018) 36.
10. D. Yin, Z. Jin, M. Liu, T. Gao, H. Yuan, D. Xiao, Microwave-assisted synthesis of the cobalt-iron phosphates nanosheets as an efficient electrocatalyst for water oxidation, *Electrochimica Acta* 260 (2018) 420.
11. C. Li, X. Mei, F. L. -Y. Lam, X. Hu, Amorphous iron and cobalt based phosphate nanosheets supported on nickel foam as superior catalysts for hydrogen evolution reaction, *ACS Applied Energy Materials* 1 (2018) 6764.
12. G. Hodes, Chemical solution deposition of semiconductor films, Marcel Dekker Inc., New York, (2001) pp. 12.
13. P. K. Katkar, S. J. Marje, S. S. Pujari, S. A. Khalate, A. C. Lokhande, U. M. Patil, Enhanced energy density of all-solid-state asymmetric supercapacitors based on morphologically tuned hydrous cobalt phosphate electrode as cathode material, *ACS Sustainable Chemistry & Engineering* 7 (2019) 11205.
14. C. Murugesan, S. Lochab, B. Senthilkumar, P. Barpanda, Earth-abundant alkali iron phosphate (AFePO_4) as efficient electrocatalysts for oxygen reduction reaction in alkaline solution, *ChemCatChem* 10 (2018) 1122.
15. H. B. Li, M. H. Yu, X. H. Lu, P. Liu, Y. Liang, J. Xiao, Y. X. Tong, G. W. Yang, Amorphous cobalt hydroxide with superior pseudocapacitive performance, *ACS Applied Materials & Interfaces* 6 (2014) 745.
16. Y. Li, Z. Wang, J. Hu, S. Li, Y. Du, X. Han, P. Xu, Metal-organic frameworks derived interconnected bimetallic metaphosphate nanoarrays for efficient electrocatalytic oxygen evolution, *Advanced Functional Materials* 30 (2020) 1910498.
17. R. Gresch, W. Muller-Warmuth, H. Dutz, X-ray photoelectron spectroscopy of sodium phosphate glasses, *Journal of Non-Crystalline Solid* 34 (1979) 127.
18. B. Li, Y. Shi, K. Huang, M. Zhao, J. Qiu, H. Xue, H. Pang, Cobalt-doped nickel phosphite for high performance of electrochemical energy storage, *Small* 14 (2018) 1703811.
19. H. Dan, K. Tao, Q. Zhou, Y. Gong, J. Lin, Ni-doped cobalt phosphite, $\text{Co}_{11}(\text{HPO}_3)_8(\text{OH})_6$, with different morphologies grown on Ni foam hydro(solvo)thermally for high-performance supercapacitor, *ACS Applied Materials & Interfaces* 10 (2018) 31340.
20. C. Chen, N. Zhang, Y. He, B. Liang, R. Ma, X. Liu, Controllable Fabrication of Amorphous Co-Ni Pyrophosphates for Tuning Electrochemical Performance in Supercapacitors, *ACS Applied Materials & Interfaces* 8 (2016) 23114.
21. H. Pang, Y. Z. Zhang, Z. Run, W. Y. Lai, W. Huang, Amorphous nickel pyrophosphate microstructures for high-performance flexible solid-state electrochemical energy storage devices, *Nano Energy* 17 (2015) 339.
22. J. B. Condon, Surface area and porosity determinations by physisorption: Measurements and theory, 1st ed., Elsevier, Amsterdam, Boston, (2006) pp. 6.
23. C. C. L. McCrory, S. Jung, J. C. Peters, T. F. Jaramillo, Benchmarking heterogeneous electrocatalysts for the oxygen evolution reaction, *Journal of American Chemical Society* 135 (2013) 16977.
24. B. S. Brunshwig, M. H. Chou, C. Creutz, P. Ghosh, N. Sutin, Mechanisms of water oxidation to oxygen: Cobalt (IV) as an intermediate in the aquocobalt (II)-catalyzed reaction, *Journal of American Chemical Society* 105 (1983) 4832.

25. Z. Wang, M. Liu, J. Du, Y. Lin, S. Wei, X. Lu, J. Zhang, A facile co-precipitation synthesis of robust FeCo phosphate electrocatalysts for efficient oxygen evolution, *Electrochimica Acta* 264 (2018) 244.
26. Y. Zhou, H. C. Zeng, 3D networks of CoFePi with hierarchical porosity for effective OER electrocatalysis, *Small* 14 (2018) 1704403.
27. Q. Yue, T. Gao, Y. Wu, H. Yuan, D. Xiao, S-doped Co-Fe-Pi nanosheets as highly efficient oxygen evolution electrocatalysts in alkaline media, *Electrochimica Acta* 362 (2020) 137123.
28. U. M. Patil, M. S. Nam, S. Kang, J. S. Sohn, H. B. Sim, S. Kang, S. C. Jun, Fabrication of ultra-high energy and power asymmetric supercapacitors based on hybrid 2D MoS₂/graphene oxide composite electrodes: A binder-free approach, *RSC Advances* 6 (2016) 43261.
29. G. Zhu, X. Xie, L. Xiao, X. Li, X. Shen, Y. -J. Liu, Co-Fe bimetal phosphate composite loaded on reduced graphene oxide for oxygen evolution, *Nano* 14 (2019) 1950003.
30. J. Hu, Z. Kang, F. Li, X. Huang, Graphene with three-dimensional architecture for high performance supercapacitor, *Carbon* 67 (2014) 221.
31. D. Li, M. B. Müller, S. Gilje, R. B. Kaner, G. G. Wallace, Processable aqueous dispersions of graphene nanosheets, *Nature nanotechnology* 3 (2008) 101.
32. C. Fu, G. Zhao, H. Zhang, S. Li, Evaluation and characterization of reduced graphene oxide nanosheets as anode materials for lithium-ion batteries, *International Journal of Electrochemical Science* 8 (2013) 6269.
33. B. M. Lee, V. T. Bui, H. S. Lee, S. K. Hong, H. S. Choi, J. H. Choi, Fabrication of hexagonally arranged porous carbon films by proton beam irradiation and carbonization, *Radiation Physics and Chemistry* 163 (2019) 18.
34. C. Zhu, S. Guo, Y. Fang, S. Dong, Reducing sugar: New functional molecules for the green synthesis of graphene nanosheets, *ACS Nano* 4 (2010) 2429.
35. C. Galande, A. D. Mohite, A. V. Naumov, W. Gao, L. Ci, A. Ajayan, H. Gao, A. Srivastava, R. B. Weisman, P. M. Ajayan, Quasi-molecular fluorescence from graphene oxide, *Scientific Reports* 1 (2011) 1.
36. D. Briggs, G. Beamson, High resolution XPS of organic polymers: The scienta esca 300 database, John Wiley and Sons, New York, (1992) pp. 128.
37. S. Zou, M. Burke, M. Kast, J. Fan, N. Danilovic, S. Boettcher, Fe (oxy)hydroxide oxygen evolution reaction electrocatalysis: Intrinsic activity and the roles of electrical conductivity, substrate, and dissolution, *Chemistry of Materials* 27 (2015) 8011.
38. C. Xu, X. Wang, J. Zhu, Graphene-metal particle nanocomposites, *Journal of Physical Chemistry C* 112 (2008) 19841.
39. A. Ramesh, M. Jeyavelan, M. S. L. Hudson, Electrochemical properties of reduced graphene oxide derived through camphor assisted combustion of graphite oxide, *Dalton Transactions* 47 (2018) 5406.
40. R. Cong, J. Y. Choi, J. B. Song, M. Jo, H. Lee, C. S. Lee, Characteristics and electrochemical performances of silicon/carbon nanofiber/graphene composite films as anode materials for binder-free lithium-ion batteries, *Scientific Reports* 11 (2021) 1.
41. H. Yue, Q. Li, D. Liu, X. Hou, S. Bai, S. Lin, D. He, High-yield fabrication of graphene-wrapped silicon nanoparticles for self-support and binder-free anodes of lithium-ion batteries, *Journal of Alloys and Compounds* 744 (2018) 243.

CHAPTER – IV

**SILAR DEPOSITED COBALT-IRON
PHOSPHATE AND COBALT-IRON
PHOSPHATE/REDUCED
GRAPHENE OXIDE HYBRID FOR
ELECTROCHEMICAL OER AND HER
APPLICATION**

CHAPTER – IV

SILAR DEPOSITED COBALT-IRON PHOSPHATE AND COBALT-IRON PHOSPHATE/REDUCED GRAPHENE OXIDE HYBRID FOR ELECTROCHEMICAL OER AND HER APPLICATION

Contents

Sr. No.	Title	Page No.
4.1	Introduction	115
4.2	Section-A: SILAR synthesis of cobalt-iron phosphate thin films and their characterization for electrochemical OER and HER	116
4.2.A.1	Introduction	116
4.2.A.2	Experimental details	116
4.2.A.2.1	Materials used and substrate cleaning	116
4.2.A.2.2	Synthesis of cobalt-iron phosphate thin films	117
4.2.A.3	Results and discussion	118
4.2.A.3.1	Reaction mechanism	118
4.2.A.3.2	XRD analysis	120
4.2.A.3.3	FTIR analysis	120
4.2.A.3.4	XPS analysis	121
4.2.A.3.5	Surface morphological and elemental analysis	122
4.2.A.3.6	N ₂ adsorption-desorption isotherm analysis	125
4.2.A.3.7	Electrochemical catalytic performance analysis	126
4.3	Conclusions	133
4.4	Section B: SILAR synthesis of cobalt-iron phosphate/reduced graphene oxide hybrid and their characterization for electrochemical OER and HER	134
4.4.B.1	Introduction	134
4.4.B.2	Experimental details	134
4.4.B.2.1	Synthesis of graphene oxide (GO)	134
4.4.B.2.2	Synthesis of cobalt-iron phosphate/reduced graphene oxide	135
4.4.B.3	Results and discussion	136

4.4.B.3.1	XRD analysis	136
4.4.B.3.2	FTIR analysis	137
4.4.B.3.3	XPS analysis	138
4.4.B.3.4	Surface morphological and elemental analysis	139
4.4.B.3.5	N ₂ adsorption-desorption isotherm analysis	141
4.4.B.3.6	Electrochemical catalytic performance analysis	143
4.5	Conclusions	150
4.6	References	151

4.1 Introduction: Synthesis process of the catalyst material is very important and plays a crucial role in the overall electrochemical performance. To synthesize cobalt-iron phosphate catalyst, there are few methods have reported till date. Chemical coprecipitation is repeatedly used method. Zhou et al. [1] reported cobalt-iron phosphate 3D hierarchically porous network synthesized via coprecipitation method using SDBS primary micelles. The synthesized cobalt-iron phosphate exhibited superior OER activity with 277 mV overpotential to attain 10 mA/cm² current density, Tafel slope of 31 mV/dec and stability around 10 h of constant electrolysis. For the OER, Wang et al. [2] synthesized cobalt-iron phosphate by coprecipitation method which required overpotentials of only 273 and 298 mV to drive current densities of 10 and 50 mA/cm² in 1 M KOH. Similarly, the solvothermal method is also applicable [3]. Microwave assisted heating method to synthesized cobalt-iron phosphate was reported by Yin et al. [4]. The synthesized material gives OER performance with 267 mV overpotential to attain 10 mA/cm², Tafel slope (30 mV/dec) and stability (catalytic activity was retained up to 94 % after 10 h water oxidation). Amorphous iron and cobalt based phosphate material was synthesized by hydrothermal method [5], similarly the hybrid material with rGO was synthesized by Zhu et al. [6] and studied their electrochemical performance. As per the knowledge, there is no single report on the synthesis of cobalt-iron phosphate catalyst material using SILAR method. SILAR is one of the simplest methods for the preparation of catalyst thin film materials with nanostructural morphology. In SILAR deposition, one can easily control the deposition rate and the thickness of the film. For the good quality films by chemical methods, SILAR method is the perfect choice.

In the present chapter, discussion about the synthesis of pristine cobalt-iron phosphate and cobalt-iron phosphate/reduced graphene oxide hybrid catalysts by using the SILAR method is given. In this study, the effect of chemical compositional variation on the physico-chemical properties was analyzed. Variation in the composition may causes the effect on electrochemical water splitting which further studied thoroughly. The present chapter is divided into two sections as section-A and section-B. In section-A, the synthesis of cobalt-iron phosphate thin films using superficial SILAR method and their characterization for physico-chemical and electrochemical water splitting is described. In section-B, the cobalt-iron phosphate/reduced graphene oxide hybrid electrodes were prepared by facile SILAR method and the effect of rGO concentration variation in the

optimized cobalt-iron phosphate sample (in section A) was studied for electrochemical water splitting.

4.2 Section-A: SILAR synthesis of cobalt-iron phosphate thin films and their characterization for electrochemical OER and HER

4.2.A.1 Introduction: Development of active, stable, and Earth abundant nonprecious-metal-based catalysts for water splitting in the form of OER and HER is a crucial task. Cobalt-iron phosphate is one of the promising material for the water oxidation [1-5,7]. According to previous reports, it is clear that, amorphous materials synthesized at low temperature are electrochemically more active than well crystalline materials synthesized at higher temperature, by the reason of huge number of coordinatively unsaturated sites and surface defects. Active sites are very important during the catalytic activity. Large open porous structure, high specific surface area, and tailored reaction interface for facilitating an accessibility of the active sites, mass transport, and gas release are the conditions of ideal water splitting catalyst. SILAR method is nothing but the best to synthesize amorphous materials and is the simplest, economically cheap, versatile and environmentally friendly knowing to soft chemical solution method to deposit thin films in ambient conditions [8]. However, there is no report on cobalt-iron phosphate by SILAR method for electrochemical water splitting.

In this section, the discussion about the cobalt-iron phosphate thin films deposited on SS substrate using SILAR synthesis as binder free approach is given. The effect of composition variation of cobalt and iron on the structural, morphological and surface properties were studied. Electrochemical tests were conducted with prepared thin film electrodes for water splitting in the form of OER and HER to investigate the best performing catalyst.

4.2.A.2 Experimental details

4.2.A.2.1 Materials used and substrate cleaning: The analytical grade chemicals were used for the preparation of cobalt-iron phosphate such as $\text{CoCl}_2 \cdot 6\text{H}_2\text{O}$, FeCl_2 , and K_2HPO_4 purchased from Sigma-Aldrich and Thomas Baker. Without any further purification, the as-purchased chemicals were used for materials synthesis. SS substrates (304 grade) were thoroughly cleaned prior to the preparation for reaction. The procedure for substrate cleaning is given earlier in **chapter-3, section A, subsection 3.2.A.2.1**.

4.2.A.2.2 Synthesis of cobalt-iron phosphate thin films: Thin films of cobalt-iron phosphate were prepared at room temperature using the facile, low cost and rapid SILAR method schematically represented in **Figure 4.1(A)**.

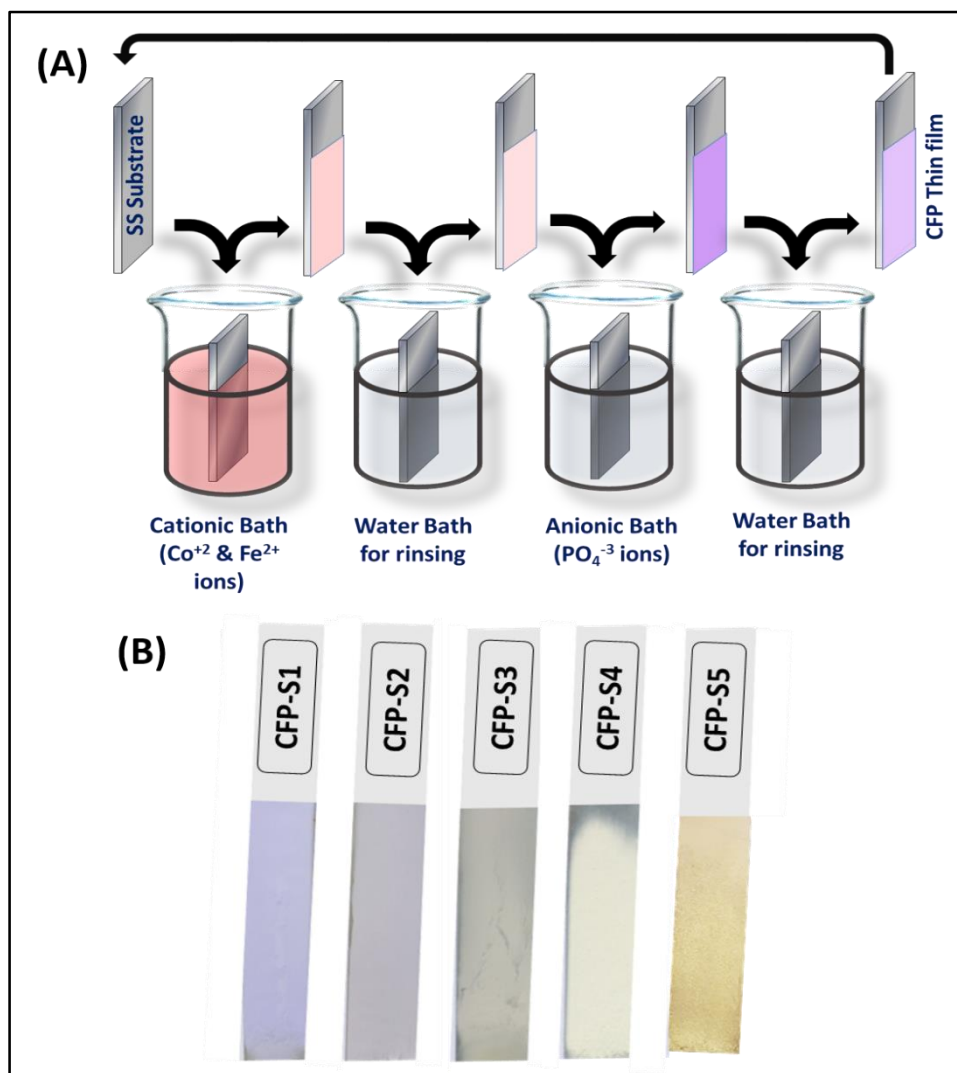


Figure 4.1: (A) Schematic representation of SILAR deposition of CFP thin films, (B) photograph of deposited films.

In the typical SILAR process, separately prepared cation and anion solutions were used. The solutions were prepared in 50 ml DDW by dissolving 0.125 M K₂HPO₄ in a beaker served as anionic precursor and another beaker was prepared containing the different concentrations of CoCl₂·6H₂O (0.08 M to 0.00 M) and FeCl₂ (0.00 M to 0.08 M) as described in **Table 4.1**, which served as cationic precursor. In between each precursor, beakers of 50 ml DDW were arranged for the rinsing purpose. That means, four beakers in sequence as cationic precursor (Co²⁺ and Fe²⁺), DDW, anionic precursor (PO₄³⁻), and DDW

were used for thin film preparation. The well cleaned SS substrates were immersed in each beaker successively. This procedure completes the one cycle of the deposition.

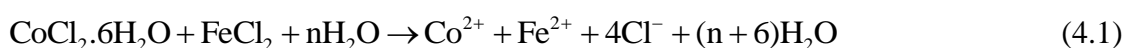
Table 4.1: Concentration variation of cobalt and iron to prepare the cobalt-iron phosphate thin films.

Sr. No.	CoCl ₂ .6H ₂ O (M)	FeCl ₂ (M)	K ₂ HPO ₄ (M)	Notation
1.	0.08	0	0.125	CFP-S1
2.	0.06	0.02	0.125	CFP-S2
3.	0.04	0.04	0.125	CFP-S3
4.	0.02	0.06	0.125	CFP-S4
5.	0	0.08	0.125	CFP-S5

For the good deposition, the concentrations of precursors, times for adsorption, reaction and rinsing, and the number of cycles are important. The adsorption time (20 s), first rinsing time (10 s), reaction time (20 s) and second rinsing time (10 s) were optimized with the 50 cycles to get well adherent and uniform film. After completion of reaction cycles, faint violet to faint yellow colored thin films were obtained as shown in **Figure 4.1(B)**. The synthesized cobalt-iron phosphate thin films were named as CFP-S2, CFP-S3, and CFP-S4. For the comparative study, the cobalt phosphate and iron phosphate materials were prepared and named as CFP-S1 and CFP-S5, respectively.

4.2.A.3 Results and discussion

4.2.A.3.1 Reaction mechanism: Basically, SILAR method is bottom-up process for material synthesis, and is nothing but the ion-by-ion nucleation to develop the solid phase and layer-by-layer film formation stages from the reaction solution. Upon immersion of substrate in Co²⁺ and Fe²⁺ cationic precursor solution, the metal ions get attracted towards the substrate by the cohesive or Van der Waals force and the Helmholtz electric double layer is formed due to the adsorption of Co²⁺ and Fe²⁺ cations present in the precursor solution [9].

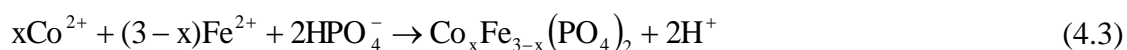


The loosely bounded ions were rinsed out by dipping substrate in the next beaker of DDW.

For the reaction with anions, the substrate then immersed in the beaker containing anionic precursor solution. As the anionic precursor is K_2HPO_4 and it becomes:



Here, the adsorbed Co^{2+} and Fe^{2+} cations get reacted with the PO_4^{3-} anions and neutralized making the solid substance on the surface of substrate.



Loosely bounded solid particles were removed by immersing the substrate in next beaker of DDW. The development of cobalt-iron phosphate at the ionic stage occurred by following heterogeneous nucleation on the surface of SS substrate. These nuclides propagate by layer-by-layer to prepare an even thin coating of cobalt-iron phosphate. The mass loading for each sample calculated by weight difference method as shown in **Figure 4.2**.

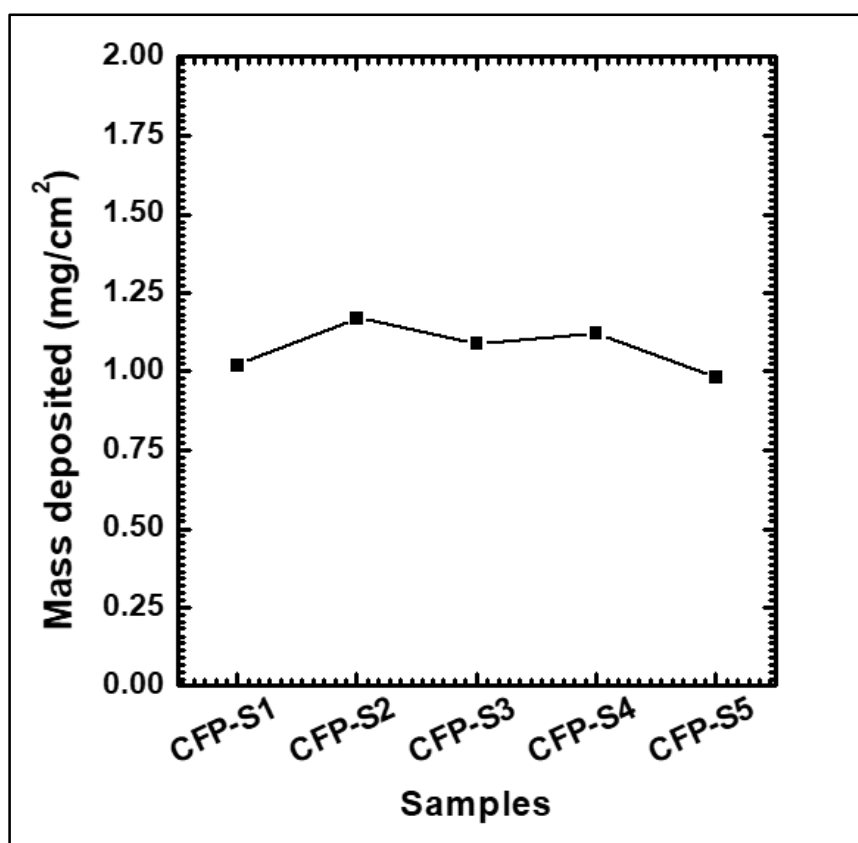


Figure 4.2: Mass loading per unit area of CFP-S series thin films.

4.2.A.3.2 XRD analysis:

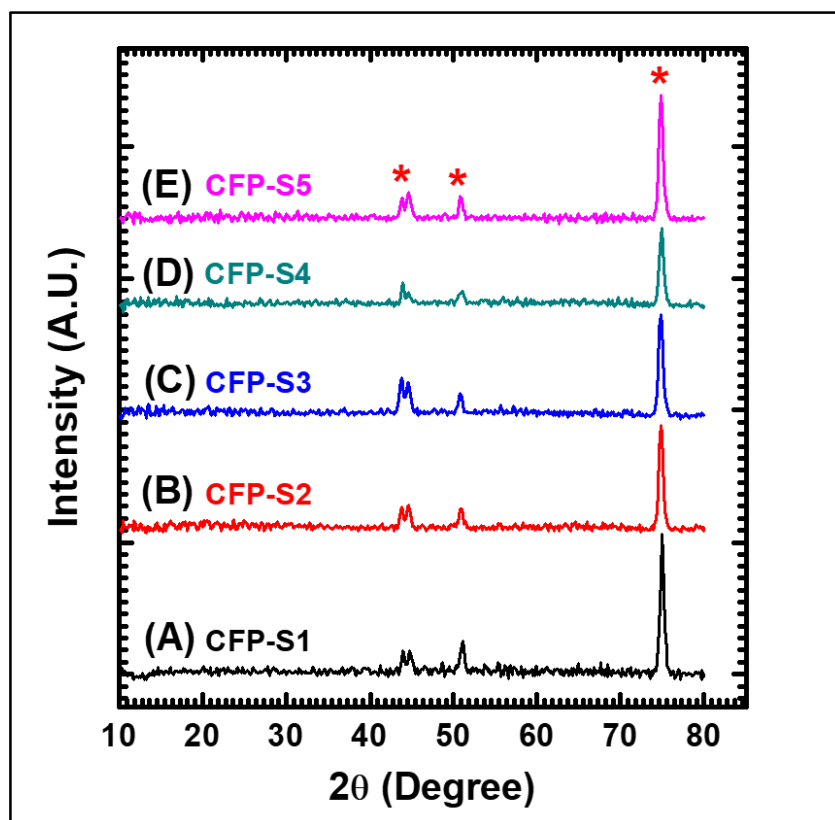


Figure 4.3: XRD patterns of SILAR deposited cobalt-iron phosphate thin films (A) CFP-S1, (B) CFP-S2, (C) CFP-S3, (D) CFP-S4, and (E) CFP-S5 on SS substrates.

To study the structural properties of the SILAR deposited CFP-S1, CFP-S2, CFP-S3, CFP-S4, and CFP-S5 materials on SS substrates, XRD patterns were recorded as shown in **Figure 4.3**. The recorded spectra of all the samples shows the amorphous nature of the prepared materials. The peaks marked with ‘*’ are the diffraction peaks of SS substrate. A well-crystallized structure can have difficulty in expanding or contracting, limiting the permeation and diffusion of ions. In contrast, the continuous redox reaction of an amorphous composite occurs not only on the surface but also in the bulk of the material, leading to better performance compared with crystallized structures [10]. The amorphous materials may give the large surface area and high electrocatalytic active sites which are favorable for water molecule adsorption and decomposition into O₂ and H₂.

4.2.A.3.3 FTIR analysis: By using the FTIR spectroscopy, SILAR deposited thin films (CFP-S1, CFP-S2, CFP-S3, CFP-S4, and CFP-S5) were characterized for the study of molecular bond development.

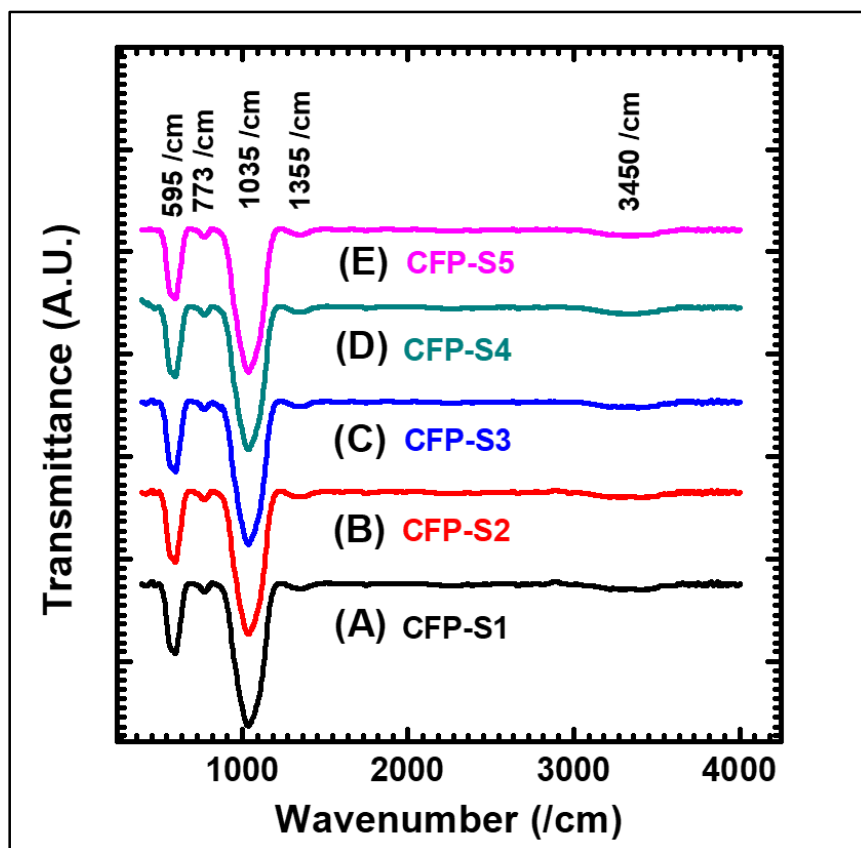


Figure 4.4: FTIR patterns of SILAR deposited cobalt-iron phosphate thin films (A) CFP-S1, (B) CFP-S2, (C) CFP-S3, (D) CFP-S4, and (E) CFP-S5.

The FTIR spectra shown in **Figure 4.4**, from wavenumber 400 to 4000 /cm containing intermolecular vibrational modes of phosphate anions (PO_4^{3-}) and structural water molecules. The absorption peak at 595 /cm reveals the asymmetric bending vibrational mode of PO_4 bond. The small absorption on 773 /cm corresponds to Co-O lattice vibration mode [11]. The sharp absorption at 1035 /cm shows the asymmetric stretching vibrations of PO_4 [12]. Very small absorption band at 1355 /cm is the indication of the surface adsorbed CO_2 molecules [13]. Broad band at higher wavenumber (3450 /cm) is attributed to the stretching vibrations of the O-H molecules from the structural water.

4.2.A.3.4 XPS analysis: It is important to know the valance states of electrons of the elements existing on the surface of synthesized materials, hence XPS analysis was conducted. XPS spectra of cobalt-iron phosphate (CFP-S2) thin film is shown in **Figure 4.5**. The survey spectrum discloses that the elements present at the surface are P, O, Fe and Co and revealed in **Figure 4.5(A)**. The high resolution $\text{Co}2\text{p}$ spectrum discloses the existence of prominent peaks at 781.76 eV for $\text{Co}2\text{p}_{3/2}$ and at 797.43 eV for $\text{Co}2\text{p}_{1/2}$ and

their alongside satellite peaks at 786.19 eV and 802.38 eV, correspondingly as shown in **Figure 4.5(B)**.

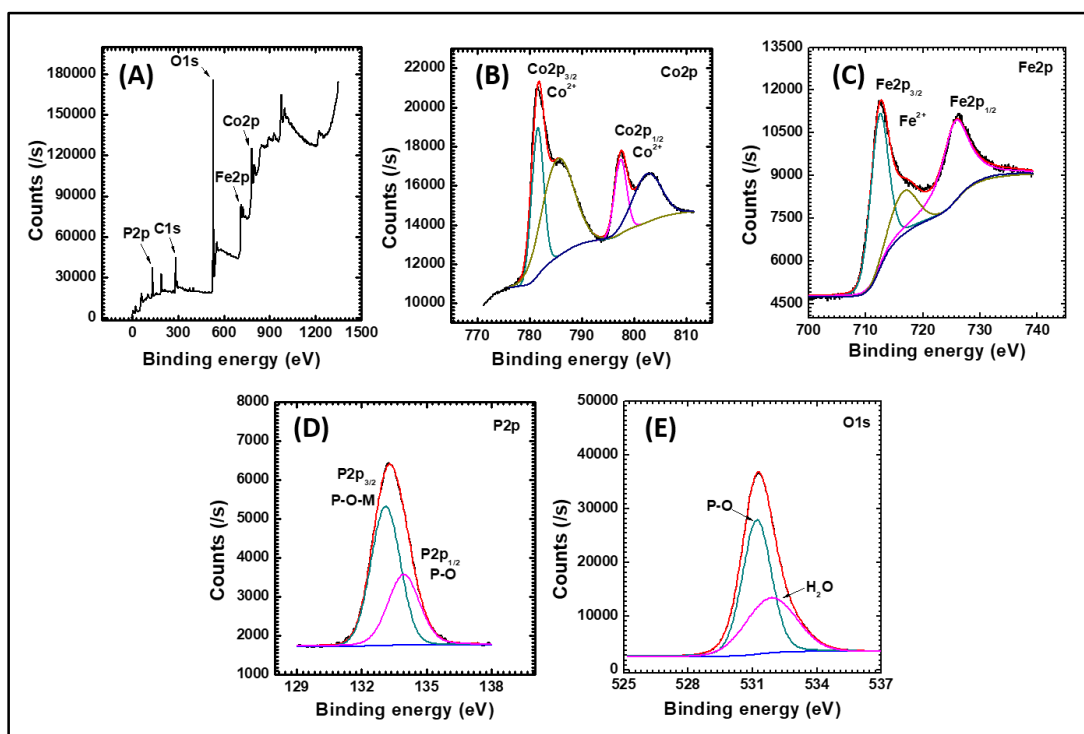


Figure 4.5: XPS spectra of CFP-S2 sample (A) survey spectrum, high resolution spectra of (B) Co2p, (C) Fe2p, (D) P2p, and (E) O1s.

It is confirmed from peak positions that Co^{2+} electronic state of Co element [14]. Also, the major peaks of $\text{Fe}2p_{3/2}$ situated at 712.21 eV and $\text{Fe}2p_{1/2}$ situated at 725.66 eV (**Figure 4.5(C)**). It ascertains that the occurrence of Fe at Fe^{2+} electronic state in the prepared material [15,16]. The high resolution XPS spectrum of P2p region is shown in **Figure 4.5(D)**. In this region, only one intense peak is observed at 133.10 eV represents P-O-M bonding and peak at 133.9 eV represents P-O bonding and pentavalent state of the phosphorus [17-19]. The O1s prominent peak is made up of three separate peaks situated at 529.56, 531.18 and 532.14 eV and given in **Figure 4.5(E)**. Deconvoluted peaks (529.58 and 530.98 eV) reveal the M-O and P-O bonding corresponds to phosphate and the peak at 531.78 eV associated to the surface adsorbed water molecules [11,20]. It confirms that, a successful preparation of cobalt-iron phosphate using SILAR method.

4.2.A.3.5 Surface morphological and elemental analysis: Surface morphological analysis of cobalt-iron phosphate thin films was studied by FESEM and shown in **Figure 4.6**. Images at different magnifications for all thin film samples showed that, as the

composition varies from cobalt phosphate (CFP-S1) to iron phosphate (CFP-S5), the topography of the materials varies from agglomerated nanoparticles to well dispersed nanoparticles and again agglomerated spherical nanoparticles.

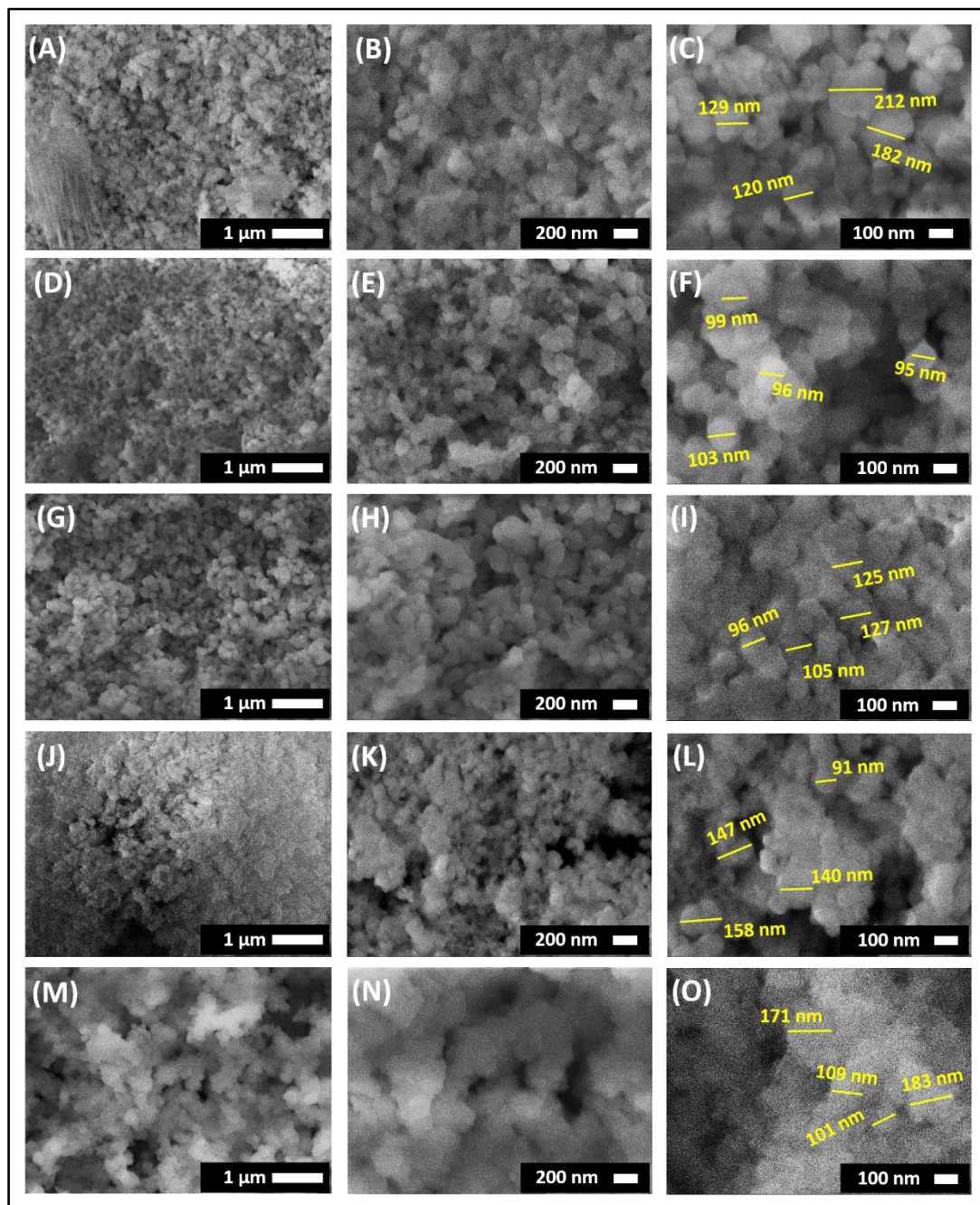


Figure 4.6: FESEM images at different magnifications (20 kX, 50 kX, and 100 kX) of (A-C) CFP-S1, (D-F) CFP-S2, (G-I) CFP-S3, (J-L) CFP-S4, and (M-O) CFP-S5.

The average particle size of CFP-S1 sample is around 160 nm, for CFP-S2 sample, it is around 98 nm. Further, for CFP-S3 sample particle size is around 113 nm, for CFP-S4

and CFP-S5, it is around 134 nm and 141 nm, respectively. It is observed that, due to the agglomeration, the particle size goes on increasing. The nanospheres are irregularly arranged over the surface forming wide porous thin films. Such a nanospherical surface morphology may offer high surface area and thus huge number of electrochemical active locations for water molecule adsorption and oxidation. The study of chemical compositional analysis made with the help of EDS analysis associated with FESEM. The as prepared materials were EDS characterized as plotted in **Figure 4.7** and their atomic percentages were tabulated in **Table 4.2**.

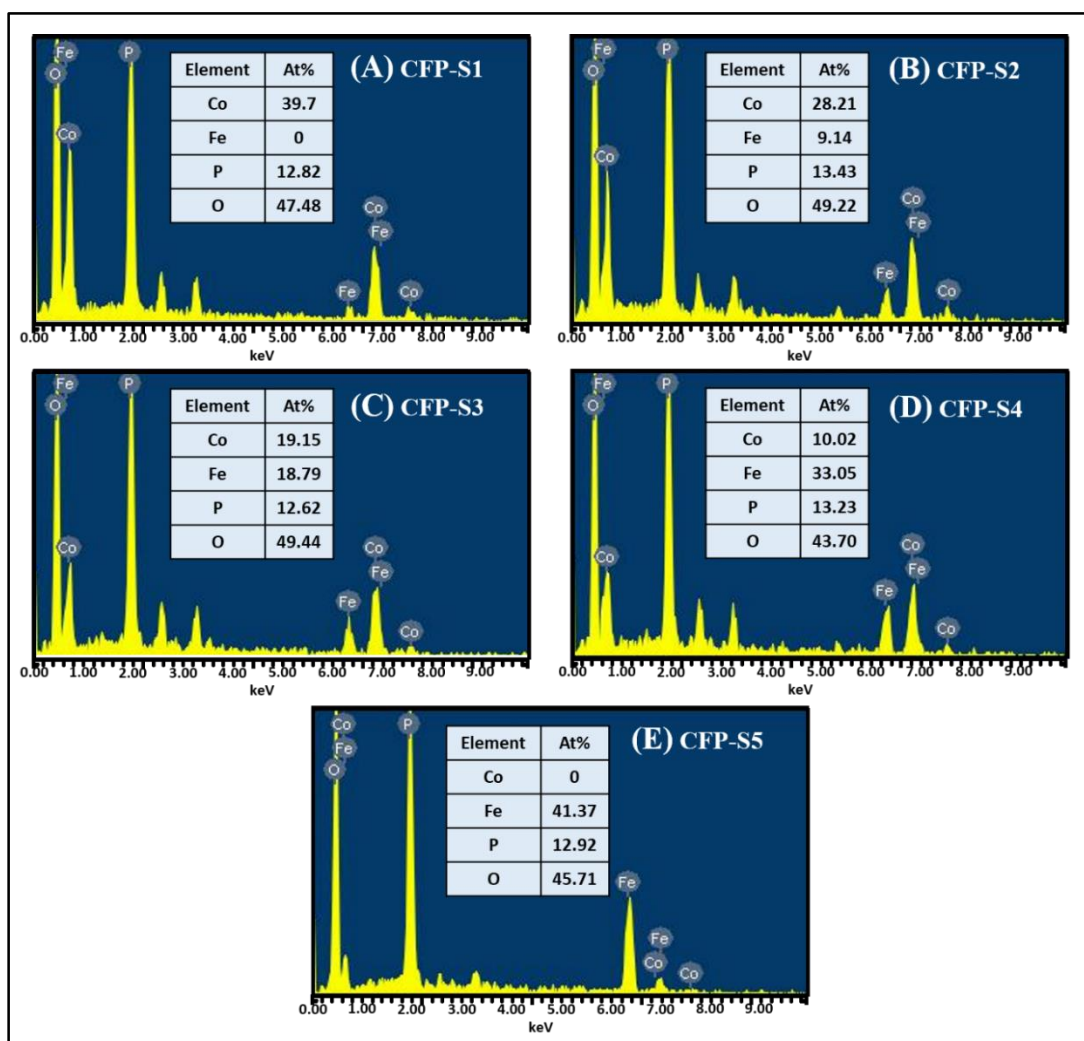


Figure 4.7: EDS spectra of cobalt-iron phosphate catalysts (A) CFP-S1, (B) CFP-S2, (C) CFP-S3, (D) CFP-S4, and (E) CFP-S5.

Form EDS spectra analysis, it is evidenced that the cobalt-iron phosphate consisted of cobalt, iron, phosphorus, and oxygen elements. The atomic percentage ratios of cobalt

to iron are 100 : 0, 75.52 : 24.28, 50.47 : 49.53, 23.26 : 76.74, and 0 : 100 for CFP-S1, CFP-S2, CFP-S3, CFP-S4, and CFP-S5, respectively.

Table 4.2: Experimental and observed cobalt and iron atomic ratio with obtained phases of cobalt-iron phosphate thin film samples.

Sample name	Experimental ratio (Co : Fe)	Observed ratio (Co : Fe)	Obtained phase
CFP-S1	100 : 0	100 : 0	$\text{Co}_3(\text{PO}_4)_2 \cdot \text{H}_2\text{O}$
CFP-S2	75 : 25	75.52 : 24.48	$\text{Co}_{2.25}\text{Fe}_{0.75}(\text{PO}_4)_2 \cdot \text{H}_2\text{O}$
CFP-S3	50 : 50	50.47 : 49.53	$\text{Co}_{1.5}\text{Fe}_{1.5}(\text{PO}_4)_2 \cdot \text{H}_2\text{O}$
CFP-S4	25 : 75	23.26 : 76.74	$\text{Co}_{0.75}\text{Fe}_{2.25}(\text{PO}_4)_2 \cdot \text{H}_2\text{O}$
CFP-S5	0 : 100	0 : 100	$\text{Fe}_3(\text{PO}_4)_2 \cdot \text{H}_2\text{O}$

In all samples P and O are in 1:4 proportion which confirms the formation of phosphate (PO_4^{3-}) rather than pyrophosphate ($\text{P}_2\text{O}_7^{4-}$) or triphosphate ($\text{P}_3\text{O}_{10}^{5-}$). As shown in **Table 4.2**, as per the synthesis ratio, the atomic percentage of cobalt in the prepared material decreases and atomic percentage of iron increases. The observed atomic ratios are very close to the experimental molar ratios of the materials.

4.2.A.3.6 N_2 adsorption-desorption isotherm analysis: The N_2 adsorption-desorption isotherm and BJH methods were used to study the surface area, pore structure and pore size distribution of the cobalt phosphate (CFP-S1), cobalt-iron phosphate (CFP-S2), and iron phosphate (CFP-S5) samples and shown in **Figure 4.8**. The adsorption-desorption isotherms of the samples are of BET category of type-IV isotherm profiles having mesoporosity showing large adsorption energy (**Figure 4.8(A)**) [21]. The specific surface area measured from the BET isotherms and have the values of surface areas as 25.63 m^2/g , 29.12 m^2/g , and 12.7 m^2/g for the samples CFP-S1 (cobalt phosphate), CFP-S2 (cobalt-iron phosphate), and CFP-S5 (iron phosphate). This result underscores the usefulness of addition of iron into the cobalt in the increasing the surface area of the material. The lower values of the surface area for CFP-S1 and CFP-S5 samples can be attributed to the observed dependence of surface area on the uneven overgrowth into a particle size distribution. The pore size distribution of the catalysts can be evaluated from BJH method as shown in **Figure 4.8(B)**.

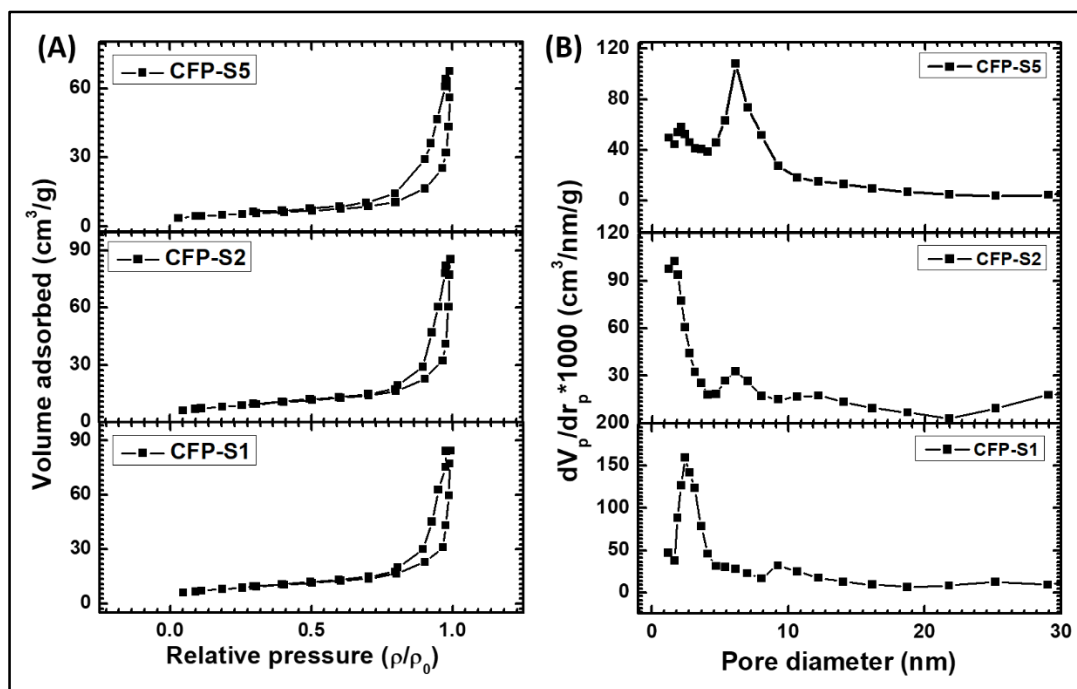


Figure 4.8: (A) N₂ adsorption/desorption isotherms (BET) and (B) pore size distribution (BJH) curves of SILAR prepared cobalt-iron phosphate thin films (CFP-S1, CFP-S2, and CFP-S5).

It demonstrates the pore sizes of the samples ranges from 1 to 10 nm, confirming the mesoporous to microporous structure of the active materials. The average pore size of cobalt phosphate (CFP-S1) is 2.42 nm and of iron phosphate (CFP-S5), it is 6.11 nm. Further, for the cobalt-iron phosphate (CFP-S2), the average pore size is 1.66 nm. The large specific surface area and small pore size may be beneficial to the electrolyte-electrode interface area, and huge number of electroactive sites for the –OH species adsorption and also mass transfer, which leads to enhanced electrochemical properties of the material.

4.2.A.3.7 Electrochemical catalytic performance analysis: Atomic percentages of cobalt and iron were optimized to choose the best catalyst since metals like cobalt and iron may influence the electrochemical catalytic performance of the materials. Aiming to confirm the hypothesis, analysis of electrocatalytic oxygen and hydrogen evolution was carried out. Electrochemical water splitting tests of thin films of cobalt phosphate (CFP-S1), cobalt-iron phosphate (CFP-S2, CFP-S3, CFP-S4) and iron phosphate (CFP-S5) materials were performed in terms of OER and HER in 1 M KOH and 1 M H₃PO₄ electrolytes, respectively.

i) ECSA analysis: Prior to electrocatalysis study in terms of OER and HER, measurement of ECSA of the materials is necessary. ECSA is directly associated to C_{dl} of the material. In order to measure C_{dl} for each electrode, CV curves were recorded in the small potential range where Faradic reactions are absent. CV curves of the electrodes recorded at different scan rates were plotted in **Figure 4.9(A-E)**. C_{dl} is calculated by plotting the anodic charging currents (i_c) of each CV curve against the scan rate. It yields a straight line with slope equals to C_{dl} as shown in **Figure 4.9(F)**.

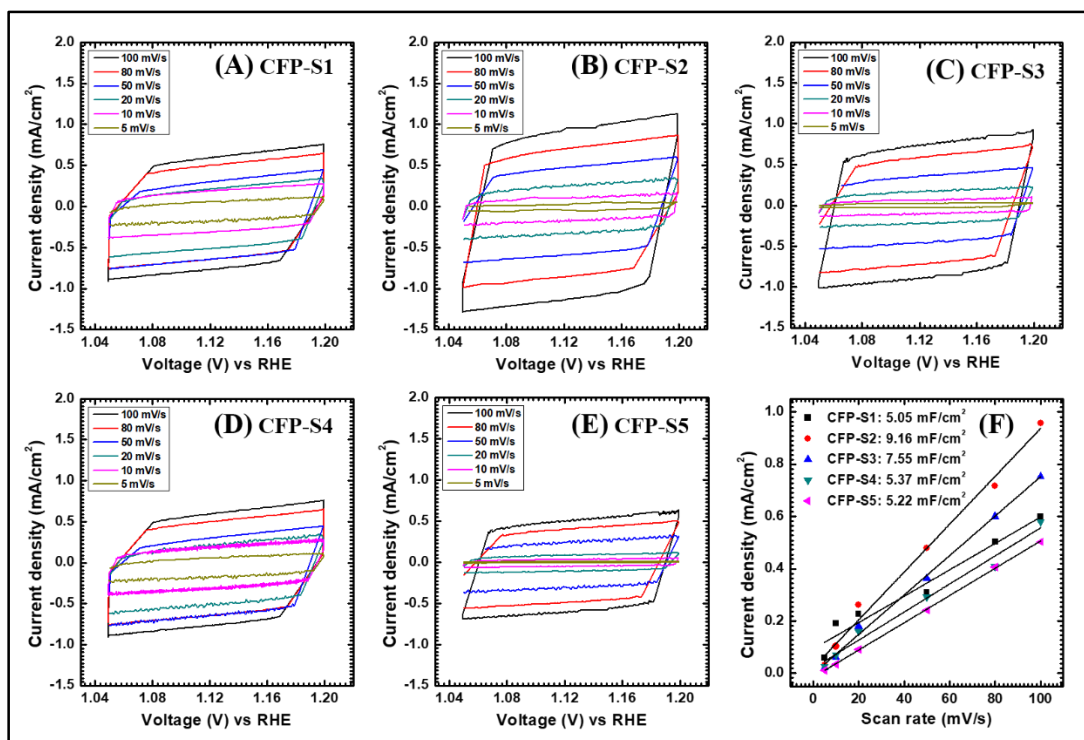


Figure 4.9: The CV curves of (A) CFP-S1, (B) CFP-S2, (C) CFP-S3, (D) CFP-S4, and (E) CFP-S5 at various scan rates in a small potential window (1.05 - 1.2 V vs. RHE), and (F) their anodic current linear fit for C_{dl} values.

The values of C_{dl} are 5.05, 9.16, 7.55, 5.37, and 5.22 mF for CFP-S1, CFP-S2, CFP-S3, CFP-S4, and CFP-S5 thin film electrodes, respectively. The corresponding ECSA are 126.25, 229, 188.75, 134.25, and 130.5 cm² for CFP-S1, CFP-S2, CFP-S3, CFP-S4, and CFP-S5 electrodes, respectively. The present comparison clarifies that, the highest ECSA calculated is 229 cm² for CFP-S2 electrode. The electrocatalytic interface texture, that is the RF calculated by dividing the ECSA with the geometric area of the electrode in contact with electrolyte. Here to measure electrochemical activity, the 1 cm² area of the film is used. Hence the RF are 126.25, 229, 188.75, 134.25, and 130.5 for CFP-S1, CFP-S2, CFP-

S3, CFP-S4, and CFP-S5 electrodes, respectively. The comparatively high RF shows the large number of electrocatalytic sites for exposing with electrolyte. The sample CFP-S2 demonstrate very high ECSA and RF than the others are consistent with the BET surface analysis.

ii) OER analysis: The electrochemical OER was studied by the LSV recorded of the prepared materials in the potential range 1.05 to 1.75 V vs. RHE at 1 mV/s scan rate as shown in **Figure 4.10(A)**.

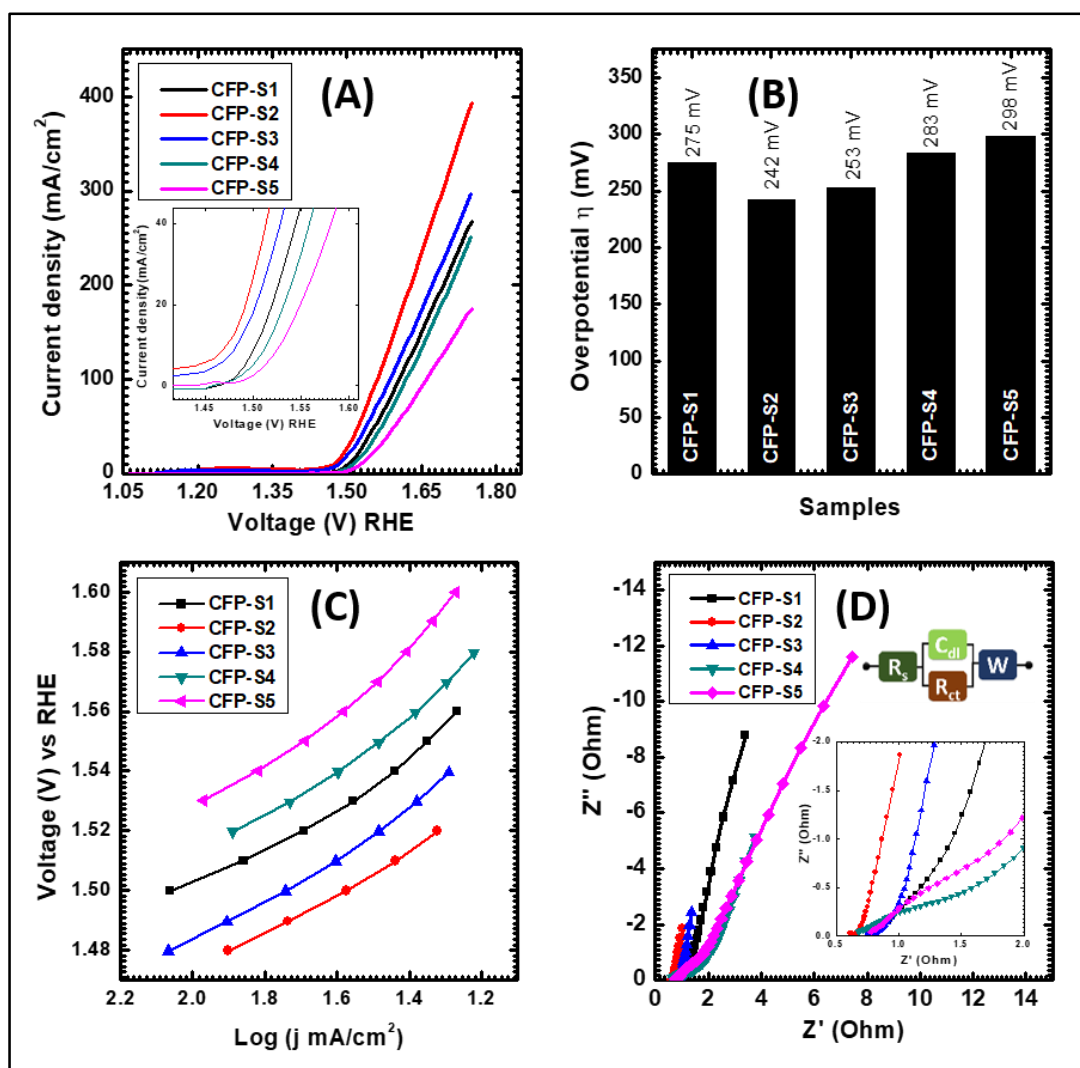


Figure 4.10: Electrochemical OER analysis (A) LSV polarization curves, (B) comparative bar diagram of overpotentials, (C) Tafel plots, (D) EIS of the cobalt-iron phosphate catalysts (CFP-S1, CFP-S2, CFP-S3, CFP-S4, and CFP-S5).

It is observed that, the nature of the all LSV polarization curves is similar and continuous rise of current density with rise in potential. Also, it is confirmed that the sample

CFP-S2 is most electrochemically active and requires lowest overpotential of 242 mV to achieve the current density of 10 mA/cm² proposing outstanding catalyst for oxygen evolution. In distinction, other materials CFP-S1 (275 mV), CFP-S3 (253 mV), CFP-S4 (283 mV) and CFP-S5 (298 mV) demonstrated considerably high overpotentials to reach the current density of 10 mA/cm² as shown by bar diagram in **Figure 4.10(B)**. The O₂ molecule development at the catalyst surface is capable only when the catalyst has greater OH⁻ ion attraction to sorb at the surface and to make an intermediary state. When those intermediate states development is more rapidly, then these reaction steps are rate determining. The reaction rate kinetics were determined by the Tafel slope as shown in **Figure 4.10(C)**.

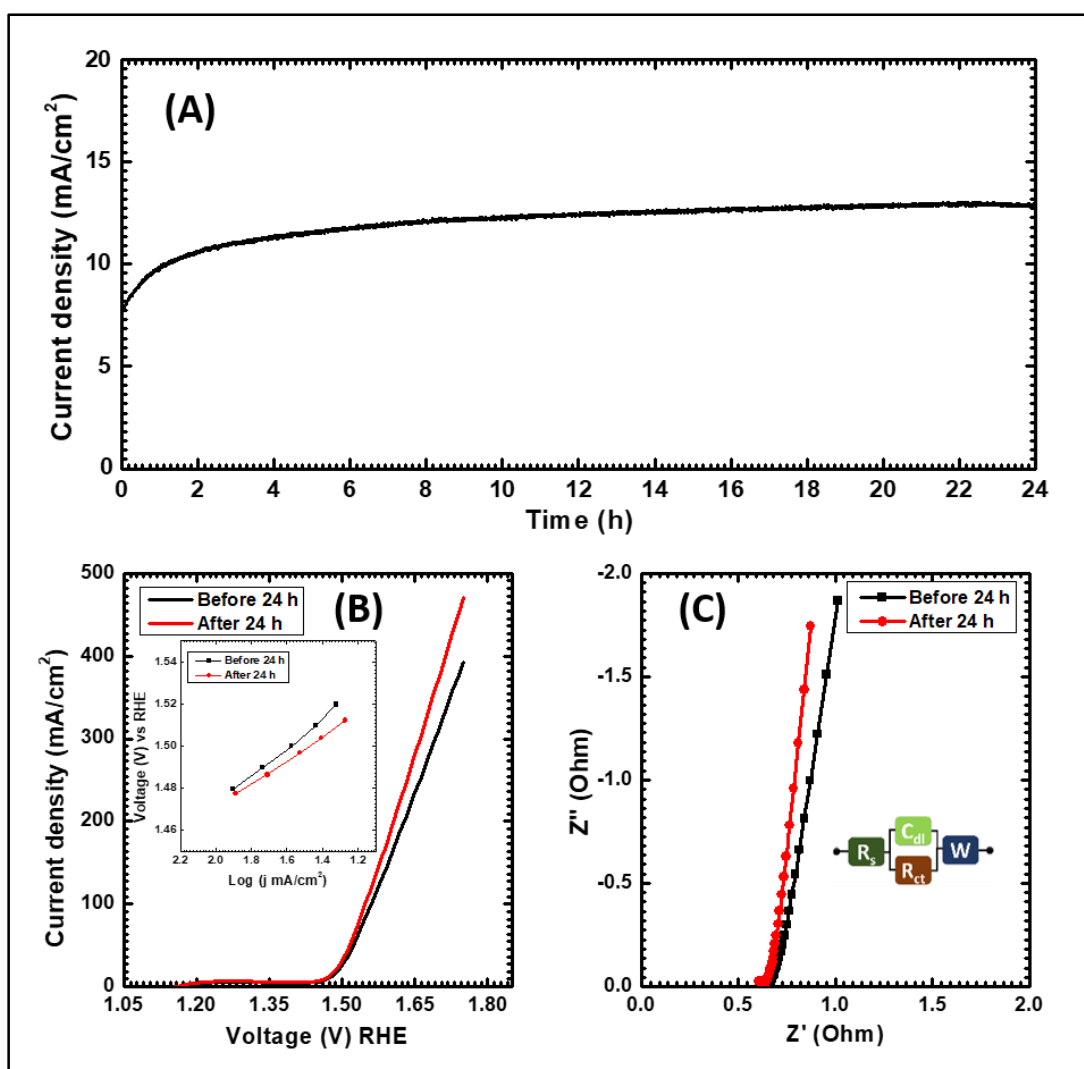


Figure 4.11: (A) CA (I-t) curve for OER stability, (B) LSV before and after 24 h OER catalysis, and (C) EIS after 24 h catalysis of cobalt-iron phosphate (CFP-S2) thin film electrode.

It reveals the Tafel slope of 38.33 mV/dec for the electrode CFP-S2 is lower than 44.73 mV/dec (CFP-S1), 46.11 mV/dec (CFP-S3), 59.52 mV/dec (CFP-S4), and 69.73 mV/dec (CFP-S5). It confirms that, highly efficient reaction kinetics at CFP-S2 electrode surface and the OER reaction process is faster which is favorable for O₂ generation. The EIS plot has shown that, there is much smaller R_{ct} of CFP-S2 electrode (**Figure 4.10(D)**). The fitted R_{ct} values are 0.89, 0.047, 0.43, 1.42, and 1.94 Ω for CFP-S1, CFP-S2, CFP-S3, CFP-S4, and CFP-S5 electrodes, respectively. It reveals that, easy charge transfer process is one of the reason for low overpotential.

Catalytic stability is vital measures to declare the electrode material as a good electrocatalyst for OER or HER. The CA test at overpotential was further studied of the best performing material (CFP-S2) for 24 h. The material was initially going to activate continuously hence, current density increased at initial stage and it remains stable up to 24 h, as shown in **Figure 4.11(A)**. Within the catalysis process, material become catalytically more active and shows improved performance. The LSV plot comparative of before and after 24 h catalysis is shown in **Figure 4.11(B)**, which unveils that overpotential decreases from 242 to 237 mV and current density increases rapidly at higher potential. Inset figure shows that Tafel slope changes from 38.33 to 34.78 mV/dec after catalytic stability. The EIS was performed after stability test and it is observed that, the R_{ct} decreases from 0.047 Ω to 0.034 Ω (**Figure 4.11(C)**). The fitted EIS parameters are tabulated in **Table 4.3**. The catalytic stability test reveals that, the SILAR synthesized cobalt-iron phosphate thin film electrode show enhanced and stable electrocatalytic performance.

iii) HER analysis: The polarization curves were recorded in the potential window of 0.33 to -0.65 V vs RHE to study HER in 1 M H₃PO₄ solution bath as shown in **Figure 4.12(A)**. The nature of the all LSV polarization curves is similar and continuous increase in current density. The overpotentials measured at 10 mA/cm² current density as 95.7, 67.9, 121.8, 177.4, and 220.9 mV for CFP-S1, CFP-S2, CFP-S3, CFP-S4, and CFP-S5 electrodes, respectively. It is observed that, to deliver 10 mA/cm² current density, CFP-S2 electrode required lowest overpotential of 67.9 mV. The trend of overpotential is shown in **Figure 4.12(B)** by bar diagram. The rate determining kinetics was studied by plotting Tafel slope to evaluate faster HER. The Tafel slopes for cobalt phosphate (CFP-S1) and iron phosphate (CFP-S5) are higher (**Figure 4.12(C)**), on the other hand, the synergy between cobalt and iron enhances the catalytic reaction.

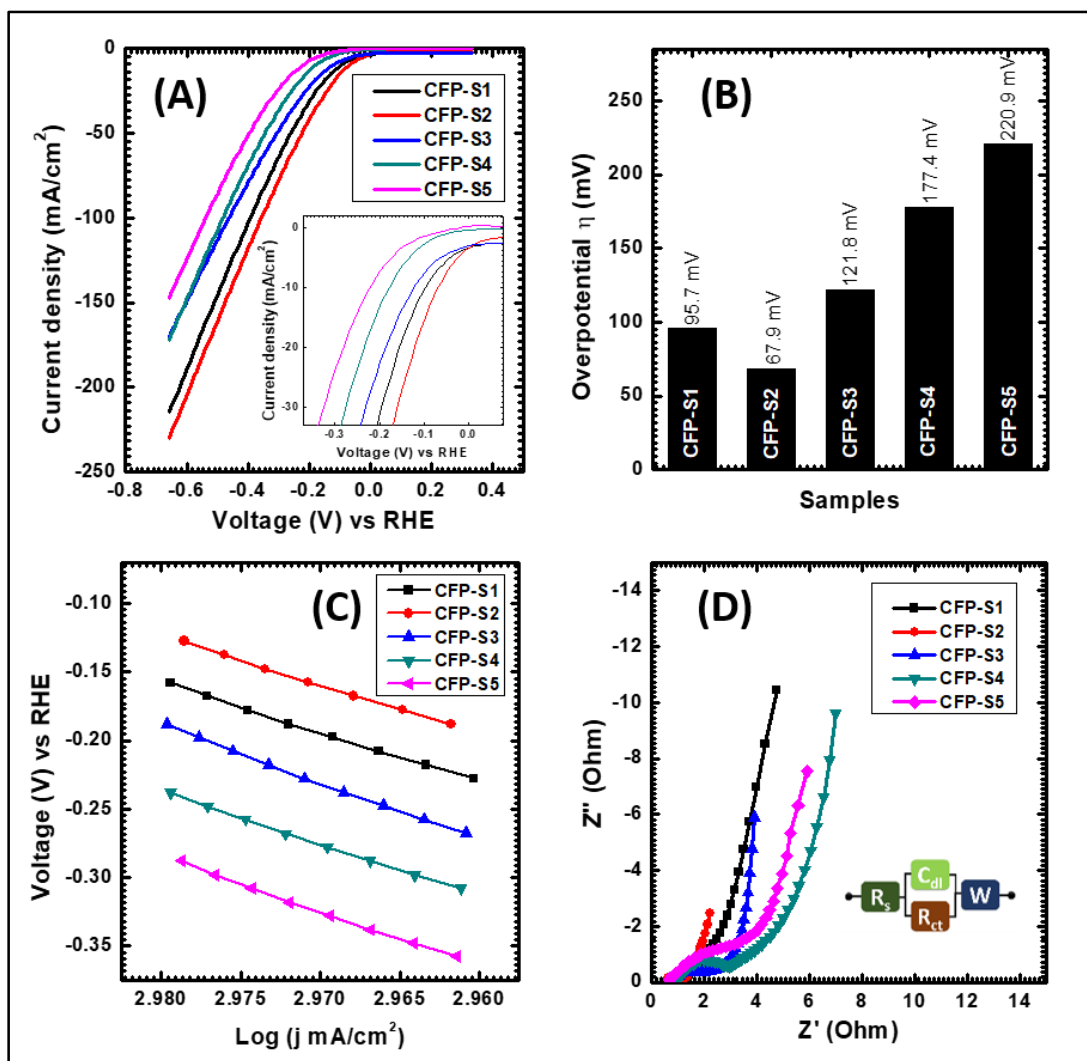


Figure 4.12: Electrochemical HER analysis: (A) LSV polarization curves, (B) comparative bar diagram of overpotentials, (C) Tafel plots, (D) EIS of cobalt-iron phosphate catalysts (CFP-S1, CFP-S2, CFP-S3, CFP-S4, and CFP-S5).

The Tafel slope for CFP-S1, CFP-S2, CFP-S3, CFP-S4, and CFP-S5 electrodes are 36.47, 35.92, 38.23, 42.26, and 40.20 mV/dec, respectively. It reveals that, the incorporation of iron up to particular extent helps to decrease the reaction potential. Besides, the R_{ct} relevant to EIS spectra of CFP-S1, CFP-S2, CFP-S3, CFP-S4, and CFP-S5 electrodes measured at OCP were compared in **Figure 4.12(D)**. The fitted R_{ct} values are 0.806, 0.589, 1.168, 2.354, and 4.273 Ω for CFP-S1, CFP-S2, CFP-S3, CFP-S4, and CFP-S5 electrodes, respectively. As expected, the CFP-S2 exhibited a small interfacial charge-transfer resistance and faster reaction rate.

Catalytic stability of best catalyst electrode (CFP-S2) was performed by CA at overpotential for 24 h. As shown in **Figure 4.13(A)**, it is observed that, after 24 h, material

become much active and delivered enhanced current density. Before and after the HER catalysis, the performances were compared by LSV curves. It is observed that, overpotential decreased after 24 h catalysis from 67.9 to 48.9 mV (**Figure 4.13(B)**). The comparative plot of Tafel slope (inset of **Figure 4.13(B)**) reveals the slope decreases to 32.56 mV/dec signifying that HER process happens earlier after 24 h catalysis.

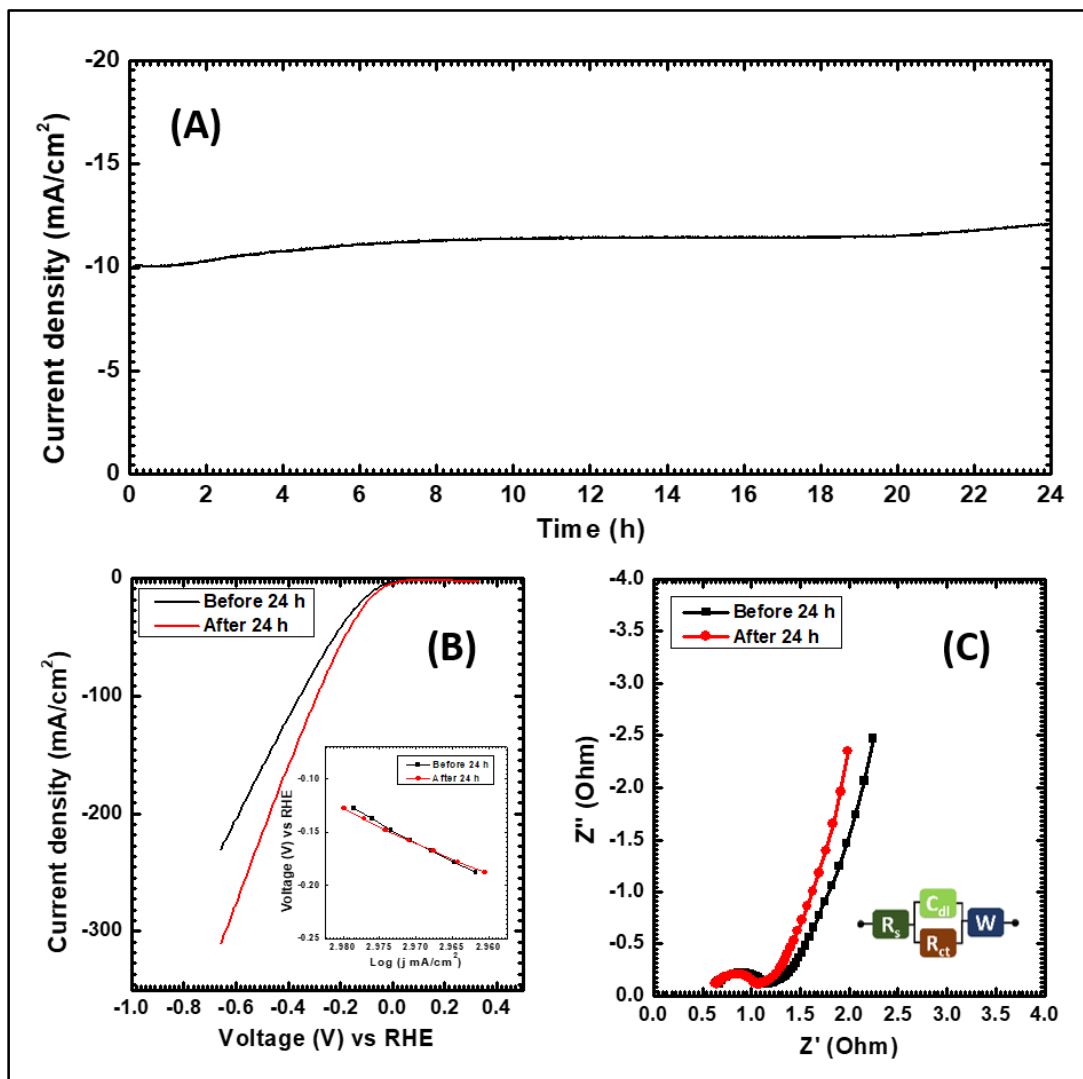


Figure 4.13: (A) CA (I-t) curve for HER stability, (B) LSV before and after 24 h HER catalysis, and (C) EIS after 24 h catalysis of cobalt-iron phosphate (CFP-S2) thin film electrode.

Fitted EIS curves before and after stability test shows that the R_{ct} decreased from 0.589 to 0.492 Ω after 24 h catalysis which is predictable for the enhancement in performance (**Figure 4.13(C)**). Electrochemical HER before and after 24 h catalysis

analysis is tabulated in **Table 4.3**. It is concluded that, the SILAR synthesized cobalt-iron phosphate thin film electrode show enhanced and stable electrocatalytic performance.

Table 4.3: Electrochemical OER and HER analysis before and after 24 h catalytic stability study.

	Test	Overpotential η (mV) at 10 mA/cm ²	Tafel slope (mV/dec)	R _s (Ω)	R _{ct} (Ω)	W (Ω)
Before stability	OER	242	38.33	0.610	0.047	0.21
After stability		237	34.78	0.607	0.034	0.18
Before stability	HER	67.9	35.92	0.644	0.589	0.29
After stability		48.9	32.56	0.628	0.492	0.27

4.3 Conclusions: The cobalt-iron phosphate thin films were deposited using the superficial SILAR method on SS substrates at room temperature. The prepared thin films were characterized physico-chemically. The XRD analysis confirmed the amorphous nature of SILAR deposited materials. Formation of cobalt-iron phosphate ($\text{Co}_x\text{Fe}_{3-x}(\text{PO}_4)_2 \cdot \text{H}_2\text{O}$) was confirmed by the elemental analysis, molecular bond formation and presence of electronic states in material. The as synthesized cobalt-iron phosphate electrodes at different compositions showed excellent electrochemical splitting of water in the forms of OER and HER. The outstanding performance of CFP-S2 thin film material catalyst showed lowest overpotential of 242 mV to attain the current density of 10 mA/cm² with Tafel slope 38.33 mV/dec for OER and enhanced catalytic OER stability with overpotential of 237 mV to attain the current density of 10 mA/cm² for 24 h in alkaline solution bath. Similarly, the HER requires 67.9 mV overpotential to attain current density of 10 mA/cm² with 35.92 mV/dec Tafel slope. After HER catalytic stability of 24 h in acidic medium, it is observed that the overpotential reduced to 48.9 mV. As a benchmark, the overpotentials for OER and HER to attain current density of 10 mA/cm², corresponding Tafel slopes and stability study were comparative to the formerly published cobalt-iron phosphate catalyst materials

[1,5,8,22,23], which confirms the outstanding performance of present investigation. The outstanding performances for OER and HER before and after catalysis with enhanced stability can be attributed to the amorphous nature of the material, synergistic effect of both the metals (Co and Fe), improved electronic conduction and metal-to-metal partial charge transfer process. Moreover, cobalt-iron phosphate increases the adsorption of OH⁻ ions at the surface of electrode with the decrease of adsorption energy of the surface by altering the surface electronic states.

4.4 Section-B: SILAR synthesis of cobalt-iron phosphate/reduced graphene oxide and their characterization for electrochemical OER and HER

4.4.B.1 Introduction: Graphene and its derivatives can be one promising solution as conducting scaffold for hybrid materials with the aforementioned electrocatalysts owing to their exotic structure and unique physical properties. The synthetic pathway of rGO enables the construction of composite materials via various chemical redox routes because the dispersion of GO is easily accomplished in a various range of solvents, facilitating the hybridization with electroactive materials [24]. In recent years, a number of publications have been reported about the application of rGO in electrochemical energy conversion reactions. Various hybrid materials have been studied till date such as, transition metal sulfides (MoS₂, WS₂, FeNiS₂) [25,26], transition metal phosphide (NiP, CoP, FeP) [27-29], transition metal carbides (TaC, Fe₃W₃C) [30,31], etc. Till date only one report is available on the cobalt-iron phosphate hybridized with rGO [6]. In the present investigation, by the facile SILAR method, cobalt-iron phosphate/reduced graphene oxide materials were synthesized. In the present work, effect of change in concentration of rGO on physico-chemical properties, and their effect on electrochemical water splitting in the forms of OER and HER is studied. Meanwhile, pristine cobalt-iron phosphate and cobalt-iron phosphate/reduced graphene oxide hybrids at different concentrations (0.02 mg/ml, 0.04 mg/ml, 0.06 mg/ml, 0.08 mg/ml, and 0.1 mg/ml) are synthesized and compared their electrochemical study to investigate the best performing catalyst.

4.4.B.2 Experimental details

4.4.B.2.1 Synthesis of graphene oxide (GO): GO was synthesized by the Hummer's method [32], as discussed in chapter-3, section B, subsection 3.4.B.2.2.

4.4.B.2.2 Synthesis of cobalt-iron phosphate/reduced graphene oxide: SILAR is the facile and low cost method to deposit hybrid thin films. The cobalt-iron phosphate/reduced graphene oxide hybrid thin films were synthesized at room temperature and schematically represented in **Figure 4.14(A)**.

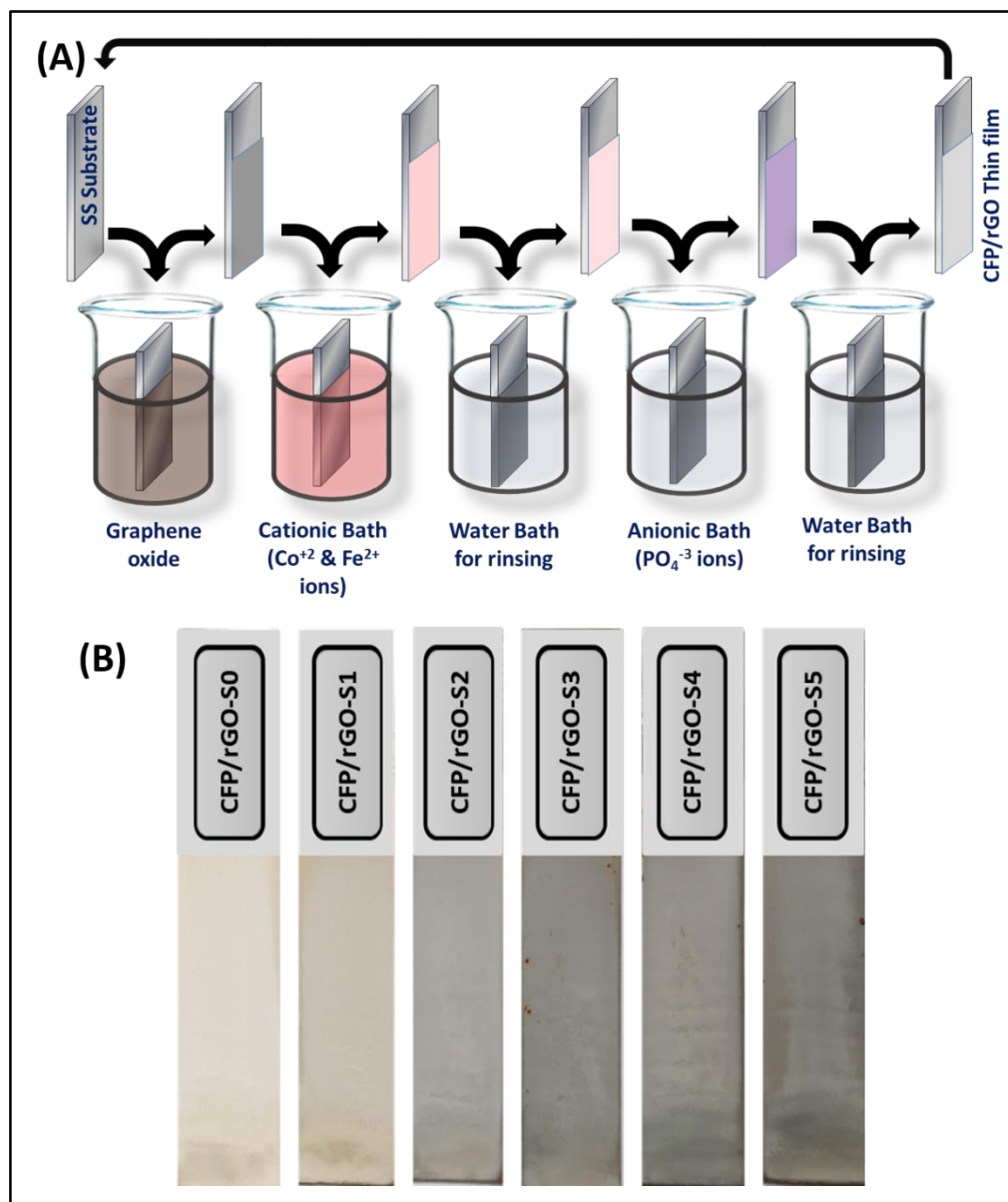


Figure 4.14: (A) Schematic representation of SILAR deposition of CFP/rGO thin films, (B) photograph of deposited thin films.

The discussion of the synthesis process of cobalt-iron phosphate thin films already given in **section A, subsection 4.2.A.2.2**. For the preparation of hybrid materials, the 50 ml beaker of GO was added prior to the cationic solution beaker. This completes five beaker system in sequence as GO solution, cationic precursor (Co^{2+} and Fe^{2+}) solution, DDW,

anionic precursor (PO_4^{3-}) solution, and DDW. The concentration of GO was varied as, 0, 0.02, 0.04, 0.06, 0.08 and 0.1 mg/ml. The substrate dipping time in GO solution was fixed for 10 s. The adsorption time (20 s), first rinsing time (10 s), reaction time (20 s) and second rinsing time (10 s) were optimized previously with the 50 cycles to get well adherent and uniform film. The synthesized cobalt-iron phosphate/reduced graphene oxide hybrid thin films were named as CFP/rGO-S0, CFP/rGO-S1, CFP/rGO-S2, CFP/rGO-S3, CFP/rGO-S4, and CFP/rGO-S5 as shown in **Figure 4.14(B)**. The mass loading per unit area calculated by mass difference method as shown in **Figure 4.15**.

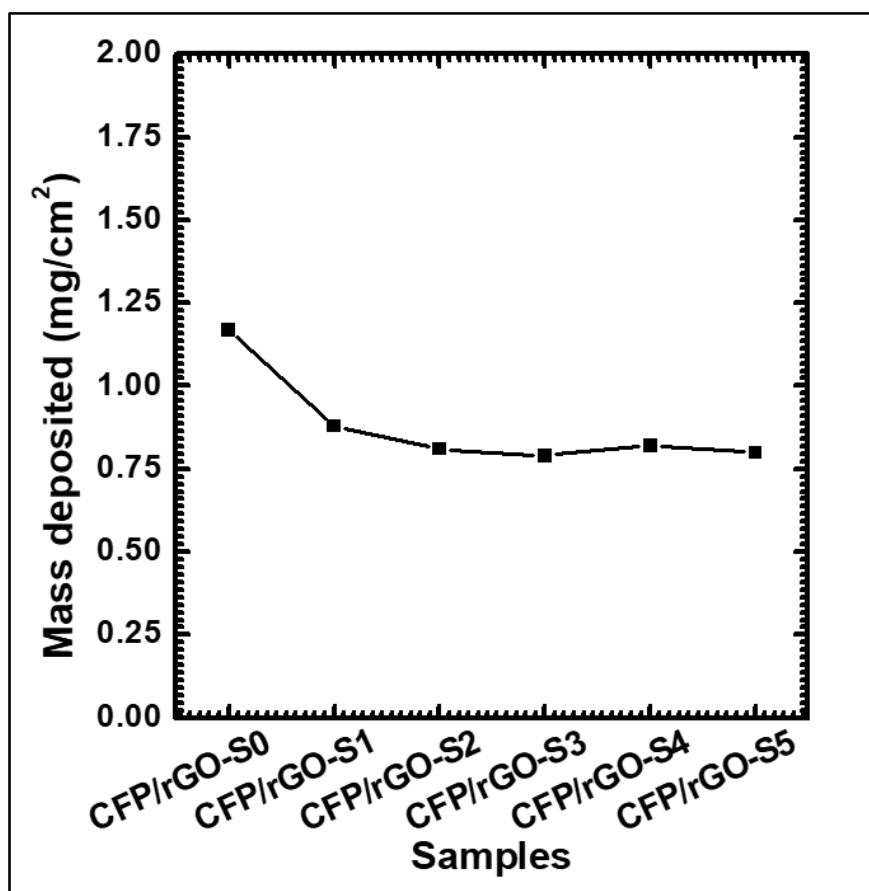


Figure 4.15: Mass loading per unit area of CFP/rGO-S series.

4.4.B.3 Results and discussion

4.4.B.3.1 XRD analysis: The XRD patterns of cobalt-iron phosphate/reduced graphene oxide hybrid materials with different concentrations of rGO were studied and shown in **Figure 4.16**. As previously observed in **section A, subsection 4.2.A.3.2**, the sample CFP-S2 showing amorphous nature, similarly, there are no peaks of the active catalyst material were observed and all the hybrids (CFP/rGO-S0, CFP/rGO-S1, CFP/rGO-S2, CFP/rGO-S3, CFP/rGO-S4, and CFP/rGO-S5) also show amorphous nature. Only, the broad hump

observed between $2\theta=22$ to 28° indicates multilayered rGO NSs of (0 0 2) planes formed due to stacking of GO sheets within the SILAR reaction [33].

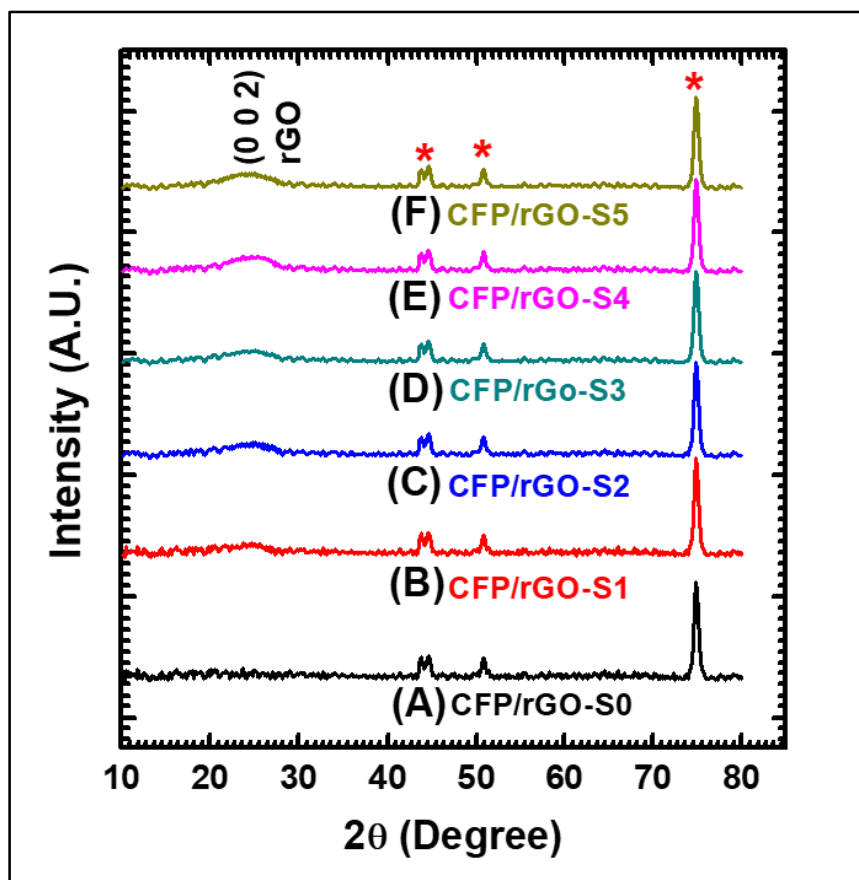


Figure 4.16: XRD patterns of cobalt-iron phosphate/reduced graphene oxide hybrid thin films.

4.4.B.3.2 FTIR analysis: By the FTIR spectroscopy, molecular bond formation in the SILAR prepared cobalt-iron phosphate/reduced graphene oxide thin films were identified. **Figure 4.17** shows the FTIR spectra from wavenumber 400 to 4000 /cm of SILAR prepared hybrid materials (CFP/rGO-S0, CFP/rGO-S1, CFP/rGO-S2, CFP/rGO-S3, CFP/rGO-S4, and CFP/rGO-S5). The absorption peaks observed at 570 /cm and 595 /cm are of PO_4 bond bending with symmetric and asymmetric vibrations, respectively. The small absorption on 773 /cm corresponds to Co-O lattice vibration mode [11]. The sharp absorption at 1035 /cm shows the asymmetric stretching vibrations of PO_4 [12]. The absorption bands of $-\text{COOH}$ symmetric stretching and C=C skeletal vibrations are observed at 1355 /cm, and 1600 /cm, respectively [34]. The high absorption band at 1631 /cm is due to the sp^2 hybridization (C=C) in rGO is confirmed. The large band of minute absorption at wavenumber 3450 /cm

shows the broad vibrational band of structural water molecules. FTIR results confirmed that, the successful hybridization of catalyst materials with rGO.

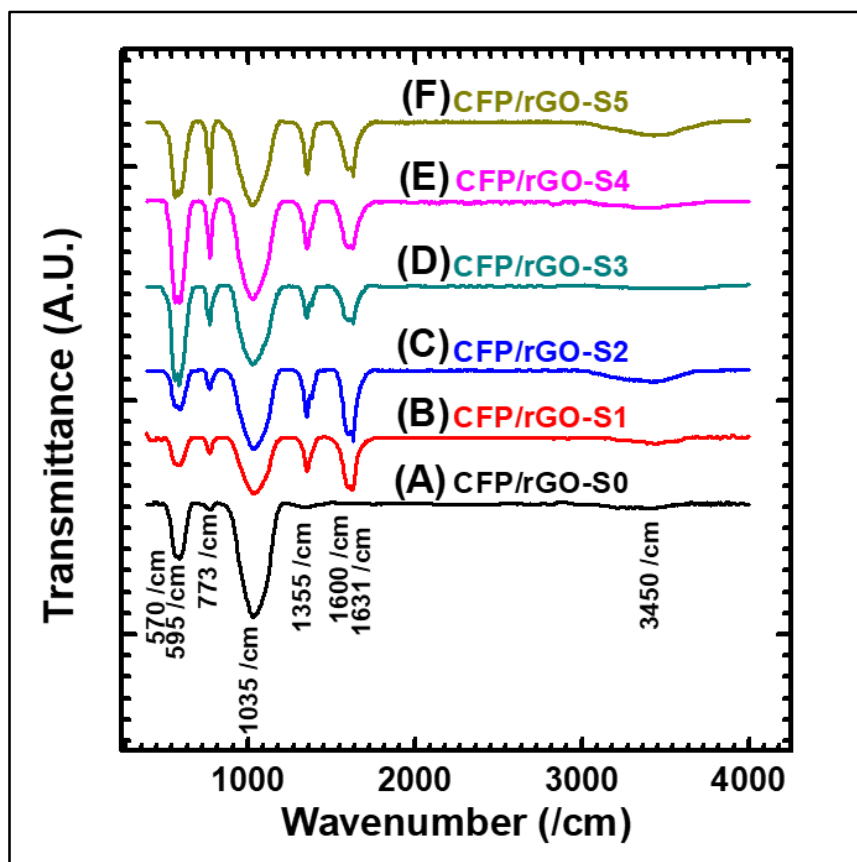


Figure 4.17: FTIR patterns of cobalt-iron phosphate/reduced graphene oxide hybrid thin films.

4.4.B.3.3 XPS analysis: From the survey spectrum, the presence of the Co, Fe, C, P, and O elements are confirmed in the cobalt-iron phosphate/reduced graphene oxide hybrid material (**Figure 4.18(A)**). Spectrum for each element can be resolved in their particular E_B range. There are two major peaks in the high resolution of cobalt (**Figure 4.18(B)**), at 781.7 eV and 797.4 eV along with two satellite peaks at 785.6 eV and 802.5 eV corresponding to $\text{Co}2p_{3/2}$ and $\text{Co}2p_{1/2}$, respectively, which confirms that the Co^{2+} electronic state of the observed Co element [14]. Similarly, the prominent peaks located at 712.0 and 724.9 eV are consisting with $\text{Fe}2p_{3/2}$ and $\text{Fe}2p_{1/2}$ in the high resolution spectrum of iron (**Figure 4.18(C)**), corresponding to Fe^{2+} state. Also, the peak of phosphorus is deconvoluted into the two peaks with $\text{P}2p_{3/2}$ at 132.9 eV accredited to the metal phosphate (P-O-M), and $\text{P}2p_{1/2}$ at 133.8 eV known as phosphate group (P-O) and consisting to P^{5+} oxidation state (**Figure 4.18(D)**) [18].

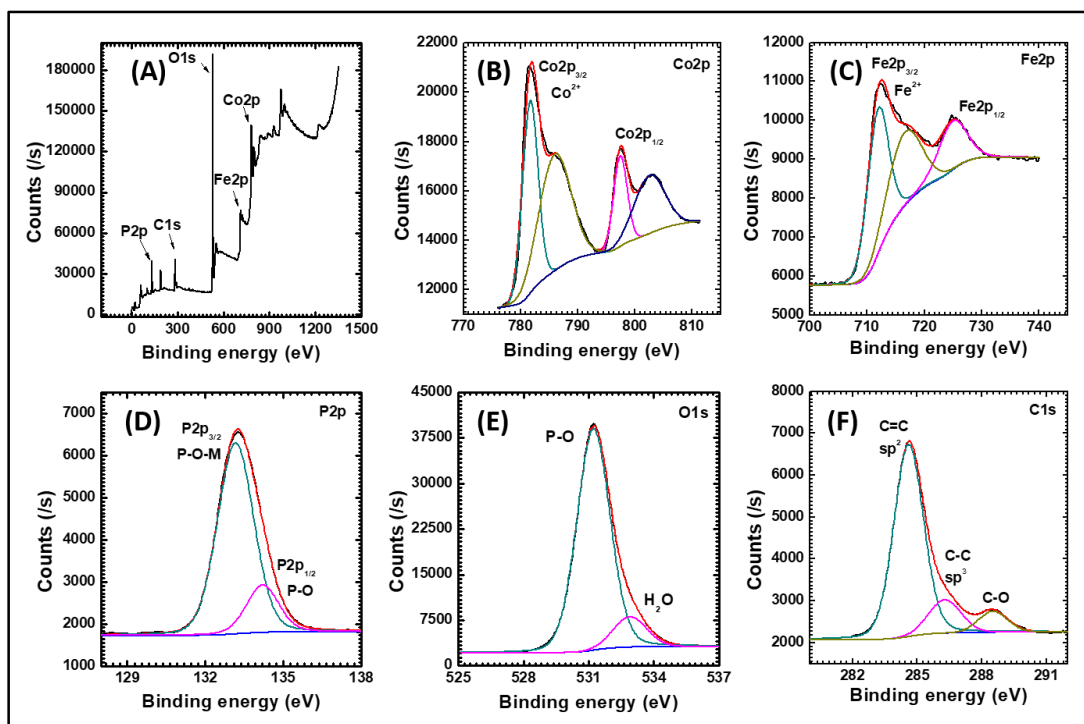


Figure 4.18: XPS spectra of CFP/rGO-S3 sample (A) survey spectrum, high resolution spectra of (B) Co2p, (C) Fe2p, (D) P2p, (E) O1s and (F) C1s.

In the spectrum of oxygen as presented in **Figure 4.18(E)**, the observed broad peak of oxygen is deconvoluted into two as 531.23 eV, and 532.83 eV, consisting of the P-O bonds in phosphate and the surface adsorbed water molecules. The intense peak at 284.7 eV is due to C=C in-plane bonding of sp^2 hybridization and out of plane bonding of sp^3 hybridized C-C at 286.3 eV is very short as compared to sp^2 hybridization as shown in **Figure 4.18(F)**. The carboxylate carbon (O-C=O) is observed at 288.5 eV [35]. High resolution XPS spectrum of carbon reveals that oxygen-containing groups have been less due to reduction of GO during the reaction. The present result confirms that, reduction of GO during the thin film deposition process.

4.4.B.3.4 Surface morphological and elemental analysis: The surface topography of SILAR synthesized cobalt-iron phosphate/reduced graphene oxide hybrid thin films are analyzed by FESEM micrographs as shown in **Figure 4.19**. It is observed that, spherical nanoparticles of cobalt-iron phosphate having size around 100 nm are covered the surface of the substrate (**Figure 4.19(A)**). The nanospheres are irregularly arranged over the surface forming wide porous thin films.

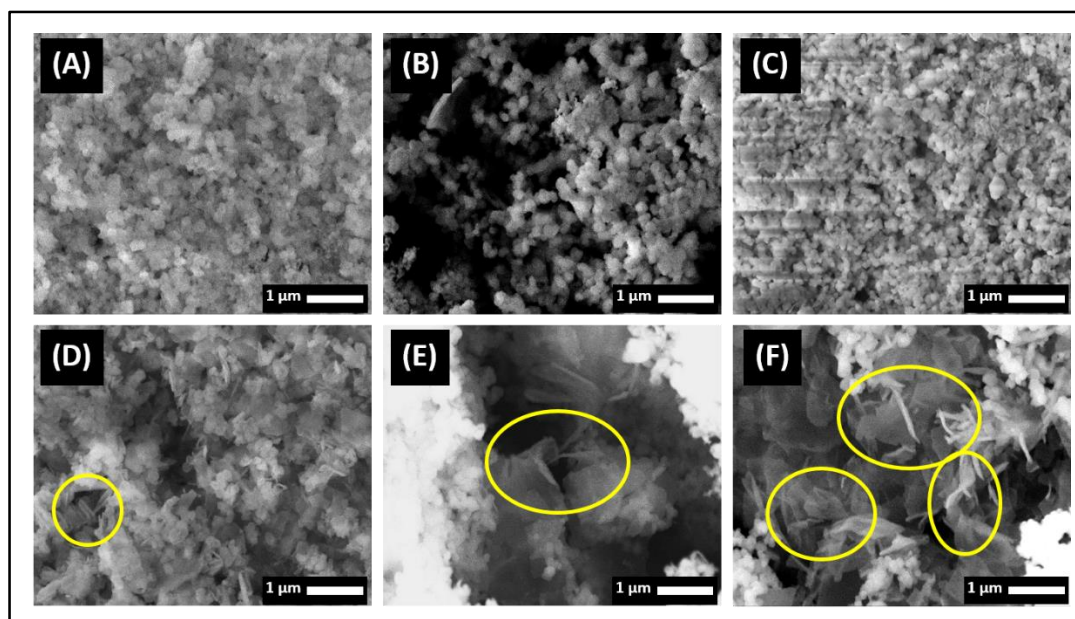


Figure 4.19: FESEM images at 20 kX magnification of (A) CFP/rGO-S0, (B) CFP/rGO-S1, (C) CFP/rGO-S2, (D) CFP/rGO-S3, (E) CFP/rGO-S4, and (F) CFP/rGO-S5.

As the content of GO introduced to the material, few NSs of rGO are observed (**Figure 4.19(B,C)**). For the sample CFP/rGO-S3, rGO NSs are well distributed throughout the material (**Figure 4.19(D)**). Upon further increase in the rGO concentration, there is the segregation of rGO due to excess amount (**Figure 4.19(E,F)**). Such a nanospherical cobalt-iron phosphate covered by the rGO NSs with well distribution, rGO nanosheets are highlighted by ovals. The hybrid surface morphology may offer huge surface area and hence more number of electrochemical active positions for water molecule adsorption and oxidation. The EDS analysis was studied further for the confirmation of presence of carbon element from the rGO.

Figure 4.20 shows the EDS spectra of the SILAR deposited thin film samples (CFP/rGO-S series) on SS substrates. It is evidenced that the cobalt-iron phosphate/reduced graphene oxide consisted of cobalt, iron, phosphorus, oxygen, and carbon elements. The observed At% of carbon in the as prepared samples are 0 %, 3.19 %, 5.37 %, 9.97 %, 12.42 % and 13.10 % for CFP/rGO-S0, CFP/rGO-S1, CFP/rGO-S2, CFP/rGO-S3, CFP/rGO-S4, and CFP/rGO-S5 hybrid thin films. The stoichiometric ratio of the cobalt to iron was maintained around 75:25 and for the phosphorous to oxygen was 20:80. The EDS analysis evidenced that the successful hybridization of cobalt-iron phosphate with the rGO nanosheets.

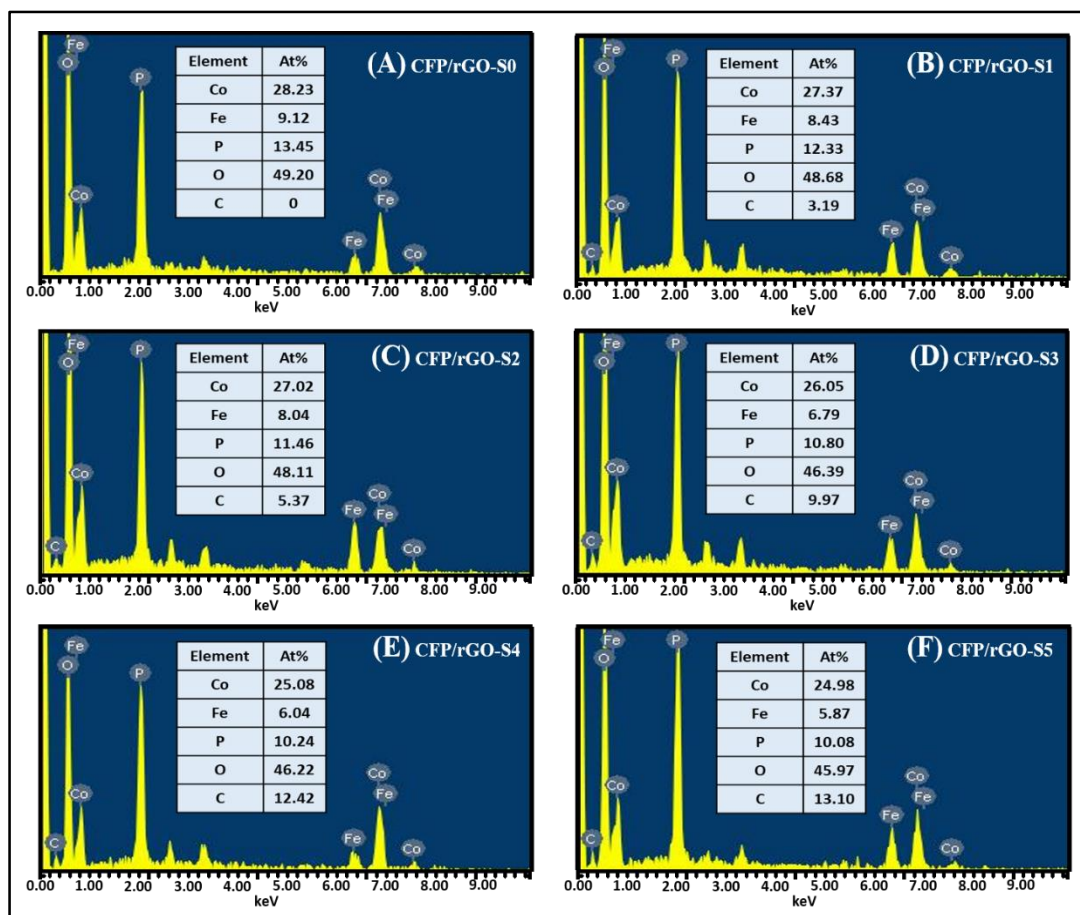


Figure 4.20: EDS spectra of cobalt-iron phosphate/reduced graphene oxide catalysts (A) CFP/rGO-S0, (B) CFP/rGO-S1, (C) CFP/rGO-S2, (D) CFP/rGO-S3, (E) CFP/rGO-S4, and (F) CFP/rGO-S5.

4.4.B.3.5 N₂ adsorption-desorption isotherm analysis: Pore size and surface area of the present CFP/rGO-S0, CFP/rGO-S1, CFP/rGO-S2, CFP/rGO-S3, CFP/rGO-S4, and CFP/rGO-S5 hybrids are investigated with N₂ adsorption-desorption isotherm measurements. The surface areas of the present hybrids are calculated based on the BET equation. BET with type-IV isotherm profiles of all the hybrid samples shown in **Figure 4.21**, which confirms all prepared materials have mesoporosity and large adsorption energy [21]. The specific surface area of pristine cobalt-iron phosphate (CFP/rGO-S0) is 29.14 m²/g and for the hybrids CFP/rGO-S1, CFP/rGO-S2, CFP/rGO-S3, CFP/rGO-S4, and CFP/rGO-S5 the values obtained are 39.64, 40.57, 56.55, 50.89, and 43.11 m²/g, respectively. It underscores that, the hybridization is useful for the enhancement of surface area.

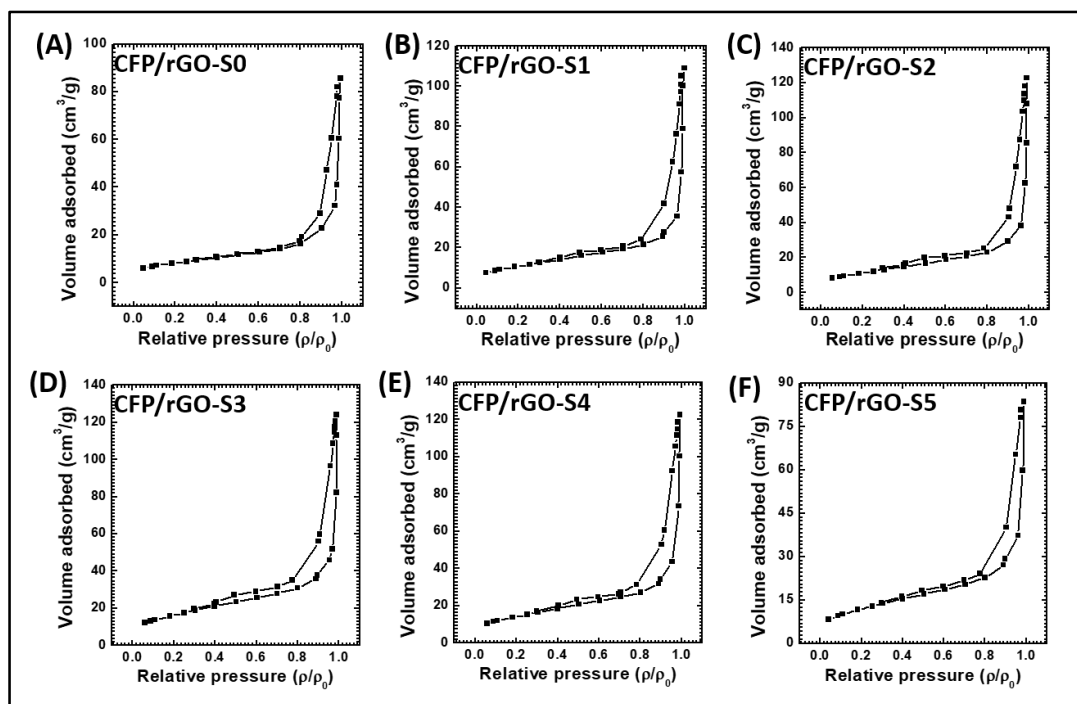


Figure 4.21: N₂ adsorption-desorption isotherms (BET) curves of (A) CFP/rGO-S0, (B) CFP/rGO-S1, (C) CFP/rGO-S2, (D) CFP/rGO-S3, (E) CFP/rGO-S4, and (F) CFP/rGO-S5.

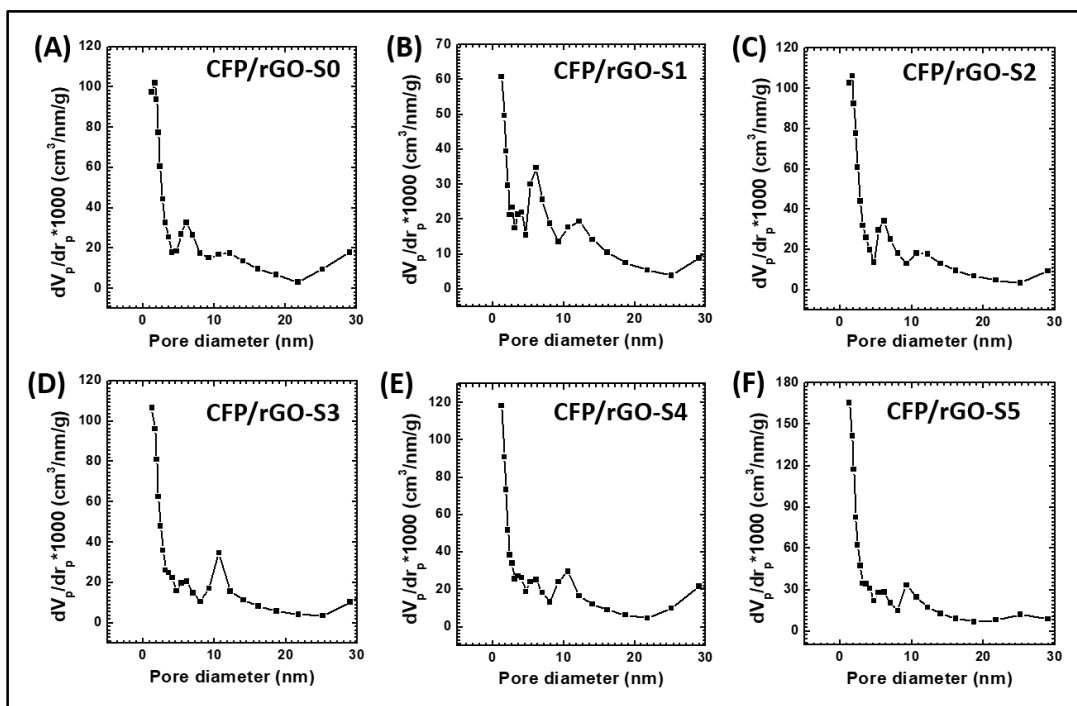


Figure 4.22: pore size distribution (BJH) curves of (A) CFP/rGO-S0, (B) CFP/rGO-S1, (C) CFP/rGO-S2, (D) CFP/rGO-S3, (E) CFP/rGO-S4, and (F) CFP/rGO-S5.

The pore-size distribution for hybrid catalysts is obtained by BJH method and becomes narrow, indicating the homogenization of the particles (**Figure 4.22**). As plotted in the figure, all of the present hybrids possess a relatively narrow distribution of pores with an average diameter of 1 to 3 nm, confirming the formation of mesoporous materials. The large specific surface and mesoporous structure of the hybrid materials can enhance the electrochemical activity by allowing huge number of active positions and rapid ion transfer from the mesopores.

4.4.B.3.6 Electrochemical catalytic performance analysis:

i) ECSA analysis: At different scan rates, the CV curves were recorded in non-Faradic region applying small potential window as shown in **Figure 4.23(A-F)**. C_{dl} is calculated by plotting the anodic charging currents (i_c) of each CV curve against the scan rate by the equation (2.3). The values of C_{dl} are 9.16, 11.62, 18.6, 30.94, 23.86, and 15.44 mF calculated by the plot of the anodic current versus scan rate (**Figure 4.24**) for CFP/rGO-S0, CFP/rGO-S1, CFP/rGO-S2, CFP/rGO-S3, CFP/rGO-S4, and CFP/rGO-S5 hybrid electrodes, respectively.

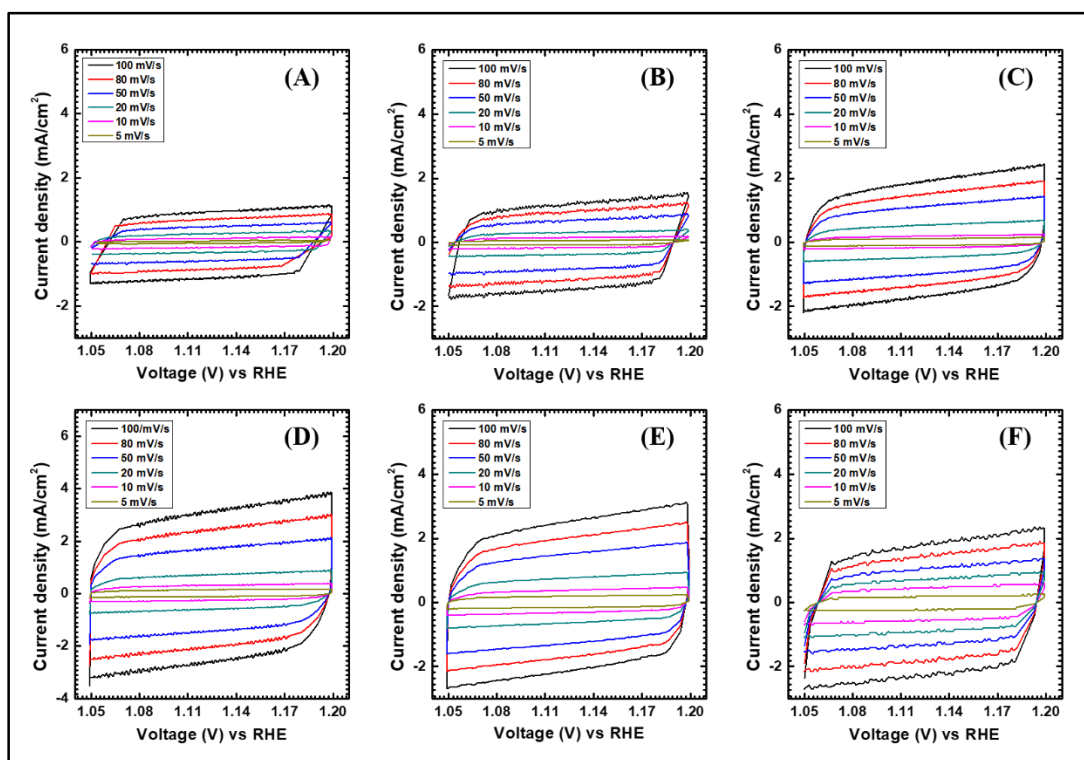


Figure 4.23: The CV curves of (A) CFP/rGO-S0, (B) CFP/rGO-S1, (C) CFP/rGO-S2, (D) CFP/rGO-S3, (E) CFP/rGO-S4, and (F) CFP/rGO-S5 at various scan rates in a small potential window (1.05-1.2 V vs. RHE).

The ECSA can be calculated by dividing the C_{dl} values by specific capacitance (C_s) of atomically smooth planar real surface area (1 cm^2) of the material under identical electrolyte conditions and are found to be 229, 290.5, 465, 773.5, 596.5, and 386 cm^2 for CFP/rGO-S0, CFP/rGO-S1, CFP/rGO-S2, CFP/rGO-S3, CFP/rGO-S4, and CFP/rGO-S5 hybrid electrodes. High ECSA and RF showed by the sample CFP/rGO-S3 than the others which is consistent with the BET surface analysis.

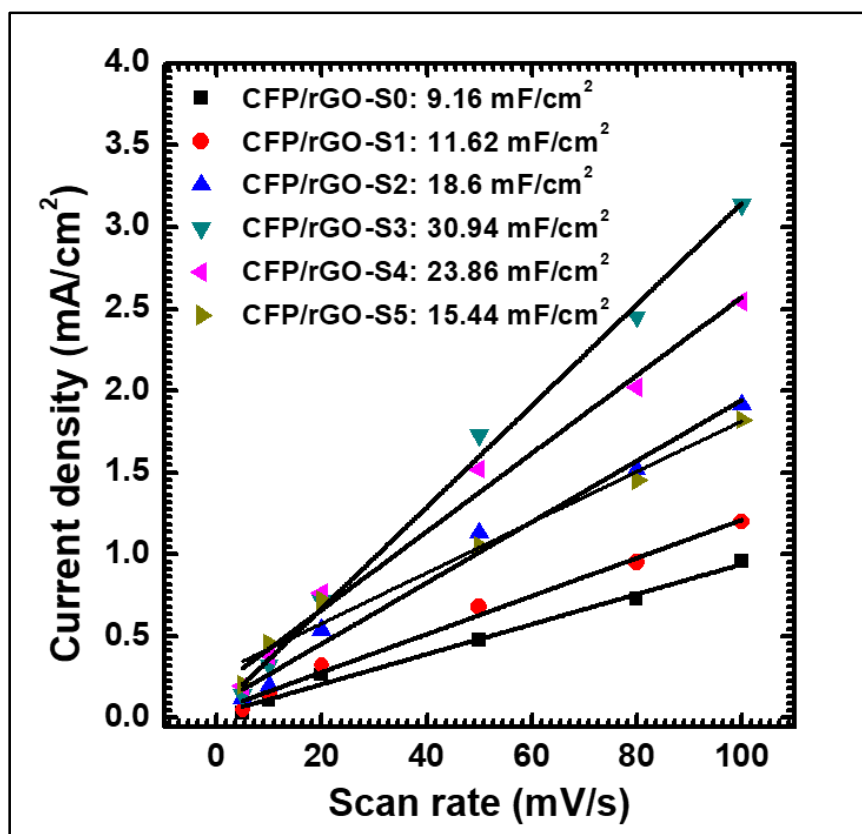


Figure 4.24: Anodic current linear fit for C_{dl} values to calculate ECSA of the cobalt-iron phosphate/reduced graphene oxide hybrid electrodes.

ii) OER analysis: The electrochemical water splitting in the form of OER properties of the as prepared hybrid electrodes were tested. The LSV analysis was conducted to evaluate the catalytic activity in 1 M KOH electrolyte at scan rate of 1 mV/s as shown in **Figure 4.25(A)**. The nature of the all LSV polarization curves is similar and continuous change in current density with change in rGO concentration from 0.00 to 0.1 mg/ml. It is observed that due to hybridization, the material become electrochemically more active. Sample CFP/rGO-S3 requires the smallest overpotential of 238 mV to deliver the current density of 10 mA/cm^2 suggesting outstanding oxygen evolution catalyst than the previously reported cobalt-iron phosphate catalysts. The bar diagram (**Figure 4.25(B)**) reveals the values of overpotential

for all other electrodes from series. The Tafel slope gives the catalytic activity in the form of reaction rate kinetics indicating diverse rate defining steps surrounded in the reaction process.

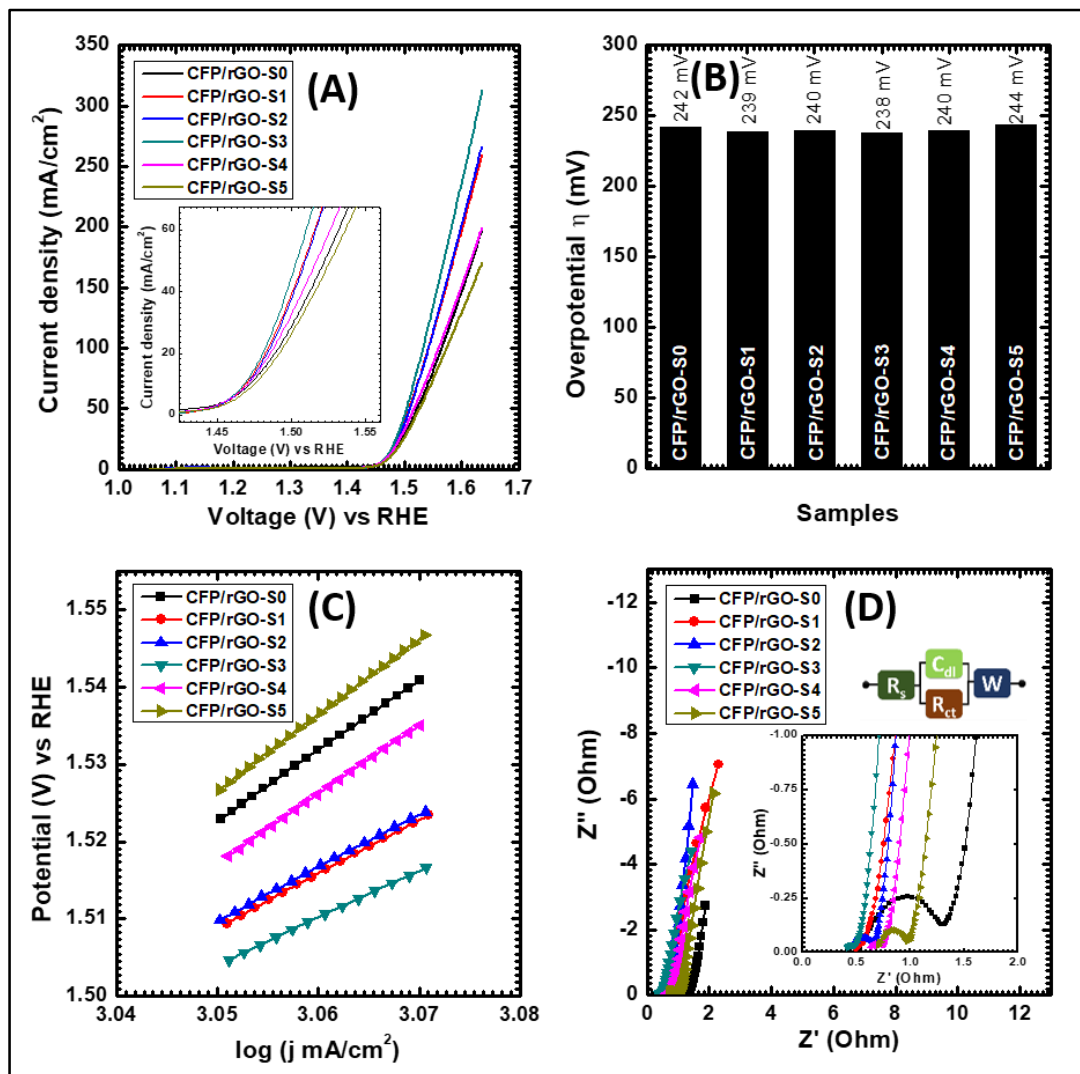


Figure 4.25: Electrochemical OER analysis (A) LSV polarization curves, (B) comparative bar diagram of overpotentials, (C) Tafel plots, (D) EIS of the cobalt-iron phosphate/reduced graphene oxide hybrid electrodes.

By plotting applied potential against the logarithmic current density at the shoot-point of current density, the Tafel plot can be obtained as shown in **Figure 4.25(C)**. Tafel slopes are 38.33, 35.12, 35.87, 33.99, 36.3, and 36.52 mV/dec for all CFP/rGO-S0, CFP/rGO-S1, CFP/rGO-S2, CFP/rGO-S3, CFP/rGO-S4, and CFP/rGO-S5 hybrid electrode samples, respectively. Figure reveals that the CFP/rGO-S3 electrode has smallest Tafel slope of 33.99 mV/dec. It suggests that, the OER reaction process is faster and highly efficient

reaction kinetics at surface of CFP/rGO-S3 electrode. The EIS was carried out to explore the electrochemical kinetics activity. The typical Nyquist plots of the CFP/rGO-S0, CFP/rGO-S1, CFP/rGO-S2, CFP/rGO-S3, CFP/rGO-S4, and CFP/rGO-S5 hybrid electrodes with fitted equivalent circuit are presented in **Figure 4.25(D)**. The fitted R_{ct} values are 0.82, 0.11, 0.17, 0.09, 0.13, and 0.29 Ω for CFP/rGO-S0, CFP/rGO-S1, CFP/rGO-S2, CFP/rGO-S3, CFP/rGO-S4, and CFP/rGO-S5 hybrid electrodes, respectively. It reveals that, easy charge transfer process is one of the reason for low overpotential. Due to the hybridization of material with rGO, the charge transfer process becomes easy. It is because of the proper amount of hybridization; the electron transfer becomes more easy by getting NSs of rGO as channels and conducting pathways.

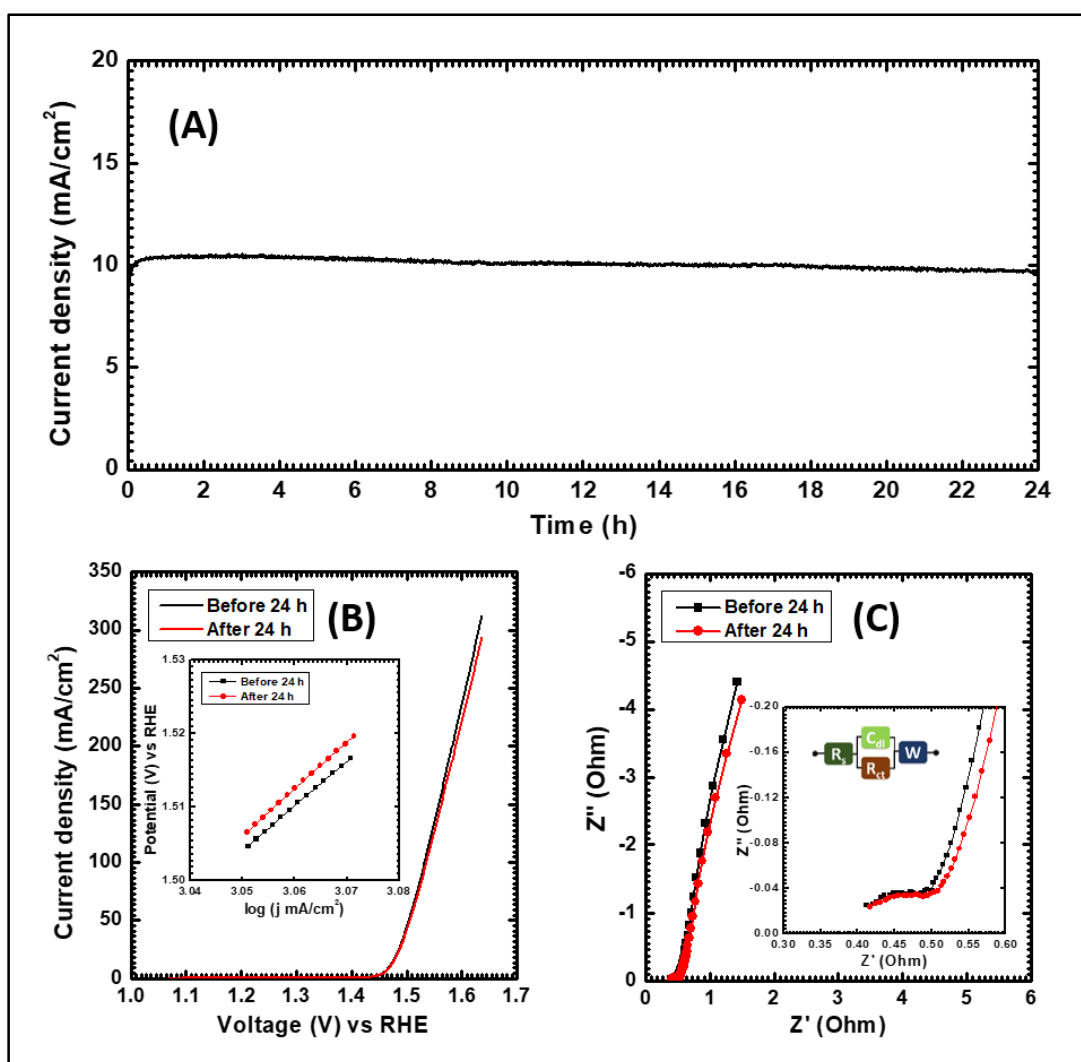


Figure 4.26: (A) CA (I-t) curve for OER stability, (B) LSV before and after 24 h OER catalysis, and (C) EIS after 24 h catalysis of cobalt-iron phosphate/reduced graphene oxide (CFP/rGO-S3) electrode.

The long-duration stability is moreover an ultimate feature to examine an OER catalyst. The OER stability was studied for the best performing catalyst in 1 M KOH electrolyte by three electrode cell at overpotential to achieve the current density of 10 mA/cm². **Figure 4.26(A)** gives the OER catalytic stability test by CA for 24 h. It is observed from the figure that, the catalysis remained stable without loss of current density throughout the period. The comparative LSV plot before and after 24 h catalysis revealed that, there is very minute change in overpotential after catalysis (**Figure 4.26(B)**). The decrease in OER performance observed in LSV curve after stability possibly caused to the material consumption in catalytic activity for long time [36]. The comparative Tafel slope before and after 24 h catalysis shown in inset (**Figure 4.26(B)**) and increase in Tafel slope predicts the quite slowed down the reaction rate after long duration catalysis. Further the EIS measurement was carried for reaction rate investigation. The typical Nyquist plots are shown in **Figure 4.26(C)**, which reveals that there is small increase in the R_{ct} from 0.09 to 0.11 Ω . The fitted EIS parameters are tabulated in **Table 4.4**.

iii) HER analysis: The prepared hybrid CFP/rGO-S0, CFP/rGO-S1, CFP/rGO-S2, CFP/rGO-S3, CFP/rGO-S4, and CFP/rGO-S5 electrodes were further characterized for HER in the potential window of 0.33 to -0.65 V vs. RHE in 1 M H₃PO₄ solution bath. The LSV curves of prepared hybrid electrodes are shown in **Figure 4.27(A)**, which reveals the fast cathodic current increase and sharper curves of all catalyst electrodes. The overpotentials of CFP/rGO-S0, CFP/rGO-S1, CFP/rGO-S2, CFP/rGO-S3, CFP/rGO-S4, and CFP/rGO-S5 hybrid electrodes are recorded as 67.9, 62.7, 55.2, 40.7, 47.5, and 77.0 mV to deliver the current density of 10 mA/cm² and shown as bar diagram in **Figure 4.27(B)**. It confirms that, the CFP/rGO-S3 material electrode demonstrates outstanding performance compared with the other electrodes. By plotting Tafel slope, the HER rate determining kinetics was studied and undoubtedly, lesser the Tafel slope takes faster rate of hydrogen evolution. The **Figure 4.27(C)** displays fast reaction rate and lower Tafel slope (33.42 mV/dec) for CFP/rGO-S6 hybrid electrode. The analysis of Nyquist plots of all the prepared electrodes to study the EIS is shown in **Figure 4.27(D)**. The R_{ct} of the CFP/rGO-S3 hybrid electrode is smaller (0.114 Ω), whereas for the other electrodes this value is quite higher as CFP/rGO-S0 (0.589 Ω), CFP/rGO-S1 (0.353 Ω), CFP/rGO-S2 (0.291 Ω), CFP/rGO-S4 (0.257 Ω), and CFP/rGO-S5 (0.435 Ω). This corroborated that, low R_{ct} leads to the fast reaction kinetics, easy catalysis process and low overpotential.

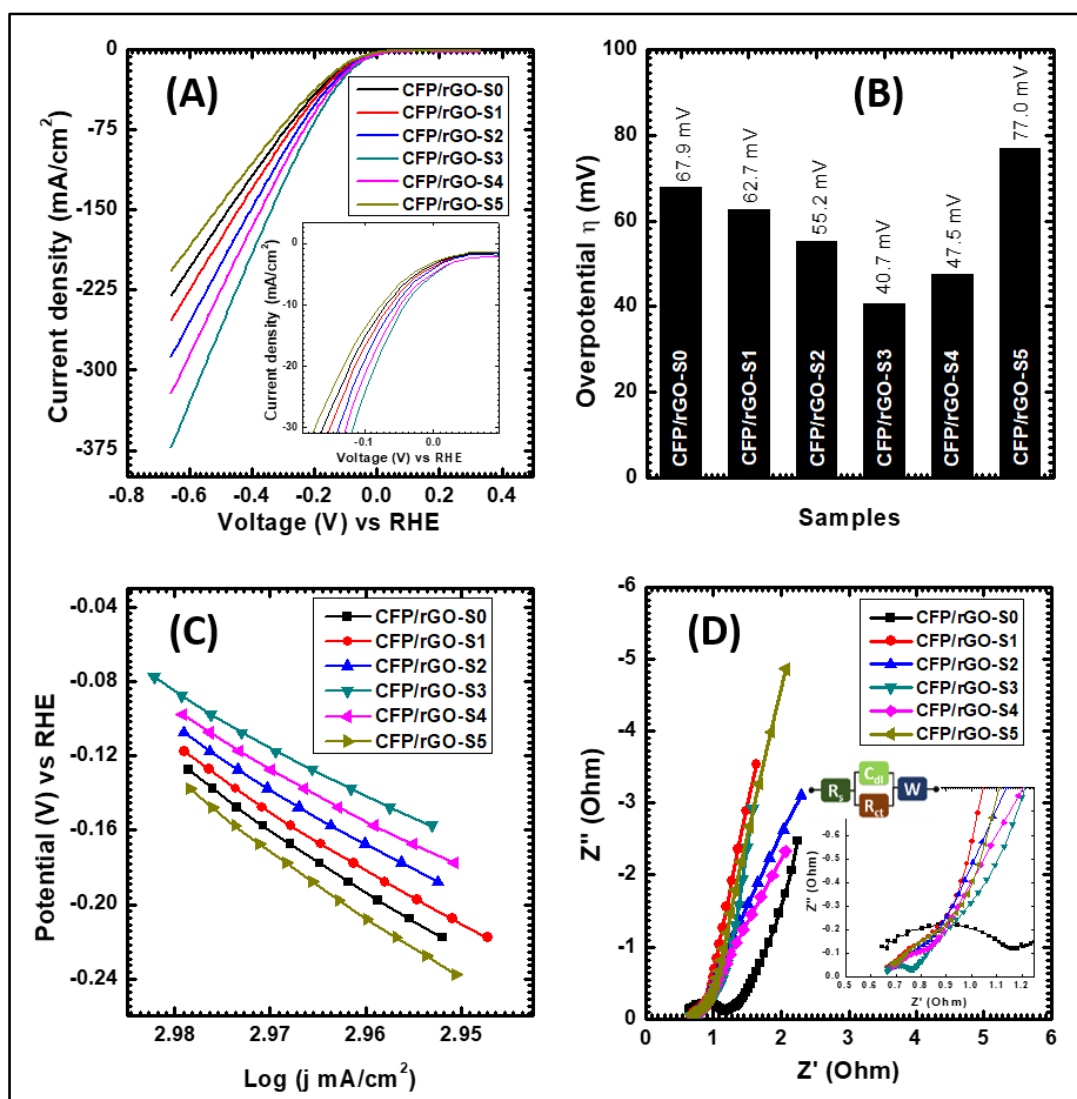


Figure 4.27: Electrochemical HER analysis: (A) LSV polarization curves, (B) comparative bar diagram of overpotentials, (C) Tafel plots, (D) EIS of cobalt-iron phosphate catalysts (CFP/rGO-S0, CFP/rGO-S1, CFP/rGO-S2, CFP/rGO-S3, CFP/rGO-S4, and CFP/rGO-S5).

The CA long term (24 h) catalytic HER stability was performed for the best hybrid electrode. A constant overpotential was provided to CFP/rGO-S3 hybrid catalyst electrode to attain current density of -10 mA/cm² as shown in **Figure 4.28(A)**. Initially, material has been started to activate electrochemically and it delivers very stable current density throughout the period of experiment. After stability, by comparing LSV curves with before stability curve, the HER catalytic performance was tested. After 24 h stability, there is no change observed in the overpotential (**Figure 4.28(B)**).

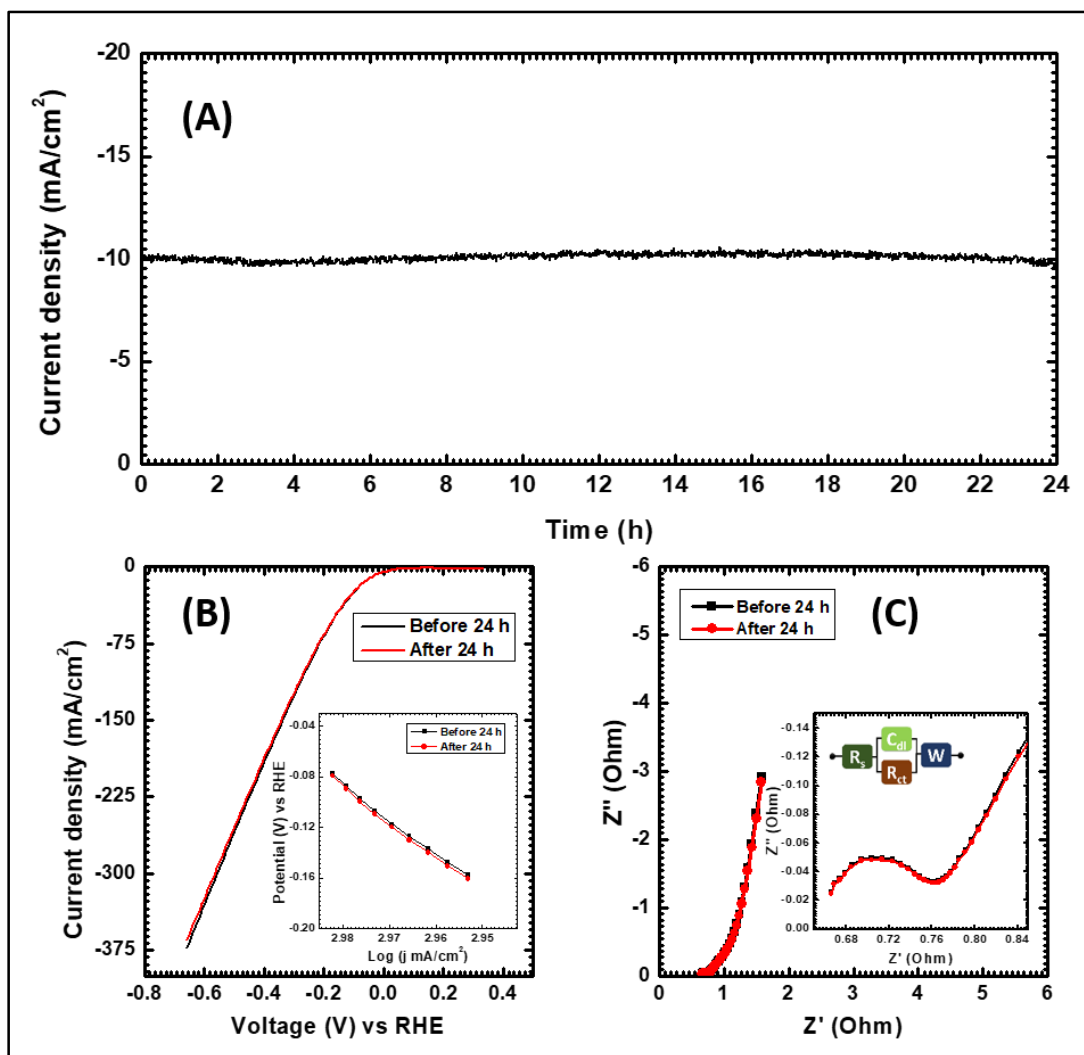


Figure 4.28: (A) CA (I-t) curve for HER stability, (B) LSV before and after 24 h OER catalysis, and (C) EIS after 24 h catalysis of cobalt-iron phosphate/reduced graphene oxide (CFP/rGO-S3) hybrid thin film electrode.

The overpotential remains the same as the overpotential before stability study (40.7 mV at current density of 10 mA/cm²). The inset figure shows the comparative plot of Tafel slopes, which reveals very small change in the reaction rate and becomes 33.43 mV/dec after 24 h catalysis. By fitting electronic equivalent circuit to the Nyquist plots as shown in **Figure 4.28(C)**, it confirmed that, there is no change in impedance after catalysis. The fitted EIS parameters are tabulated in **Table 4.4**. It is attributed that, the rGO can sustain the material structure and enhance the stability by providing their conductivity along with the active material [37,38].

Table 4.4: Electrochemical OER and HER analysis before and after 24 h catalytic stability study.

	Test	Overpotential η (mV) at 10 mA/cm ²	Tafel slope (mV/dec)	R _s (Ω)	R _{ct} (Ω)	W (Ω)
Before stability	OER	238	33.99	0.41	0.09	0.19
After stability		239	33.52	0.41	0.11	0.20
Before stability	HER	40.7	33.42	0.66	0.114	0.24
After stability		40.7	33.43	0.66	0.114	0.24

4.5 Conclusions: In conclusion of section-B, by using SILAR method, cobalt-iron phosphate/reduced graphene oxide hybrid material thin films at various amount of rGO concentrations were synthesized. For the material identification, the synthesized hybrid materials were characterized physico-chemically. By the XRD analysis, the amorphous nature of cobalt-iron phosphate/reduced graphene oxide hybrid materials was confirmed. The formation of cobalt-iron phosphate/reduced graphene oxide material confirmed via FTIR, EDS and XPS by observing metal phosphate content and their corresponding bonds in the prepared samples. The thin films deposited on SS substrates were examined for electrochemical water splitting in the forms of OER and HER. Best performing CFP/rGO-S3 electrode required lowest overpotential of 238 mV for OER to attain the current density of 10 mA/cm² with Tafel slope of 33.99 mV/dec. The best performing electrode show more than 99 % catalytic OER retention after 24 h in alkaline bath. Moreover, for the HER, the same material required overpotential of only 40.7 mV to perform current density of 10 mA/cm² with 33.42 mV/dec Tafel slope. After catalytic HER stability for 24 h in acidic bath, it is observed that the 100 % catalytic stability without loss of catalyst material. The results concluded that, the cobalt-iron phosphate/reduced graphene oxide hybrid electrode shows best performance than the pristine materials. The appropriate amount of rGO may help to increase the conductivity and the pathway for the electron transfer without covering the active material. The electrode CFP/rGO-S3 gives the outstanding performance for OER

and HER, that means the 0.06 mg/ml solution concentration of GO gives the proper amount of rGO (9.77 At%) which can contribute for the electrochemical catalytic activity.

4.6 References:

1. Y. Zhou, H. C. Zeng, 3D networks of CoFePi with hierarchical porosity for effective OER electrocatalysis, *Small* 14 (2018) 1704403.
2. Z. Wang, M. Liu, J. Du, Y. Lin, S. Wei, X. Lu, J. Zhang, A facile co-precipitation synthesis of robust FeCo phosphate electrocatalysts for efficient oxygen evolution, *Electrochimica Acta* 264 (2018) 244.
3. J. Zhang, X. Tan, W. Wang, L. Cao, B. Dong, Iron-doped cobalt phosphate 1D amorphous ultrathin nanowires as highly efficient electrocatalyst for water oxidation, *Sustainable Energy & Fuels* 4 (2020) 4704.
4. D. Yin, Z. Jin, M. Liu, T. Gao, H. Yuan, D. Xiao, Microwave-assisted synthesis of the cobalt-iron phosphates nanosheets as an efficient electrocatalyst for water oxidation, *Electrochimica Acta* 260 (2018) 420.
5. C. Li, X. Mei, F. L. -Y. Lam, X. Hu, Amorphous iron and cobalt based phosphate nanosheets supported on Ni foam as superior catalysts for hydrogen evolution reaction, *ACS Applied Energy & Materials* 1 (2018) 6764.
6. G. Zhu, X. Xie, L. Xiao, X. Li, X. Shen, Co-Fe bimetal phosphate composite loaded on reduced graphene oxide for oxygen evolution, *Nano* 14 (2019) 1950003.
7. Y. Zou, Z. Liu, R. Liu, D. Liu, C. Dong, Y. Wang, S. Wang, Disordered CoFePi nanosheets with rich vacancies as oxygen evolving electrocatalysts: Insight into the local atomic environment, *Journal of Power Sources* 427 (2019) 215.
8. R. B. Kale, C. D. Lokhande, Room temperature deposition of ZnSe thin films by successive ionic layer adsorption and reaction (SILAR) method, *Materials Research Bulletin* 39 (2004) 1829.
9. H. M. Pathan, C. D. Lokhande, Deposition of metal chalcogenide thin films by successive ionic layer adsorption and reaction (SILAR) method, *Bulletin of Materials Science* 27 (2004) 85.
10. Z. Jiang, W. Lu, Z. Li, K. H. Ho, X. Li, X. Jiao, D. Chen, Synthesis of amorphous cobalt sulfide polyhedral nanocages for high performance supercapacitors, *Journal of Materials Chemistry A* 2 (2014) 8603.
11. P. K. Katkar, S. J. Marje, S. S. Pujari, S. A. Khalate, A. C. Lokhande, U. M. Patil, Enhanced energy density of all-solid-state asymmetric supercapacitors based on morphologically tuned hydrous cobalt phosphate electrode as cathode material, *ACS Sustainable Chemistry & Engineering* 7 (2019) 11205.
12. C. Murugesan, S. Lochab, B. Senthilkumar, P. Barpanda, Earth-abundant alkali iron phosphate (AFePO_4) as efficient electrocatalysts for oxygen reduction reaction in alkaline solution, *ChemCatChem* 10 (2018) 1122.
13. H. B. Li, M. H. Yu, X. H. Lu, P. Liu, Y. Liang, J. Xiao, Y. X. Tong, G. W. Yang, Amorphous cobalt hydroxide with superior pseudocapacitive performance, *ACS Applied Materials & Interfaces* 6 (2014) 745.
14. Y. Li, Z. Wang, J. Hu, S. Li, Y. Du, X. Han, P. Xu, Metal–organic frameworks derived interconnected bimetallic metaphosphate nanoarrays for efficient electrocatalytic oxygen evolution, *Advanced Functional Materials* 30 (2020) 1910498.

15. N. Roy, Y. Sohn, K. T. Leung, D. Pradhan, Engineered electronic states of transition metal doped TiO₂ nanocrystals for low overpotential oxygen evolution reaction, *Journal of Physical Chemistry C* 118 (2014) 29499.
16. Q. Zhang, T. Li, J. Liang, N. Wang, X. Kong, J. Wang, H. Qian, Y. Zhou, F. Liu, C. Wei, Y. Zhao, X. Zhang, Highly wettable and metallic NiFe-phosphate/phosphide catalyst synthesized by plasma for highly efficient oxygen evolution reaction, *Journal of Materials Chemistry A* 6 (2018) 7509.
17. N. Jiang, B. You, M. Sheng, Y. Sun, Bifunctionality and mechanism of electrodeposited nickel–phosphorous films for efficient overall water splitting, *ChemCatChem* 8 (2016) 106.
18. R. Gresch, W. Muller-Warmuth, H. Dutz, X-ray photoelectron spectroscopy of sodium phosphate glasses, *Journal of Non-Crystalline Solid* 34 (1979) 127.
19. B. Li, Y. Shi, K. Huang, M. Zhao, J. Qiu, H. Xue, H. Pang, Cobalt-doped nickel phosphite for high performance of electrochemical energy storage, *Small* 14 (2018) 1703811.
20. H. Dan, K. Tao, Q. Zhou, Y. Gong, J. Lin, Ni-doped cobalt phosphite, Co₁₁(HPO₃)₈(OH)₆, with different morphologies grown on Ni foam hydro(solvo)thermally for high-performance supercapacitor, *ACS Applied Materials & Interfaces* 10 (2018) 31340.
21. J. B. Condon, Surface area and porosity determinations by physisorption: Measurements and theory, 1st Ed., Elsevier, Amsterdam, Boston, (2006) pp. 6.
22. M. Liu, Z. Qu, D. Yin, X. Chen, Y. Zhang, Y. Guo, D. Xiao, Cobalt-iron pyrophosphate porous nanosheets as highly active electrocatalysts for the oxygen evolution reaction, *ChemElectroChem* 5 (2018) 36.
23. Q. Yue, T. Gao, Y. Wu, H. Yuan, D. Xiao, S-doped Co-Fe-Pi nanosheets as highly efficient oxygen evolution electrocatalysts in alkaline media, *Electrochimica Acta* 362 (2020) 137123.
24. O. C. Compton, S. T. Nguyen, Graphene oxide, highly reduced graphene oxide, and graphene: Versatile building blocks for carbon-based materials, *Small* 6 (2010) 711.
25. Y. Li, H. Wang, L. Xie, Y. Liang, G. Hong, H. Dai, MoS₂ nanoparticles grown on graphene: An advanced catalyst for the hydrogen evolution reaction, *Journal of American Chemical Society* 133 (2011) 7296.
26. M. Chatti, T. Gengenbach, R. King, L. Spiccia, A. N. Simonov, Vertically aligned interlayer expanded MoS₂ nanosheets on a carbon support for hydrogen evolution electrocatalysis, *Chemistry of Materials* 29 (2017) 3092.
27. M. Wang, M. Lin, J. Li, L. Huang, Z. Zhuang, C. Lin, L. Zhou, L. Mai, Metal-organic framework derived carbon-confined Ni₂P nanocrystals supported on graphene for an efficient oxygen evolution reaction, *Chemical Communication* 53 (2017) 8372.
28. L. Jiao, Y. -X. Zhou, H. -L. Jiang, Metal-organic framework-based CoP/reduced graphene oxide: High-performance bifunctional electrocatalyst for overall water splitting, *Chemical Science* 7 (2016) 1690.
29. M. Liu, L. Yang, T. Liu, Y. Tang, S. Luo, C. Liu, Y. Zeng, Fe₂P/reduced graphene oxide/Fe₂P sandwich-structured nanowall arrays: A high-performance non-noble-metal electrocatalyst for hydrogen evolution, *Journal of Materials Chemistry A* 5 (2017) 8608.
30. C. He, J. Tao, Two-dimensional TaC nanosheets on a reduced graphene oxide hybrid as an efficient and stable electrocatalyst for water splitting, *Chemical Communication* 52 (2016) 8810.

31. C. He, T. Bo, B. Wang, J. Tao, RGO induced one-dimensional bimetallic carbide nanorods: an efficient and pH-universal hydrogen evolution reaction electrocatalyst, *Nano Energy* 62 (2019) 85.
32. J. Hu, Z. Kang, F. Li, X. Huang, Graphene with three-dimensional architecture for high performance supercapacitor, *Carbon* 67 (2014) 221.
33. C. Fu, G. Zhao, H. Zhang, S. Li, Evaluation and characterization of reduced graphene oxide nanosheets as anode materials for lithium-ion batteries, *International journal of Electrochemical Science* 8 (2013) 6269.
34. C. Galande, A. D. Mohite, A. V. Naumov, W. Gao, L. Ci, A. Ajayan, H. Gao, A. Srivastava, R. B. Weisman, P. M. Ajayan, Quasi-molecular fluorescence from graphene oxide, *Scientific Reports* 1 (2011) 1.
35. D. Briggs, G. Beamson, High resolution XPS of organic polymers: The scienta esca 300 database, John Wiley and Sons, New York, (1992) pp. 128.
36. S. Zou, M. Burke, M. Kast, J. Fan, N. Danilovic, S. Boettcher, Fe (oxy)hydroxide oxygen evolution reaction electrocatalysis: Intrinsic activity and the roles of electrical conductivity, substrate, and dissolution, *Chemistry of Materials* 27 (2015) 8011.
37. R. Cong, J. Y. Choi, J. B. Song, M. Jo, H. Lee, C. S. Lee, Characteristics and electrochemical performances of silicon/carbon nanofiber/graphene composite films as anode materials for binder-free lithium-ion batteries, *Scientific Reports* 11 (2021) 1.
38. H. Yue, Q. Li, D. Liu, X. Hou, S. Bai, S. Lin, D. He, High-yield fabrication of graphene-wrapped silicon nanoparticles for self-support and binder-free anodes of lithium-ion batteries, *Journal of Alloys and Compounds* 744 (2018) 243.

CHAPTER – V

COBALT-IRON PHOSPHATE/REDUCED GRAPHENE OXIDE HYBRID ELECTRODES FOR OVERALL WATER SPLITTING

CHAPTER – V

COBALT-IRON PHOSPHATE/REDUCED GRAPHENE OXIDE HYBRID ELECTRODES FOR OVERALL WATER SPLITTING

Contents

Sr. No.	Title	Page No.
5.1	Introduction	157
5.2	Overall water splitting analysis of cobalt-iron phosphate/reduced graphene oxide hybrid electrodes synthesized by SILAR method	158
5.2.1	Electrochemical analysis	158
5.2.2	Post-mortem analysis	161
5.3	Conclusions	164
5.4	References	164

5.1 Introduction: Recently, different green energy sources like solar, wind, hydro (dynamic, tidal, etc.) are growing rapidly [1-4]. Also, there is one more potential renewable energy source, hydrogen. Hydrogen is one of the cleanest renewable energy sources, which can be generate through the various techniques including water splitting by means of electrolysis in the form of H_2 and O_2 [5-11]. As we know, in water splitting by electrolysis, OER is sluggish reaction, which follows four proton-coupled electron transfer process; on the other hand, HER is quite easier. During electrolysis, on the surface of anode, water splits into oxygen in gas form by the OER with accompanying protons and electrons, simultaneously, on the surface of cathode, hydrogen in gas form evolves through HER by the recombination of the protons and electrons [12]. For efficient water splitting in the smallest energy loss, apposite electrocatalysts are crucial components. As discussed in earlier chapters that, large catalytic activity, greater conductivity and acceptable electrocatalytic stability are the characteristics of good electrocatalyst for efficient water splitting. The replacement of conventional electrocatalysts for example platinum, ruthenium/iridium based oxides which are rare and costly is required to produce the substantial improvement in the area of electrocatalysis. When the electrolyzer containing same catalyst material at both electrodes (for HER and OER), there is an additional advantage with respect to its facile applicability, e.g., for deposition of both catalysts in one step by simultaneous coating of anodes and cathodes in integrated systems for electrochemical water splitting [13]. For the splitting of water electrochemically in alkaline electrolyte, transition metal phosphate and their hybrid with carbon based materials are favorable by facilitating active centers for adsorption and oxidation of water molecules by disturbing native atomic configuration and allowing the oxidation of metal atoms at the time of proton coupled electron transfer. Catalysts of transition metal phosphate are promising for electrochemical water splitting who facilitates adsorption and stabilizing active centers. Cobalt-iron phosphate is one of the promising material for the water oxidation [14-20]. From the previous study, cobalt-iron phosphate has great potential for OER and HER.

From the previous chapters (chapter 3 and 4) it is seen that, the cobalt-iron phosphate/reduced graphene oxide (marked as CFP/rGO-S3) synthesized by SILAR method is the superior electrocatalyst for OER and HER. This chapter gives the study of cobalt-iron phosphate/reduced graphene oxide hybrid materials synthesized by means of SILAR method for overall water splitting in same alkaline solution. For the comparison,

pristine cobalt-iron phosphate thin film electrodes (CFP-S2) were also studied at same conditions. By preparing alkaline electrolyte and the same catalyst material as both (cathode and anode) electrodes, overall water electrolysis was tested. The photograph of two electrode cell for overall water splitting is shown in **Figure 5.1(A, B)**. For the study of robustness of the catalyst materials, long term water splitting stability (100 h) was conducted for each best performing catalyst (CFP-S2 and CFP/rGO-S3). The effect of long duration water splitting process on the structural, surface electronic states, and morphological properties of the catalyst material is also studied by conducting post-mortem characterizations.

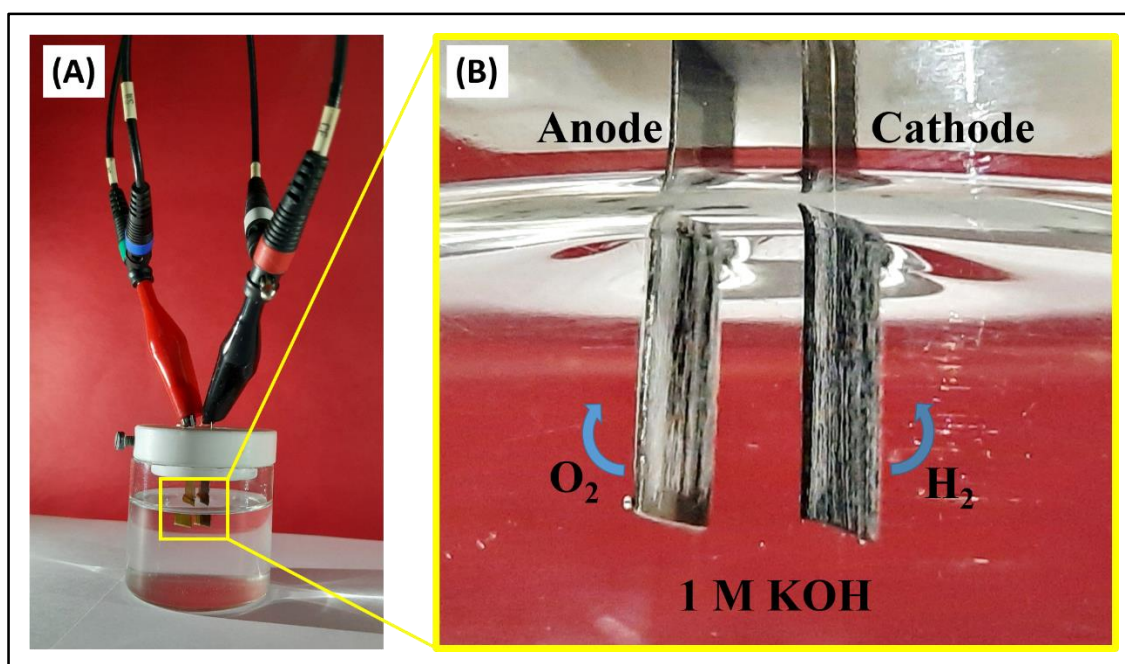


Figure 5.1: (A) Photograph of overall water splitting cell, (B) the magnified portion at electrodes of the cell.

5.2 Overall water splitting analysis of cobalt-iron phosphate/reduced graphene oxide hybrid electrodes synthesized by SILAR method

5.2.1 Electrochemical analysis: SILAR deposited cobalt-iron phosphate/reduced graphene oxide hybrid thin film electrodes (CFP/rGO-S3) were used as an anode and a cathode in full cell electrochemical electrolyzer for overall water splitting. The LSV at 1 mV/s scan rate was conducted in the potential window of 0 to 2 V for overall water splitting. Long term electrolysis was studied by CA recording at potential to attain the current density of 10 mA/cm² for 100 h. For the comparison, the pristine cobalt-iron phosphate thin film

electrodes were tested for overall water splitting with same conditions. The CA I-t curves are shown in **Figure 5.2(A)**. It is seen that, a continuous rise in current density and become stable throughout the time period of CA study of cobalt-iron phosphate/reduced graphene oxide hybrid (CFP/rGO-S3 electrode). The rise in current density is attributed to the continuous material activation. With the full activation, catalyst material delivers almost constant current. On the other hand, for pristine cobalt-iron phosphate (CFP-S2) electrodes, current density increased initially and again decreased slightly due to the degradation of catalyst material. The LSV was recorded after 100 h continuous catalysis and compared with the LSV before catalysis for both cobalt-iron phosphate/reduced graphene oxide hybrid (CFP/rGO-S3) electrode and pristine cobalt-iron phosphate (CFP-S2) electrode electrolyzers as shown in **Figure 5.2(B)**.

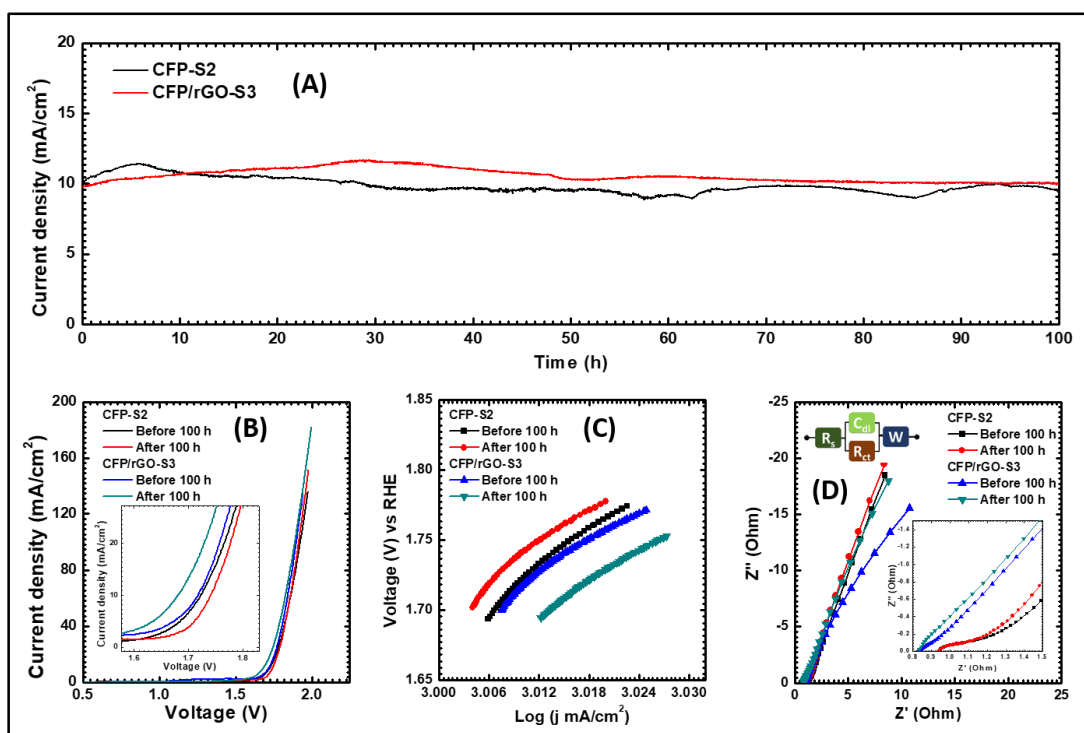


Figure 5.2: Electrochemical overall water splitting stability of the CFP-S2 and CFP/rGO-S3 catalysts (A) CA (I-t) plot, (B) LSV before and after 100 h catalysis, (C) Tafel plots and (D) EIS spectra recorded at OCP.

The comparative LSV plots confirmed that there is enhancement in the performance of water splitting for CFP/rGO-S3. Initially the potential value was 1.71 V and after 100 h catalysis, the potential get decreased to 1.68 V, it is due to the material activation in catalysis process. By comparing LSV of pristine CFP-S2 before and after catalysis, it is observed that, initially the potential value was 1.72 V and after 100 h catalysis, the potential

get increased to 1.74 V. The increase in potential attributed to material degradation in the electrolyte during catalysis process. **Figure 5.2(C)** shows the Tafel plots of CFP-S2 and CFP/rGO-S3 before and after 100 h catalysis. From the plot it is observed that, the value of Tafel slope for CFP-S2 electrode increases from 46.37 mV/dec to 47.74 mV/dec after catalysis. On the other hand, the CFP/rGO-S3 electrode has smaller value of 40.27 mV/dec before catalysis and it becomes 38.57 mV/dec after the 100 h continuous catalysis. It indicates that, cobalt-iron phosphate/reduced graphene oxide hybrid (CFP/rGO-S3) electrode electrolyzer has fast reaction rate. The reaction rates depend on the charge transfer process within the electrolyte to electrode and can be measured by EIS analysis. The Nyquist plots recorded before and after 100 h catalysis for both the electrolyzers are shown in **Figure 5.2(D)**.

Table 5.1: Electrochemical OER and HER analysis before and after 100 h catalytic stability study.

Electrode	Performance measured	Potential (V) at 10 mA/cm ²	Tafel slope (mV/dec)	R _s (Ω)	R _{ct} (Ω)	W (Ω)
CFP-S2	Before stability	1.72	46.37	0.53	0.70	0.336
	After stability	1.74	47.74	0.54	0.56	0.358
CFP/rGO-S3	Before stability	1.71	40.27	0.83	0.21	0.67
	After stability	1.68	38.57	0.83	0.14	0.59

The R_{ct} decreased from 0.21 Ω to 0.14 Ω after catalytic stability for CFP/rGO-S3, which gives the confirmation for increase in water splitting performance. For CFP-S2 electrolyzer, R_{ct} values are higher as compared to CFP/rGO-S3 electrolyzer. All electrochemical analyses of cobalt-iron phosphate/reduced graphene oxide hybrid (CFP/rGO-S3) electrode electrolyzer and pristine cobalt-iron phosphate (CFP-S2) electrode electrolyzer are summarized in **Table 5.1**.

5.2.2 Post-mortem analysis: The photograph of the CFP/rGO-S3 electrode after 100 h catalysis is shown in **Figure 5.3(A)**. By carrying out the analyses of the thin films after stability study, the effect of long term electrochemical catalysis on the physico-chemical properties of material were studied. The restored thin films were placed in DDW to remove the adsorbed ions of electrolyte.

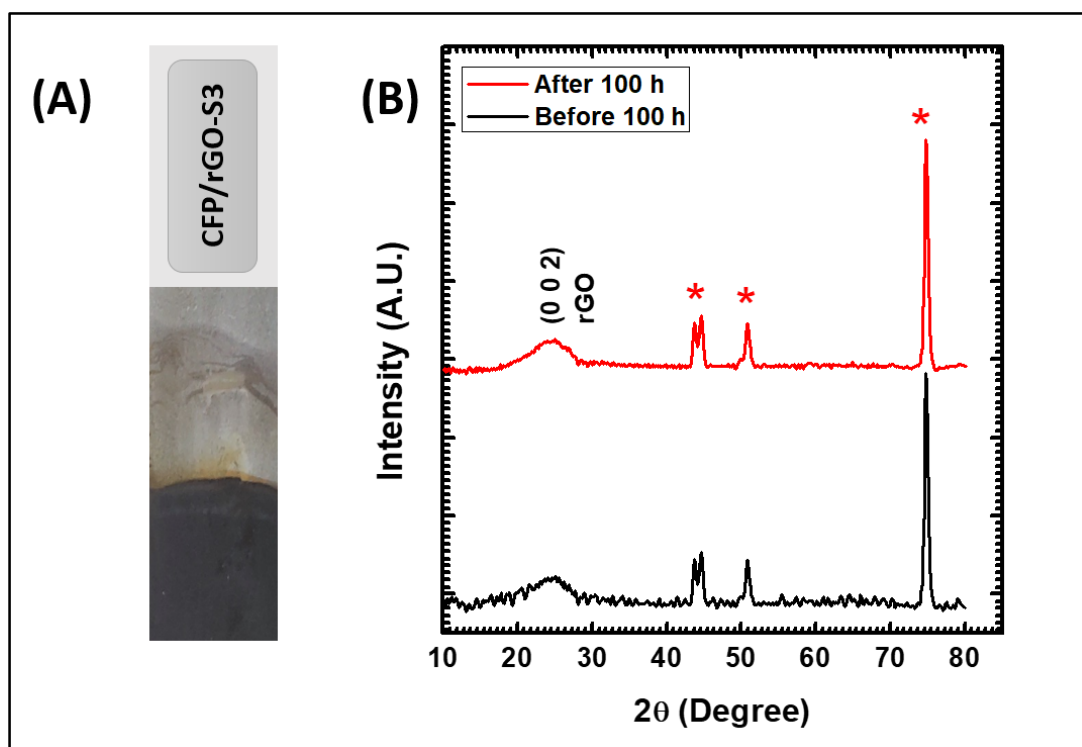


Figure 5.3: (A) Photograph of CFP/rGO-S3 electrode after 100 h catalysis, (B) XRD patterns of CFP/rGO-S3 electrode before and after 100 h catalysis.

Figure 5.3(B) shows the XRD compared with the pattern of same material before electrolysis. Not a single diffraction peak of the material is observed, it discloses that the material remains amorphous in nature after long term electrochemical testing. The peaks marked with star (*) are due to the diffraction from the planes of SS substrate. The broad hump at about 25° corresponds to the rGO, observed before and after the catalysis.

The surface morphology and elemental composition study were conducted by FESEM and EDS analyses of SILAR deposited cobalt-iron phosphate/reduced graphene oxide (CFP/rGO-S3) hybrid thin film electrode after 100 h continuous catalysis. **Figure 5.4(A, C)** gives the comparative of FESEM images of the catalyst, which uncovers the conversion of spherical nanoparticles of cobalt-iron phosphate to NSs like holey surface morphology.

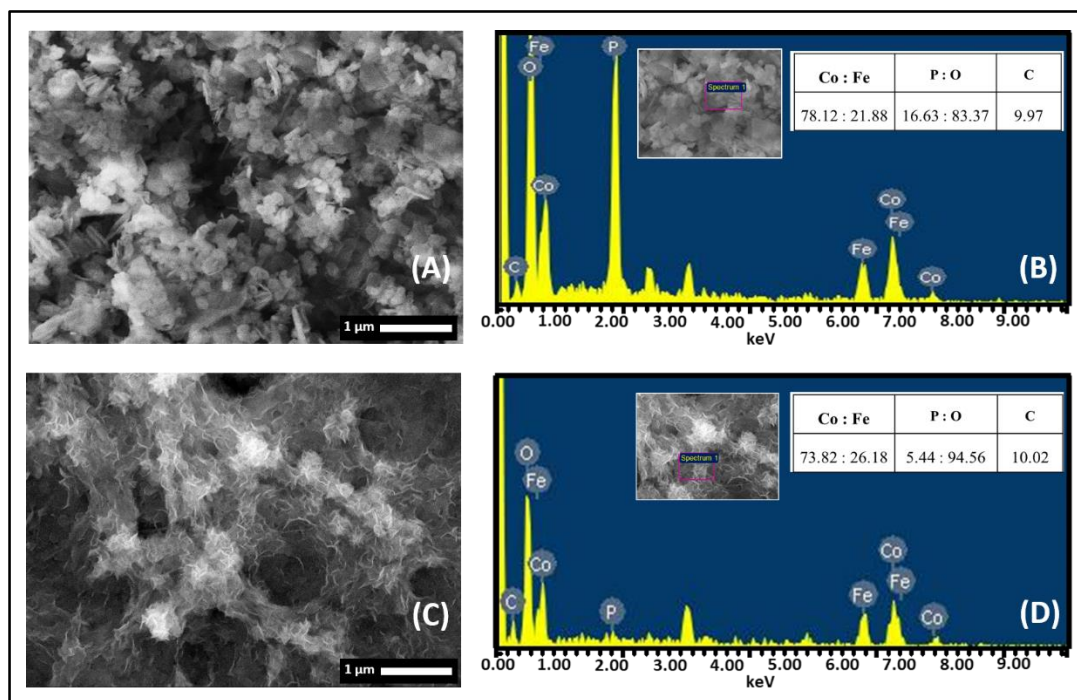


Figure 5.4: (A, C) FESEM images and (B, D) EDS of CFP/rGO-S3 before and after 100 h electrocatalytic stability test.

Also, the EDS analysis gives the proportion of cobalt to iron remain almost maintained as shown in **Figure 5.4(B, D)**. Due to long term catalysis phosphorous content reduced and simultaneously, in proportionality of phosphorous to oxygen, oxygen becomes 94.56 At%. It is attributed that, after long duration catalysis in alkaline medium, metal phosphate partially converted into metal oxide.

After continuous water splitting test, the electronic oxidation states existing in the catalyst material were carried out by the examination of XPS. The existence of P, C, O, Fe, and Co elements confirmed by the survey spectrum of catalyst material as shown in **Figure 5.5(A)**. At high resolution spectrum of Co2p (**Figure 5.5(B)**), the occurrence of prominent peaks at 779.88 eV for Co2p_{3/2} and at 794.99 eV for Co2p_{1/2} with the alongside satellite peaks at 787.67 eV and 803.60 eV, correspondingly. The Co2p_{3/2} peak is composed by the peaks at 779.80 eV and 781.34 eV correlated to Co³⁺ and Co²⁺, individually. Also, the Co2p_{1/2} peak composed of the peaks at 794.83 eV and 796.38 eV correlated with Co³⁺ and Co²⁺, individually [21]. Also, XPS spectrum of Fe2p state as presented in the **Figure 5.5(C)**. From the figure, the observed peak Fe2p_{3/2} situated at 711.02 eV and a satellite peak at 717.55 eV. The peak Fe2p_{1/2} located at 723.98 eV alongside satellite peak at 732.61

eV. The prominent peaks Fe2p_{3/2} composed with two peaks at binding energies 710.13 and 712.00 eV related to Fe³⁺ and Fe²⁺ states, individually. Also, Peak Fe2p_{1/2} is composed with 723.89 eV and 726.44 eV peaks corresponds to Fe³⁺ and Fe²⁺ states, individually. As compared to the XPS before catalysis, the peak intensities increased for Co and Fe elements. Existence of Fe²⁺ and Fe³⁺ electronic oxidation states together of Fe atoms and Co²⁺ and Co³⁺ electronic oxidation states of Co seen because of the oxidation of the catalyst material and partial transformation from Fe²⁺ to Fe³⁺ and Co²⁺ to Co³⁺ during 100 h continuous electrolysis.

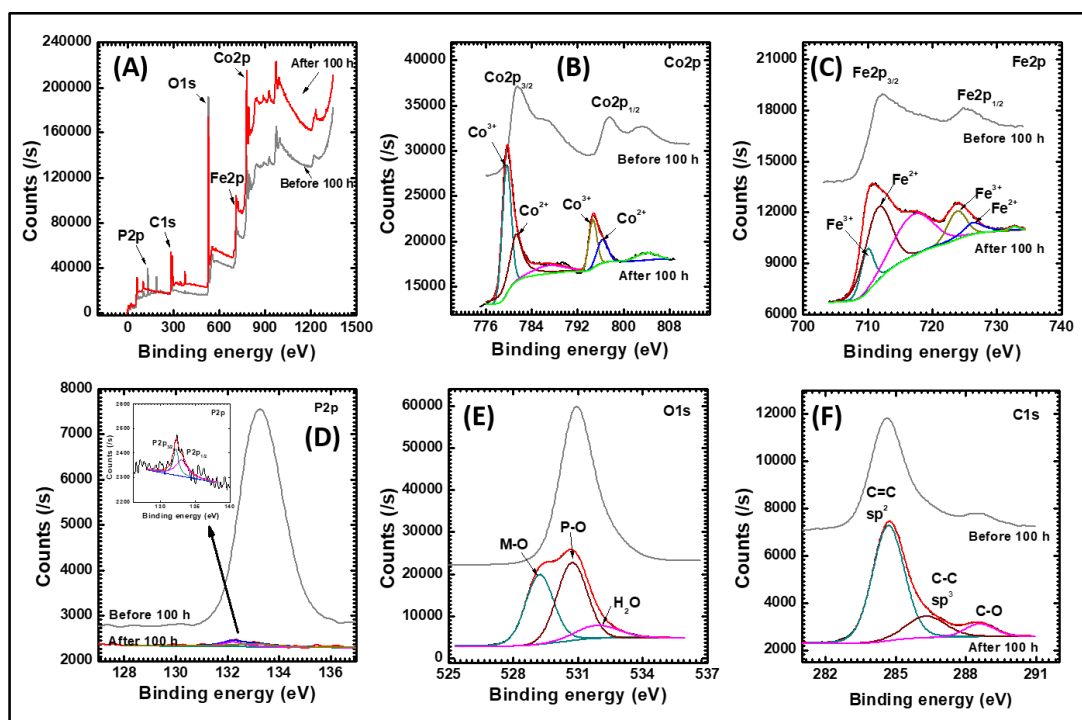


Figure 5.5: XPS spectra of CFP/rGO-S3 catalyst electrode (A) survey spectrum, high resolution XPS spectra of (B) Co2p, (C) Fe2p, (D) P2p, (E) O1s, and (F) C1s after 100 h catalysis.

The phosphorous P2p shows two peaks at 132.19 and 132.99 eV corresponds to P2p_{3/2} and P2p_{1/2}, respectively (**Figure 5.5(D)**). Low peak intensity compared with the XPS before catalysis confirms that there is loss of phosphorous content with the partial transformation of phosphate into the stable metal oxides after 100 h catalysis. The O1s prominent peak is made up of three distinctive peaks as shown in **Figure 5.5(E)**. The strong peak at 529.25 eV accredited to the M-O bonding and peaks at 530.73, 532.02 eV corresponds to P-O bond and surface adsorbed water molecules, respectively [22]. As compared to the XPS before catalysis, P-O bond intensity decreased and M-O bonding

increased. High resolution C1s peaks in the XPS prove that due to reduction of GO during the thin film deposition process, oxygen containing groups are very less. The out of plane bonding of sp^3 hybridized C-C is very short observed at 286.33 eV. The intense peak at 284.83 eV is due to C=C in-plane bonding of sp^2 hybridization as shown in **Figure 5.5(F)**. The present result gives the confirmation about the reduction of GO. Also, the carboxylate carbon (O-C=O) is observed at 288.28 eV [23].

Summarizing, the cobalt-iron phosphate/reduced graphene oxide hybrid thin films synthesized by SILAR method were applied as anode and cathode for overall water splitting in alkaline solution bath, which require only 1.68 V potential to split water and attain the current density of 10 mA/cm² after very long duration (100 h) electrochemical overall water splitting process. The post-mortem analysis confirms the partial conversion of phosphate into the oxide due to catalysis process and also, it revealed that, the conversion of spherical nanoparticles to the NSs like structure over the surface.

5.3 Conclusions: In conclusion, cobalt-iron phosphate/reduced graphene oxide hybrid material thin films synthesized by SILAR method were used as cathode and anode electrodes for electrochemical water splitting and compared with pristine material electrodes. The CA tests were carried out in same alkaline electrolyte bath for long duration (100 h) catalysis and it is observed that, due to material activation with time, the potential required from 1.70 V to 1.68 V, that is around 101.2 % catalytic stability. Also, Tafel slope was decreased from 40.27 mV/dec to 38.57 mV/dec, which indicate the increase in reaction rate after 100 h catalysis. The post-mortem analysis confirmed that, cobalt-iron phosphate/reduced graphene oxide hybrid electrodes synthesized by SILAR method are robust and delivering long term catalysis for water splitting.

5.4 References:

1. S. A. Khalate, R. S. Kate, R. J. Deokate, A review on energy economics and the recent research and development in energy and the Cu_2ZnSnS_4 (CZTS) solar cells: A focus towards efficiency, *Solar Energy* 169 (2018) 616.
2. J. Bosch, I. Staffell, A. D. Hawkes, Temporally explicit and spatially resolved global offshore wind energy potentials, *Energy* 163 (2018) 766.
3. Z. Şen, 1.14 Hydro Energy, *Comprehensive Energy Systems* 1 (2018) 606.
4. V. Khare, C. Khare, S. Nema, P. Baredar, *Tidal energy systems design, optimization and control*, Elsevier, The Netherlands, (2019).
5. S. Chu, A. Majumdar, Opportunities and challenges for a sustainable energy future, *Nature* 488 (2012) 294.

6. I. Roger, M. A. Shipman, M. D. Symes, Earth-abundant catalysts for electrochemical and photoelectrochemical water splitting, *Nature Reviews Chemistry* 1 (2017) 1.
7. A. Indra, P. W. Menezes, I. Zaharieva, E. Baktash, J. Pfrommer, M. Schwarze, H. Dau and M. Driess, Active mixed-valent MnO_x water oxidation catalysts through partial oxidation (corrosion) of nanostructured MnO particles, *Angewandte Chemie* 52 (2013) 13206.
8. M. S. Dresselhaus, I. L. Thomas, Alternative energy technologies, *Nature* 414 (2001) 332.
9. X. Zou, Y. Zhang, Noble metal-free hydrogen evolution catalysts for water splitting, *Chemical Society Reviews* 44 (2015) 5148.
10. B. Liu, Y. Zhao, H. Peng, Z. Zhang, C. Sit, M. Yuen, T. Zhang, C. Lee, W. Zhang, Nickel–cobalt diselenide 3D mesoporous nanosheet networks supported on Ni foam: An all-pH highly efficient integrated electrocatalyst for hydrogen evolution, *Advanced Materials* 29 (2017) 1606521.
11. C. C. L. McCrory, S. Jung, J. C. Peters, T. F. Jaramillo, Benchmarking heterogeneous electrocatalysts for the oxygen evolution reaction, *Journal of American Chemical Society* 135 (2013) 16977.
12. Y. Jiao, Y. Zheng, M. T. Jaroniec, S. Z. Qiao, Design of electrocatalysts for oxygen-and hydrogen-involving energy conversion reactions, *Chemical Society Reviews* 44 (2015) 2060.
13. P. W. Menezes, C. Panda, S. Loos, F. Bunschei-Bruns, C. Walter, M. Schwarze, X. Deng, H. Dau, M. Driess, A structurally versatile nickel phosphite acting as a robust bifunctional electrocatalyst for overall water splitting, *Energy & Environmental Science* 11 (2018) 1287.
14. C. Li, X. Mei, F. L. Y. Lam, X. Hu, Amorphous iron and cobalt based phosphate nanosheets supported on Ni foam as superior catalysts for hydrogen evolution reaction, *ACS Applied Energy Materials* 1 (2018) 6764.
15. Y. Zhou, H. C. Zeng, 3D networks of CoFePi with hierarchical porosity for effective OER electrocatalysis, *Small* 14 (2018) 1704403.
16. J. Zhang, X. Tan, W. Wang, L. Cao, B. Dong, Iron-doped cobalt phosphate 1D amorphous ultrathin nanowires as highly efficient electrocatalyst for water oxidation, *Sustainable Energy & Fuels* 4 (2020) 4704.
17. D. Yin, Z. Jin, M. Liu, T. Gao, H. Yuan, D. Xiao, Microwave-assisted synthesis of the cobalt-iron phosphates nanosheets as an efficient electrocatalyst for water oxidation, *Electrochimica Acta* 260 (2018) 420.
18. Y. Zou, Z. Liu, R. Liu, D. Liu, C. Dong, Y. Wang, S. Wang, Disordered CoFePi nanosheets with rich vacancies as oxygen evolving electrocatalysts: Insight into the local atomic environment, *Journal of Power Sources* 427 (2019) 215.
19. Z. Wang, M. Liu, J. Du, Y. Lin, S. Wei, X. Lu, J. Zhang, A facile co-precipitation synthesis of robust FeCo phosphate electrocatalysts for efficient oxygen evolution, *Electrochimica Acta* 264 (2018) 244.
20. G. Zhu, X. Xie, L. Xiao, X. Li, X. Shen, Co-Fe bimetal phosphate composite loaded on reduced graphene oxide for oxygen evolution, *Nano* 14 (2019) 1950003.
21. Y. Li, Z. Wang, J. Hu, S. Li, Y. Du, X. Han, P. Xu, Metal–organic frameworks derived interconnected bimetallic metaphosphate nanoarrays for efficient electrocatalytic oxygen evolution, *Advanced Functional Materials* 30 (2020) 1910498.

22. H. Dan, K. Tao, Q. Zhou, Y. Gong and J. Lin, Ni-doped cobalt phosphite, $\text{Co}_{11}(\text{HPO}_3)_8(\text{OH})_6$, with different morphologies grown on Ni foam hydro(solvo)thermally for high-performance supercapacitor, ACS Applied Materials & Interfaces 10 (2018) 31340.
23. D. Briggs, G. Beamson, High resolution XPS of organic polymers: The scienta esca 300 database, John Wiley and Sons, New York, (1992) pp. 128.

CHAPTER – VI

SUMMARY AND CONCLUSIONS

Summary and conclusions: Nowadays, attention towards renewable energy technology is growing rapidly due to the depletion of fossil fuels and increase in the worldwide energy demand. The view towards hydrogen is as the cleanest and strongest renewable energy sources. To generate hydrogen as a renewable energy, the electrolysis of water is the profitable and competent method. Electrochemical water splitting is the superior way to produce gaseous hydrogen and oxygen which mainly involves two half-reactions: HER on the cathode and OER on the anode. Although, due to the kinetics effects, additional potential is required between the cathode and anode to regulate the reaction process. Hence, too much efforts have been dedicated to synthesize outstanding catalysts to diminish the overpotential for overall water splitting.

The aim of present research was to develop non-noble nanomaterial catalysts for efficient electrochemical water splitting. To fulfil the requirement, cobalt-iron phosphate and cobalt-iron phosphate/reduced graphene oxide hybrid electrodes were prepared via the hydrothermal and SILAR methods on SS substrates. By these two methods, pristine cobalt-iron phosphate was synthesized by varying the compositional ratio of cobalt and iron. Further in the optimized cobalt-iron phosphate, rGO concentration was varied and cobalt-iron phosphate/reduced graphene oxide hybrid electrodes were synthesized for the study of water splitting electrochemically in the forms of OER, HER, and overall water splitting.

Chapter-1 gives an introduction about the energy economics and the present situation of energy generation. The drawbacks of fossil fuels and the need of renewable energy sources for example solar, wind, and hydrogen energy were discussed. For the hydrogen production from the water, an electrochemical water splitting concept have explained in detail. The reaction mechanisms of HER and OER along with performance parameters have discussed thoroughly. The objectives of the research work such as to develop nanomaterial cobalt-iron phosphate/reduced graphene oxide hybrid electrodes, using effective synthesis methods, which can work as efficient electrocatalysts for OER, HER and overall water splitting. For this purpose, literature of the cobalt phosphate, iron phosphate, cobalt-iron phosphate and cobalt-iron phosphate/reduced graphene oxide hybrid materials was surveyed for water splitting in the forms of OER, and HER. The orientation and purpose of dissertation along with the outline of the thesis have given in short.

Chapter-2 contains the theoretical background of material synthesis methods and characterization techniques. The ideal requirements of the catalyst for electrochemical

water splitting and the basic properties of transition metal phosphate with their favorable conditions for water splitting were discussed in brief at the initial part of the chapter. Further, introduction of different material synthesis methods with the broad spectrum of physical and chemical methods have been discussed. Theoretical background of hydrothermal method and SILAR deposition method with numerous preparative parameters and advantages were briefly explained. In the characterization techniques, for the physico-chemical characterizations as, XRD, FTIR spectroscopy, XPS, FESEM, EDS analysis, surface area analysis (BET, BJH), etc. were discussed in brief. The electrochemical analysis techniques such as CV, LSV, CA, and EIS were discussed thoroughly.

The hydrothermally synthesized cobalt-iron phosphate and cobalt-iron phosphate/reduced graphene oxide hybrid electrodes were studied in chapter-3. This chapter have two sections (A and B). Section A contained the synthesis, physico-chemical characterizations and electrochemical study of cobalt-iron phosphate for OER and HER. The effect of chemical composition of cobalt and iron was studied by varying the atomic ratio of cobalt and iron from 100:0 to 0:100. With the variation in composition, morphological evolution was observed. The impact on structure, surface electronic and surface morphology were studied by the XRD, XPS, FE-SEM and EDS analyses. Crystalline to amorphous phase conversion from cobalt phosphate to iron phosphate was observed in XRD analysis. The cobalt, iron, phosphorous and oxygen elements with expected composition were detected in EDS study. As the composition varied from cobalt phosphate to iron phosphate, the topography varied from microchips to submicrometric strips having nanometric thickness and then to the micrometric cubes and pyramids. The water splitting in the forms of OER and HER were studied in basic and acidic solution medium, respectively. Best performing cobalt-iron phosphate (CFP-H3) catalyst electrode demonstrated minimum overpotential of 251.9 mV for OER to attain the current density of 10 mA/cm² with Tafel slope 39.3 mV/dec with greater than 100 % catalytic OER stability for 24 h in alkaline electrolyte bath. Furthermore, the same material was performed HER with 55.5 mV overpotential to deliver the current density of 10 mA/cm² with 73.64 mV/dec Tafel slope. After catalytic HER stability for the duration of 24 h in acidic medium, it is observed that the overpotential reduced to 37.3 mV. The performance has caused due to synergistic effect of both the metals (Co and Fe) enhances the electronic conduction and metal-to-metal partial charge transfer process and the decrease of ion adsorption energy of

the surface by altering the surface electronic properties of cobalt-iron phosphate. In section B, the study of cobalt-iron phosphate/reduced graphene oxide hybrid electrodes synthesized by hydrothermal process is discussed. For the purpose, GO was synthesized by Hummer's method. The concentration of rGO was varied in the pre-optimized cobalt-iron phosphate. The prepared cobalt-iron phosphate/reduced graphene oxide hybrid materials were characterized physico-chemically for the material determination. The amorphous nature of cobalt-iron phosphate/reduced graphene oxide materials was confirmed by XRD analysis. The formation of cobalt-iron phosphate/reduced graphene oxide materials confirmed by analysing composition and their corresponding bonds via FTIR, EDS and XPS. The prepared materials along with carbon black and PVDF binder were coated on SS substrates by slurry coating technique and tested electrochemically for water splitting in the forms of OER and HER. CFP/rGO-H0 electrode demonstrated low overpotential of 266 mV for OER to achieve the current density of 10 mA/cm^2 with Tafel slope 61.5 mV/dec and almost 98 % catalytic OER retention after 24 h in alkaline medium. Also, the same material performed HER with 110.7 mV overpotential to attain the current density of 10 mA/cm^2 with 74.6 mV/dec Tafel slope. After catalytic HER stability for the duration of 24 h in acidic medium, it is observed that the overpotential reduced to 95.5 mV. After evaluation of all the hybrid samples, it is observed that, due to the restacking of rGO NSs due to chemical reduction and the aggregation of material with rGO. Also, rGO may cover the active material due to which the electrochemical active centers may get reduced, and require higher overpotential for hybrid materials.

The chapter-4 deals with the synthesis of cobalt-iron phosphate and cobalt-iron phosphate/reduced graphene oxide hybrid electrodes via SILAR deposition method on SS substrates. Chapter-4 have two sections (A and B), in section A, pristine cobalt-iron phosphate thin films were prepared by varying composition of cobalt and iron. The prepared thin films were characterized physico-chemically for material identification and analysis of surface properties. The XRD analysis confirmed the amorphous nature of SILAR deposited cobalt-iron phosphate thin films. Formation of spherical nanoparticles of cobalt-iron phosphate ($\text{Co}_x\text{Fe}_{3-x}(\text{PO}_4)_2 \cdot \text{H}_2\text{O}$) was confirmed by the surface morphology, elemental analysis, molecular bonding and electronic states present in the material by FESEM, EDS, FTIR and XPS, respectively. Large surface area was observed by BET analysis for the sample CFP-S2. The as synthesized cobalt-iron phosphate electrodes at different compositions demonstrated exceptional water splitting in the forms of OER and

HER. The outperforming CFP-S2 thin film electrode required minimum overpotential of 242 mV for the delivery of 10 mA/cm² current density with Tafel slope 38.33 mV/dec for OER and enhanced catalytic OER stability with overpotential of 237 mV to attain the current density of 10 mA/cm² after 24 h in alkaline bath. Moreover, for the HER, 67.9 mV overpotential was required for the current density of 10 mA/cm² and 35.92 mV/dec Tafel slope. After catalytic HER stability for the duration of 24 h in acidic medium, it is observed that the overpotential reduced to 48.9 mV. The outstanding performances for OER and HER before and after catalysis with enhanced stability can be attributed to the amorphous nature of the material, synergistic effect of both the metals (Co and Fe), improved electronic conduction and metal-to-metal partial charge transfer process. Furthermore, in section B, the cobalt-iron phosphate/reduced graphene oxide hybrid thin film electrodes were deposited on SS substrates by SILAR method. The concentration of GO was varied in the pre-optimized best performing cobalt-iron phosphate (CFP-S2) thin films. The material hybridization, structural, morphological, elemental composition, surface area, electronic states, etc. were studied by conducting various physico-chemical analyses. XRD analysis confirmed the amorphous nature of the cobalt-iron phosphate/reduced graphene oxide hybrid thin films. The largest surface area of 56.55 m²/g was observed for the hybrid material containing 0.06 mg/ml rGO. The examinations were carried out for electrochemical water splitting of the thin films deposited on SS substrates in the forms of OER and HER. Best performing CFP/rGO-S3 electrode required lowest overpotential for OER of 238 mV for the delivery of 10 mA/cm² current density with Tafel slope 33.99 mV/dec. The best performing electrode show greater than 99 % catalytic retention after 24 h in alkaline electrolytic bath. Moreover, for the HER, the same material required only 40.7 mV overpotential to perform the current density of 10 mA/cm² with 33.42 mV/dec Tafel slope. After catalytic (HER) stability for the duration of 24 h in acidic medium, the 100 % catalytic stability was observed without loss of catalyst material. The appropriate amount of rGO may help to increase the conductivity and the pathway for the electron transfer without covering the active material. It is observed that, the cobalt-iron phosphate/reduced graphene oxide hybrid (CFP/rGO-S3) electrode shows best performance than the pristine (CFP-S2) materials.

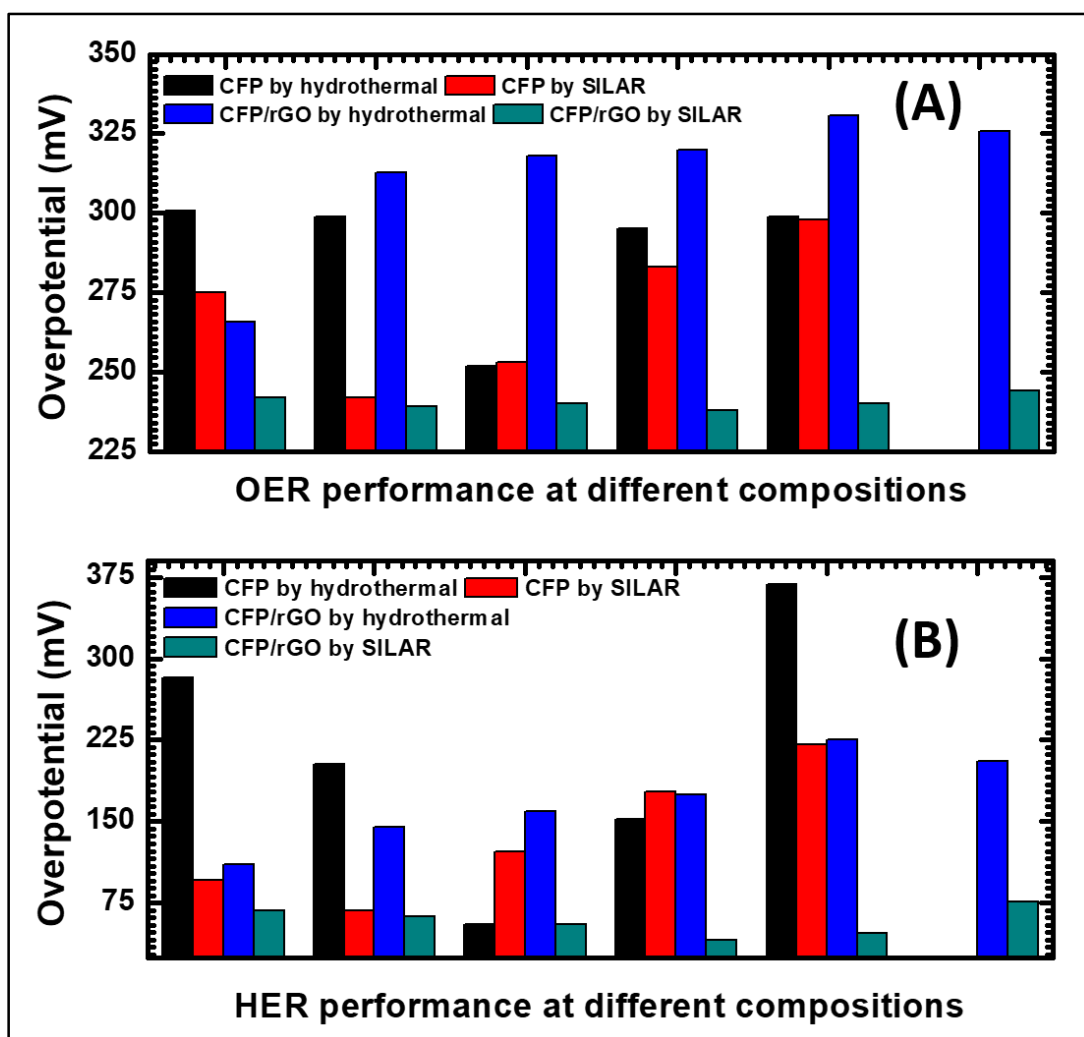


Figure 6.1: The comparative electrochemical performance in terms of overpotentials for (A) OER, and (B) HER of all the prepared cobalt-iron phosphate (CFP) and cobalt-iron phosphate/reduced graphene oxide (CFP/rGO) hybrid electrocatalysts synthesized by hydrothermal and SILAR methods.

To summarize and quantify the materials developed in this thesis, the electrochemical performance in terms of overpotentials for OER and HER of the all cobalt-iron phosphate (CFP) and cobalt-iron phosphate/reduced graphene oxide (CFP/rGO) electrocatalysts synthesized by different methods are compared with the help of bar diagrams. **Figure 6.1** shows the (A) OER and (B) HER performances of pristine and hybrid electrodes having different compositions. By comparing the electrodes synthesized via hydrothermal and SILAR methods, the hydrothermally synthesized pristine cobalt-iron phosphate electrodes gives the better results for OER and HER shown in **Figure 6.1(A,B)** with black bars (CFP by hydrothermal). But, by making the hybrid of best performing pristine cobalt-iron

phosphate with rGO, overpotentials increased suddenly for both the OER and HER as shown by blue bars (■ CFP/rGO by hydrothermal) due to material aggregation. On the other hand, by using the same strategy, pristine cobalt-iron phosphate thin film electrodes prepared by SILAR delivers very good results as compared to the hydrothermal. The lower overpotentials were recorded for OER and HER indicated in red bars (■ CFP by SILAR). In the best performing SILAR deposited cobalt-iron phosphate thin film electrode, the variation of rGO results the outstanding performance. Due to the hybridization, the electron transfer process becomes easier and both the performances of OER and HER were enhanced. In **Figure 6.1(A,B)** the aqua colored bars represent the OER and HER performances in terms of overpotentials of cobalt-iron phosphate/reduced graphene oxide hybrid electrodes (■ CFP/rGO by SILAR).

The overall water splitting tests were performed in same alkaline electrolyte bath for the electrodes of pristine cobalt-iron phosphate and cobalt-iron phosphate/reduced graphene oxide hybrids synthesized by SILAR method in chapter-5. For the study of overall water splitting, the best performing catalyst electrode was selected from the electrodes studied and discussed in previous chapters (chapter 3 and 4). The best performing thin film electrode as discussed earlier in chapter-4 was selected for this study and have applied as anode and cathode in the same alkaline electrolyte. As per the previous literature given in **Table 3.4**, KOH electrolyte is the best as alkaline electrolyte, hence for this present study, 1 M KOH was selected for overall water splitting. SILAR deposited pristine cobalt-iron phosphate and cobalt-iron phosphate/reduced graphene oxide hybrid electrodes were studied comparatively for overall electrochemical analysis and long term stability. During the 100 h continuous catalysis, the electrolyzer performance was slightly changed. For the pristine cobalt-iron phosphate, increase in potential from 1.72 V to 1.74 V to the delivery of current density of 10 mA/cm² was observed. On the other hand, cobalt-iron phosphate/reduced graphene oxide hybrid electrode gives the enhanced electrochemical water splitting performance and delivered the current density of 10 mA/cm² by the application of only 1.68 V potential to the cell. To summarize and quantify the materials developed in this thesis work, the overall performances of the best electrocatalysts from the thesis is listed in **Table 6.1**. The obtained results suggest commercial usefulness of SILAR deposited cobalt-iron phosphate/reduced graphene oxide hybrid electrodes for water splitting.

Table 6.1: Summary of overall water splitting performances of the synthesized best electrocatalysts in the thesis.

Catalyst	Synthesis method	Performance measured	Overpotential η @ 10 mA/cm ² (mV)		Tafel slope value (mV/dec)		Two electrode performance (V)
			OER	HER	OER	HER	
			1 M KOH	1 M H ₃ PO ₄	1 M KOH	1 M H ₃ PO ₄	1 M KOH
Cobalt-iron phosphate	Hydrothermal	Before stability	251.9	55.5	39.3	73.64	--
		After stability	250	37.3	35.2	68.97	--
		Before stability	266	110.7	61.5	74.6	--
		After stability	271	95.5	62.7	72.3	--
Cobalt-iron phosphate	SILAR	Before stability	242	67.9	38.33	35.92	1.72
		After stability	237	48.9	34.78	32.56	1.74
Cobalt-iron phosphate/reduced graphene oxide		Before stability	238	40.7	33.99	33.42	1.71
		After stability	239	40.7	33.52	33.43	1.68

PUBLICATIONS



Hydrothermally synthesized Iron Phosphate Hydroxide thin film electrocatalyst for electrochemical water splitting

Suraj A. Khalate ^a, Sujit A. Kadam ^b, Yuan-Ron Ma ^b, Sachin S. Pujari ^a, Supriya J. Marje ^a,
Pranav K. Katkar ^a, Abhishek C. Lokhande ^c, Umakant M. Patil ^{a,*}

^a Centre for Interdisciplinary Research (CIR), D. Y. Patil Education Society (Deemed to Be University), Kolhapur, 416 006, India

^b Department of Physics, National Dong Hwa University, Hualien, 97401, Taiwan

^c Department of Physics, Khalifa University of Science and Technology (KUST), Abu Dhabi, United Arab Emirates (UAE)



ARTICLE INFO

Article history:

Received 6 March 2019

Received in revised form

31 May 2019

Accepted 27 June 2019

Available online 28 June 2019

Keywords:

Electrochemistry

Hydrothermal synthesis

Heterogeneous catalysis

Ligand effects

Transition metals

Voltammetry

ABSTRACT

Hydrogen production is an immediate need to replace the fossil fuels to keep environmental balance, and water splitting is an effective solution in presence of catalyst through oxygen evolution reaction (OER) and hydrogen evolution reaction (HER). Herein, for the first time, we have synthesized Iron Phosphate Hydroxide ($\text{Fe}_{2.95}(\text{PO}_4)_2(\text{OH})_2$) thin film electrode as a superior electrocatalyst by facile hydrothermal method using binder free approach. The crystallographic properties are studied from X-ray diffraction pattern, and Reitveld refinement analysis shows best fit with the tetragonal Lipscombite structure of Iron Phosphate Hydroxide ($\text{Fe}_{2.95}(\text{PO}_4)_2(\text{OH})_2$). Flower like structure consist of agglomerated nanorods on micro and sub-micrometric spheres of $\text{Fe}_{2.95}(\text{PO}_4)_2(\text{OH})_2$ exhibits lower overpotential of 281 mV at 10 mA/cm² current density towards OER in alkaline (1 M KOH) medium and maintains its activity after 12 h catalytic stability test. Moreover, prepared electrode shows HER with overpotential 165.7 mV at current density 10 mA/cm² in acidic (1 M H₃PO₄) medium and demonstrates enhanced performance (126.4 mV overpotential) after 12 h catalytic stability. The $\text{Fe}_{2.95}(\text{PO}_4)_2(\text{OH})_2$ thin film electrodes show superior performance in OER and HER, compared with its oxide counterpart (Fe_2O_3).

© 2019 Elsevier Ltd. All rights reserved.

1. Introduction

Now days, a very intense work focused on the renewable energy generation by different sources such as wind [1], solar [2], hydrodynamical [3], tidal [4] and geothermal [5], and utilization in terms of electrical energy to control the global energy crisis and reduce environmental issues. Hydrogen is one of the most clean and potential renewable energy sources and the electrolysis of water to generate Oxygen and Hydrogen molecules is the cost-effective and efficient approach to get renewable energy [6–9]. The hydrogen evolution reaction (HER) and oxygen evolution reaction (OER) are the fundamentals of typical water splitting reaction and HER is comparatively easy which takes place at low overpotential. On the other hand, water splitting efficiency is largely constrained by the rate determining sluggish oxygen evolution reaction (OER), which involves four proton-coupled electron transfer causes high overpotential for O₂ assembly. In

electrochemical energy sources, appropriate electrocatalysts are crucial components of an energy efficient hydrogen generation. To minimize the overpotential for OER and energy losses, a good electrocatalyst must have high catalytic activity, superior conductivity and adequate electrocatalytic stability. The state-of-the-art electrocatalysts considered to the noble metal-based valuable materials such as Platinum (Pt), Ruthenium (Ru) and Iridium Oxides (IrO₂) have an identity as best OER catalysts due to low overpotential [10–12]. However, these metals are very rare in the Earth's crust, thus it is difficult to commercialize them. To create the significant development in the field of electrocatalysis and there is need to replace the conventional electrocatalysts. Amongst various non-noble metal catalysts, transition metals are the promising alternative for these rare metal electrocatalysts due to their smaller d orbitals, lower crystal-field activation energies and competent bifunctional catalytic properties for water splitting. The materials of transition metals as Hydroxides, Sulphides, Selenides, Phosphates, Phosphides, Nitrides, have great interest due to their Earth abundance, high-efficiency and stability for large-scale energy production [13–20].

* Corresponding author.

E-mail address: umakant.physics84@gmail.com (U.M. Patil).



Cobalt doped iron phosphate thin film: An effective catalyst for electrochemical water splitting

Suraj A. Khalate^a, Sujit A. Kadam^b, Yuan-Ron Ma^b, Sachin S. Pujari^a, Umakant M. Patil^{a,*}

^a Centre for Interdisciplinary Research (CIR), D.Y. Patil Education Society, Kolhapur 416006, India

^b Department of Physics, National Dong Hwa University, Hualien 97401, Taiwan

ARTICLE INFO

Article history:

Received 26 March 2021

Received in revised form 9 June 2021

Accepted 19 June 2021

Available online 24 June 2021

Keywords:

Catalytic stability

Doping

Electrochemistry

Heterogeneous catalysis

Water splitting

ABSTRACT

For practically feasible water splitting to fulfill the need of energy, the development of efficient, robust and long lasting catalyst is necessary. Transition metal compounds facilitates the good catalytic properties due to facile transition of their oxidation states. We here reported a novel process for the synthesis of novel material as cobalt doped iron phosphate thin films. The pristine iron phosphate thin films have synthesized by regular facile hydrothermal method and to achieve doping of the cobalt into iron phosphate, second step hydrothermal ion-exchange process was used. The as synthesized cobalt doped iron phosphate thin film electrode exhibits excellent electrochemical OER and HER catalytic water splitting performance. The prepared material was demonstrated by two electrodes overall water splitting electrolyzer in alkaline medium at lowest potential of 1.72 V to deliver 10 mA/cm² current density after 4 days' continuous water splitting test. The outstanding catalytic stability proved 0.4 Co:FePi thin film electrodes are robust water splitting electrocatalyst.

© 2021 Elsevier B.V. All rights reserved.

1. Introduction

Upon looking at the present scenario of the energy generation and consumption, an eye capturing fact can be realized that we need greater energy than what we have today. It is the necessity to produce energy from green and sustainable energy resources to maintain our benign environment and future from the energy crisis, global warming and environmental pollution. Hydrogen is one of the best energy sources from clean and green energy sources, and is expected to play a major role in a future sustainable energy sector [1,2]. Hydrogen from energy sources such as solar or wind electricity is the clean production of energy, also the storage of energy in the clean form as a standby during the ups and downs of solar and wind power. Electrochemical water splitting is an effective technique to convert electrical energy into chemical energy in the form of hydrogen by using proper catalyst electrode. Electrochemical water splitting is the combined reaction of two half reactions as oxygen evolution reaction (OER) and complimentary hydrogen evolution reaction (HER). These reactions of water splitting (OER and HER) are constrained by the rate determining sluggish four electron coupled proton transfer process and hence have low conversion efficiency

[3–5]. At present, the best electrocatalysts with high efficiency are the state-of-the-art materials as platinum, ruthenium/iridium based oxides which are widely used. The best electrocatalyst for HER is platinum, which only requires onset overpotential of nearly zero. But the commercial use of these state-of-the-art catalyst materials is limited by their scarcity, high cost, large overpotentials at high current densities and poor stability [6]. Many researchers are interested and engage in the development of alternative cost-effective, non-noble metal and highly stable electrocatalysts for efficient overall water splitting. Variety of new non-noble metal based catalysts are under research and development process. First row (3d) transition metal based materials have good catalytic properties due to facile transition of their oxidation states. Transition metal based materials such as, transition metal-transition metal alloys (TMAs), transition metal oxides (TMOs), transition metal nitrides (TMNs), transition metal dichalcogenides (TMDs), transition metal phosphides (TMPs), transition metal carbides (TMCs), transition metal borides (TMBs), etc. are playing leading role in water splitting [7]. Few reports are available on transition metal phosphate electrode materials for electrochemical water splitting. Transition metal phosphates play an important role by facilitating adsorption and stabilizing active centers, also phosphate ligands give the favorable conditions for electrolyte ion adsorption and oxidation by distorting local atomic geometry and facilitating the oxidation of metal atoms during proton coupled electron transfer [8].

* Corresponding author.

E-mail address: umakant.physics84@gmail.com (U.M. Patil).

Enhanced Energy Density of All-Solid-State Asymmetric Supercapacitors Based on Morphologically Tuned Hydrous Cobalt Phosphate Electrode as Cathode Material

Pranav K. Katkar,[†] Supriya J. Marje,[†] Sachin S. Pujari,[†] Suraj A. Khalate,[†] Abhishek C. Lokhande,[‡] and Umakant M. Patil^{*,†}

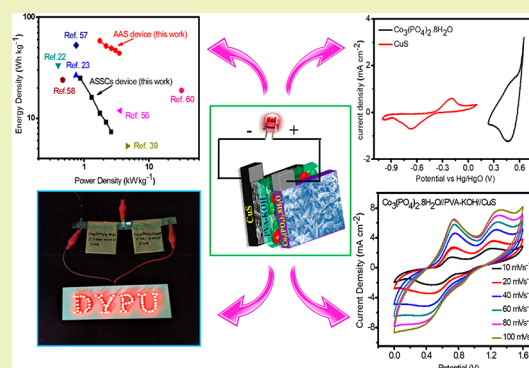
[†]Centre for Interdisciplinary Research, D. Y. Patil Education Society (Deemed to be University), Kasaba Bawada, Kolhapur, 416 006 Maharashtra, India

[‡]Department of Material Science and Engineering, Chonnam National University, Yongbong-dong, Puk-Gu, Gwangju 500 757, Republic of Korea

Supporting Information

ABSTRACT: In the present investigation, microflowers-like hydrous cobalt phosphate is prepared via a facile single-step hydrothermal method on stainless steel substrate. The microflowers-like morphology of hydrous cobalt phosphate thin film consists of microplates and further microplates converted to flakes by means of a change in length, width, and thickness with urea variation. Hydrous cobalt phosphate thin film electrode demonstrates a high specific capacitance of 800 F g^{-1} at 2 mA cm^{-2} with 33.62 Wh kg^{-1} energy density and 3.12 kW kg^{-1} power density. By taking advantage of hydrous cobalt phosphate thin film (as a cathode electrode) and copper sulfide thin film (as an anode electrode), the asymmetric devices (aqueous/all-solid-state) are fabricated. Aqueous asymmetric device shows a high specific capacitance of 163 F g^{-1} at 2 mA cm^{-2} with an energy density of 58.12 Wh kg^{-1} and power density of 3.52 kW kg^{-1} . Moreover, the all-solid-state asymmetric supercapacitor device delivers a high specific capacitance of 70 F g^{-1} at 2 mA cm^{-2} with 24.91 Wh kg^{-1} energy density and 2.63 kW kg^{-1} power density in PVA–KOH gel electrolyte. The long-term cyclic stability (94% after 3000 cycles) and actual practical demonstration (lightning 65 red LEDs) suggest an industrial application of the all-solid-state asymmetric device.

KEYWORDS: Cobalt phosphate, Hydrothermal method, Microflowers, Solid-state asymmetric supercapacitor, Thin film



INTRODUCTION

Increasing demand for portable electronics (like mobile phones, e-papers, laptops, etc.) has significantly encouraged the research community to fabricate high-performing electric energy storage devices.^{1–3} Among the various types of energy storage devices, a supercapacitor (SC) is the supreme choice for clean and green energy, which offers excellent characteristics such as good cycle stability, high power density, and environmental benignity and is presently employed in hybrid vehicles, consumer electronics, and renewable energy storage devices,^{2–5} though the major challenges of a supercapacitor are less stability at high-rate conditions and low energy density (as compared to batteries), which significantly constrains its application.⁵ As per the energy density equation (0.5 CV^2), to increase the energy density development of new electrode materials with a high capacitance (C) is one way and another is to build a supercapacitor device with a wide operating potential window (V). Thus, new superior electrode materials having high specific capacitances, long cycling lives, and rational assemblies of anode and cathode materials in a supercapacitor device are required to be investigated. Therefore, extensive

research has been devoted to fabricating asymmetric supercapacitor devices using different cost-effective electrode materials with high specific capacitance.^{6,7}

Generally, carbon-based materials, e.g., carbon nanotubes (CNTs), graphene and activated carbon (AC), conducting polymers (e.g., polythiophene, polypyrrole, and polyanilines), transition metal oxides/hydroxides/sulfides, and their composites, are employed as active materials for supercapacitors. The transition-metal oxides, metal hydroxides, and metal sulfides such as Co_3O_4 ,⁸ MnCoO ,⁹ RuO_x ,¹⁰ $\beta\text{-Co}(\text{OH})_2$,¹¹ CoS ,¹² CoS_2 ,¹³ etc., have attracted significant attention as pseudocapacitive electrode material, but they suffer from low specific capacitance and energy density due to poor conductivity.^{14,15} Thus, there is a need to develop low-cost alternative electrode materials to improve the performance of supercapacitors. Recently, for supercapacitor as well as catalysis application, various transition-metal phosphates have been studied and

Received: January 25, 2019

Revised: June 7, 2019

Published: June 7, 2019



Effect of phosphate (anion) precursor on structural and morphology behavior of nickel phosphate thin films and its supercapacitive performance

Supriya J. Marje^a, Pranav K. Katkar^a, Sachin S. Pujari^a, Suraj A. Khalate^a, Prashant R. Deshmukh^b, Umakant M. Patil^{a,*}

^a Centre for Interdisciplinary Research, D. Y. Patil Education Society (Deemed to be University), Kasaba Bawada, Kolhapur 416 006, M.S., India

^b Department of Mechanical Engineering, Chungnam National University, Daejeon, South Korea

ARTICLE INFO

Keywords:

Anion precursor effect
Asymmetric supercapacitor
Binder-free synthesis
Chemical bath deposition method
Nickel phosphate
Thin film electrode

ABSTRACT

In present work, reproducible and economic chemical bath deposition method is used to deposit nickel phosphate thin films on stainless steel substrate for supercapacitor application and effect of anion precursors on structure and morphology of prepared thin film is studied. Change in structure from crystalline to amorphous is observed in prepared thin films due to precursor variation. Also, microplate to microsphere like morphological alteration is observed with the same. The microsphere like morphology of amorphous nickel phosphate thin film electrode exhibits the highest specific capacitance of $\sim 1031 \text{ F g}^{-1}$ (specific capacity 114.6 mAh g^{-1}) at 0.5 mA cm^{-2} current density. Its practical application is tested by preparing asymmetric supercapacitor device comprising amorphous nickel phosphate thin film as positive electrode and reduced graphene oxide as negative electrode. Asymmetric device delivers highest specific capacitance of $\sim 100 \text{ F g}^{-1}$ at 6 mA cm^{-2} current density with energy density of 45.33 Wh kg^{-1} at a high power density of 1.5 kW kg^{-1} and offers 80% capacitance retention over 3000 cycles.

1. Introduction

Today's increasing requirement of energy storage devices for high power applications catches researcher's attention. Main requirements of energy storage device are reversible and fast release of electrical energy and that can be fulfilled by supercapacitor devices [1,2]. Numerous materials has been developed and studied by researcher for supercapacitor application such as, transition metal oxides [3], hydroxides [4], sulfides [5] and phosphides [6]. To develop economical stabled material with high energy and power density for supercapacitor application needs to explore new materials. In the search of inexpensive electrochemically active material, many researchers attracted towards metal phosphate materials for supercapacitor application [7].

Among metal phosphates, nickel and cobalt phosphate were widely studied for different application due to its earth abundancy and high conductivity. Moreover, several chemical methods were used to prepare nickel phosphate materials for supercapacitor application such as hydrothermal [8–12], microwave assisted [13], calcination [14,15], co-precipitation [16,17] and sonochemical [18,19] etc. Different chemical method offers different microstructure of nickel phosphate such as nano-microrod, microflower, nanosphere etc. that ultimately exhibits

different electrochemical capacitive performances.

However, very few reports explored the effect of precursor source on the microstructure and ultimately supercapacitive performance of the material. Li et. al achieved different morphologies of Ag_3PO_4 material using simple way phosphate precursor variation from H_3PO_4 to Na_2HPO_4 in hydrothermal synthesis process. This experiment resulted tremendous change in morphologies in prepared material with respect to precursor variation. Analogous effects are studied in terms of supercapacitive performance, 3D tetrapod like microcrystals of Ag_3PO_4 sample shows 1.6 times higher capacitance than a sample composed with irregular particles and some polyhedrons [20]. Selective shapes/morphology of material can be prepared by changing precursors and these results are observed by Bi. et. al. only changing silver precursor from acetate to nitrate in the preparation of silver phosphate using precipitation process. Without using capping agent selective shapes from rhombic dodecahedrons to perfect cubes of silver phosphate were prepared. Photocatalytic activity of controlled but different morphologies were studied and reported that, the rhombic dodecahedrons are more catalytically active than perfect cubic structured material [21]. Similar type of results obtained by Gunjekar et. al. in the simple chemical bath preparation of silver phosphate thin films. Authors obtained

* Corresponding author.

E-mail address: umakant.physics84@gmail.com (U.M. Patil).

<https://doi.org/10.1016/j.mseb.2020.114641>

Received 30 January 2020; Received in revised form 8 June 2020; Accepted 16 July 2020

0921-5107/ © 2020 Elsevier B.V. All rights reserved.



Highly sensitive hydrothermally prepared nickel phosphate electrocatalyst as non-enzymatic glucose sensing electrode

Sachin S. Pujari¹ · Sujit A. Kadam² · Yuan-Ron Ma² · Suraj A. Khalate¹ · Pranav K. Katkar¹ · Supriya J. Marje¹ · Umakant M. Patil¹

© Springer Science+Business Media, LLC, part of Springer Nature 2020

Abstract

Present investigation describes a successful preparation of nickel phosphate ($\text{Ni}_3(\text{PO}_4)_2 \cdot 8\text{H}_2\text{O}$) thin film electrodes by facile one pot hydrothermal method. As developed $\text{Ni}_3(\text{PO}_4)_2 \cdot 8\text{H}_2\text{O}$ thin film electrodes with the variation of thickness are examined for morphological change and glucose sensing. The $\text{Ni}_3(\text{PO}_4)_2 \cdot 8\text{H}_2\text{O}$ thin film electrodes exhibit linear response with respect to the variation in glucose concentration from 2.5 to 30 mM and acquire the sensitivity of $8312 \mu\text{A mM}^{-1} \text{cm}^{-2}$ with 437 μM LOD. Selectivity performance of $\text{Ni}_3(\text{PO}_4)_2 \cdot 8\text{H}_2\text{O}$ thin film electrode towards glucose in presence of dopamine, fructose and lactose is studied. The results suggest that $\text{Ni}_3(\text{PO}_4)_2 \cdot 8\text{H}_2\text{O}$ thin film electrode is beneficial for glucose sensing application due to enormous active sites with the high specific surface area of the active material.

Keywords Nickel phosphate · Hydrothermal method · Microplates · Non-enzymatic glucose sensor · Thin film electrode

1 Introduction

Nowadays, biosensors are mostly investigated in the area of biomedical analysis, food industry, and clinic diagnosis [1, 2]. Glucose sensors are widely used in clinical diagnostics because of their fast examination and reliability [3]. Therefore, a lot of efforts are underway for the construction of rapid, reliable and reproducible glucose sensing devices [4]. Electrochemical sensors are known as a good scientific device due to their fast and low-cost glucose recognition [5, 6]. Biosensors prepared by various methods have been studied from past few years. Based on the multiple characteristics and phenomena of the techniques as well as detector, applied biosensors would be classified into electrical biosensors, vibrational biosensors, electrochemical

biosensors, optical biosensors and mechanical biosensors. Chronoamperometric or electrochemical glucose sensors are classified into two types an enzymatic and non-enzymatic glucose sensor. In the type first, enzymatic oxidase on the surface of electrode is immobilized and dioxygen quantitatively reduced to the hydrogen peroxide and monitored by chronoamperometric method [7]. The traditional enzymatic glucose sensor offers high selectivity, better time response but some drawbacks are associated such as, limited stability and difference in response with the changing pH as well as temperature [8]. On the other hand, non-enzymatic glucose sensors offer many advantages such as stability, reproducibility and their mechanism for detecting glucose molecules is based on redox reaction of active material [5, 9]. Among different biosensors, electrochemical biosensors involve easy mechanism and fabrication processes, simple operation and quick response time. It is familiar that, transition metal based electrodes are extremely cost-effective, facile to synthesize, highly electroactive and exhibit good glucose sensing [10, 11].

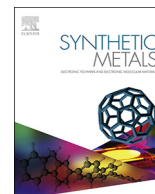
In recent times, there are lots of efforts undergoing for glucose detection using nickel based catalysts. Almost all of them shown improved performance of glucose sensor by developing nickel catalyst on the conductive materials like as carbon nanofiber [12], Mxene [13] and graphene [14]. Yet few works were prepared to simultaneously modify

Electronic supplementary material The online version of this article (<https://doi.org/10.1007/s10934-020-01000-0>) contains supplementary material, which is available to authorized users.

✉ Umakant M. Patil
umakant.physics84@gmail.com

¹ Centre for Interdisciplinary Research, D. Y. Patil Education Society, Kasaba Bawada, Kolhapur 416 006, India

² Department of Physics, National Dong Hwa University, Hualien 97401, Taiwan



Regulated micro-leaf like nickel pyrophosphate as a cathode electrode for asymmetric supercapacitor

Supriya J. Marje^a, Pranav K. Katkar^a, Sachin S. Pujari^a, Suraj A. Khalate^a, Abhishek C. Lokhande^b, Umakant M. Patil^{a,*}

^a Centre for Interdisciplinary Research, D.Y. Patil Education Society (Deemed to be University), Kasaba Bawada, Kolhapur, 416 006, Maharashtra, India

^b Department of Physics, Khalifa University of Science and Technology (KUST), Abu Dhabi, United Arab Emirates

ARTICLE INFO

Keywords:

Asymmetric supercapacitor
Chemical bath deposition method
Composition variation
Nickel pyrophosphate
Thin film electrode

ABSTRACT

In present work, nickel pyrophosphate ($\text{Ni}_2\text{P}_2\text{O}_7 \cdot 8\text{H}_2\text{O}$) thin film on stainless steel substrate synthesized using facile chemical bath deposition method and used as cathode electrode for asymmetric supercapacitor. Three compositions of nickel phosphate with varying of nickel:phosphate (2:1, 1:1 and 1:2) molar ratio are prepared to study composition effect on microstructure and subsequently on supercapacitive performance. Morphology changes with composition from microflower to leaf like, consequently supercapacitive performance influences with increasing phosphate content in material. The well dispersed leaf like microstructure (nickel:phosphate;1:2) of nickel pyrophosphate offers more active sites and it shows maximum specific capacitance of 482 F g^{-1} at current density of 3 mA cm^{-2} along with 99.73% capacitive retention over 2500 cycles. Moreover, an asymmetric device fabricated using nickel pyrophosphate and reduced graphene oxide as a positive and negative electrode, respectively. Prepared asymmetric supercapacitor offers specific capacitance of 74.81 F g^{-1} at 0.9 mA cm^{-2} current density with 26.6 Wh kg^{-1} energy density at a moderately high power density of 870.6 W kg^{-1} . Also, exhibits 87.35% of capacitive retention over 5500 cycles at 4 mA cm^{-2} current density.

1. Introduction

To reduce global warming, promote green and clean energy, and fight with energy crisis, usage of sustainable energy sources increased [1]. Fulfil increasing demand in global power supply for different application, have to store electricity efficiently produced from sustainable energy sources [2]. So, attention shifted towards cost effective, easy to use and maintenance free energy storage devices with high stability [3]. Supercapacitor come in focus because it offers high energy and power density as compare to conventional capacitors and batteries, respectively [4,5]. These amazing properties of supercapacitor encourage to use it either individually or in combination with batteries/fuel cell for different application [6,7].

Supercapacitors are divided into three categories on the basis of charge storage mechanism such as EDLC, pseudocapacitor and hybrid supercapacitor [8]. There are numerous materials were investigated as an supercapacitor electrode material such as, metal oxides [9,10], hydroxides [11] and sulfides [12] but they suffers from some limitations such as, poor stability, poor conductivity and lower specific capacitance [13,14]. To reach high energy and economical demands, need to

develop electrode material has low-cost, high specific capacitance and favourable cycling ability [15].

Transition metal phosphates widely studies for decades and used in various applications as, catalysis/photocatalysis [16,17], energy storage devices [18] and sensors [19]. Recently, they fascinated for energy storage application owing to their excellent conductivity, abundant active sites, wide structural channels for electrolyte ions percolation and most importantly offer stable structure due to P–O covalent bond [20]. Among metal phosphates, nickel and cobalt aided in energy storage due to excellent redox action and also, they are earth abundant and widely distributed. Various structures of nickel phosphates such as pyrophosphate and orthophosphate, can facilitates different ionic conductivity and consequently rate capability [21].

So, different microstructure and polymorphs of nickel phosphate were prepared using various methods for supercapacitor application and reported in literature. Sankar et al. grown one dimensional nanorods of nickel pyrophosphate on nickel foam by simple hydrothermal method [22]. Similarly, Pang et al. [23] synthesized nickel pyrophosphate microrods by calcination of ammonium nickel phosphate material and Senthilkumar et al. [24] prepared nano grains of nickel

* Corresponding author.

E-mail address: umakant.physics84@gmail.com (U.M. Patil).

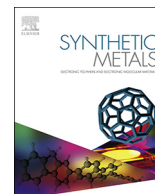


Facile Synthesis of Microstrip-Like Copper Phosphate Hydroxide Thin Films for Supercapacitor Applications

SACHIN S. PUJARI,¹ SUJIT A. KADAM,² YUAN-RON MA,²
PRANAV K. KATKAR,¹ SUPRIYA J. MARJE,¹ SURAJ A. KHALATE,¹
ABHISHEK C. LOKHANDE,³ and UMAKANT M. PATIL^{1,4}

1.—Centre for Interdisciplinary Research, D. Y. Patil Education Society, Kasaba Bawada, Kolhapur 416 006, India. 2.—Department of Physics, National Dong Hwa University, Hualien 97401, Taiwan. 3.—Department of Physics, Khalifa University of Science and Technology (KUST), Abu Dhabi, United Arab Emirates. 4.—e-mail: umakant.physics84@gmail.com

Binder-free copper phosphate hydroxide $[\text{Cu}_2(\text{PO}_4)(\text{OH})]$ thin films have been prepared on stainless-steel (SS) substrates at 393 K via a facile hydrothermal method. X-ray diffraction analysis confirmed the formation of orthorhombic-structured copper phosphate hydroxide $[\text{Cu}_2(\text{PO}_4)(\text{OH})]$ thin films with uniform microstrip-like morphology and Brunauer–Emmett–Teller (BET) surface area of $5.26 \text{ m}^2 \text{ g}^{-1}$. The electrochemical performance of the films depended on their thickness, with a maximum specific capacitance of 280 F g^{-1} at a scan rate 5 mV s^{-1} in 1 M KOH electrolyte. The $[\text{Cu}_2(\text{PO}_4)(\text{OH})]$ electrode delivered an energy density of 3.85 Wh kg^{-1} and a power density of 264.70 W kg^{-1} with excellent (91%) capacitive retention after 2000 cycles. This excellent electrochemical performance shows that such microstrip-like $\text{Cu}_2(\text{PO}_4)(\text{OH})$ thin films are promising electrodes for high-performance supercapacitors.



Single-pot hydrothermal synthesis of manganese phosphate microrods as a cathode material for highly stable flexible solid-state symmetric supercapacitors

Pranav K. Katkar^a, Supriya J. Marje^a, Sachin S. Pujari^a, Suraj A. Khalate^a, Prashant R. Deshmukh^b, Umakant M. Patil^{a,*}

^a Centre for Interdisciplinary Research, D. Y. Patil Education Society (Deemed to Be University), Kasaba Bawada, Kolhapur, 416 006, M.S, India

^b Department of Mechanical Engineering, Chungnam National University (CNU), Daejeon, 34137, Republic of Korea



ARTICLE INFO

Keywords:

Hydrothermal method
Manganese phosphate
Microrods
Flexible symmetric solid-state device
Supercapacitor
Thin film

ABSTRACT

Here, we report a binder-free synthesis of microrods-like manganese phosphate thin film over stainless steel substrate by a facile, single-pot hydrothermal method. The XRD analysis reveals that, the formation of manganese phosphate $[\text{Mn}_3(\text{PO}_4)_2]$ material of a monoclinic crystal structure. From SEM images observed microrods like morphology of manganese phosphate with an average width of $\sim 25 \mu\text{m}$. The manganese phosphate electrode shows a better electrochemical performance with a specific capacitance of 145 F g^{-1} at 0.2 mA cm^{-2} current density in $1.0 \text{ M Na}_2\text{SO}_4$ electrolyte. Moreover, the flexible solid-state symmetric electrochemical energy storage device was assembled with PVA- Na_2SO_4 solid gel-electrolyte consists of manganese phosphate as anode and cathode electrode. The corresponding symmetric supercapacitor achieves a high energy density of 11.7 Wh kg^{-1} at a high power density of 1.41 kW kg^{-1} with an excellent specific capacitance of 37 F g^{-1} at 0.1 mA cm^{-2} current density. Manganese phosphate shows long-term electrochemical cyclic stability at a current density of 0.8 mA cm^{-2} for 9000 galvanostatic charge-discharge cycles with excellent capacitance retention (99 %). This excellent capacitive performance confirms that the manganese phosphate is promising material and fabricated flexible solid-state symmetric supercapacitor has high potential in the field of portable and bendable energy storage devices.

1. Introduction

Global extensions have stimulated the rate of energy consumption to very high levels, and the utilization of highly efficient, clean and sustainable energy conversion technologies and renewable energy resources are getting much attention. Among the existing energy generation and storage devices, supercapacitors (SCs) are considerably well attractive to solve the increasing concern about the energy crisis. [1]. Supercapacitor provides high power density, moderate energy density, longer durability and fast charging capability than batteries or fuel cells. Remarkably, flexible device with long cycle life has attracted significant attention in the field of power-source applications such as portable electronics, rollup/wearable displays, energy back-up device, sensor networks, electric vehicles, and mobile phones [2–4]. On the basis of energy storage mechanism, electrochemical capacitors are categorized into mainly two types, pseudocapacitors and electric double-layer capacitors (EDLCs). The EDLCs based materials with large specific

surface area, like carbonaceous materials, are storing the energies through electrical double layers. However, pseudocapacitor materials display quite a lot of oxidation states and store energy in electric double layers, as well as redox reaction at the electrode surfaces as like the transition metal oxides/hydroxides, sulfides, and conductive polymers [5–7]. Therefore, comparing pseudocapacitors with the EDLCs, pseudocapacitor shows good capacitive behavior with excellent specific capacitance [8].

Significantly more effort for fabricating high-performance supercapacitors has been done using various materials, such as $\text{Co}(\text{OH})_2$ [9], MnCo_2O_4 [10], rGO-MnO_2 [11], $\alpha\text{-MnO}_2$ [12], and $\text{Mn}(\text{OH})_2$ [13]. Mn-based oxide/hydroxides are hard to reach the theoretical capacitance, power and energy density values because of poor electrical conductivity and the less specific capacitance due to the lower ion transfer rate [10,14]. The cobalt-based materials are more concentrated because of their attractive capacitance values, but they shows less cyclic stability compared to manganese based materials [15].

* Corresponding author.

E-mail address: umakant.physics84@gmail.com (U.M. Patil).

<https://doi.org/10.1016/j.synthmet.2020.116446>

Received 7 February 2020; Received in revised form 26 May 2020; Accepted 29 May 2020

0379-6779/ © 2020 Elsevier B.V. All rights reserved.